LBNL-42255

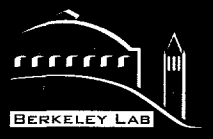

ERNEST ORLANDO LAWRENCE
BERKELEY NATIONAL LABORATORY

6459

Proton-Decay Spectroscopic Studies of the Exotic Nuclides ^{23}Al, ^{23}Si, ^{22}Al and ^{77}Rb

Michael William Rowe

Nuclear Science Division

September 1998

Ph.D. Thesis

DISCLAIMER

Portions of this document may be illegible in electronic image products. Images are produced from the best available original document.

LBNL-42255

Proton-Decay Spectroscopic Studies of the Exotic Nuclides ^{23}Al, ^{23}Si, ^{22}Al and ^{77}Rb

Michael William Rowe
Ph.D. Thesis

Department of Chemistry
University of California, Berkeley

and

Nuclear Science Division
Ernest Orlando Lawrence Berkeley National Laboratory
University of California
Berkeley, CA 94720

September 1998

This work was supported by the Director, Office of Energy Research, of the U.S. Department of Energy under Contract No. DE-AC03-76SF00098.

Proton-Decay Spectroscopic Studies of the Exotic Nuclides ^{23}Al, ^{23}Si, ^{22}Al and ^{77}Rb

by

Michael William Rowe

Proton-Decay Spectroscopic Studies of the Exotic Nuclides ^{23}Al, ^{23}Si, ^{22}Al and ^{77}Rb

by

Michael William Rowe

B. S. (University of Vermont) 1990

A dissertation submitted in partial satisfaction of the requirements for the degree of

Doctor of Philosophy

in

Chemistry

in the

GRADUATE DIVISION

of the

UNIVERSITY OF CALIFORNIA, BERKELEY

Committee in charge:

Professor Joseph Cerny, Chair

Professor Darleane C. Hoffman

Professor Stanley G. Prussin

Fall 1998

ABSTRACT

Proton-Decay Spectroscopic Studies of the Exotic Nuclides ^{23}Al, ^{23}Si, ^{22}Al and ^{77}Rb

by

Michael William Rowe

Doctor of Philosophy in Chemistry
University of California, Berkeley
Professor Joseph Cerny, Chair

Aluminum-23 was produced by 40 MeV $^{3}He^{2+}$ bombardments of Mg targets in four experiments at the LBNL 88" Cyclotron. Reaction products were transported via helium-jet to a detection chamber where they were counted using two low-energy particle-identification (PI) telescopes. New proton groups were observed with laboratory energies (and intensities relative to the known peak at 838±5 keV) of 246±20 (33±3%) and 556±5 keV (68±5%), respectively. Several possible decay assignments are discussed for the former group. The possibility that it originates from the decay through the isobaric analog state (IAS) and corresponding implications for isospin mixing and the proton-capture resonance strength are discussed. The Gamow-Teller strength function has been deduced from these and several weaker proton transitions; the results are compared with theoretical predictions.

Silicon-23 and ^{22}Al were produced in a 110 MeV $^{3}He^{2+}$ bombardment of a ^{24}Mg target; reaction products were transported via helium jet and observed by two PI telescopes with proton sensitivity from 0.35-12.5 MeV. Three weak proton peaks at 7673±33, 9642±57 and

10861±68 keV have been tentatively assigned to the beta-delayed proton decay of ^{23}Si through its IAS. From these results, the estimated ^{23}Si mass excess is 23.25±0.05 MeV. Beta-delayed two-proton sum peaks were observed at 4478±15 and 6111±15 keV (c.m.), in agreement with earlier work on the decay of ^{22}Al at wide relative-emission angles. The energies of several weaker two-proton sum peaks were compared with predicted and experimental values for the β-2p decay of ^{23}Si.

A search for proton emission from a predicted $19/2^-$ isomer of ^{77}Rb has been performed in three bombardments of Ca targets by ^{40}Ca beams at energies of 145, 160 and 132 MeV. Products of the first two bombardments were transported via helium jet and observed by two PI telescopes. In the third bombardment, the mass separator RAMA transported mass-77 products to a PI telescope and two gamma-ray detectors. The direct and mass-separated measurements set limits of ~5×10^{-6} and 1×10^{-5}, respectively, on production of the isomer relative to the ground state, assuming an isomer half-life of 240 ms or longer.

For Mom and Dad,

with love

T A B L E O F

CONTENTS

L I S T O F

FIGURES

L I S T O F

TABLES

ACKNOWLEDGMENTS

I wish to thank my research advisor, Professor Joseph Cerny, for his years of guidance and inspiration. Thanks also for patiently listening to the many wild (and often incorrect) claims I have made in the course of my graduate career; one learns the most through making mistakes. I also thank Dr. Dennis Moltz, for teaching me the nitty-gritty, hands-on part of the job and the value of persistence in the face of experimental adversity. His knowledge of experimental systems for the detection of proton-rich nuclides was invaluable to this work.

I am greatly indebted to the other members of the Cerny Group, both past and present, including graduate students Jon Batchelder, Ted (Satan) Ognibene, and Fanqing Guo, post-docs Rich Tighe, James Powell, and Rainer Joosten, and "adjunct" members Peter Haustein, Xiaoji Xu, Steve Thompson, Celine Détraz and Eric Wang. Aside from doing an awful lot of the work that made this thesis possible, you have taught and inspired me a lot, served as all-purpose sounding boards for my ideas (you're right, it'll never work...) and generally made the work enjoyable. I also wish to thank the rest of the scientific staff at the 88-Inch Cyclotron for helping me out countless times and making LBL a great place to do research.

No matter how talented the brewer or great their inspiration, without quality ingredients and sound equipment, they will be damned lucky to make Budweiser. (And no, rice is NOT a quality ingredient!) The success of this laboratory rests critically on the shoulders of its technical staff, and LBL is truly blessed by some of the most talented, helpful and friendly people I've ever met. Without the people who maintain the pumps, make the targets, fix the electronics, wire the buildings, build the crazy stuff I've designed (and I need it yesterday!), and keep us from contaminating the world or electrocuting ourselves, this thesis would be shorter than a third grade book report. Particular thanks go to Fred Perry, Ed

Chubak and the rest of the 88" shop staff for all the excellent equipment they built for me (and for providing a cool place to hang), to Aran Guy and the whole cyclotron crew for providing great beams and stimulating conversation at 4 AM, to Bill Rathbun for bringing order to CHAOS no matter what the time, and to Bob Fairchild for keeping the regulatory dragons at bay. My sincere gratitude to all of you. Thanks also to the administrative staff for transparently shuffling the money, scheduling the runs and fixing the messes I've usually made of things by forgetting deadlines.

Neither last nor least, thank you to my past and present house mates (especially Rick, Maria, Sony and Luka Linguica de Santa Maria de Guadeloupe) and all my other friends for, well, for making getting up in the morning (or in the afternoon, at least) a worthwhile proposition. Most of all, thanks to my family for their many years of love and support. Couldn't have done it without you all...really.

And finally, the great teat I have suckled over the course of my long graduate career: Uncle Sam. (What?! Does Uncle Sam have TEATS? What does this mean?!!) This work was supported by the Director, Office of Energy Research, Division of Nuclear Physics of the Office of High Energy and Nuclear Physics of the U. S. Department of Energy under Contract DE-AC03-76SF00098.

C H A P T E R 1

INTRODUCTION

1.1 Studies of Proton-Rich Nuclei

Most of our understanding of nuclear systems has been gained by examining trends in stable or near-stable nuclei. By extending measurements to nuclei far from stability, the degree to which this understanding remains valid may be judged. Effects that are non-existent or too subtle to be noticed among nuclei near stability may become observable in exotic nuclei. These studies shed light on such topics as the variation of the nuclear mass surface, unusual decay modes that only occur far from stability, and the structure of exotic nuclei. This thesis examines the properties of several proton-rich exotic nuclei using the techniques of proton-decay spectroscopy.

Near–drip-line nuclides may be produced in fusion-evaporation reactions, although the cross sections tend to be fairly small. Such reactions are not very selective; many other radioactive nuclei will be produced simultaneously in far greater yields. Most other reaction products will decay primarily by beta emission. Because direct- and beta-delayed proton decays (and among light nuclides, beta-delayed alpha decays) are energetically possible only in nuclei far from stability, drip-line nuclei can be distinguished from other reaction products by observing these decay modes. Proton-decay spectroscopy has thus proved to be a useful tool for the determination of properties of nuclides near the proton drip line (e.g., see Har89, Mol89, Hof89, Roe92, Woo97). Proton decay measurements can provide information on the existence, masses, half-lives and level structures of exotic nuclides. In some cases, studies of proton decay can also elucidate nucleosynthesis processes (Cha92).

Several factors make the study of near-drip line nuclei particularly challenging. The high levels of radiation surrounding the target during bombardment often require that the activity be transported away from the target area for counting. Further, it is common for exotic nuclei to have half-lives shorter than 1 s because the energy available for beta decay increases rapidly as the drip line is approached. This necessitates that transport methods be very fast. Beta-activity levels observed in these experiments are many orders of magnitude greater than the activities of interest; thus it is critical that the protons can be unambiguously separated from the beta-decay "background." Furthermore, the small reaction cross sections for the production of nuclei far from stability make the maximization of transport and detection efficiencies critical. These challenges have spurred the development of many novel experimental techniques.

1.2 Thesis Organization

Following this introduction, Chapter 2 will present the general theoretical framework necessary for understanding the experimental measurements in this thesis. Chapter 3 discusses the experimental apparati and techniques that have been utilized in this work. Chapters 4-6 present detailed studies of the decays of four proton-rich nuclides: ^{23}Al, ^{23}Si, ^{22}Al and ^{77m}Rb. Chapter 7 contains concluding remarks.

^{23}Al was discovered and its mass was determined in 1969 via the ^{28}Si(p,^{6}He)^{23}Al reaction (Cer69). Then, in 1972, decay experiments observed a beta-delayed proton decay branch (Gou72). In 1994, the strength of its beta-delayed proton decay through an excited state of ^{23}Mg that is unbound to proton decay by only 215 keV was measured (Tig95) using specially designed detectors with a very low-energy threshold (Row97). The proton-decay branch from this state is significantly stronger than had been predicted from shell-model calculations, suggesting much greater isospin mixing than would have been expected between the state of interest and other nearby states of differing isospin. Aside from its intrinsic interest, this result also has significance for nucleosynthesis by hydrogen burning (Rol88, Wie86b, Cha92). To verify this result and increase the precision of the measurement, this decay branch has been measured again using low-energy particle-identification telescopes

designed to minimize contamination due to beta-decay residues. These low-energy beta-delayed proton decay measurements will be discussed in Chapter 4.

Using a fragment mass analyzer, ^{23}Si was observed as a residue of the ^{40}Ca + ^{nat}Ni reaction at a bombardment energy of 3096 MeV (Lan86). Muto, *et al.*, (Mut91) have predicted a half-life of 47 ±7 ms for ^{23}Si. Various mass models (Hau88) have predicted that its mass excess is between 23.4 and 25.4 MeV. Based on these mass predictions, the isobaric analog state of ^{23}Si in ^{23}Al should be unbound to one, two and three-proton emission. We have searched for both the beta-delayed one- and two-proton decay branches of this nuclide. Observation of either of these branches would allow a reliable estimate of the ^{23}Si ground state mass to be made; this would then serve as a stringent test of the different mass models. While the data from this experiment were being analyzed, a paper was published by Blank, *et al.*, (Bla97) that measured the beta-delayed one- and two-proton decays of ^{23}Si, as well as the half-life. The results of this measurement will be compared to the present work.

^{22}Al was discovered in 1983 by observation of its beta-delayed proton-decay branch (Cab82). Shortly thereafter, beta-delayed two-proton emission was observed for the first time as another decay branch of this nuclide (Cab83a). To date, ^{22}Al has provided the most information about the mechanism of this rare decay mode (Cab84, Mol89). As part of the search for ^{23}Si described in Chapter 5, the decay of ^{22}Al has been measured again and compared to previous results. In this experiment searches for evidence of a highly asymmetric two-proton decay branch through a low-lying intermediate state in the proton daughter was also undertaken; a significant branching ratio has been predicted for this decay by Brown (Bro90).

In 1971 Peker, *et al.*, (Pek71) predicted the existence of a many-particle isomeric state of ^{77}Rb that would be unbound to proton emission by 2.93 MeV. A later paper by Bugrov, *et al.*, (Bug85b) predicted the proton-decay partial half-life of this isomer to be 240 ms. This result was calculated using a proton decay formalism that utilizes detailed nuclear wave functions which take into account collective deformation and two-body interactions (Bug85a, Bug85b, Bug89, Dav98). It has been able to reproduce the partial half-life of an isomer of ^{53}Co (Bug85b); direct proton emission was first observed from this isomer (Jac70, Cer70), and this remains the only known case of proton radioactivity from an isomer of a nuclide bound to

proton emission from its ground state (Woo97). Although many excited states of ^{77}Rb have been studied via gamma-ray decay studies (Lis83, Har96), the predicted isomer has not been observed. Using helium-jet techniques and a recoil-atom mass analyzer (RAMA; Mol80a, Mol80b, Ogn96), we have searched for direct proton emission from this postulated isomeric state of ^{77}Rb.

By presenting the results of the measurements discussed in the preceding paragraphs, it is a goal of this thesis to further demonstrate the value of proton-decay spectroscopy as a tool for probing the properties of highly unstable proton-rich nuclides.

C H A P T E R 2

GENERAL THEORY

2.1 Chapter Overview

In this chapter, various theoretical aspects of proton-decay spectroscopy and its applications will be reviewed. In this overview, an attempt will be made to synthesize a coherent picture of the theoretical issues involved and how they are related. The reader is directed to the introductory sections of the individual experimental chapters for a more detailed discussion of theoretical matters pertaining to the particular measurements.

Proton-decay spectroscopy is the primary tool utilized in these studies to extract information about proton-rich nuclei near the limits of stability. Because of its central importance, proton decay will be discussed first. Proton emission was first proposed as a decay mode by Marsden as long ago as 1915 (Mar15; see Gol66a for a historical review). However, the decay of nuclides by direct-proton emission was not observed until many years later (Jac70, Hof82) due to two factors. First, the energetics of proton decay and the shape of the mass parabola prevent proton emission from occurring except in nuclei far from stability. Such nuclei are produced in very low yields relative to the many other radioactive species produced concurrently. Second, proton decay is a very rapid process, which leads to difficulties in counting the activity. By convention, only nuclides with half-lives longer than 10^{-12} s are considered to "exist". The proton drip line, where proton decay becomes energetically allowed, defines the limit of existence along much of the proton-rich side of the valley of beta stability, particularly among the light elements. Only nineteen ground-state proton emitters have been observed to date (Woo97, Bat98, Dav98). Although the energetics and the sensitivity of the decay rate to the angular momentum transmitted in the decay make

direct-proton spectroscopy a sensitive probe of nuclear structure (Dav97, Dav98), the experimental hurdles limit the widespread application of this technique.

The study of beta decay provides other information on the properties of the nucleus. It is common for the beta decay of a parent nuclide to feed both the ground state and many excited states in the daughter. The relative population of the excited states is dependent on the beta-transition rate for each state. If one removes the energy dependence of the decay rate, the resulting comparative half-life values depend directly on the overlap integral between the initial- and final-state wave functions (Mar69). Thus, comparisons between the predicted and measured half-lives present an excellent test of the shell-model wave functions commonly used for prediction (Bro90a).

Unfortunately, extraction of decay energy and branching ratios directly from measurements of the emitted positron (or electron) is complicated. This arises from the three-body nature of beta decay. Most decay processes emit radiation with a discrete energy which may easily be converted to the energy of the decay for the transition. If the energy of one of the participating states is known, this allows the determination of the energy of the other state. However, in beta decay the energy is shared by the daughter, the beta particle (electron or positron) and a neutrino that is extremely difficult to detect. This leads to a continuous distribution of beta-particle energies observed for each discrete transition (Mar69). If beta decays are observed to several different levels (or from different parent nuclides), this makes the extraction of precise energy or intensity information very difficult and prone to error.

However, with the exception of beta decays between ground states, the beta transition will be followed by a secondary decay. In most cases, gamma-rays will be emitted as the excited state de-excites towards the ground state. However, as the proton-drip line is approached, beta emission may feed excited states of the daughter nucleus which are unbound to proton emission. Beta-delayed proton emission (Har89) is observed among nuclei closer to stability than direct proton emission; thus cross sections for production of these nuclides are larger. Since beta decay is governed by the weak interaction, it is a rather slow decay mode, with half-lives of at least milliseconds. This "bottleneck" in the beta-delayed proton (or other delayed-decay) process permits the transport of activity away from the target for

counting in a lower background area. The discrete energy of delayed protons or gamma rays may be used to determine the energy of the intermediate (beta-daughter) state provided that the energy of the final state is known. Transition rates for proton emission tend to be much faster than gamma decay rates unless the proton decay is significantly hindered by very low energy or by a large angular-momentum barrier; generally the proton decay branch from the intermediate state is close to 100%. This permits beta-decay branching information to be extracted directly from the observed proton intensities. The rarity of proton-decay modes gives a way of identifying and studying the decays of near-drip line nuclei produced in much smaller yield than neighboring nuclides closer to stability.

The discussion of beta decay will begin with a review of the energetics involved. This will be followed by an analysis of the rate dependence on energy, angular momentum and the structure of the initial and final states. Decays between analog states, states in isobars with nearly identical wave functions, merits special discussion. The extraction of beta-decay strength functions-- the variation of the beta-decay matrix element as a function of excitation energy in the daughter-- will also be explored. This will be followed by a discussion of beta-delayed decay processes, including the competition between different delayed-decay modes, and the extraction of useful experimental information from beta-delayed decay processes.

The second half of this chapter focuses on the applications of proton-decay spectroscopy. An overview of nuclear mass models will be presented. Beta-delayed proton emission between analog states permits accurate estimates of the beta-parent mass to be made if the mass of the proton daughter is known. Many of the results obtained from proton-decay spectroscopy provide a way of testing various shell-model types of calculations. Methods of obtaining wave functions and energies of nuclear states employing both single-particle shell-model wave functions and realistic two-body interactions will be presented first. Application of these wave functions to the prediction of beta-decay rates will follow. The discussion of theoretical predictions will conclude with a presentation of an isospin-nonconserving Hamiltonian that can be used to determine the isospin purity of shell-model states.

The chapter will conclude with a short presentation of nuclear astrophysics for which proton spectroscopy can provide important information. Nucleosynthesis via explosive hydrogen-burning processes will be discussed in the context of stellar evolution.

Finally, the estimation of stellar reaction rates will be covered, with particular attention to the importance of isolated resonances in the proton-capture cross section.

In the preparation of this chapter, several texts provided significant background information on the following topics: direct- and beta-delayed proton-decay modes, *Particle Emission from Nuclei* (Hof89, Har89, Mol89); beta decay, *Physics of Nuclei and Particles* (Mar69); the shell model, *Shell-Model Applications in Nuclear Spectroscopy* (Bru77) and *The Nuclear Shell Model* (Hey94); and nuclear astrophysics, *Cauldrons in the Cosmos* (Rol88).

2.2 Proton Decay

2.2.1 Energetics and Selection Rules

Proton emission becomes a viable decay channel when there is a positive Q-value:

$$Q_p = (M_Z - M_{Z-1} - M_p - M_e)c^2 > 0 \qquad (2\text{-}1)$$

where M_Z and M_{Z-1} are the atomic masses of the parent and daughter, respectively, and M_p and M_e are the proton and electron masses. If mass excesses $\Delta(Z,A)$ are used to calculate the available energy:

$$Q_p = \Delta(Z,A) - \Delta(Z-1, A-1) - \Delta(H) \qquad (2\text{-}2)$$

In this case, $\Delta(H)$ is the mass excess of the hydrogen atom, which includes the mass of the electron. When protons are observed in spectroscopic measurements, conservation of linear momentum requires that the decay energy be shared between the proton and the recoil. The decay energy is:

$$Q_p = E_p (M_{Z-1} + M_p) / M_{Z-1} \qquad (2\text{-}3)$$

Here E_p is the energy of the proton in the laboratory frame. The energy detected will be somewhat smaller (<20 keV) than calculated from the atomic masses due to energy losses by the emitted proton as it passes through the electron cloud. These losses are due to ionization and excitation of the bound electrons; this correction to the decay energy is typically estimated from neutral-atom electron binding energies, e.g., from the relativistic Hartree-Fock-Slater calculations of Huang, *et al.* (Hua76).

Conservation of angular momentum and parity lead to the following selection rules for proton decay:

$$I_i = I_f + l + s \tag{2-4}$$

$$\pi_i = \pi_f(-1)^l \tag{2-5}$$

where the subscripts i and f label the initial and final states in the decay, l is the angular momentum of the emitted proton and the spin s of the proton is 1/2.

The concept of isospin was first suggested by Heisenberg (Hei32). This quantum number treats the proton and neutron as different states of a single particle, the nucleon, with isospin **T** = 1/2. The proton is assigned an isospin projection T_z (with respect to an arbitrary z-axis) of –1/2; T_z for the neutron is +1/2. For a given nucleus, the total isospin is a combination of the isospin vectors of the individual nucleons:

$$T = \sum_{i=1}^{A} T_i \tag{2-6}$$

The z-projection of isospin is found from the number of protons and neutrons:

$$T_z = (N - Z)/2 \tag{2-7}$$

The isospin of the ground state of a particular nuclide is almost always equal to the absolute value of its z-axis isospin projection:

$$T_{g.s.} = | T_Z | \tag{2-8}$$

There are a few exceptions to this rule; for example, both of the T_Z=0 nuclides ^{34}Cl and ^{42}Sc have T=1 ground states (End90).

Among the light nuclei, isospin is useful in explaining similarities in the level structures of mirror nuclei, isobars with the numbers of neutrons and protons reversed, e.g., ^{13}C and ^{13}N or ^{23}Ne and ^{23}Al. If the two projections corresponding to the proton and neutron were degenerate, the masses and level structures of mirrors would be identical (Hen69). However, it is clear that at least two factors break this degeneracy: the Coulomb charge of the proton and the neutron-proton mass difference. Figure 2-1 shows the energy levels of the T = 1/2 mirror nuclides ^{23}Na and ^{23}Mg. Although the excited states of mirror nuclei correspond very closely to each other, the correspondence is not perfect. This suggests that there is also a

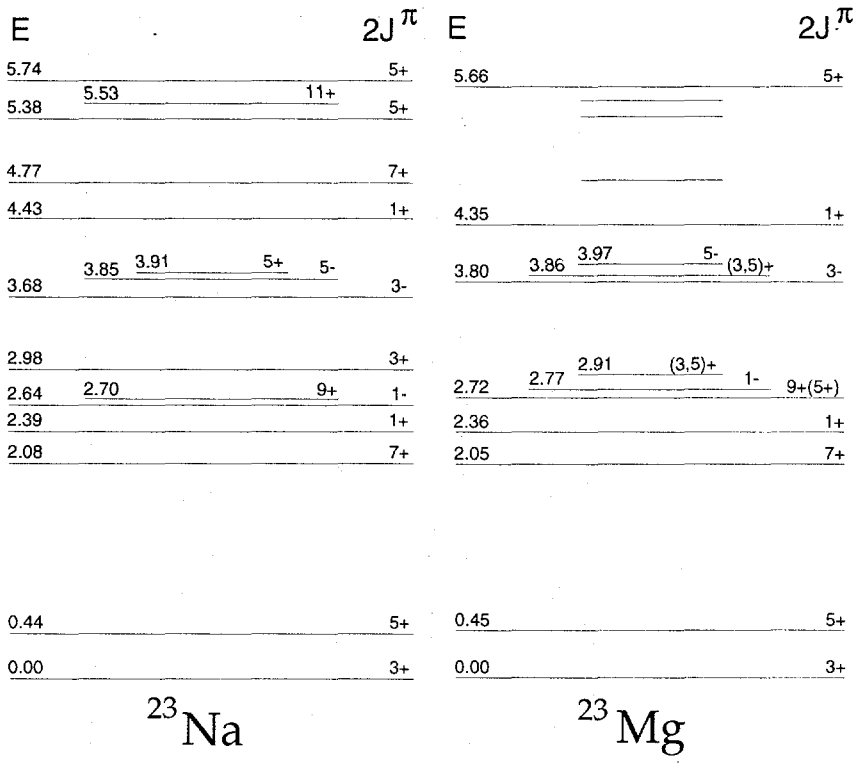

FIG. 2- 1: Energy levels of the mirror nuclides ^{23}Na and ^{23}Mg (Endt90).

charge-dependence to the nuclear force, such that n-n, n-p and p-p strong interactions are not identical (Mil90). However, isospin is nearly a good quantum number because the charge dependence of the nuclear force is small (Mil90). Conservation of isospin leads to the following isospin selection rule for proton decay:

$$\mathbf{T}_f = \mathbf{T}_i + \mathbf{T}_p \tag{2-9}$$

As stated above, the isospin of the proton is 1/2, so the isospin may only change by ±1/2 unit in proton decay. The extent to which this selection rule is obeyed provides a measure of the charge independence of the strong nuclear force (Orm86).

2.2.2 Proton Decay Rates

2.2.2.1 The semi-classical (WKB) approximation

Like alpha decay and fission, proton decay falls into the general class of problems which may be described using the Wentzel-Kramers-Brillouin (WKB) approximation

applied to barrier penetration (Hof89). In this approach, the trajectory of the proton is assumed to follow the principle of least action, where the action S is:

$$S = \frac{1}{\hbar}\int |p| dr = \frac{1}{\hbar}\int \sqrt{2m(V-E)}dr; \tag{2-10}$$

p and E are the proton momentum and kinetic energy, respectively, V is the interaction potential between the proton and the daughter nucleus as a function of radius r, and m is the reduced mass of the proton/daughter system. The penetration probability P is equal to e^{-2S}:

$$P_{Q,j,l} = \exp\left(-2\sqrt{\frac{2m}{\hbar^2}}\int_{r=R_{in}}^{R_{out}}\sqrt{V(r)_{total}-Q_p}dr\right) \tag{2-11}$$

where the kinetic energy has been replaced by Q_p. The integration over the radius r is performed for the classically forbidden region, where the kinetic energy of the proton is less than the potential energy barrier (from R_{in} to R_{out}).

The real part of an optical model potential may be used for V(r) (Hof89). A recent paper by Åberg, *et al.*, (Åbe97) has compared calculations using optical model parameters obtained by Becchetti and Greenlees (Bec69) from low-energy proton scattering data on A>40 nuclei, to the "universal" Woods-Saxon parameter set of Dudek, *et al.* (Dud81), from scattering data in the Pb region. The calculations using the Becchetti-Greenlees parameters predicted the half-lives of the known ground-state proton emitters with better accuracy. The optical-model potential used consists of a superposition of nuclear, spin-orbit, Coulomb and angular momentum potentials (Bec69):

$$V(r,l)_{total} = V(r)_{nuclear} + V(r,l)_{spin\text{-}orbit} + V(r)_{Coulomb} + V(r,l)_{centrifugal} \tag{2-12}$$

$$V(r)_{nuclear} = \frac{-V_0}{1+e^{(r-R_0)/a_0}} \tag{2-13}$$

$$V(r,l)_{spin\text{-}orbit} = (\sigma\cdot l)\frac{\lambda_\pi^2}{r}\frac{d}{dr}\left(\frac{V_{so}}{1+e^{(r-R_{SO})/a_{SO}}}\right) \tag{2-14}$$

$$(\sigma\cdot l) = -(l+1) \quad \text{for } j = l - 1/2 \tag{2-15}$$
$$= l \qquad \text{for } j = l + 1/2$$

$$V(r)_{Coulomb,r<R} = \frac{zZe^2}{2R_C}\left(3 - \frac{r^2}{R_C^2}\right) \quad (2\text{-}16a)$$

$$V(r)_{Coulomb,r>R} = \frac{zZe^2}{r} \quad (2\text{-}16b)$$

$$V(r,l)_{centrifugal} = \frac{l(l+1)\hbar^2}{2mr^2} \quad (2\text{-}17)$$

Except where noted below, the symbols are defined as in previous equations. The symbol λ_π represents the Compton wavelength of the pion. The depth of the nuclear potential in MeV, V_0, is given by:

$$V_0 = 54.0 - 0.32\,E_p + 0.4\,Z\,A^{-1/3} + 24.0\,(N - Z)\,A^{-1} \quad (2\text{-}18)$$

The strength of the spin-orbit potential is determined by its depth parameter V_{SO}. The

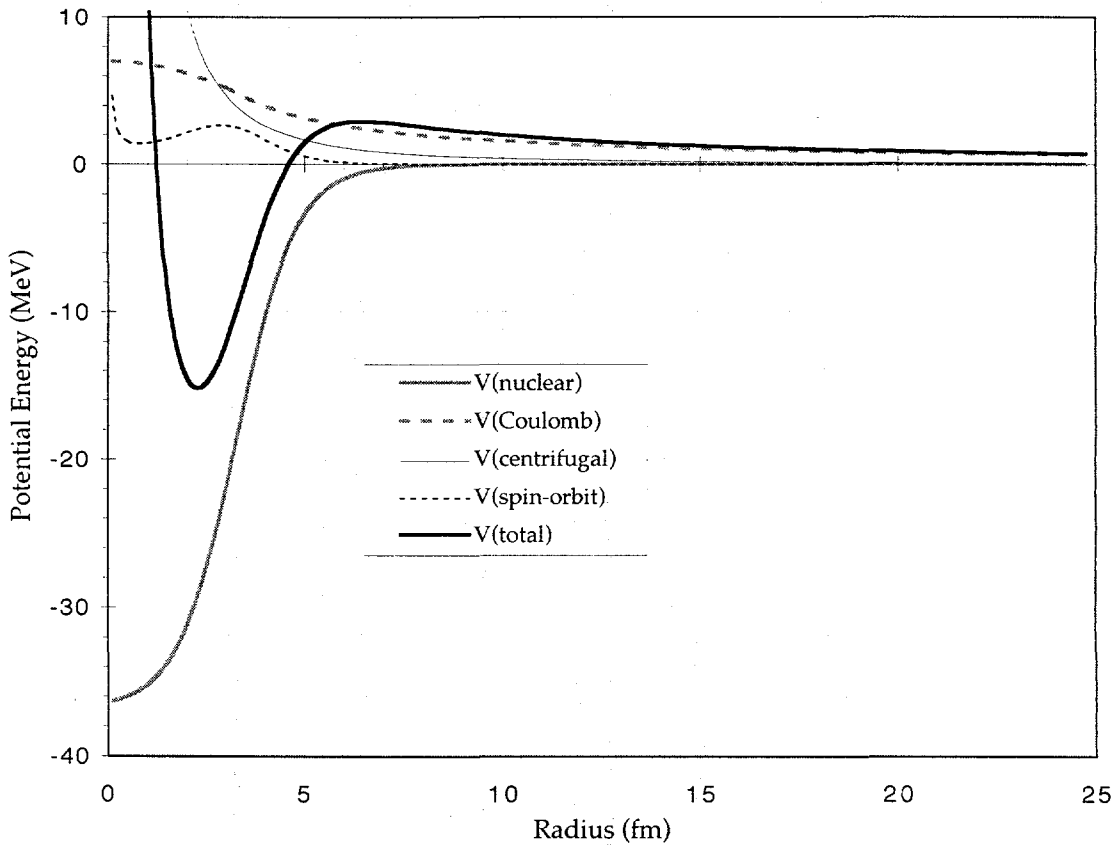

FIG. 2- 2: Potential barrier for proton decay from the IAS of ^{23}Al, calculated from the optical-model parameterization of Becchetti and Greenlees (Bec69) for an l=0 decay from the $0d_{5/2}$ orbital.

nuclear, spin-orbit, and Coulomb radii, R_0, R_{SO} and R_C, respectively, each have the form $R = r_x A^{1/3}$, where r_x is the appropriate radius parameter. The diffuseness parameters a_0 and a_{SO} determine the sharpness of the nuclear and spin-orbit potentials, respectively. Becchetti and Greenlees obtained the best fit to the scattering data using the values r_0 = 1.17 fm, r_{SO} = 1.01 fm, r_C = 1.21 fm, V_{SO} = 6.2 MeV, and $a_0 = a_{SO}$ =0.75 fm. These potentials are shown in Fig. 2-2 for proton emission from the isobaric analog state (IAS) of ^{23}Al.

The decay probability for a given decay branch is determined from the product of the penetration probability with a frequency factor υ that represents the number of times per second that the proton attempts to tunnel through the barrier. The half-life is inversely proportional to the decay probability:

$$T_{1/2} = \frac{\ln 2}{\nu \times P_{Q,j,l}}, \text{ where} \tag{2-19}$$

$$\nu = \frac{\sqrt{2}\pi^2\hbar^2}{m^{3/2}R^3\sqrt{\frac{zZe^2}{R} - Q_p}}. \tag{2-20}$$

The computer code thruBarrier (Row98a) calculates proton decay rates using the WKB approximation and the Becchetti-Greenlees optical model parameters. The source code is provided in Appendix A.

A shortcoming of the semi-classical approach is that it fails to take into account important structural details of the parent and daughter nuclei. For instance, if there is a dramatic change in the deformation of the nucleus between the initial and final states, this is expected to hinder the transformation. Methods which attempt to include structural effects will be presented shortly. Experimentally, these effects may be seen in the spectroscopic factor S_{exp}, defined as the ratio of the predicted to experimental proton-decay partial half-lives. In attempting to calculate spectroscopic factors S_{th}, it is assumed that they arise from the deficiencies of the single-particle shell model. If two-body interactions are included in shell model calculations, the eigenfunctions will consist of mixtures of the single-particle basis states (see Section 2.5.2.). This fragmentation of the single-particle states will hinder the transitions relative to the rates calculated assuming pure single-particle states. Recent attempts to predict spectroscopic factors from the independent-quasiparticle (BCS)

approximation (Åbe97), or from a low-seniority shell-model calculation (Dav97) have achieved reasonable agreement with S_{exp} for most of the known direct proton emitters.

TABLE 2- 1: Ground-state and isomeric proton emitters observed to date.

Parent	E_p (keV)	$\Delta J, \Delta\pi$	$t_{1/2,p}$ (exp)	$t_{1/2,p}$ (WKB)	S_{exp} (%)	discovery
^{53m}Co	1590(30)	19/2, yes	~17 s	---	---	(Jac70)
^{105}Sb	478(15)	5/2, no	~50 s	11.8 s	24	(Tig94)
^{109}I	813(4)	5/2, no	103(5) μs	5.7 μs	5.5	(Fae84)
^{112}Cs	807(7)	5/2, no	500(100) μs	41 μs	8	(Pag94)
^{113}Cs	959(4)	5/2, no	17 (2) μs	0.32 μs	1.9	(Fae94)
^{131}Eu	950(8)	---	32(9) ms	---	---	(Dav98)
^{141}Ho	1169(8)	---	4.2(4) ms	---	---	(Dav98)
^{145}Tm	1728(10)	11/2, yes	3.5(10) μs	1.8 μs	51(16)	(Bat98)
^{146}Tm	1119(5)	11/2, yes	>235(27) ms	442 ms	---	(Liv93a)
^{146m}Tm	1189(5)	11/2, yes	>72(23) ms	67 ms	---	(Liv93a)
^{147}Tm	1051(3)	11/2, yes	3.7 (13) s	3.2 s	85(30)	(Kle82)
^{147m}Tm	1119(5)	3/2, no	360(40) μs	130 μs	36(7)	(Hof84)
^{150}Lu	1263(3)	11/2, yes	>35(10) ms	37 ms	---	(Hof84)
^{151}Lu	1233(3)	11/2, yes	120(40) ms	74 ms	62(21)	(Hof82)
^{156}Ta	1007(5)	3/2, no	>144(24) ms	81 ms	---	(Pag92)
^{156m}Ta	1108(8)	11/2, yes	8.9(23) s	8.2 s	92(24)	(Liv93)
^{157}Ta	927(7)	1/2, no	300(110) ms	166 ms	55(24)	(Irv97)
^{160}Re	1261(6)	3/2, no	870(200) μs	195 μs	22(6)	(Pag92)
^{161}Re	1192(6)	1/2, no	370(40) μs	141 μs	38(8)	(Irv97)
^{161m}Re	1315(7)	11/2, yes	325(44) ms	107 ms	33(7)	(Irv97)
^{165m}Ir	1707(7)	11/2, yes	350(70) μs	123 μs	36(8)	(Dav97)
^{166}Ir	1145(8)	3/2, no	152(71) ms	18.1 ms	12(7)	(Dav97)
^{166m}Ir	1316(8)	11/2, yes	860(290) ms	340 ms	40(16)	(Dav97)
^{167}Ir	1064(6)	1/2, no	110(15) ms	28.3 ms	26(7)	(Dav97)
^{167m}Ir	1238(7)	11/2, yes	7.5(19) s	2.46 s	33(11)	(Dav97)
^{171}Au	1444(17)	1/2, no	17(9) μs	4.4 μs	26(16)	(Dav97)
^{171m}Au	1692(6)	11/2, yes	2.22(29) ms	0.41 ms	18(3)	(Dav97)
(^{177}Tl)	1126(44)	1/2, no	60(50) ms	73 ms	~1.2	(Woo97)
(^{177m}Tl)	1958(10)	11/2, yes	450(100) μs	15.1 μs	3.4(10)	(Woo97)
^{185m}Bi	1585(9)	1/2, no	44(16) μs	2.5 μs	6(2)	(Dav96)

Table 2-1 lists all isomeric- and ground-state (Woo97, Bat98, Dav98) proton emitters that have been observed to date, along with the proton energies, the changes in total angular momentum j and parity π for each transition, experimental and calculated partial half-lives, experimental spectroscopic factors and the original references. For those emitters where the proton branching ratio, and thus the partial half-life, is not known, the total half-life is shown as a lower limit; S_{exp} is not calculated for these nuclides. The nuclides ^{131}Eu and ^{141}Ho are thought to be highly deformed. Whereas for the other proton emitters the orbital from which the proton is emitted has been chosen on the basis of agreement with the WKB predictions, this approach was not applicable to these two cases. Predicted half-lives have been calculated using the code thruBarrier (Row98a). This table has been adapted from a similar table by Woods and Davids (Woo97). The location of these direct proton emitters on the Chart of the Nuclides is indicated in Fig. 2-3.

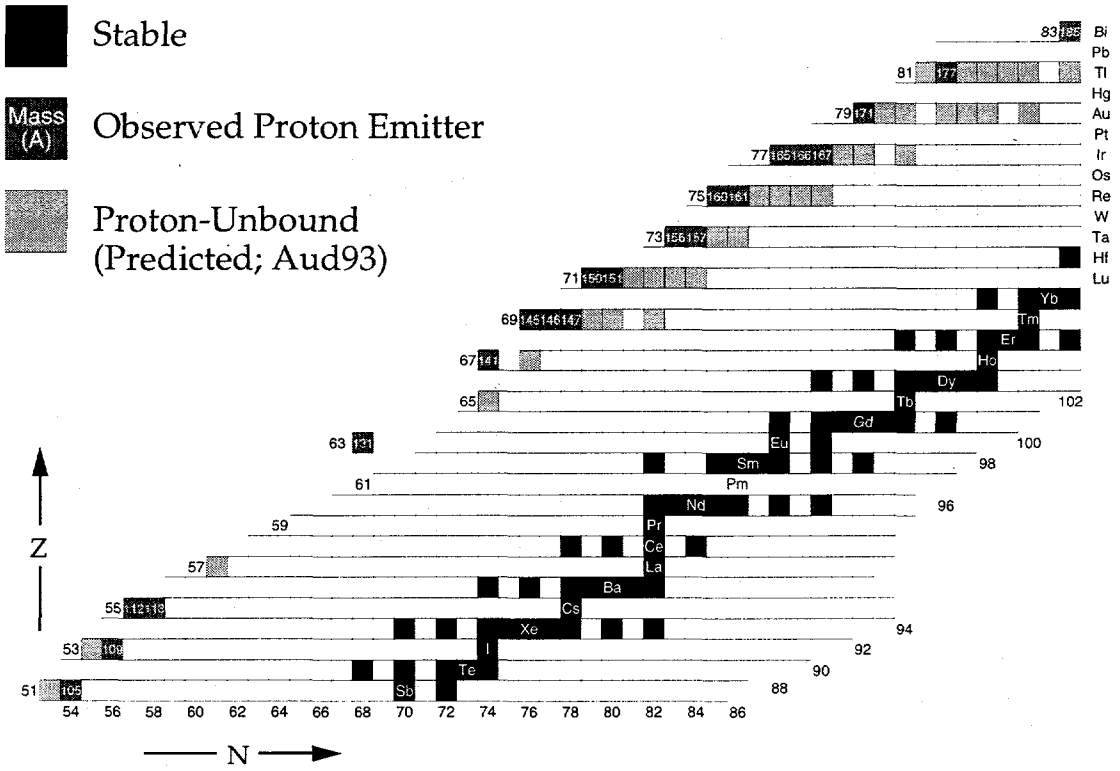

FIG. 2- 3: Location of observed proton emitters on the Chart of Nuclides.

2.2.2.2 Proton decay rates from reaction theory

Other treatments of proton decay have been developed in analogy with reaction theory (Fes92). This is a logical starting point, since proton decay may be considered as a time-reversed proton-capture reaction. The half-life is then related to the resonance width Γ by:

$$t_{1/2} = \frac{\hbar}{\Gamma} \ln 2. \tag{2-21}$$

In the distorted-wave Born approximation (DWBA) the resonance width is:

$$\Gamma = 2\pi \left\langle \psi_{Ap} \Psi_{Ap} \middle| V_{Ap} \middle| \Psi_{A+1} \right\rangle^2 \tag{2-22}$$

where ψ_{Ap} is the outgoing spherical wave representing the motion of the emitted proton relative to the daughter, Ψ_{Ap} is the product of the intrinsic wave functions of the proton and daughter, V_{Ap} is the interaction potential between the proton and daughter, and Ψ_{A+1} is the meta-stable initial state of the parent nucleus.

In the treatment of Åberg, *et al.*, (Åbe97) the potential is assumed to be comprised of nuclear (consisting of Woods-Saxon and spin-orbit potentials as in equations 2-13 and 2-14, respectively) and Coulomb parts: $V = V_N + V_C$. The wave function of the final-state proton interacting with a point-charge Coulomb potential may be given in terms of the regular Coulomb wave function, $F_l(r)$. The Coulomb part of the potential may then be replaced by a correction δV_C that accounts for the difference between the Coulomb potential for a point-charge and for the (finite) daughter nucleus (Sat83). Thus:

$$\Gamma = 2\pi \left\langle \Psi_{Ap} \psi^{C}_{Ap} \middle| V + \delta V_C \middle| \Psi_{A+1} \right\rangle^2 \tag{2-23}$$

$$\psi_l(r) = \sqrt{\frac{2m}{\pi \hbar^2 k}} \frac{F_l(r)}{r} \tag{2-24}$$

where $\psi_l(r)$ is the radial part of ψ^{C}_{Ap} and $k = 2\pi(2mE)^{1/2}/h$. As stated above, the final-state wave function Ψ_{Ap} is approximated by the product of the proton intrinsic wave function and the daughter-nucleus wave function Φ_A, which is treated as an inert core.

Similarly, Åberg, *et al.*, approximate the initial-state wave function Ψ_{A+1} as the product between the inert (daughter) core Φ_A and the proton in its quasi-bound state ϕ_{nlj}, with quantum numbers n, *l* and j. The radial part of the proton wave function is:

$$\Phi_{nlj}(r) = \frac{\phi_{nlj}(r)}{r} \tag{2-25}$$

inside the nuclear volume. Since the proton is only quasi-bound, its wave function will extend outside of the nucleus; its behavior asymptotically approaches that of the irregular Coulomb wave function $G_l(r)$ as r goes to infinity. In order to smoothly join the wave function in the interior, $\phi_{nlj}(r)$, to $G_l(r)$, Åberg, *et al.*, iteratively adjust the depth of the nuclear potential (while holding the radius and diffuseness parameters constant). The resonance strength is then determined from:

$$\Gamma = \frac{4m}{\pi\hbar^2 k}\left(\int_0^\infty F_l(r)[V_N + \delta V_C]\phi_{nlj}(r)\,dr\right)^2 \tag{2-26}$$

where the integration is carried out numerically.

Åberg *et al.*, (Åbe97) have compared the results of this DWBA method to the WKB approximation results for the observed direct proton emitters. They find that the predictions obtained from the two methods differ by less than 10%. This is not very surprising; although the problem has been treated entirely within the framework of quantum mechanics (unlike the semi-classical approximation), the simplistic treatment of the daughter nucleus as an inert core does no more to accommodate the effects of collective deformation or configuration mixing of the single-particle shell model states than the WKB approach does.

The code COCAGD3, which has been used to predict some proton decay rates, uses a method similar to (though more simplistic than) the DWBA method (Sex73; see also Bla52, pp. 329-335). Although COCAGD3 does not predict the partial half-lives of the known proton emitters as accurately as the WKB methods, it may be more accurate in predicting partial half-lives for (beta-delayed) proton emission among light nuclei where the code thruBarrier, based on the WKB method, often fails (see Appendix A).

Bugrov, Kadmensky and Furman (BKF) have developed an integral formula for the proton decay of a quasi-stationary state (Bug85a, Bug85b, Bug89) in analogy with earlier work on alpha decay (Kad75):

$$\Gamma = 2\pi \left| \left\langle \hat{A} \left[U_C^{J_i M_i} \frac{\tilde{F}_l(r_p)}{r_p} \middle| V_{pA} - V_{Coul}^0(r_p) \right] \middle| \psi_{\sigma_i}^{J_i M_i} \right\rangle \right|^2 \qquad (2\text{-}27)$$

where $\hat{A}$ is the antisymmetrization operator, V_{pA} is the nuclear interaction between the proton and the daughter, and V_{Coul}^0 is the Coulomb interaction between the proton and the daughter, assuming a point-like charge distribution as above. The outgoing channel U_C is assumed to be the product of the daughter nucleus wave function and the spin-orbit function for the proton coupled to the parent-nucleus orbital it occupied. $F_l(r)$ is again the regular Coulomb function, with a somewhat different normalization. The wave function of the parent nucleus is represented by $\psi_{\sigma_i}^{J_i M_i}$, where J and M are the total angular momentum and its z-projection, and σ represents other quantum numbers. This equation for the decay width was derived from the R-matrix reaction formalism; it can be shown to be equivalent to the DWBA approach described above (Dav98).

A full presentation of this formalism is beyond the scope of this thesis; the reader is referred to the references given in the preceding paragraph. The BKF theory extends the DWBA method discussed above so that the nuclear system is treated in a more realistic manner. The Hamiltonian employed in this method (Bug85a) includes two-body pairing interactions, diagonalized via the Bogolyubov transformation (Bog58). Thus the theory is able to handle multi-particle configurations ignored by the single-particle shell model. Unlike the DWBA treatment of Åberg, *et al.*, the core wave functions of the parent and daughter are taken into account. Furthermore, by making the nuclear potential dependent on emission angle and describing the Coulomb interaction as a sum of quadrupole and hexadecapole moments (Bug89), this approach is able to predict the effects of collective deformation (where known) on half-lives or, conversely, to estimate deformations on the basis of experimental half-lives.

In a recent paper, Davids, *et al.*, (Dav98) used this theory to predict the deformations of two recently discovered ground-state proton emitters, ^{131}Eu and ^{141}Ho. Unlike most

previously known proton emitters, these nuclides are thought to be in a region of pronounced deformation. The experimental partial-decay widths were replicated by varying the deformations; the experimental widths were reproduced at deformations that are in excellent agreement with those predicted by Möller, *et al.* (Möl95). This method of predicting deformations by replicating proton decay half-lives has also been applied to ^{113}Cs, ^{147}Tm, ^{150}Lu and ^{151}Lu (Bug89, Kad96). The results are in reasonable agreement with predictions based on systematics.

The BKF theory was able to predict the partial half-life of the first direct-proton emitter observed, ^{53m}Co, with reasonable accuracy (Bug85b). It has been used to estimate the proton-decay half lives (Bug85b) of a number of other many-particle isomers predicted by Peker, *et al.* (Pek71). Unfortunately, none of these other isomers have been observed to date. A search for one of these isomers, ^{77m}Rb, is the subject of Chapter 6.

2.2.3 Proton Decay Versus Alpha Decay

The processes of proton and alpha decay are very similar in several respects, but important differences also exist. The calculation of decay rates discussed above has been developed in analogy with alpha decay (Hof89, Kad75). While both modes may be treated as barrier penetration processes, where the emitted particle is assumed to tunnel through a potential energy barrier created by the nucleus as a whole, proton decay is somewhat simpler. Before alpha emission can occur, the alpha must be formed in the interior of the nucleus; no such pre-formation factor is required in the proton decay case. Because of this, spectroscopic factors for proton emission tend to be closer to unity than for alpha decay.

Alpha decay has been studied much more than proton decay. This is due to the energetics of the decay processes. Creation of an alpha particle from two protons and two neutrons is an energetically favorable process; the binding energy of the alpha is 28.3 MeV. Because of this, alpha decay can occur among nuclides much closer to stability than proton emission. As shown earlier in Fig. 2-3, proton decay only occurs near the limits of stability, where beta-decay half lives are on the order of tens or hundreds of milliseconds (Fir96). Whereas the partial half-lives of the known proton emitters range from a few μs to ~1 minute (see Table 2-1), alpha decay half-lives cover more than 24 orders of magnitude, from

milliseconds to $>10^{15}$ years. Longer proton-decay half-lives are not observed since beta-emission will dominate by an increasingly-large margin when proton partial half-lives are longer than ~500 ms.

Angular momentum is a more important factor for determining decay rates for proton decay than alpha decay due to two factors. The inverse dependence of the centrifugal barrier on the mass of the emitted particle (see equation 2-17) leads to an absolute increase in this barrier for proton emission. Additionally, the smaller charge of the proton leads to a reduction of the Coulomb barrier by a factor of two; the importance of the centrifugal barrier is thus relatively enhanced as well. This makes proton decay a more sensitive probe of nuclear structure than alpha decay. In several cases, proton decay half-lives have been used to determine level orderings near the drip line based on the calculated half-lives for decays of differing angular momenta (e.g., Tig94, Dav96, Irv97, Dav97). Figure 2-4 shows calculated

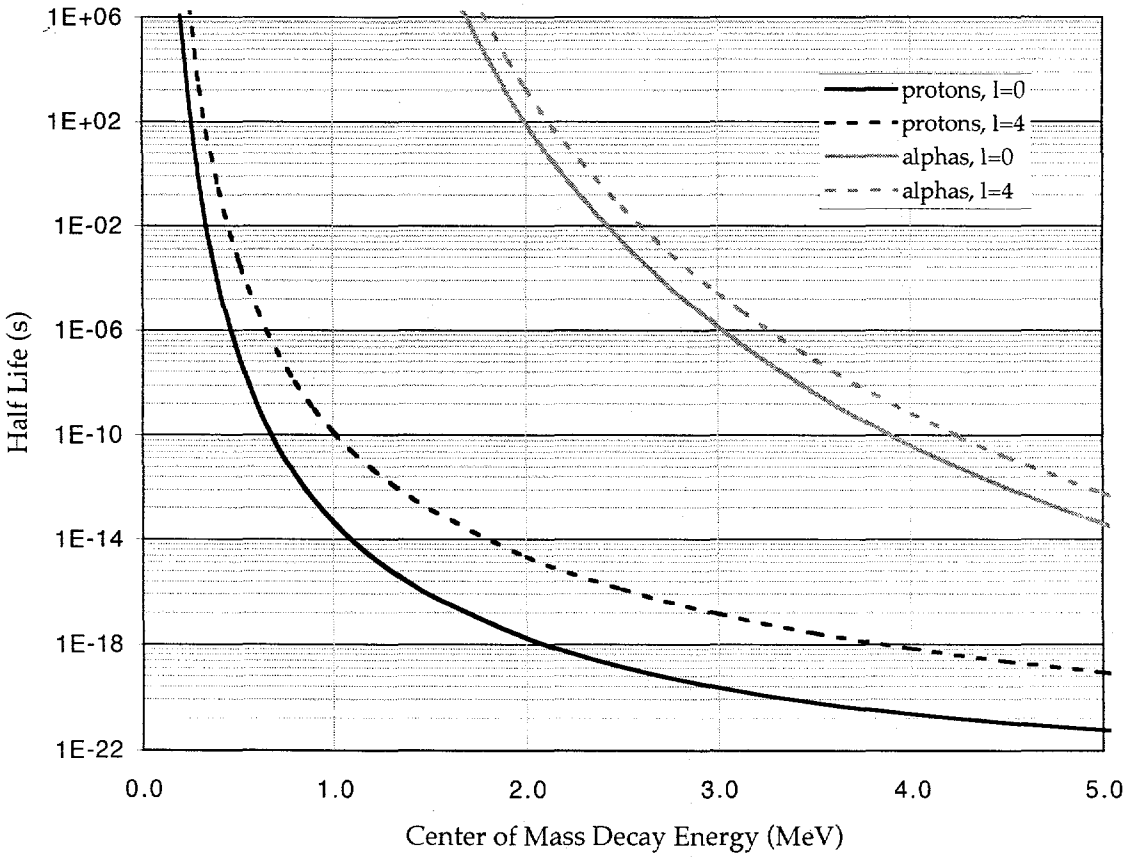

FIG. 2- 4: Calculated alpha- and proton-decay rates as a function of (hypothetical) decay energy from ^{73}Rb.

partial half-lives for proton and alpha emission from ^{73}Rb. It is seen that for the same Q-value, the slope of the curves (and thus the sensitivity of the half-life to decay energy) is greater for proton emission. A greater sensitivity to angular momentum is also illustrated by the relative differences between the l=0 and l=4 curves for each decay.

2.3 Beta-Decay

2.3.1 Energetics

Beta decay refers to those weak interaction decay modes that alter the z-projection of isospin T_z of a nuclide without altering its mass number. Thus a proton is converted to a neutron, or *vice versa*. These modes also involve two leptons, an electron (e^-) or positron (e^+), and an antineutrino ($\overline{\upsilon}_e$) or a neutrino (υ_e). Three variants are observed in which a nuclide N with mass A and charge Z is transformed with the following energetics:

EC (electron capture) decay: $N(A,Z) + e^- \rightarrow N(A,Z-1) + \upsilon_e$

$$Q_{EC} = [M(A,Z) - M(A,Z-1)]c^2 = \Delta(A,Z) - \Delta(A,Z-1) \quad (2\text{-}28)$$

β^- (electron) decay: $N(A,Z) \rightarrow N(A,Z+1) + e^- + \overline{\upsilon}_e$

$$Q_{\beta^-} = [M(A,Z) - M(A,Z+1)]c^2 = \Delta(A,Z) - \Delta(A,Z+1) \quad (2\text{-}29)$$

β^+ (positron) decay: $N(A,Z) \rightarrow N(A,Z-1) + e^+ + \upsilon_e$

$$Q_{\beta^+} = [M(A,Z) - M(A,Z-1) - 2m_e]c^2 = \Delta(A,Z) - \Delta(A,Z-1) - 1.022\,\text{MeV} \quad (2\text{-}30)$$

In the above equations, Q is the available decay energy; the reaction is energetically allowed when Q is positive. M is the *nuclear* mass, Δ is the mass excess, m_e is the electron mass and c is the speed of light. Beta decay often leaves the daughter nucleus in an excited state; in this case the excitation energy of the final state must be subtracted from the Q-value.

It is difficult to extract nuclear structure information from measured positron spectra. This is partially due to the difficulty of measuring the (anti-)neutrino, since this particle

interacts only via the weak force. The recoil energy imparted to the daughter nucleus is also difficult to measure, since most of the decay energy is imparted to the leptons in the laboratory frame. Unlike decay processes that involve only two particles in the final state, in β^+ and β^- decays the leptons are emitted with a spectrum of energies; thus measurement of the positron or electron by itself does not reveal the transition energy. The spectrum of momenta observed in these processes is determined by the phase space available to the leptons in the final state (Mar69); for allowed decays (see Section 2.3.2) it has the form:

$$N(p)dp = C(E_0-E)^2F(E,Z)p^2dp \tag{2-31}$$

where C is a constant, p and E are the momentum and energy of the positron or electron, and E_0 is the total decay energy shared by the electron and the neutrino. The function F(E,Z) is the Fermi function; it corrects for the interaction between the emitted particle and the nuclear charge. If equation 2-31 is rearranged to the form:

$$\sqrt{\frac{N(p)}{p^2F(E,Z)}} = C(E_0 - E) \tag{2-32}$$

it becomes clear that the transition energy may be extracted by plotting the quantity on the left of equation 2-32 versus energy of the emitted positrons or electrons. Unfortunately, C is not a constant for forbidden transitions (see the following section for a discussion of allowed and forbidden decays). Furthermore, if several final states are populated in a given decay (or more than one beta-emitting nuclide is present), an additional linear component will be observed for each transition, making this procedure difficult and error prone. Because of this, it is currently common to extract spectroscopic information from beta-delayed decay processes (see Section 2.4) rather than from beta decay directly.

2.3.2 Transition Rates

The theory within which beta-decay rates are predicted was developed by Fermi (Fer50) and is derived from his "Golden Rule #2":

$$\lambda_{fi} = \frac{2\pi}{\hbar}\rho(E_f)\left|H'_{fi}\right|^2. \tag{2-33}$$

The quantity $\rho(E_f)$ is the statistical factor, a measure of the phase space available to the leptons in the final state. It is equal to the integral of equation 2-31 over the energy available to the leptons. The expression $|H'_{fi}|^2$ is the overlap integral between the final state and the initial state modified by the transition interaction; a large overlap integral indicates that the decay is allowed. For the case of beta decay, this integral has the following form:

$$\left|H'_{fi}\right| = \int \Psi_f^* H' \Psi_i d\Omega = g \int [\psi_f^* \varphi_e^*(r) \varphi_\upsilon^*(r)] M \psi_i d\Omega \qquad (2\text{-}34)$$

where the Ψ's represent the total final and initial states of the system, g is a coupling constant representing the strength of the beta interaction, the ψ's represent the final and initial *nuclear* states and M is a Hamiltonian operator which converts the system from the initial to the final state. The $\phi(r)$'s are the wave functions of the emitted leptons. If the Coulomb interaction of the positron is removed, the leptons may be represented as normalized plane waves that may be expanded in a power series with respect to the radius r:

$$\phi_p(r) = N_p e^{i(\mathbf{k}\cdot\mathbf{r})} = V^{-1/2}[1 + i(\mathbf{k}_p\cdot\mathbf{r}) + \cdots] \qquad (2\text{-}35)$$

where the subscript p's denote the lepton (i.e., e or ν), N is a normalization constant, which may be set equal to $V^{-1/2}$, the normalization volume over which the lepton final-state phase space is integrated, and k is the lepton wave number ($=2\pi\mathbf{p}/h$). To a first approximation, only the first term of the expansion is important over the nuclear volume. (This term is zero for forbidden transitions. For an *n*th-order forbidden transition, the first *n* terms of the expansion are equal to zero.) The lepton wave functions may thus be removed from the overlap integral.

Equation 2-33 may now be rewritten in the form:

$$\lambda = \frac{g^2 m_e^5 c^4}{2\pi^3 \hbar^7} \left|M_{fi}\right|^2 f(W_0, Z). \qquad (2\text{-}36)$$

The constants on the left are collectively known as the "universal beta-decay time" τ_0, which is ~7000 s. The overlap integral between the final and (perturbed-) initial *nuclear* states are designated by the matrix element $|M_{fi}|$. The expression $f(W_0,Z)$ is known as the "integral Fermi function"; it derives from the integral over the phase space taken with respect to the energy:

$$f(W_0,Z) = \int_1^{W_0} F(W,Z)W(W_0 - W)^2\sqrt{W^2 - 1}dW \qquad (2\text{-}37)$$

where the energy has been referred to the electron rest mass, such that $W = (E + m_ec^2)/m_ec^2$. The Coulomb interaction of the positron, which was removed from equation 2-35, is included in the Fermi function F(W,Z). The Fermi function is the ratio of the electron density at the daughter nucleus to the density at infinity; it is less than unity for positron emission and greater than unity for β^- decay. Equation 2-36 may be rewritten in terms of the decay half-life ($=\ln 2/\lambda$) to get the comparative half life, *ft*:

$$ft \equiv f(W_0,Z)T_{1/2} = \frac{\tau_0 \ln 2}{|M_{fi}|^2} \qquad (2\text{-}38)$$

The significance of equation 2-38 is that it represents a separation of the nuclear structure effects from the effects due to energy and the nuclear charge on half-life. This allows comparisons between different decays to be made on a more meaningful basis, since the effects of nuclear structure are generally more interesting than those due to the energy and the Coulomb interaction. If a partial half-life has been measured for a particular decay branch, the *ft*-value is easily determined; the integral Fermi function may be calculated in a straight-forward manner if the transition energy is known. It is then a trivial matter to deduce the value of the interaction matrix element. Since this is directly related to the wave functions of the states involved, prediction of beta-decay probabilities between nuclear states provides an excellent opportunity for the testing of nuclear models at a microscopic level (Wil83). (This, of course, assumes that a realistic interaction Hamiltonian is also known.)

As was mentioned above, beta-decay transitions are classified according to which is the first–non-zero term in the expansion of the lepton wave functions (Mar69). This is determined by the changes in spin I and parity π between the initial- and final-state wave functions of the nucleus. In general, an *n*th-forbidden transition has the following selection rules:

$$\Delta I = n \text{ or } (n+1) \quad \text{and} \quad \pi_i\pi_f = (-1)^n \qquad (2\text{-}39)$$

(where allowed transitions are zeroeth order.) To first order, there is a correlation between the degree of forbiddeness of a given transition and its *ft*-value, with lower-order transitions

having the smallest values of ft. For allowed transitions, the logarithms of the *ft*-values (log*ft*) typically range from 2.9 to 6.0; superallowed transitions (to be discussed shortly) have log*ft*'s ranging from ~2.9-3.7.

For allowed decays, the matrix element is typically broken into two components. In Fermi (or "superallowed") decays, the leptons are emitted with their intrinsic spins coupled to zero (opposed). In Gamow-Teller decays, they are coupled to one (spins aligned). Thus the equation for the *ft*-value may be rewritten as (Goo82):

$$ft = \frac{\tau_0 \ln 2}{g_V^2 |\mathrm{F}|^2 + g_A^2 |\mathrm{GT}|^2} . \tag{2-40}$$

The expressions |F| and |GT| are the Fermi and Gamow-Teller (GT) matrix elements, respectively. It is known from various experiments that the form of the Fermi part of the beta interaction involves a vector transformation; the GT interaction has the form of an axial-vector (Mar69). Thus the coupling constants g, which relate the strengths of the two interactions, are known as the vector and axial-vector coupling constants, respectively. The selection rules that correspond to non-zero values of these matrices are:

$$\text{Fermi:} \quad \Delta I = 0; \ \Delta\pi\text{=no} \tag{2-41}$$

$$\text{Gamow-Teller:} \quad \Delta I = 0 \text{ or } 1, \text{ but no } 0 \rightarrow 0; \ \Delta\pi\text{=no}$$

Note that in many cases, including the decay of the (bare) neutron, a particular allowed transition will have contributions from both Fermi and Gamow-Teller matrix elements.

Although the above discussion applies specifically to β^+ and β^- decays, much of it also applies to electron capture as well. Because there is only a single lepton, the neutrino, in the final state, the energy spectrum of the neutrino will be discrete and the final-state phase space available depends on the momentum of the neutrino alone. The wave function of the neutrino in the final state may again be described as a plane wave. However, the electron in the initial state is bound to the atom and should thus be described by an atomic wave function. The total transition probability should be summed over all the available electrons; however, the inner shell electrons dominate since they have much greater overlap with the nucleus than the valence electrons. The Fermi integral function for a given electronic shell will now depend on the wave function of the bound electron:

$$f_K^{EC} = 4\pi\left(\frac{Ze^2}{\hbar c}\right)^3 (W_0 - \varepsilon_K)^2 \qquad (2\text{-}42)$$

where ε_K is the binding energy of the electron. Note that it is no longer necessary to include the Fermi function, since only the daughter nucleus is charged in the final state. The transition probability may now be written in the form of equation 2-36 and the preceding discussion of matrix elements remains valid.

When both modes are energetically viable (i.e., $Q_{EC} > 1.022$ MeV), electron capture and positron emission compete with each other. Above (approximately) mass 70, electron capture tends to dominate. This is because the radii of the inner shell electrons (which experience the nuclear charge nearly unscreened) decrease with increasing Z, and the nuclear radius increases as $A^{1/3}$. Both factors lead to larger overlap integrals between the electrons and the nucleus, giving electron capture an advantage over positron emission. Among the light nuclides (A<40), the opposite is true and positron emission dominates. The stronger energy dependence of positron emission also favors this mode as the drip line is approached. In intermediate regions, both decay modes may be observed.

Beta-decay half-lives range from a few milliseconds to billions of years. Proton decay becomes energetically possible before beta-decay energies are large enough to lead to microsecond beta transitions. Because proton emission occurs much more rapidly than beta-decay when the proton energy is more than a few hundred keV (less in the very light nuclides), beta emission is not observed with decay times less than milliseconds.

2.3.3 Beta-Decay Strength Functions

By examining the selection rules for allowed decays, realistic transition operators may be determined for the matrix elements in equation 2-40. In Fermi decay, the spin and parity of the nucleus is unchanged, but the z-component of isospin T_z is altered by one unit. This suggests a Fermi matrix element of the form (Bro85):

$$|F| = \left\langle \psi_f^* \left| \tau_Z^{\pm} \right| \psi_i \right\rangle. \qquad (2\text{-}43)$$

The ψ's represent the final- and initial-state wave functions of the nucleus. The operator τ_Z^+ (τ_Z^-) is the isospin-raising (-lowering) operator; it is a standard quantum-mechanical ladder

operator and has the desired effect of increasing (decreasing) the z-component of isospin T_z of the initial state by one unit for β^+ or EC decay (β^- decay). The wave function of the initial state is otherwise unchanged. This transition corresponds to changing a proton into a neutron (or *vice versa*) while keeping it in the same nuclear orbital.

For Gamow-Teller decays, the interaction is a bit more complicated. The selection rules dictate that not only is the z-component of isospin altered, but the spin of the neutron or proton that is transformed is flipped as well. Thus the matrix should have the form (Bro85):

$$|GT| = \left\langle \psi_f^* \left| \tau_Z^{\pm} \sigma \right| \psi_i \right\rangle. \tag{2-44}$$

In this case, the operator σ is the spin-flip operator, which (as the name suggests) flips the spin of the proton or neutron before it is then transformed. All other symbols have the same significance as above.

One might expect that the total decay strength could be easily determined relative to the strength observed for the decay of the neutron. For the neutron, the normalized strengths are (Goo82):

$$|F_n|^2 = 1 \text{ and } |GT_n|^2 = 3 \tag{2-45}$$

The GT strength is expected to be three times the Fermi strength since the leptons are emitted in triplet and singlet states for GT and Fermi transitions, respectively. This means that while the Fermi strength is concentrated in a single final state, the GT interaction may leave the transformed nucleon in the same orbital it was in prior to transformation, or in a state with total angular momentum that is different from the original by $\pm\hbar$. For an imaginary nucleus containing only neutrons or protons, the expected total strength would be equal to the neutron strength multiplied by the number of nucleons A (Goo82): $|F|^2$=A and $|GT|^2$=3A. However, for real nuclei, many transitions will be blocked by nucleons which are already occupying orbitals, since the Pauli principle forbids the occupation of a single quantum mechanical state by more than one fermion. Thus for realistic nuclei, the strength should be at least (Goo82):

$$|F|^2 = |N-Z| \text{ and } |GT|^2 = 3|N-Z| \tag{2-46}$$

This simple sum rule was proposed by Ikeda, *et al.*, in a somewhat different form (Ike63).

Unfortunately, when beta-decay half-lives were compared with those predicted on the basis of this sum rule, it was found that they were much longer than expected (Dan97). This led to the question of what had happened to the remaining strength. This question was partially answered with the discovery of the isobaric analog state (IAS), which was observed for the first time in a medium-mass nuclide as a resonance in a (p,n) transfer reaction (And61; see also Wil69).

As was stated above, most of the Fermi strength is concentrated in a single state (Doe75), that corresponds to changing the valence nucleon from a proton to a neutron (or *vice versa*) while otherwise leaving the wave function of the nucleus virtually unchanged (Wil69). This state is the IAS of the decaying parent; both have the same isospin quantum number but different isospin projections T_Z. A nuclear state with isospin T will be part of an isospin multiplet with $2T_Z + 1$ members (corresponding to the possible projections of this isospin) in nuclides with T_Z ranging from -T to +T. An IAS with $T > T_Z$ will almost always be at some excitation above the ground state; this arises from the Pauli principle. The Fermi matrix element may be determined in analogy with general angular momentum theory; one obtains (Bli69):

$$|F| = \langle T,T_Z \pm 1 | \tau^{\pm} | T,T_Z \rangle = \sqrt{(T \mp T_Z)(T \pm T_Z + 1)} \qquad (2\text{-}47)$$

Because the only differences between two analog states are due to the conversion of a proton to a neutron, the difference in energy between the two states may be found (to first order) from the neutron-proton mass difference Δ_{nH} (=782.354 keV) and the change in the Coulomb interaction between the nuclei (Pap88, Ant97):

$$M_{Tz} - M_{Tz+1} = \Delta_{nH} + \frac{2e^2 Z_{AVG}}{r_o A^{1/3}} \qquad (2\text{-}48)$$

where M_{Tz} and M_{Tz+1} are the masses of two analog states related by the change of a proton in the former to a neutron in the latter. The second term on the right of equation 2-48 is the derivative of the Coulomb potential; e is the electron charge, Z_{AVG} is the average number of protons of the parent and daughter, r_0 is the radius constant and A is the mass number. This term is known as the Coulomb displacement energy (CDE). Since both terms on the right are always positive, one can see that the mass of the proton-rich analog will always be greater

than that of the neutron-rich analog. For this reason, β^- decay between isobaric analogs is always energetically forbidden.

In 1963 it was proposed by Ikeda, Fujii and Fujita (Ike63) that the majority of GT strength would be located in states forming a broad continuum at an energy above the IAS. This energy would correspond to the energy required to flip the spin of the transformed nucleon. It might be expected that this strength would be located in three discrete states (corresponding to $\Delta I = 0, \pm 1$), in analogy to the concentration of the Fermi strength in a single state, the IAS. However, at these excitation energies, the density of states, as known from experiments, or as predicted, e.g., from the Fermi gas model of the nucleus, is very high. Furthermore, two-body (pairing) interactions not treated by the single-particle shell model will lead to configuration mixing between single-particle states (Ber81). This pairing effect may be treated as a perturbation to the standard shell-model Hamiltonian. First-order perturbation theory (Bra89) predicts that the mixing amplitudes between states at high excitation will be relatively large, since the degree of mixing is inversely proportional to the energy difference between states with the same spin, parity and isospin quantum numbers (Orm95). Thus the GT-transition strength is spread among many states at high excitation (Ber81), collectively known as the Gamow-Teller Giant Resonance (Goo82). This is contrary to the case of the IAS; because it is the analog of the ground state, there are no nearby states of the same isospin with which it can mix.

A probe was necessary to confirm this hypothesis. Because of its high excitation, most of the GT strength is energetically inaccessible to beta decay. The net result of charge-exchange reactions such as (p,n) or (^{3}He,^{3}H) is to exchange one proton for a neutron (or *vice versa*); thus, their cross sections rely on the same matrix elements as beta decay (Goo82). Because of this, these reactions make excellent probes, requiring only corrections for the angular and linear momenta transfer in order to extract information about the beta strength at a given excitation. Evidence for the GT giant resonance hypothesis was first observed in 1975 using the (p,n) reaction on ^{90}Zr, ^{48}Ca, ^{120}Sn and ^{208}Pb (Doe75).

However, after many such studies had been performed, the GT strength in nuclei was still found to be only about 60-80% of that predicted by equation 2-46. Many possible explanations of this "quenching" have been proposed. Recently, experiments by Akimune, *et*

al., (Aki95) and Wasaka, *et al.*, (Wak97) claim to have observed additional strength at even higher excitations. Dang, *et al.*, (Dan97) explain these observations in the context of two-particle–two-hole configuration mixing. Measurements of the Gamow-Teller strength (i.e., $|GT|^2$ as a function of excitation in the daughter) still remain interesting and serve as an excellent test of the shell model (Bro85). Among proton-rich nuclides near the drip line, the rapid increase in available beta-decay energy means that both the IAS and the low energy tail of the GT giant resonance are experimentally accessible (e.g., Bor87, Rob93). Since probing these nuclei using charge exchange reactions would require the use of (generally very short-lived) radioactive targets or beams, beta-decay studies of nuclides far from stability are an important tool for testing the shell model under extreme conditions.

2.4 Beta-Delayed Decay Processes

2.4.1 Energetics and Competition Between Decay Modes

As was stated earlier, beta decay often feeds not only the ground state but also one or more excited states in the daughter nucleus. In most cases, the primary decay mode of these excited states is gamma-ray emission. (Although beta decay of the excited state may also be energetically possible, beta decay is not observed except in the case of high-spin isomers, where the relatively-slow beta-decay process can compete with high-multipole gamma emission.) This process is collectively known as beta-delayed gamma decay. It is a two-step process where the relatively-slow beta decay determines the overall half-life. This makes beta-delayed gamma emission a useful tool, since the longer half-life may permit the activity to be transported to detectors away from the primary beam for counting. Additionally, the gamma rays are emitted with a discrete energy corresponding to the energy difference between the initial and final states. By measuring sequences of gamma decays leading to the ground state, the energies of the excited states may be determined. The relative intensities of the gamma decays may be used to determine the beta feeding to the various excited states (e.g., Lis83). Thus some of the experimental difficulties associated with direct measurements of beta decay can be eliminated. Angular correlations between

gamma decays in a cascade can be used to determine the multipole order of the transitions, often allowing the spins of the states involved to be deduced.

However, there are several problems associated with beta-delayed gamma-ray spectroscopy. First, gamma-decay schemes can be very complicated and difficult to deduce since they often involve several different gamma-decay transitions for each beta-decay transition. Both prompt and beta-delayed gamma decay are also very common decay modes. This means that if a production reaction is not selective or the counting area is close to the target it can be extremely difficult to determine what decays are from nuclides other than the one of interest. A third problem is that detector efficiencies are not very large for high-energy gamma-ray transitions, even for rather large solid-angle detectors; the full photopeak energy will be detected only a small fraction of the time and background from Compton-scattered or escape events will lower sensitivity.

As the proton drip line is approached along a series of isobars, the available beta-decay energy increases quadratically, allowing states at high excitation in the daughter to

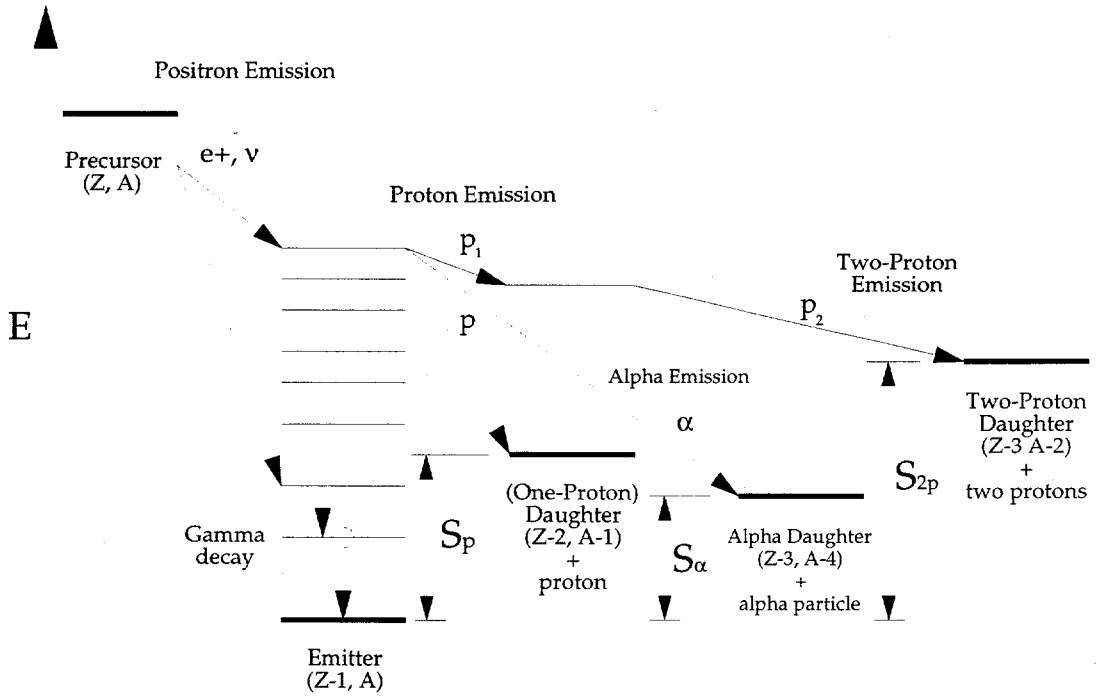

FIG. 2- 5: Schematic depiction of beta-delayed gamma, proton, alpha and (sequential) two-proton decay modes.

be populated. Because of this, ever more exotic beta-delayed decay modes become energetically viable as the limits of stability are approached. These include beta-delayed alpha, proton, two-proton, diproton (^{2}He) and proton-alpha decays. The energetics of several of these decay modes are shown schematically in Figure 2-5.

In regions of the Chart of Nuclides where fission barriers are small, beta-delayed fission becomes energetically viable. In this case, electron capture procedes to states in the daughter nucleus which are unbound to fission and the daughter splits into two intermediate mass fragments. However, since this decay mode only occurs among the heaviest elements ($Z > 92$), it will not be discussed further here.

As is the case among nuclides for which several possible decay modes are energetically allowed from the ground state, the mechanism by which the excited states, fed by beta decay, themselves decay is determined from the partial half-lives of the competing decay processes. The total decay constant for the states is the sum of the individual decay constants:

$$\lambda_{total} = \lambda_\gamma + \lambda_p + \lambda_\alpha + \ldots = \ln 2/T_{1/2} \tag{2-49}$$

The partial half-lives for each decay branch may be determined from the decay constant for that branch (e.g., $t_{1/2,p} = \ln 2/\lambda_p$). The branching ratio (B.R.) for a particular decay branch is related to the partial and total half lives:

$$B.R.(p) = T_{1/2}/t_{1/2,p}. \tag{2-50}$$

Note that in the case of an intermediate state fed by beta decay, the total half-life $T_{1/2}$ in equation 2-50 refers to the half-life of the intermediate state, not the total half-life of the two-step decay process (which will generally be equal to the relatively-long beta-decay half life.)

2.4.2 Beta-Delayed Proton Emission

Beta-delayed proton decay is a two-step process in which beta emission of the "precursor" nuclide feeds an excited state in the "emitter" that is unbound to proton emission; this state subsequently emits a proton, transforming it into the "daughter" (Äys89). The beta-decay is the rate-limiting step in this process and to high accuracy determines the overall

half-life of the process. Because of this, it becomes possible to study proton emission from light nuclides and with high Q_p values, since the beta decay half-life is generally long enough to transport the activity away from the target area for counting.

The intermediate state in the daughter is also unbound to both gamma-ray emission and beta-decay, and near the proton drip line, other more-exotic decay modes. Beta decay of the intermediate proceeds too slowly to effectively compete with the other decay processes and may generally be ignored. When the proton-decay energy is greater than a few hundred keV, proton emission will occur much more rapidly than gamma de-excitation, especially among light nuclides (Hof89). In these cases, the beta feeding to intermediate states in the emitter may be inferred directly from the relative intensities of the proton groups. It is only when the energy of the proton is small relative to the Coulomb and centrifugal barriers that gamma emission must be taken into account. (An exception to this rule of thumb may occur for emission from the isobaric analog state of the precursor, for reasons to be discussed shortly.)

In most cases, proton decay proceeds from the intermediate state in the emitter to the ground state of the daughter. In these cases, it is a trivial matter to deduce the energy of the excited state in the emitter by measuring the proton energy and then correcting it for the energy of the recoil (see equation 2-3.) In some cases, proton emission may occur to excited states of the daughter, either exclusively or accompanying a branch to the ground state (e.g., Rob93). In the latter case, knowledge of the excited states in the daughter will allow a correct assignment to be made, since the two proton energies, converted to the center of mass, will differ by the excitation energy of the excited state in the daughter. If proton emission occurs to an excited state exclusively, it will be more difficult to make a correct assignment of the intermediate state unless p-γ coincidence data is taken. In all cases, knowledge of excited states in the emitter and daughter is invaluable in making the proper assignment for a given decay branch.

Of particular interest are beta-delayed proton decays that proceed from the ground state of the precursor to its isobaric analog state (IAS) in the emitter. These decays are important for determining absolute intensities and for studying the role that isospin plays in nuclear physics. Additionally, the energy relationship between the precursor and its IAS may allow the determination of the mass of the precursor with very good accuracy (Har89).

As was discussed in Section 2.4.3, beta-decay to the IAS is favored relative to decays to other states at high excitation because the wave function of the IAS is nearly identical to that of the parent. This assures that there will be one relatively-large beta-delayed proton decay branch among nuclides where the IAS is both accessible by beta emission and unbound to proton decay. Precursors with isobaric analog states that meet both of these conditions are called "strong" since delayed-proton decay through the IAS will tend to be a rather strong decay branch, i.e., > 10% (Äys89). This condition is met among the A=4N+1, T_Z=-3/2 series of precursors; nuclides closer to stability will be "weak" beta-delayed proton emitters. Clearly this distinction is important primarily from an experimental viewpoint; beta-delayed proton emission from these strong precursors is easier to measure.

Of particular importance is the fact that the mass of the precursor may be related to that of its IAS in the emitter via equation 2-48. By measuring the proton energy from the decay of the IAS, the excitation of the IAS may be determined to an accuracy of a few keV. Since the energy of the precursor and its IAS (to first order) differ by the Coulomb displacement energy and neutron-proton mass difference (Ant97), the mass of the precursor may be deduced with very good accuracy. Thus, measurement of beta-delayed proton emission through the IAS provides a way of determining the mass of the precursor which in turn may provide a test of mass models (see Section 2.5.1) far from stability (e.g., Hot87, Bat93).

Isospin is not a "good" quantum number, strictly speaking. Obviously, both the Coulomb force and the neutron-proton mass difference break the symmetry (Orm89). However, these deviations may be calculated in a straight-forward manner, as is seen from equation 2-48. Additionally, experiments have indicated that there may also be an isospin-nonconserving (INC) component to the nuclear force as well (Hen69). It was shown by Wigner (Wig57) that the energies of the states comprising an isospin multiplet may be fit by:

$$E(T, T_Z, \sigma) = a(T, \sigma) + b(T, \sigma)T_Z + c(T, \sigma)T_Z^2 \qquad (2\text{-}51)$$

This is known as the isobaric multiplet mass equation (IMME); the coefficients of the expansion in T_Z are dependent on both the total isospin T of the multiplet and other quantum numbers σ of the states. The quadratic term is due to the existence of short-range (i.e., strong-nuclear) forces which do not conserve isospin (Orm89). Fits to $T \geq 3/2$ multiplets have in most

cases shown no evidence for higher-order terms (Ant85). If the masses of three or more members of an isospin multiplet are known, the coefficients of the IMME may be determined. The IMME may then be used to predict the masses of other members with an accuracy that depends on the precision of the input masses and the goodness of the fit.

Information gained from beta-delayed proton decay through the IAS may also be used to ascertain the degree to which isospin invariance is violated. If one examines the total isospin of the states involved in these decays, it is clear that if isospin is a good number then proton emission from the IAS is forbidden (Bro90b). For instance, in the case of the decay of ^{23}Al (Gou72, Tig95), the ground-state of ^{23}Al and its ^{23}Mg IAS are both T=3/2 states; the ground state of the daughter ^{22}Na has an isospin of zero. Since the proton isospin is 1/2, there is no way to couple the isospin vectors of the initial state so that it is equivalent to the final state isospin.

However, because isospin is not a good quantum number, states will contain a small admixture of single-particle states with different isospin T, but with all other quantum numbers σ the same (Har71). Proton emission from an IAS to the daughter ground state occurs via this admixture; the decay is hindered, but not forbidden. The isospin impurity of a state may be predicted from first-order perturbation theory if a suitable form for the isospin-nonconserving Hamiltonian can be determined. This will be the subject of Section 2.5.3. Experimentally, the isospin admixture can be estimated by comparing the actual (isospin-hindered) proton-decay rate to the predicted (unhindered) rate. This is somewhat simplified by the fact that reliable estimates for the beta-decay feeding to the IAS can be made from equation 2-47; by comparing the observed intensity to that predicted from the feeding, the proton to gamma-ray branching ratio can be extracted. Knowledge of the gamma-decay partial half-life then suffices to extract the proton decay-constant; this is compared with that expected from calculations to estimate the hindrance and thus isospin mixing in the IAS. Clearly, such estimates will be much more reliable if both the proton- and gamma-decay widths have been measured; however, it may be necessary to rely on predictions of the gamma-decay width if it has not been measured directly. Comparison to the analog(ous) state in the mirror nuclide may be helpful in such situations.

2.4.3 Beta-Delayed Two-Proton Emission

Two-proton emission, either beta-delayed or direct, becomes viable as the proton drip line is approached. Two-proton decay is energetically allowed when the following Q-value is positive:

$$Q_{2p} = \Delta(Z, A) - \Delta(Z-2, A-2) - 2\Delta(^1H) \quad (2\text{-}52)$$

The term $\Delta(Z, A)$ is the mass of the emitter state: either the ground-state (direct emission) or an excited-state fed by beta-decay (beta-delayed emission). To date, ground-state two-proton emission has not been observed. Figure 2-6 shows the location of all known beta-delayed two-proton emitters on the Chart of the Nuclides. Because of nuclear pairing it is possible that a particular state may be bound to single-proton decay, yet unbound to two-proton emission (Gol60, Col96). This will restrict the mechanism of the decay, as will be discussed shortly.

Three different mechanisms have been proposed for two-proton decay: sequential, pre-equilibrium and pair emission (Gol66, Cab84, Mol89). Each mechanism has different characteristic energy distributions for the emitted protons that may be predicted from the

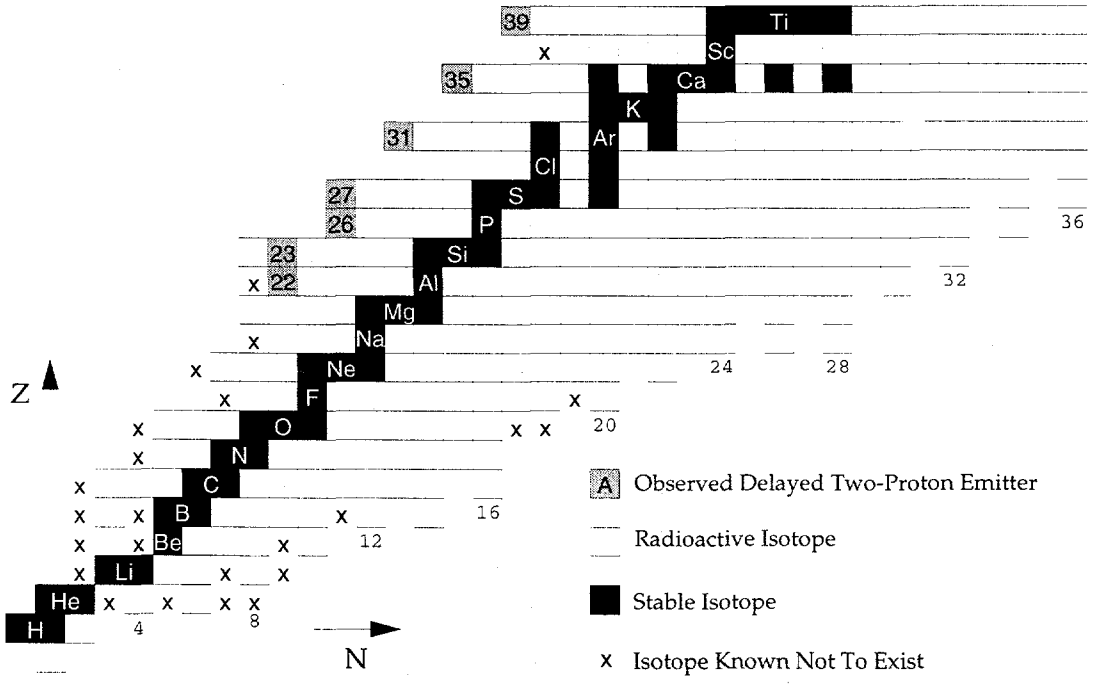

FIG. 2- 6: Region of the Chart of Nuclides where beta-delayed two-proton decay has been observed.

kinematics of the decay. These features may be used to identify which mechanism is dominant for a given nuclide's decay. At the simplest level, the different mechanisms correspond to the number of steps involved in the decay and the time interval between those steps. Of course, in the case of beta-delayed two-proton emission, the initial beta decay adds an additional, rate-limiting step.

Sequential emission is a two-step process; it is shown schematically in Fig. 2-7. The first proton decay proceeds to a quasi-stationary intermediate state in the one-proton daughter. This state is also unbound to proton emission and immediately decays to the two-proton daughter in turn. The first proton emitted will have the laboratory energy for single proton emission; it is determined from equation 2-3. The energy E_{p_2} of the second proton in the laboratory frame will be Doppler shifted since it is emitted from the recoil of the first decay. It will thus depend on its emission angle relative to the first proton (Cab84):

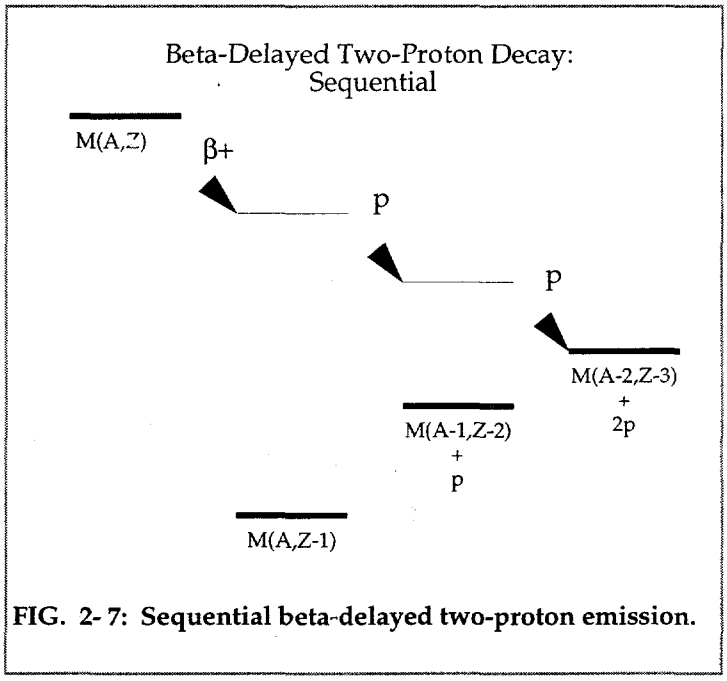

FIG. 2- 7: Sequential beta-delayed two-proton emission.

$$E_{p_2} = \left(\frac{m_{R_2}}{m_{R_1}}\right)Q_{p_2} + \left(\frac{m_p^2}{m_{R_0} m_{R_1}}\right)Q_{p_1} - \left(\frac{2m_p \cos\theta'}{m_{R_1}}\right)\sqrt{\frac{m_{R_2} Q_{p_1} Q_{p_2}}{m_{R_0}}} \qquad (2\text{-}53)$$

where Q_{p_1} and Q_{p_2} are the energies of the first and second decays ($Q_{2p} = Q_{p_1} + Q_{p_2}$); m_p, m_{R_0}, m_{R_1}, and m_{R_2} are the masses of the proton and the states involved in the 2p-emitter, the proton daughter and the 2p-daughter, respectively. The relative-emission angle between the two protons in the center-of-mass frame is given by θ'. Alternatively, Q_{p_2} may be calculated from the observed energies of the two protons and the relative emission angle in the laboratory frame, θ:

$$Q_{p_2} = \left(\frac{m_{R_1}}{m_{R_2}}\right)E_{p_2} + \left(\frac{m_p^2}{m_{R_1}m_{R_2}}\right)E_{p_1} + \left(\frac{2m_p\cos\theta}{m_{R_2}}\right)\sqrt{E_{p_1}E_{p_2}} \qquad (2\text{-}54)$$

This second equation is perhaps more useful than equation 2-53 to the experimentalist.

The energy width of the first-proton peak will be determined by the intrinsic width Γ of the intermediate state and the resolution of the detection system; the latter typically dominates. Because the finite size of detectors leads to summing over a range of angles, the width of the second-proton peak will be dependent on the solid angle subtended (Cab84). In sequential decays where neither of the protons is emitted with zero angular momentum, there will be an additional angular dependence on the emission probability (Bie60). However, this effect is only expected to be of order 10-20% (Cab84) and will be ignored.

The pre-equilibrium mechanism, depicted in Fig. 2-8, occurs when the intermediate state in the one-proton daughter can not be approximated as a stationary state. If the time interval between emission of the first and second protons is very short ($\Delta t < 10^{-20}$s), the intermediate state in the proton-daughter nucleus will not have a well-defined energy. This mechanism is also known as uncorrelated simultaneous emission. Although the two-proton sum energy will be well defined, both of the individual proton spectra will show energy continua whose widths will be determined by the half-life of the intermediate state, as expected from the Heisenberg uncertainty principle. The

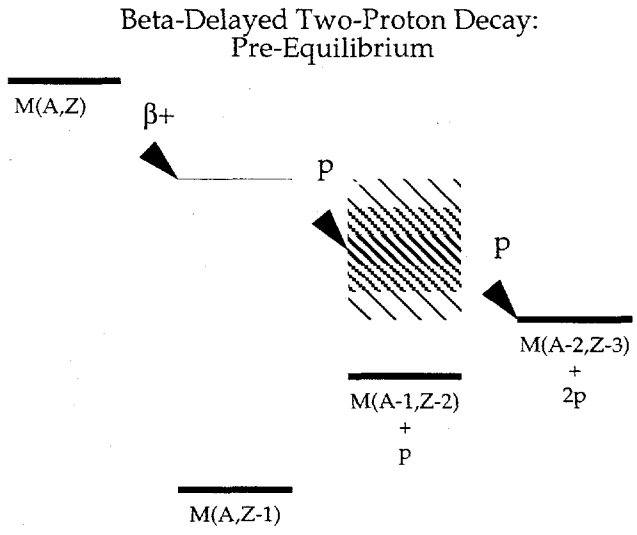

FIG. 2- 8: Pre-equilibrium beta-delayed two-proton emission.

kinematics may be calculated analytically in the limit of $\Delta t = 0$ s; in this case, the energies of the emitted protons are determined solely by the available phase space.

A third possibility, depicted in Fig. 2-9, occurs if the two protons are emitted simultaneously as a pair; this correlated, simultaneous emission is alternately referred to as ^{2}He or diproton decay (Mol89). Because the two protons are paired, the Pauli exclusion principle requires that the two protons be coupled to a $^1S_0$ configuration, i.e., with their spins anti-parallel. The emitted pair is unbound outside of the nucleus and the protons will thus rapidly separate. Although the diproton-decay process occurs in two steps, the parent nucleus is transformed in a single step, with no intermediate state of the parent involved.

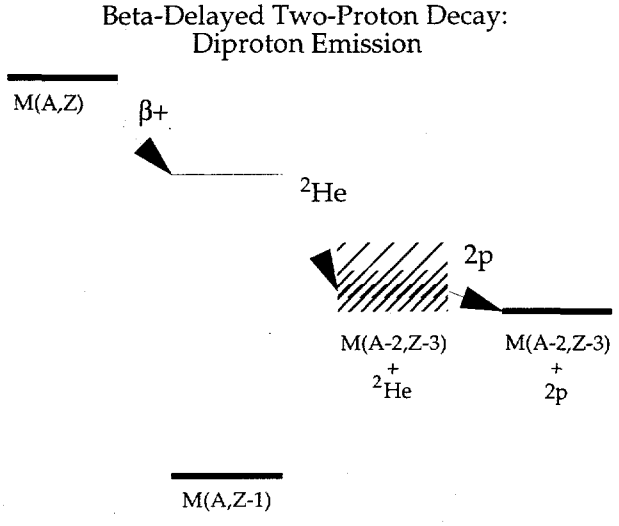

FIG. 2-9: Beta-delayed diproton (^{2}He) emission and subsequent break-up.

Diproton emission is certainly the most interesting of the three decay mechanisms discussed from a quantum mechanics perspective. It is also the least clearly understood. The ^{2}He nucleus, or diproton, has been observed as a virtual state in various nuclear reactions, e.g., the (^{3}He, ^{2}He), (α, ^{2}He) and (d, ^{2}He) reactions (Con80, Jah78, Sta79a). It has been found experimentally that the kinematics of these reactions may be predicted by assuming that there are two steps to the reaction process (Con80). The initial reaction is described using the distorted-wave Born approximation (DWBA) with the diproton as one of the outgoing particles. The diproton then breaks up with an energy determined by the final state interaction (FSI) between the two protons. In order to conserve energy, the break-up energy of the diproton ε must be subtracted from the Q-value of the initial reaction; it then "returns" in the break-up. Estimations of the FSI based on the scattering-lengths observed in proton-

proton scattering predict a distribution of break-up energies rising rapidly from zero, reaching a maximum near ~250 keV, then decreasing slowly; this distribution has been deduced from the kinematics of the ^{2}H(p,^{2}He)n reaction (Sim67). When heavier target nuclei are used, the distribution is observed to be sharply peaked at low energies with a significant high-energy tail (Gav76); using mid-mass nuclei, the peak is centered at roughly 500 keV, with a full-width at half maximum (FWHM) of about 600 keV (Sta79b, Con80). The success of the two-step approach suggests that the break-up of the ^{2}He nucleus occurs well-outside the potential barrier of the nucleus.

This approach may be applied to predict the kinematics of the diproton-decay mechanism. Conservation of energy reduces the recoil momentum by a fraction of the break-up energy ε; the observed two-proton sum energy E_{2p} is:

$$E_{2p} = \frac{m_{R_2} Q_{2p} + 2m_p \varepsilon + \varepsilon^2}{m_{R_2} + 2m_p} \tag{2-55}$$

where m_{R_2} is the mass of the two-proton daughter. Conservation of momentum requires that the two protons separate at 180° relative to each other in the rest frame of the diproton. The relative emission angle θ between the two protons in the laboratory may be determined from:

$$\cos\theta = \frac{E_{p_1} + E_{p_2} - 2\varepsilon}{2\sqrt{E_{p_1} E_{p_2}}}. \tag{2-56}$$

Since the decay energy is reduced by the break-up energy of the FSI, only the low-energy peak of the ε distribution is expected to contribute in decays; the penetrability of the pair decreases exponentially for increasing ε. If Q_{2p} is several times larger than ε (as is normally the case), protons will only be observed at small relative emission angles. The maximum value of θ may be found from:

$$\tan\theta_{max} = \sqrt{\frac{m_{R_0} \varepsilon}{m_{R_2} Q_{2p}}} \tag{2-57}$$

where m_{R_1} is the mass of the parent nuclide. At this angle (for a particular value of ε), the two protons will be detected with equal energies.

In distinguishing between the mechanisms that have been proposed, the energy spectra of the individual protons are of particular importance. For sequential emission they

have well-defined energies, unlike the other two cases where continua will be observed. Simultaneous and pair emission have different distributions of the relative-emission angle. In simultaneous emission, the protons will be emitted isotropically. Pair emission will only be detected at small angles when Q_{2p} is significantly larger than ε. Only sequential emission has been observed (Cab83a, Jah85, Mol89). In cases where sequential emission is energetically forbidden, Gol'danskii predicts that pair emission will dominate over simultaneous-uncorrelated emission (Gol66). The decay widths of the emitter states observed in beta-delayed proton emission with large proton-decay energies and small centrifugal barriers are generally small (Har89), suggesting that hindrance factors make observation of simultaneous emission unlikely.

2.5 Theoretical Models and Predictions

Much of the motivation for the experiments described herein is related to the testing of various nuclear-model predictions. In particular, these experiments provide tests of mass models as well as shell-model predictions of both beta-decay strength and isospin mixing. A qualitative overview of the workings of these models follows.

2.5.1 Mass/Binding Energy

Mass is arguably the most important characteristic of a given nuclide. It is directly related to the binding energy of the nucleus and thus provides a window into the forces holding the nucleus together. Clearly, the degree to which masses can be accurately predicted over a large portion of the Chart of the Nuclides is an important indicator of the extent to which nuclear systems are understood. Additionally, knowledge of masses allows calculation of the Q-values for both reactions and decays, which in turn are intimately associated with the likelihood of those processes occurring. Accurate mass models provide an important guide to experimenters when the mass of a system to be studied is not known experimentally. Two broad classes of mass models may be defined: semi-empirical and those based on mass relations.

Much theoretical work has gone into the development of various models of the nucleus; models provide a framework within which experimental data may be interpreted

and new properties predicted. Unfortunately, no single model is able to predict all the properties of nuclei; different models explain different aspects of nuclear systems. The Liquid Drop Model of von Weisäcker (Wei35) in its modern forms (e.g., Mye66) is able to predict the shape of the mass surface over the entire Chart of the Nuclides to about 1% accuracy. Its extension, the Collective Model of Bohr and Mottelson (Boh69), treats nuclides with non-spherical equilibrium shapes. The Fermi-Gas and Statistical Models attempt to apply thermodynamics to the nucleus (see Mar69, pp. 1229-1261); they are successful at predicting level densities and the neutron-proton asymmetry. The Shell Model of Mayer and Jensen (May55), in its single-particle form, explains the extra stability of the "magic" nucleon numbers and predicts spins and parities of nuclear states near closed shells. Numerous extensions of this model exist that attempt to correct for two-body interactions; these are useful for calculating more realistic wave functions and predicting the properties of excited states (see Section 2.5.2). The Nilsson Model (Nil55) applies the Shell Model to deformed nuclides.

In attempting to predict the masses of nuclides, semi-empirical models generally combine the above models (as well as others) in different proportions to obtain a global fit to experimental mass data (Aud93). The various mass models differ mainly in the emphasis they place on the different nuclear models listed above and the methods and number of free parameters used in the fit. A potential problem with this approach occurs if too many free parameters are used. In this case, an excellent fit may be achieved between the predicted masses and the input masses, but when attempts are made to extrapolate to unknown masses, the predictive power of the model is poor (Hau88).

A good example of this semi-empirical approach is the Unified Macroscopic-Microscopic Model of Möller and Nix (Möl88a). In principle, the mass of a given nuclide could be determined from the shell model by multiplying the energy eigenvalues with the occupation numbers of each state and then summing over all occupied states. Unfortunately, this approach has not been successful, because small errors in the predicted energies of the individual states lead to a large error in the total mass when combined. Strutinskii pioneered an approach that used the liquid-drop model to predict the gross properties of the nucleus, such as approximate mass and deformation, and then used the shell-model to make

fine corrections (Str67). The work of Möller and Nix (Möl88a) represents a refinement of this approach; the average root-mean-squared (rms) deviation from the predicted masses of 1323 nuclides from their experimental values is 835 keV using the Unified model. Examples of other semi-empirical mass model are given in references Möl88b, Sat88, Tac88, Spa88, Han92, Nay95 and Möl95.

The second class of mass models uses relationships between the nuclear masses, based on observed systematic behaviors, to estimate the mass of a given nuclide from the masses of its neighbors. Two important mass relations used for determining the masses of nuclides near the proton drip line are the IMME (Ant97), discussed in Section 2.4.2, and the Kelson-Garvey mass relation (Jän88). The latter is based on the assumption of the charge-symmetry of the nuclear force. It estimates the mass of a Z>N nucleus from the mass of its mirror and the masses of nearby T=1/2 mirror pairs:

$$M(A,T_Z=-T) = M(A,T_Z=T) + \sum_{i=-(2T+1)}^{+(2T-1)} [M(A+i,T_Z=-\tfrac{1}{2}) - M(A+i,T_Z=\tfrac{1}{2})] \qquad (2\text{-}58)$$

where the summation is only over values of i for which (A+i) is odd. Other mass relations are given in references Dus88, Com88, Mas88, Pap88 and Ber90.

The mass relations give generally better estimates of masses than semi-empirical mass models do, but tend to be useful over only specific regions of the Chart of Nuclides. Furthermore, the success of these relations does not necessarily reflect a deep understanding of nuclear properties, since they are based on systematics rather than broad assumptions about the nature of nuclear forces.

2.5.2 Wave Functions and Energy Levels

Ideally, the wave functions of the various states of a particular nucleus should be calculated based on the two-body forces between all nucleons involved. However, this multi-body problem becomes practically intractable for all but the very lightest nuclei. The single-particle shell model was developed as an alternative to this approach. This model assumes that all the two-body forces between individual nucleons sum to create a central potential. It is further assumed that relevant observables may be predicted based on the interactions between the valence nucleons and an inert core. This single-particle model is very successful

at predicting the properties of nuclei near major closed shells, where the assumption of an inert core is most appropriate, and when excitation energies are low.

To account for the properties of nuclei with two or more nucleons outside of the inert core, two-body forces must be included. This leads to mixing between the single-particle wave functions. There are many different methods for treating two-body interactions (Hey94, Bro88a) and it is far beyond the scope of this thesis to present all of them. In the 1*s*0*d*-shell, the W-interaction of Chung and Wildenthal has been most successful at predicting wave functions (Wil83). This method of determining the two-body interactions will be presented briefly; its application to decay rates will be presented in Sections 2.5.3 and 2.5.4. Examples of work along similar lines in other shells is presented in references Coh65, Ree73, Hse85 and van81.

In order for the problem to be tractable, the number of nucleons outside the core for which two-body interactions will be treated must be limited (Bro90a). The number of basis states required in the expansion of the nuclear wave function (the dimension D of the model configuration-space) is strongly dependent on the total angular momentum of the single-particle states involved and the number of nucleons outside of the core (Wil77). Since the early 1980's, computer memories and processing speeds have been sufficient to treat all couplings of the $0d_{5/2}$-$1s_{1/2}$-$0d_{3/2}$ wave functions as the basis. An important part of shell-model studies is determining the effect of excluded configurations (e.g., the 0*p* and 0*f*1*p* shells in calculations using the *sd*-shell basis) on the results of these calculations (Bro90a); in general, some renormalization of the relevant operators will be required in order to match theoretical predictions with experimental results.

In the Chung and Wildenthal approach (Wil83), the state vector Ψ^{NJT} for a given nuclear state with N active nucleons in the *sd*-shell, total angular momentum **J** and isospin **T** is treated as an expansion over all available basis vectors:

$$\Psi^{NJT} = \sum_{i}^{D} \alpha_i \varphi_i^{NJT} \qquad (2\text{-}59)$$

The basis consists of all possible N-particle (or hole) configurations with J and T of the active subshells (e.g., $0d_{5/2}$, $1s_{1/2}$ and $0d_{3/2}$ for a "full-basis" *sd*-shell calculation) using the *jj*-coupling scheme (Wil77):

$$\varphi_i^{\mathrm{NJT}} = d_{\frac{5}{2}}\left|{}^{n_1}_{J_1T_1}\; s_{\frac{1}{2}}\right|{}^{n_2}_{J_2T_2}\Big)^{n_1+n_2}_{J_{12}T_{12}}\; d_{\frac{3}{2}}\left|{}^{n_3}_{J_3T_3}\right)^{N=n_1+n_2+n_3}_{JT} \tag{2-60}$$

The coefficients of the expansion α_i (i.e., the fractions of each basis state in the observed state) are determined by a diagonalization of the Hamiltonian, which includes both one- and two-body interactions.

The Hamiltonian determines not only the mixing coefficients of the basis states, but also the energy of the nuclear state:

$$\mathrm{E}^{\mathrm{NJT}} = \langle\Psi|\mathrm{H}|\Psi\rangle^{\mathrm{NJT}} = \sum_{i,j}^{D} \alpha_i \alpha_j \langle\varphi_i|\mathrm{H}|\varphi_j\rangle^{\mathrm{NJT}} \tag{2-61}$$

It may be specified in terms of the single-particle energies $\mathrm{E_{sp}}$ and the two-body matrix elements $<\mathrm{M_{TB}}>$ that exist for couplings within the model space:

$$\langle\varphi_i^{\mathrm{NJT}}|\mathrm{H}|\varphi_j^{\mathrm{NJT}}\rangle = \sum_k \mathrm{C}_k^{\mathrm{ij}} \langle\mathrm{M_{TB}}\rangle_k + \sum_l n_l^{\mathrm{ij}} \mathrm{E}_{sp,l}\,\delta(i,j). \tag{2-62}$$

Determination of the coefficients $\mathrm{C}_k^{\mathrm{ij}}$ and $\mathrm{n}_k^{\mathrm{ij}}$ is the primary aim of a shell-model code (Wil77). Using the full *sd*-shell basis, there are three $\mathrm{E_{sp}}$ and 63 $<\mathrm{M_{TB}}>$; the latter is determined from the number of combinations of the possible two-body pairs (compliant with the Pauli principle) that couple to the same total values of J and T. The form of the $<\mathrm{M_{TB}}>$ may be specified by an assumed interaction, e.g., a surface-delta function, and then the individual matrix elements parameterized based on that form (Bro88a). Alternatively, the matrix elements themselves may be treated as parameters; this empirical approach is used by Chung and Wildenthal (Wil83) to define the W-interaction. The energy level of a given state is found by combining equations 2-61 and 2-62:

$$\mathrm{E}^{\mathrm{NJT}} = \sum_k^m \left\{\sum_{i,j} \alpha_i \alpha_j C_k^{ij}\right\} \langle\mathrm{M_{TB}}\rangle_k + \sum_l^n \left\{\sum_i \alpha_i^2 n_l^i\right\} \mathrm{E}_{sp,l}\,. \tag{2-63}$$

The calculation proceeds as follows (Wil77, Bru77, Hey94). A reasonable guess is made for the starting Hamiltonian. This is used to determine the mixing coefficients α for a number of experimentally-measured states of known binding energy lying within the *sd*-shell.

Using these α values, a least-squares linear fit to the experimental binding energies is used to determine the coefficients C_k^{ij} and n_k^{ij} in equation 2-63 for all the states. The coefficients in turn specify an improved Hamiltonian, which may be used to again determine values of α. The whole process is repeated until the values of the coefficients converge. In practice it has been found that applying a slight mass-dependence to the two-body matrix elements of the form $\langle M_{TB} \rangle_A = \langle M_{TB} \rangle_{18}(A/18)^{-1/3}$, where the subscript denotes the value of the matrix element for a particular mass number A, is necessary to obtain a good fit over the entire *sd*-shell (Bro88b).

Using this method to construct a universal effective interaction in the *sd*-shell, the rms deviation in the fit to the binding energies of 447 states was 185 keV. Wave functions determined in this manner have been used to successfully predict not only the energy levels of states not included in the fit, but also magnetic dipole and Gamow-Teller transition rates (Bro88b). This approach is limited to the lighter shells, since the ratio of experimentally-measured states to fit parameters decreases drastically in heavier regions. However, examination of the effective interaction for this region may eventually lead to analytical expressions for two-body interactions that could be applied to heavier nuclei.

2.5.3 Gamow-Teller Decay Strength

As mentioned in Section 2.3.2, the simplicity of the operator for Gamow-Teller beta transitions and the ease with which the observed intensity of a given transition can be related to the overlap integral between the final- and initial-state wave functions makes the study of these decays ideal for testing shell model predictions (Bro88b). For transitions between the 1*s*0*d*-shell states, there are four unique single-particle matrix elements, governing transitions between $0d_{5/2}$-$0d_{5/2}$, $0d_{5/2}$-$0d_{3/2}$, $1s_{1/2}$-$1s_{1/2}$ and $0d_{3/2}$-$0d_{3/2}$ single-particle states (Bro83, Bro85). The wave functions generated by the effective interaction discussed in the previous section contain a high degree of configuration mixing; thus the single-particle operators can not be applied to the wave functions directly. Using these wave functions, one can calculate a multiparticle transition amplitude A between the initial and final-state wave functions (Bro78, Bro85):

$$A = \frac{\left\langle \Psi_f^{J'T'} \left\| \left[a_j^+ a_{j'} \right] \right\| \Psi_i^{JT} \right\rangle}{\sqrt{(2\Delta J+1)(2\Delta T+1)}} = \frac{\sum_{n,m} \alpha_n' \alpha_m \left\langle \varphi_{f,n}^{J'T'} \left\| \left[a_j^+ a_{j'} \right] \right\| \varphi_{i,m}^{JT} \right\rangle}{\sqrt{(2\Delta J+1)(2\Delta T+1)}} . \quad (2\text{-}64)$$

The operator $[a_j^+ a_{j'}]$ is of rank ΔJ, ΔT; it destroys a particle in orbit j′ and creates one in orbit j. In the second term, the wave functions have been expanded in the *sd*-shell multiparticle basis, as per equation 2-59. The Gamow-Teller strength will be given by the sum of the products of each single-particle matrix element and the appropriate amplitude A:

$$M(GT) = \sum_{j,j'} \left\langle \psi_{sp,j'} \left\| Op_{jj'} \right\| \psi_{sp,j} \right\rangle \times A_{jj'} \quad (2\text{-}65)$$

Because the *sd*-shell model basis is truncated relative to the true configuration space of the nucleus, the matrix elements obtained from equation 2-65 must be renormalized to account for the excluded configurations (Bro83). This renormalization could be applied to the axial-vector coupling constant g_A in equation 2-40. Brown and Wildenthal instead apply corrections to the "free-nucleon" values of the single-particle matrix elements, creating an "effective" operator for use in conjunction with the *sd*-shell wave functions (Bro85). The magnitude of the corrections is determined by a least-squares fitting routine applied to experimental transition-rate data; the renormalization has been found to be ~0.76 for each single-particle matrix element relative to the free-nucleon value. Details of the fitting procedure may be found elsewhere (Bro85).

This method has proved to be very effective for predicting log*ft* values of transitions to low-lying states in the daughter nucleus. For example, in the case of ^{23}F decaying to ^{23}Ne, the difference between calculated and measured log*ft* values is ~0.2. Of course, this method only applies to allowed decays. At high excitation energies, the level density is generally too high to allow resolution of individual levels. When levels with the same J and T values are very close in excitation energy, perturbations between them become large, such that they are not well described by the full-basis shell model calculations. At these excitations, it is more reasonable to compare the Gamow-Teller strength functions rather than the strengths of individual transitions. Moderately good agreement is observed.

2.5.4 Isospin Mixing

The effective Hamiltonian discussed in Section 2.6.2 assumes that isospin is a conserved quantity. However, as mentioned in Sections 2.2.1 and 2.4.2, this is not rigorously true. Both the Coulomb interaction and differences between the np interaction and the nn and pp interactions lead to a breaking of isospin symmetry. In order to attain agreement between the predictions of the full-basis shell model calculations and the energy levels of nuclei, a correction for the Coulomb potential must be introduced. Furthermore, mixing occurs between states of different isospin; this is not treated at all in the work of Chung and Wildenthal (Wil83) (or other theorists who have applied similar methods to obtain effective two-body interactions in different model spaces.) To calculate the effects of isospin using full-basis shell-model calculations, Ormand and Brown have determined an isospin non-conserving (INC) Hamiltonian empirically (Orm89). Their work is an extension of earlier efforts (see references 11-14 in Orm89).

The nuclear Hamiltonian may be decomposed into isoscalar (k=0), isovector (k=1) and isotensor (k=2) components; these reflect the relative validity of assumptions of the charge-independence ($V_{nn}=V_{pp}=V_{np}$), charge-asymmetry ($V_{nn}\neq V_{pp}$) and charge-dependence ($2V_{np}\neq V_{nn}+V_{pp}$) of the nucleon-nucleon interaction. Since the explicit form of the Hamiltonian is unknown, Ormand and Brown have used a phenomenological approach. The total nucleon-nucleon Hamiltonian is written in terms of the T=0 and T=1 configurations:

$$H_{total} = v^{(0)}_{T=0} I^{(0)}_{T=0} + \sum_{k=0}^{2} v^{(k)}_{T=1} I^{(k)}_{T=1} \qquad (2\text{-}66)$$

where the operators $I^{(k)}$ separate the isospin dependence from the radial and spin components. The T=1 part of the Hamiltonian is assumed to be comprised of a weighted sum of several potentials:

$$v^{(k)}_{T=1} = \sum_{\mu}^{C,\pi,\rho,0} S^{(k)}_{\mu} V_{\mu}(r) \qquad (2\text{-}67)$$

where the coefficient S is the relative strength of each potential, and μ labels the different potentials. The Coulomb potential V_C has the standard e^2/r form, V_π and V_ρ are Yukawa potentials for pi- and rho- mesons, respectively, and V_0 represents the T=1 part of the initial

isoscalar two-body Hamiltonian. The relative strengths of the various interactions $V_\mu(r)$ determines the INC Hamiltonian. Equation 2-67 may be recast in terms of nn, pp and np two-body matrix elements for use with shell-model calculations. In the work of Ormand and Brown, these were evaluated using harmonic-oscillator radial wave functions.

Because the energy shifts between analog states, characterized by the IMME (equation 2-51), are small relative to the total energy of the system, the effects of the isovector and isotensor components of the nuclear Hamiltonian may be treated as perturbations to an isoscalar Hamiltonian, e.g., the Hamiltonian of Chung and Wildenthal (see Section 2.5.2). By separating the Hamiltonian into these components and applying the Wigner-Eckart theorem, Ormand and Brown derive the coefficients of the IMME:

$$\begin{aligned} a(T,\sigma) &= E^{(0)}(T,\sigma) - T(T+1)E^{(2)}(T,\sigma) \\ b(T,\sigma) &= E^{(1)}(T,\sigma) \\ c(T,\sigma) &= 3E^{(2)}(T,\sigma). \end{aligned} \tag{2-68}$$

where T is the isospin of the multiplet and σ stands for all other quantum numbers. The energies $E^{(k)}$ of the isoscalar, isovector and isotensor (k = 0, 1 and 2, respectively) components of the Hamiltonian $H^{(k)}$ are given by:

$$E^{(0)}(T,\sigma) = [(2J+1)(2T+1)]^{-1/2}\langle\psi(T,\sigma)\,|\,H^{(0)}\,|\,\psi(T,\sigma)\rangle \tag{2-69}$$

$$E^{(1)}(T,\sigma) = [(2J+1)T(T+1)(2T+1)]^{-1/2}\langle\psi(T,\sigma)\,|\,H^{(1)}\,|\,\psi(T,\sigma)\rangle$$

$$E^{(2)}(T,\sigma) = [(2J+1)(2T-1)(2T+1)(T+1)(2T+3)]^{-1/2}\langle\psi(T,\sigma)\,|\,H^{(2)}\,|\,\psi(T,\sigma)\rangle$$

where the matrix elements $\langle\psi\,|\,H^{(k)}\,|\,\psi\rangle$ are reduced in both angular-momentum and isospin space.

The relationship between the IMME and the INC components of the Hamiltonian provides a method for determining the strengths of the two-body interactions in equation 2-67. In order to determine the empirical INC Hamiltonian, Ormand and Brown first used full-basis shell model wave functions in the $0p_{3/2}$-$0p_{1/2}$ (Coh65), $0p_{1/2}$-$0d_{5/2}$-$1s_{1/2}$ (Ree73), $0d_{5/2}$-$1s_{1/2}$-$0d_{3/2}$ (Wil83), $0d_{3/2}$-$0f_{7/2}$ (Hse85) and $0f_{7/2}$-$1p_{3/2}$-$0f_{5/2}$-$1p_{1/2}$ (van81) model spaces to determine the one-body and two-body transition densities for the states of isospin multiplets over a range of masses. The isovector single-particle energies and strength coefficients were

then determined from a least-squares fit to the experimental b and c coefficients of the IMME for these multiplets, using the pp, nn and np two-body matrix elements derived from equation 2-67.

The fit obtained from this procedure is quite good. For the *sd*-, *df*- and *fp*-shell multiplets, the rms deviation between the experimental and calculated b-coefficients is ≤ 30 keV. The fit to the lower mass regions is less good; the harmonic oscillator radial wave functions used to evaluate the nucleon-nucleon interactions may be inappropriate in these shells. This empirical INC Hamiltonian may be used with first-order perturbation theory to determine isospin-mixing in nuclei.

2.6 Astrophysics and Nucleosynthesis

The study of the structure and evolution of stars is perhaps the ultimate test of physics. In stars, all four of the fundamental forces of nature (gravitation, electromagnetism and the strong and weak nuclear forces) play roles of almost equal importance. Astrophysics makes use of nearly all of the tools developed by physicists: quantum, statistical and classical mechanics; thermodynamics, optics, spectroscopy, and fluid dynamics; particle, nuclear and atomic physics.

Nuclear reactions play a particularly central role as the main power source for stars over their long lifetimes. The idea that the energy derived from nuclear reactions was responsible for the sun's brilliance is generally ascribed to Eddington. Seminal papers by Burbridge, Burbridge, Fowler and Hoyle (Bur57) and Cameron (Cam57) explored this hypothesis in a quantitative manner and established the correlation between the reaction pathways in stars and the elemental and isotopic abundances observed in the universe. This connection is still one of the most important criteria by which stellar models are judged: a model that correctly reproduces these abundances while explaining the observed evolutionary stages of stars is likely to be sound.

Several nucleosynthesis processes involve nuclei near the proton drip line; studies of these nuclides can thus provide important information about the specific reaction pathways followed in these processes. A brief discussion of the NeNa and MgAl cycles (Rol88) and the

rapid-proton (rp) process follows (Wal81). The measurements of the beta-delayed proton decay of ^{23}Al, discussed in Chapter 4, were meant to provide information that is important to the understanding of these processes.

2.6.1 Nucleosynthesis Near the Proton Drip Line

After a long period of hydrogen burning, ranging from ~10^8 - 10^{11} years, depending on the initial mass of the star, the supply of hydrogen "fuel" in the core of the star will be exhausted. Hydrogen burning will slowly migrate outward in an expanding shell around the core. As this occurs, the outer layers of the star will expand and cool; it becomes a red giant. The core of the star continues to contract under gravitation. Most stars, including the sun, are thought to have sufficient mass for other reactions to occur. New hydrogen-burning cycles can occur using isotopes of Ne, Na, Mg and Al as catalysts (if these isotopes are present in sufficient abundances):

$^{20}Ne(p,\gamma)^{21}Na(e^+\nu)^{21}Ne(p,\gamma)^{22}Na(e^+\nu)^{22}Ne(p,\gamma)^{23}Na(p,\alpha)^{20}Ne$ NeNa Cycle

$^{24}Mg(p,\gamma)^{25}Al(e^+\nu)^{25}Mg(p,\gamma)^{26m}Al(e^+\nu)^{26}Mg(p,\gamma)^{27}Al(p,\alpha)^{24}Mg$ MgAl Cycle

Although these cycles are not a primary source of energy in such stars, they influence the observed abundances of these elements/isotopes. The primary sources of energy at this stage of stellar evolution are fusion reactions between relatively heavy elements. Nucleosynthesis will proceed through He, then C, O, Ne, and finally Si burning stages if the star is sufficiently massive.

In old stars, explosive events can occur that provide a high proton flux for a short period of time, on the order of seconds or minutes (Wal81). In such an environment, a large number of proton-capture reactions will rapidly occur, producing heavier elements. If the proton flux is sufficiently high, the process will be beta-decay limited; proton capture will typically occur until the proton drip line is reached and then be halted until beta decay occurs. How far up the Chart of the Nuclides the process proceeds under these conditions will be determined by the half-lives of these "bottle-neck" nuclides; significant synthesis of higher-Z nuclides via proton burning can not occur if the half-life is longer than the duration of the explosive-burning event.

Nucleosynthesis involving explosive hydrogen burning is referred to as the rapid-proton or rp-process (Wal81, Cha92). The reaction pathways will be strongly influenced by both the temperature and the proton flux. Which reactions occur will also be very sensitive to the chemical (and isotopic) composition of the outer layers of the star at the onset of explosive burning (Wie86a). If this material is mainly C, N and O, the process will be nearly identical to the hot CNO cycles (Rol88). Figure 2-10 shows calculated pathways for the rp-process at two different temperatures (Wie86a). Although the rp-process is not thought to strongly influence isotopic abundances observed in nature as a whole (Cha92), it may be important in explaining abundances observed in these types of violent stellar events.

Two types of explosive events are thought to be the most likely environments for rp-process nucleosynthesis: type II supernovae and novae (Wal81). Type II supernovae occur when a very massive star exhausts all the fuel in its core. Silicon burning converts the core of

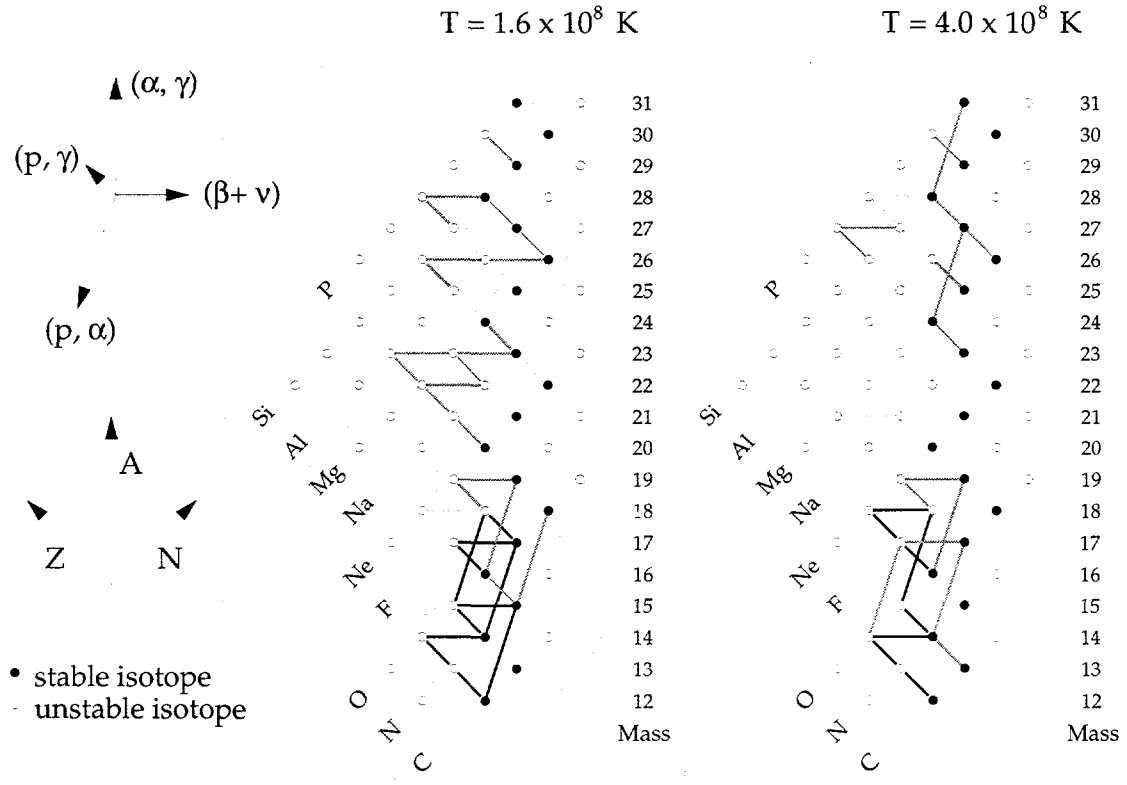

FIG. 2- 10: Reaction pathways in explosive hydrogen burning processes in novae at two temperatures, as calculated by Wiescher, *et al.* (Wie86a). The darkness of the lines is an indication of the flux strength.

the star to Fe and Ni; because the stable isotopes of these elements have the greatest binding energy of all nuclides, all reactions on these species are endothermic. Without further energy generation, the core, containing perhaps 20% of the total mass of the star, collapses under its own mass, releasing an enormous amount of energy in the process.

Due to Coulomb repulsion between nuclei, burning of increasingly heavy elements must occur at ever higher temperatures, furnished by gravitational contraction. White dwarves are stars that are insufficiently massive to continue burning; their store of the current "fuel" is exhausted but their mass is insufficient to overcome the Coulomb repulsion and fuse heavier elements. Such stars will then slowly cool over eons; this is thought to be the fate of most stars. However, if a white dwarf is part of a close binary system, mass transfer between the two stars can re-ignite burning in the dwarf. This will lead to either a nova or a type I supernova. If the companion star becomes a red giant, its radius may swell beyond its Roche lobe (the gravitational equipotential surfaces surrounding the two stars, joined at their center of mass), leading to accretion of matter onto the surface of the white dwarf. Depending on the accretion rate and the elemental composition of the dwarf, burning may be re-ignited either in a thin shell of hydrogen on the stellar surface (novae) or within the carbon core of the dwarf (type I supernovae). In the case of the nova phenomenon, the strong degeneracy of the dwarf will lead to a runaway reaction in which the hydrogen fuel is consumed in about a minute and the outermost layer is ejected from the star. Temperatures in this process are thought to range from about 0.1 - 0.4 x 10^9 K.

2.6.2 Stellar Reaction Rates

It is clear that the determination of reaction networks in stellar environments depends sensitively on the competition between beta decay and the various capture reactions which can occur, especially the (p,γ), (p,α), (α,γ) and (α,p) reactions. Laboratory measurements of the reaction rates are complicated by several factors. The cross sections σ(E) involved in these reactions are very small at the relevant stellar temperatures; often the rate must be estimated by downward extrapolation from higher energies. Additionally many of the reactions involve unstable species, thus requiring the use of radioactive targets and/or radioactive beams. In many cases the reaction rates have been estimated from other available data rather than measured directly.

For a reaction A(a,b)B, the total rate r is determined from the number densities of the reactants, N_A and N_a, and the reaction rate per particle pair $<\sigma v>$ (Rol88):

$$r = N_A N_a <\sigma v> (1+\delta_{Aa})^{-1} \tag{2-70}$$

where the Kronecker delta function δ_{Aa} prevents double counting in the case of identical particles A and a. The rate per particle pair $<\sigma v>$ depends on the local stellar temperature and the cross section for the particular reaction. The velocity distribution in stars is generally assumed to be Maxwellian; most reactions occur not at the average energy of the ions in the gas but instead between ions with energies in the high energy part of the distribution. To illustrate, the mean energy of protons in the sun is about 10 keV; the Coulomb barrier between two protons is about 550 keV. The total reaction rate per particle pair $<\sigma v>$ is determined from the cross section as a function of energy averaged over the Maxwell-Boltzmann energy distribution:

$$\langle \sigma v \rangle = \left(\frac{8}{\pi \mu} \right)^{1/2} \frac{1}{(kT)^{3/2}} \int \sigma(E) E e^{-E/kT} dE \tag{2-71}$$

where μ is the reduced mass of the two ions and E is in the center of mass. The cross section $\sigma(E)$ will generally have contributions from both non-resonant direct reactions and from resonant reactions leading to the formation of an intermediate excited state of the compound nucleus.

The non-resonant cross section will be dominated by the penetrability of the combined Coulomb and centrifugal barriers, as given in equations 2-16 and 2-17. If the energy is much less than these barriers, the cross section may be approximated by the expression:

$$\sigma(E) = \frac{S(E)}{E} e^{-2\pi\eta} \tag{2-72}$$

where the 1/E factor arises from the geometric cross section and the quantity η is called the Sommerfeld parameter:

$$\eta = \frac{Z_A Z_a e^2}{\hbar v} = 4.980 Z_A Z_a \left(\frac{\mu}{E} \right)^{1/2} \tag{2-73}$$

with μ in amu and E in keV. The expression S(E) in equation 2-72 is the astrophysical S-factor; the dependence of the cross section upon nuclear structure effects is contained in this factor. Since the penetrability increases exponentially with energy as the velocity distribution decreases exponentially, substitution of equation 2-72 into 2-71 results in a peak centered at an energy several times kT. Most reactions will occur within the energy range under this "Gamow" peak.

Non-resonant reactions are assumed to take place in a single step. Alternatively, the reaction may proceed through the formation of a compound nucleus in an excited state that then decays via two or more channels. The intermediate state corresponds to a meta-stable configuration of the compound nucleus; when the reaction energy matches the energy of such a configuration, the reaction is said to be resonant and the cross section is enhanced. The cross section for a resonance is given by the Breit-Wigner formula:

$$\sigma(E) = \pi\lambda\!\!\!^{-2}\frac{2J+1}{(2J_A+1)(2J_a+1)}(1+\delta_{Ab})\frac{\Gamma_a\Gamma_b\cdots}{(E-E_R)^2+(\Gamma/2)^2} \qquad (2\text{-}74)$$

where J_A and J_a are the angular momenta of the heavy and light nuclei in the entrance channel, J is the angular momentum of the compound-nuclear state, and E_R is the energy of the resonance. The factor $\pi\lambda\!\!\!^{-2}$ is the geometric cross section. The quantities Γ_n are the partial-decay widths of all the channels by which the compound nuclear state can decay, including the entrance channel; the total width of the state Γ is the sum of all of the individual channels. The widths may be related to the partial half lives for each decay process by the uncertainty principle (see equation 2-21).

If a resonance is narrow and isolated (i.e., $E_R >> \Gamma$), the Breit-Wigner formula for the cross section may be substituted into equation 2-71. Since there is little change in the Maxwell-Boltzmann distribution over the width of the resonance, it may be taken outside of the integral. Integration then yields:

$$\langle\sigma v\rangle = \left(\frac{2\pi}{\mu kT}\right)^{3/2}\hbar^2(\omega\gamma)_R e^{-E_R/kT} \qquad (2\text{-}75)$$

where the factor ωγ is the resonance strength; it consists of the statistical factor ω and the ratio γ of the products of the partial widths to the total width:

$$(\omega\gamma)_R = \omega\frac{\Gamma_a\Gamma_b}{\Gamma} = \frac{2J+1}{(2J_A+1)(2J_a+1)}\frac{\Gamma_a\Gamma_b}{\Gamma}. \qquad (2\text{-}76)$$

A particular compound nucleus may have many resonances at different excitation energies (corresponding to different energies in the entrance channel); the total cross section is thus given as a sum of the contributions of all the resonances R_i:

$$\langle\sigma v\rangle = \left(\frac{2\pi}{\mu kT}\right)^{3/2}\hbar^2\sum_{R_i}(\omega\gamma)_i e^{-E_i/kT}. \qquad (2\text{-}77)$$

Thus the calculation of stellar reaction rates relies principally on the determination of the astrophysical S-factor S(E) and the resonant reaction strengths $(\omega\gamma)_R$. As stated earlier, these measurements are generally very difficult to perform since the cross sections are typically very small at the relevant energies; one is often forced to rely on extrapolations of the cross section from higher energies. The determination of resonance strengths is of particular importance since the cross section may be greatly enhanced over the narrow energy range of the resonance.

However, it is one of the tenets of the theory of compound nuclear reactions that the decay of the compound nucleus is independent of how it was formed. Thus the cross section can be determined using a different reaction to create the compound nuclear state than is utilized in stars; the total width of the state may be inferred from the sum of all possible decay widths. In particular, an important excited state of the compound nucleus that corresponds to a resonance may sometimes be populated by beta decay. If the state is unbound to proton emission, the partial widths for proton decay and gamma emission can then be measured directly or inferred from the competition between the two decay modes. Since the total width is the sum of the proton and gamma-decay partial widths, this may provide a way to determine the proton-capture strength, and thus the cross section, for that particular resonance (Tig95).

C H A P T E R 3

EXPERIMENTAL EQUIPMENT AND TECHNIQUES

3.1 Preparation of Nuclides

3.1.1 The 88-Inch Cyclotron

All experiments in this thesis were performed at the 88-Inch Cyclotron at Lawrence Berkeley National Laboratory, shown in Fig. 3-1. The 88-Inch Cyclotron (Kel62, Lyn98) is an azimuthally-varying field (AVF) cyclotron that has been in operation since 1962. Although originally designed to accelerate light ions exclusively, currently two electron-cyclotron resonance (ECR) ion sources permit ions as heavy as uranium to be accelerated (Cla83, Xie91). The maximum energy (and corresponding intensities) for the ion beams used in this work are (Lyn98): ^{1}H, 55 MeV/u (6 eμA); ^{3}He, 45 MeV/u (10 eμA); ^{40}Ca, 23 MeV/u (40 enA). For certain experiments, the ion beam may be deflected electrostatically in the axial-injection line between the ECR and the cyclotron to produce a pulsed beam. This feature may be exploited to eliminate background radiation arising from fast neutrons, which are produced in high yield when light-ion beams are used.

For all of the experiments in this thesis, the beam was extracted from the cyclotron and directed into Cave 2. Cave 2 has three different target systems, as shown in Fig. 3-1. The upstream helium-jet target is used for experiments that measure the properties of low-yield nuclides with half-lives longer than ~20 ms. The downstream helium-jet target assembly transports activity into the Recoil Atom Mass Analyzer, RAMA (Mol80a, Mol80b, Ogn96).

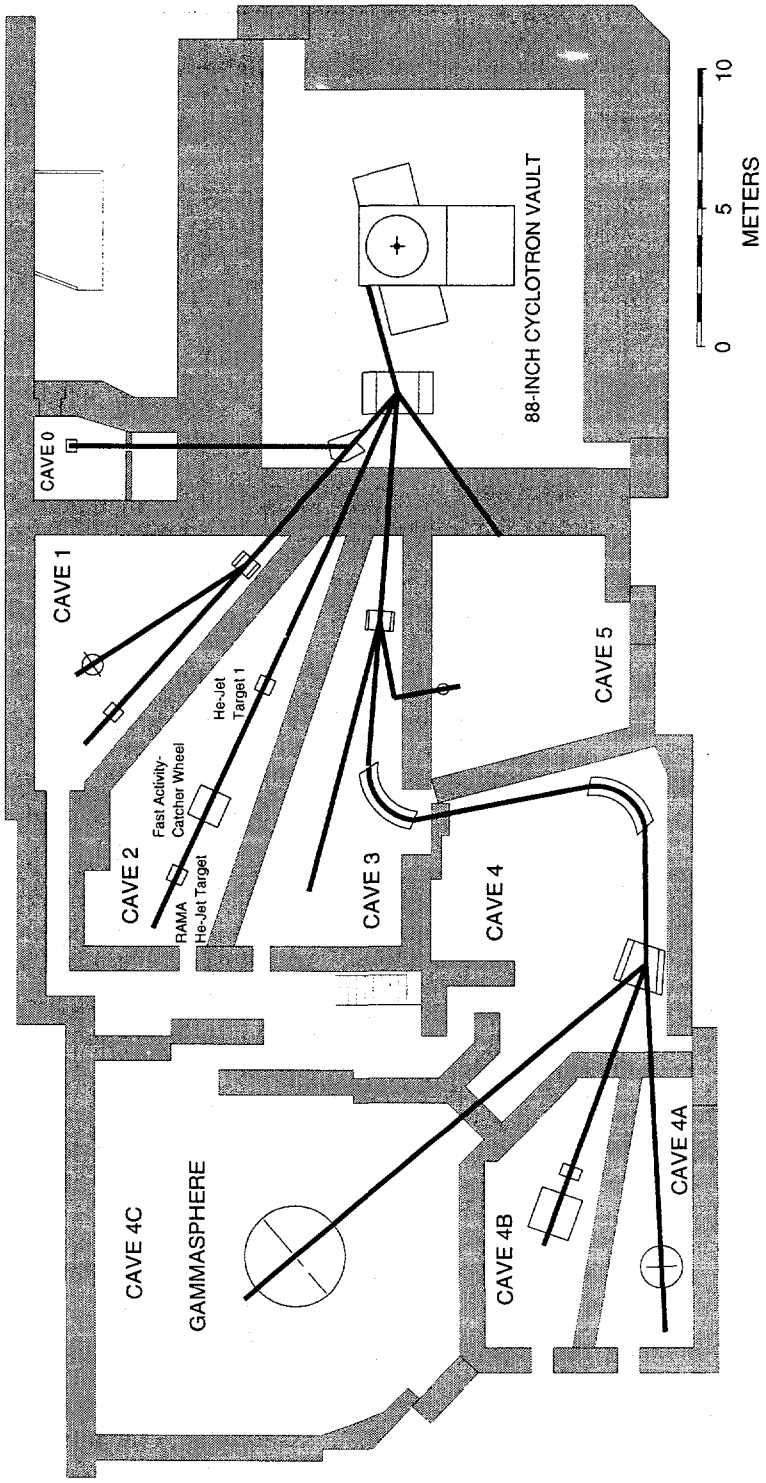

FIG. 3- 1: The 88-Inch Cyclotron Facility. All experiments were performed in Cave 2. A more detailed diagram of Cave 2 will be presented later in Fig. 3-4.

RAMA is used when mass separation is necessary and the yield of the activity of interest is relatively high; its operation will be discussed in Section 3.1.4. The fast activity–catcher-wheel target system is used for very short-lived nuclides; it was not utilized in any of the experiments discussed herein.

3.1.2 Production Reactions for Proton-Rich Nuclides

Most studies of proton-rich exotic nuclides have used one of three different nuclear reaction types to produce the activity of interest: direct, fusion-evaporation or fragmentation. All nuclides studied in this thesis were produced using fusion-evaporation reactions; however, a brief discussion of the alternative reaction types will clarify why they were not used. A more detailed discussion of nuclear reactions may be found elsewhere (e.g., Sat83, Fes92).

In direct reactions such as (p,n), (p,d) or (^{3}He,^{3}H), the reaction products are formed in a single step which occurs in ~10^{-21} s. By measuring the energy of the reaction products, the energy (and thus mass) of the ground and excited states of the product nuclei may be determined directly. Angular distribution measurements may allow the spins of the states to be deduced. For example, the mass of ^{23}Al was first determined using the ^{28}Si(p,^{6}He)^{23}Al pick-up reaction with a cross section of ~100 nb/sr. (Cer69). As this example demonstrates, increasingly exotic reactions (with decreasing cross sections) on N=Z targets are required to approach the proton drip line at higher masses. Thus direct reactions have mainly been employed for studies of very light proton-rich nuclides.

Fragmentation (or spallation) reactions employ high-energy, heavy-ion projectiles (typically, 50-100 MeV/A) to produce light, proton-rich nuclides. Impact between projectile and target causes fragmentation of the target nuclides into a wide variety of lighter-mass products. In order to study the reaction products of interest, the fragments are typically directed into a mass analyzer which allows their Z and A to be identified based on their energy, magnetic rigidity and time of flight (TOF) through the system. The lightest isotopes of silicon, ^{22}Si (Sai87) and ^{23}Si (Lan86), were discovered using this technique. Direct identification of the reaction products and the virtual elimination of contaminant species removes much of the ambiguity from decay studies of the products. Furthermore, because transport of the activity to the detectors is very rapid (~μs), very short-lived species can be

studied. However, since the products are generally implanted into the detectors, decay-particle identification is more difficult and spectra tend to have lower resolution (than if the decays were to occur external to the detectors). Since the stable nuclei used as beams and targets become increasingly neutron rich, cross sections for production of proton-rich nuclei ($T_z < 0$) decrease as the masses of the projectile and target nuclei increase. Clearly the instrumentation requirements for the use of fragmentation reactions are extensive.

Fusion-evaporation reactions occur at relatively low energies. Products are formed in a series of steps, beginning with fusion of the projectile and target nuclei to form a compound nucleus. The compound nucleus is created in a highly excited state, but is meta-stable. Through a series of collisions, the energy of the original projectile is distributed among many nucleons in the compound system. Over a period of 10^{-19} to 10^{-12} s, the excitation energy is removed from the system, first by emission of particles (usually neutrons, protons or alpha particles), then by gamma-ray emission. For particles to be emitted, sufficient excitation energy to overcome the binding energy must be re-concentrated in a single ejectile (n, p, or α) via random collisions. Decays to nuclides closer to stability are strongly favored.

The collision between projectile and target often imparts a large amount of angular momentum to the compound nucleus, which must be shed as the system rids itself of excitation. The centrifugal barrier favors emission of particles with little angular momentum. After emission of a few particles, the system nears the yrast line, which is defined by the lowest energy state of a nucleus for a given angular momentum. At this point, essentially all of the excitation energy is involved in rotational degrees of freedom and no additional particles can be emitted. As the compound nucleus approaches the yrast line, energy and angular momentum are increasingly shed by gamma-ray emission, generally through a cascade of E2 gamma rays down a rotational band built on a low-lying state of the daughter nucleus.

It is a central tenet of the theory of compound-nucleus reactions that this decay process is statistical in nature and independent of how the compound system was formed. If it is suspected that a reaction product from a target contaminant is interfering with detection of the species of interest, this feature may be exploited by using a different entrance channel to form a particular compound-nucleus system with the same excitation energy (e.g., $^{16}O + ^{24}Mg$ instead of $^{20}Ne + ^{20}Ne$ to form ^{40}Ca). As a practical matter, the intensity of beams provided by

the 88-Inch Cyclotron generally decreases with increasing mass; thus a higher reaction yield for a given compound nucleus is usually obtained by using the lightest, highest-intensity beam available.

Two computer codes have been used in this work for the estimation of fusion-evaporation reaction cross sections: ALICE (Bla82) and PACE2 (Gav80). ALICE analytically calculates the probability of decay via each energetically-viable reaction channel; the sum of these probabilities is normalized to the geometric cross section. PACE2 uses a Monte Carlo method to estimate the cross section for each decay channel by following the decay sequences of a large ensemble of compound nuclei and seeing how often each possible final nuclide results. Both codes include a fission probability calculated from the density of states at the fission-barrier saddle point. Of the two codes, PACE2 has generally been found to give closer agreement with experimental cross sections. However, PACE2 is less useful than ALICE for calculating cross sections for weak (<~1 mb) reaction channels; because PACE2 uses a Monte Carlo approach, enormous numbers of trials are required to obtain sound predictions of these cross sections.

3.1.3 Helium-Jet Target Systems

When an ion beam is on target, a great deal of prompt radiation will be produced. This radiation will make decay studies of the reaction products difficult directly in the target chamber. Furthermore, fast neutrons produced as a result of direct reactions, or emitted from excited compound nuclei, will cause damage to solid-state radiation detectors, degrading resolution and eventually rendering the detectors unusable. For both of these reasons, it is highly advantageous if the reaction products can be transported to a separate area for counting. Clearly this must be done as quickly and efficiently as possible if one wishes to study the properties of nuclei with short half-lives and low production yields.

One method which accomplishes these goals reasonably well is the helium-jet recoil transport technique (Mac74). Figure 3-2 shows the helium-jet system used to transport activity to detectors for immediate counting. The target is placed in a small chamber which is separated from the high-vacuum beam line by thin windows through which the beam enters and exits. This chamber is filled with helium gas. When a reaction occurs, the projectile imparts forward momentum to the product nucleus; this momentum is dispersed through

collisions with atoms first in the back side of the target, then with the helium. The target thickness and gas pressure are adjusted so as to maximize the fraction of products that will finally be "stopped" (thermalized) in the gas. The gas is continuously swept from the target chamber through a capillary by differential pumping; the capillary entrance is positioned behind the target so as to efficiently collect reaction products, which are carried along by the gas into the capillary. For non-gaseous products, it has been found that the transport efficiency is increased by addition of chemical additives as aerosols or clusters to the gas. The reaction products tend to stick to the surface of these additives (by a mechanism that is not well understood). To maintain a high transport efficiency the flow of gas in the capillary should be laminar; the heavy, activity-laden clusters then travel through the center of the capillary where the gas velocity is the highest. Upon exiting the capillary, the activity is deposited onto a collection surface where it will be counted. Alternatively, the gas jet may be fed into an ion source for ionization and subsequent re-acceleration (see Section 3.1.4). Helium-jet systems can achieve transport efficiencies as high as 90% (Mac69).

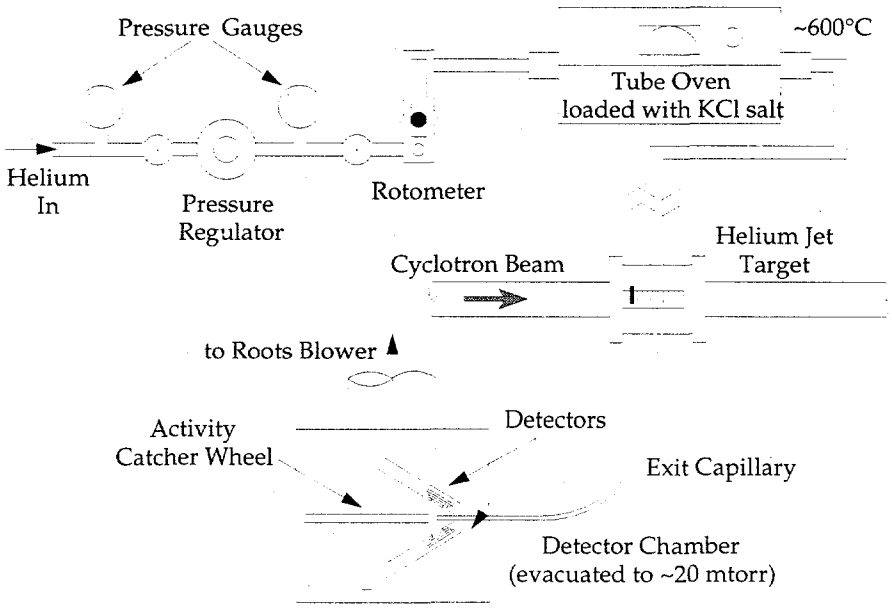

FIG. 3- 2: Helium-jet transport system. A single-capillary He-jet configuration is shown. See text.

Figure 3-3 depicts a detailed schematic diagram of the helium jet target used in these experiments. For scale, the beam line shown is ~10 cm in diameter. The beam enters the target

chamber through two 23 μm thick HAVAR (Ham98) windows; a flow of chilled N_2 gas is maintained between the two windows to prevent them from melting as a result of energy lost by the beam. To achieve a high transport efficiency, the helium gas is allowed to flow over KCl salt that has been heated to ~600 °C prior to being introduced into the target chamber; this leads to saturation of the gas with KCl aerosols. The flow rate of He is adjusted to maintain a pressure of ~1.3 atm inside the target chamber; the specific flow rate used varies from experiment to experiment and depends mainly on the inner diameter and length of the exit capillary. Typical flows are from 50-130 mL/s at room temperature.

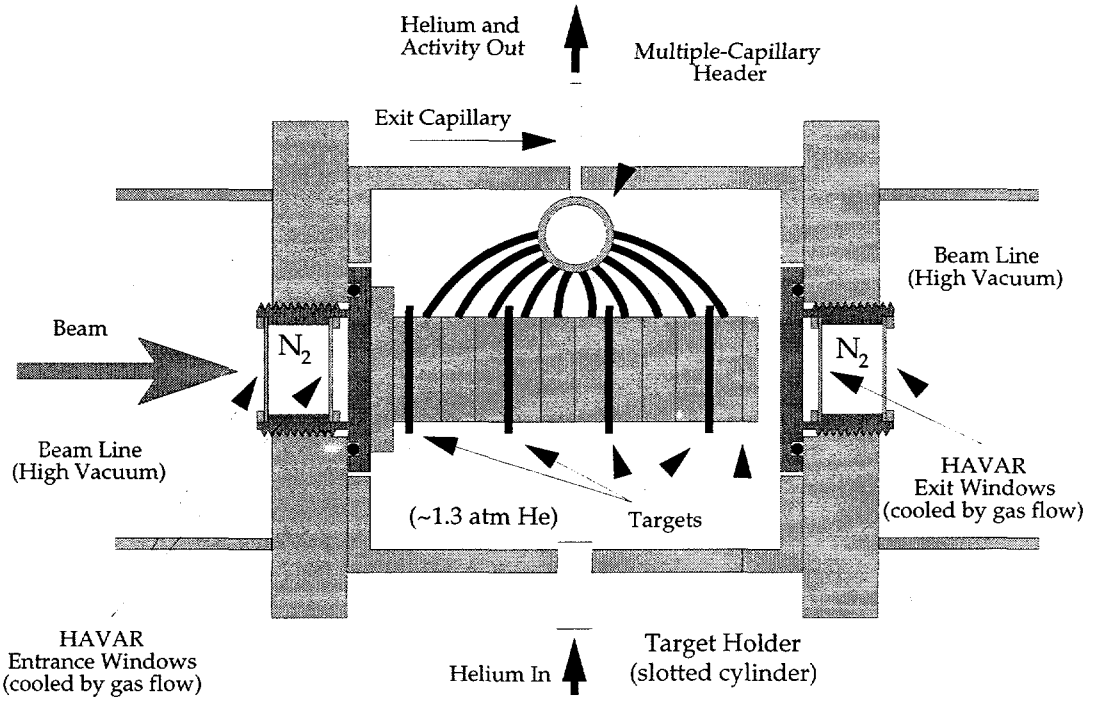

FIG. 3- 3: Helium-jet target. In the multiple-capillary system shown, ten small capillaries sweep the activity from behind each of ten target-holder slots. These small capillaries then feed into the single exit capillary. In the configuration shown, a target is placed in every third slot; the other slots are left empty.

The target foils are placed in slots in a ~1 cm dia. by 7.5 cm long cylinder; the target slots are situated at regular intervals approximately 7 mm apart. Figure 3-3 shows a

multiple-capillary system, in which the volume behind each of the ten target slots is evacuated by a 1 mm i.d. capillary that then feeds through a header into a single exit capillary. Two other target-cylinder configurations are used: one with only a single capillary and an intermediate system with four feeder-capillaries leading to the header. In each design, the aerosol-loaded He flows into the target cylinder through the target slots (the targets fit into the slots loosely). By minimizing the volume behind the targets, these target cylinders minimize the sweep-out time. In the experiments in this thesis, the length of the capillary was relatively short; in measurements that did not use the mass separator RAMA, the detector chamber was placed approximately 60 cm from the He-jet target. The minimum transport times using the single, 4- and 10-capillary systems were of order 20, 50 and 100 ms, respectively.

The choice of target thickness is important when using a He-jet transport system. This is especially true if a high-Z beam is used since the targets may significantly degrade the beam energy. Typically only a fraction of the target thickness will actually be sampled; products made in the front of the target may not have sufficient momentum to exit the target, whereas products from the back will not be stopped in the helium but will become imbedded in the downstream target. The stopping power tables of Northcliffe and Schilling (Nor70) are useful for estimating the effective target thickness.

In choosing whether to use the single-, four-capillary or ten-capillary He-jet target, a compromise must be made between the transport time and the production yield. For very short-lived species (< ~20 ms), the fast single-capillary system should be used to prevent excessive losses in transit. For species with relatively-long half-lives, use of the ten-capillary system with ten targets may be advantageous due to increased production from the additional targets. However, if the products exit the target with a large recoil energy, e.g., in ~symmetric heavy-ion reactions, they may require more than 7 mm of He (at ~1.3 atm) to be stopped. In such a case, the yield of activity transported does not scale with the number of targets. The configuration shown in Fig. 3-3 might be used in such a situation, provided that the half-life of the activity were long enough that the slower transport time through ten capillaries was less important than the improved collection this system provides over the four-capillary system.

It is important that the gas flow in the capillary remain laminar and not become turbulent (Mac74). (If the flow is turbulent, the clusters will tend to be deposited on the walls of the capillary.) When the flow is laminar, the flow is fastest in the center of the capillary and slower near the edges; a Bernoulli force F_B tends to guide clusters into the center of the capillary:

$$F_B = m^{4/3} v^2 r^2 g_s \tag{3-1}$$

where m is the mass of the cluster, v the velocity of the gas, r the radial distance from the center of the capillary and g_s is the specific gravity ($\approx$ density) of the gas (Wol76). The Reynolds number R_e (Mac74) is calculated from the velocity v (cm/s), the capillary radius a (cm), and the density ρ (g/cm^3) and viscosity η (poise $\equiv$ dyne·s/cm^2) of the gas:

$$R_e = 2va\rho/\eta \tag{3-2}$$

For laminar flow, the Reynolds number will tend to be below 1000; helium-jet systems typically operate just below this limit.

Many different aerosols have been used in helium-jet systems. The mass dependence on the restoring force (equation 3-1) suggests that larger aerosols will have higher transport efficiencies since they will be guided away from the capillary walls. Heating KCl above ~580 °C leads to formation of cluster aerosols that have an average mass of ~10^5 atomic mass units. One must be careful not to heat the KCl above ~640 °C or a glass will be formed on the surface of the KCl, preventing further generation of aerosols. Unlike liquid aerosols such as ethylene glycol, pump oil or water [Jun71], KCl does not require interaction with the beam in order for high molecular weight clusters to be formed.

The capillary carries the activity away from the target area to an evacuated detector chamber. A vacuum of ~20 mtorr is maintained in this box by a large-throughput Roots blower (700-2400 L/s); this differential pumping drives the gas flow through the capillary. Upon exiting the capillary, the activity-laden clusters are deposited onto a collection surface for counting. Since the activity of interest is generally very short-lived, it is advantageous to remove longer lived activities. This may be accomplished by depositing the activity onto a wheel or magnetic tape that will slowly move the activity out of range of the detectors. The

different activity-catcher systems used in this work will be discussed in the chapters describing each of the measurements.

3.1.4 Mass Separation

As discussed in Section 3.1.2, fusion-evaporation reactions are not very selective; cross sections decrease rapidly for nuclides increasingly far from stability. Because of this, most of the activity produced will consist of beta-delayed gamma emitters which may interfere with the detection of the species of interest. Generally these experiments rely on the rarity of proton emission as a way of identifying very proton-rich isotopes. However, in some reactions more than one (generally, beta-delayed) proton emitter may be produced, possibly leading to ambiguity. This is particularly problematic among heavier nuclides; beta-delayed proton emitters in the higher mass regions often emit a pseudo-continuum of protons (rather than having discrete peaks), since the density of beta-decay accessible, proton-unbound states is much higher than in light nuclei (Har89). In these situations, mass separation of reaction products may be beneficial, provided that the reduced yield due to inefficiencies in the separation process can be tolerated. For one of the experiments described herein, the recoil atom mass analyzer (RAMA) system shown in Fig. 3-4 was used.

RAMA (Mol80a, Mol80b, Ogn96) is an isotope separator on-line (ISOL) system that is coupled to the production target via a He-jet transport system, as shown in the inset of Fig 3-4. This approach was first proposed by J. M. Nitschke (Nit70). To summarize, the activity is removed from the target by He-jet and transported to the entrance of RAMA. Most of the carrier gas is pumped away; the remaining gas, aerosols and activity are then ionized. A high-voltage potential field extracts the ions from the ion source as a beam, which is then guided by a series of electrostatic and magnetic focusing elements into a large dipole magnet. It is here that the activity of interest is physically separated from the other ions on the basis of its magnetic rigidity. More beam-transport elements then direct the remaining beam to a neutron-shielded detector station (SDS), where the activity is embedded in a catcher foil for counting.

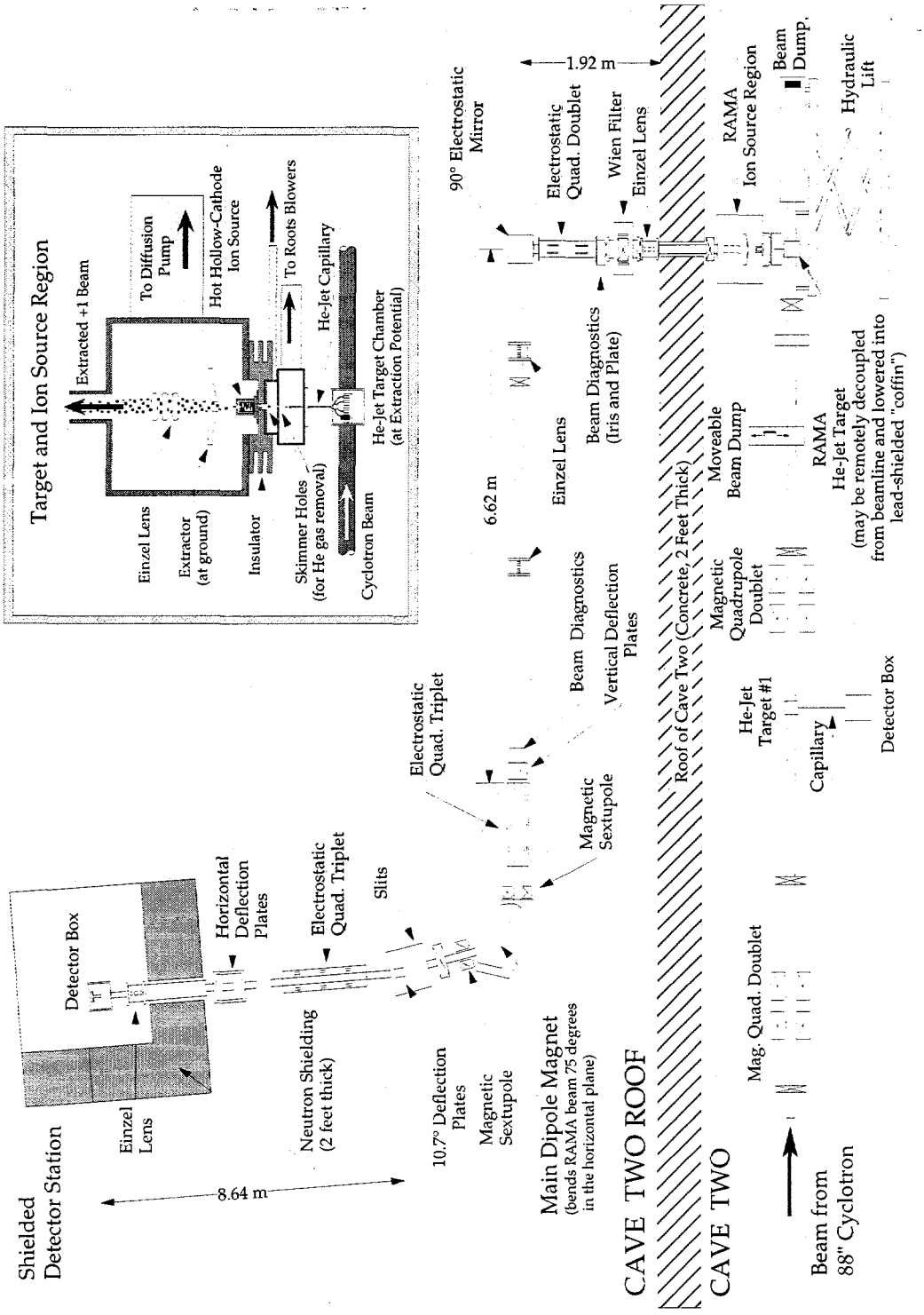

FIG. 3- 4: Schematic diagram of the Cave 2 beam line and RAMA. The inset at upper right shows the He-jet target, skimmers and ion–source/extractor box.

The He-jet target for RAMA is essentially identical to that described in Section 3.1.3; a 0.61 mm (i.d.) x 30 cm exit capillary transports the activity to the ion source. With the ion source in Cave 2, the transport time is limited by the target-cylinder sweep-out time: depending on whether a single- or multiple-capillary system is used, the transport time is ~20-100 ms. In order to get efficient ionization and beam transport of the activity it is necessary to minimize the ratio of carrier gas to aerosols in the RAMA ion source. This is accomplished with a two-stage gas skimmer system. The activity, attached to the surfaces of the relatively-massive aerosol clusters, exits the capillary with more forward momentum on average than the carrier-gas molecules. The opening (half-) angle of the cone is determined by the size of the clusters; it is approximately 1.5° for KCl aerosols. The clusters exit the capillary in a chamber evacuated by a high-capacity Roots blower; the flow is directed through a hole in this chamber. The size of the hole is chosen to allow the clusters to pass through while most of the carrier gas is pumped away. This hole leads to a second chamber where the process is repeated; the exit hole of this chamber leads to the ion source. Typical vacuum levels achieved in this manner are a few hundred millitorr in the first chamber and ~1×10^{-5} torr in the ion-source/extractor box, which is evacuated by a 10" diffusion pump.

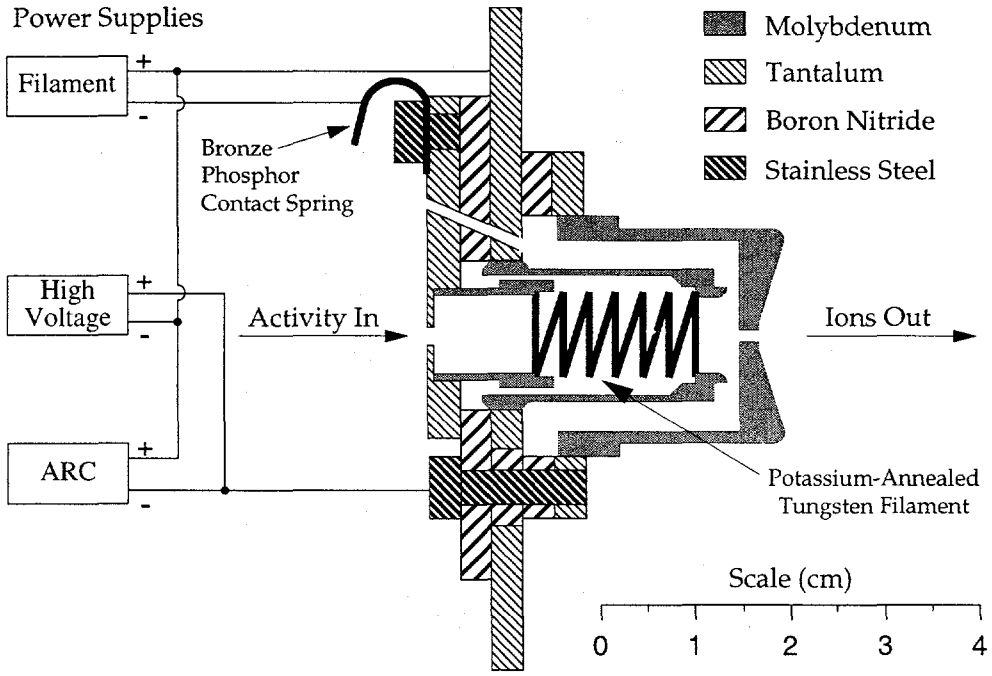

FIG. 3- 5: The RAMA ion source and associated power supplies (Ogn96).

RAMA uses a hot hollow-cathode ion source; it is shown schematically in Fig. 3-5. It consists of two concentric cylinders, mounted on a plate and electrically isolated from each other. The inner cylinder surrounds a 0.76 mm potassium-annealed tungsten filament wound into a helix of ~7 turns. Resistively heating the filament to ~2300 °K with ~600 W of DC current causes thermionic emission of electrons from the filament. Group I elements may be ionized to a +1 charge state by the hot filament alone when operating in "filament mode." To ionize other elements, a plasma is generated by striking an electrical arc between the end cap of the inner anode cylinder and the surrounding cathode cylinder using ~1.7 A at 220 V. This ionizes the remaining He carrier gas; ionization of other species is then accomplished through charge exchange with the He^+ ions (i.e., $A + He^+ \rightarrow A^+ + He$), since He has the highest first-ionization potential of any element. This mode of operation is referred to as "arc mode."

During operation, the He-jet target, capillary, skimmer apparati and ion source are all placed at a potential of +30 kV; the ions are extracted from the ion source to ground by extractors ~2 cm above the source. Immediately after extraction, the beam is focused by a series of einzel lenses and an electrostatic quadrupole doublet. Space charge effects, the Coulomb repulsion of the ions from each other, will tend to cause divergence of the beam, especially for low-energy beams. Since most of the beam initially consists of He^+, this problem may be alleviated somewhat by doing a crude separation soon after extraction. A Wien filter, which separates species based on their velocities by using opposing magnetic and electric fields, deflects the He^+ ions from the remaining beam after the initial focusing. An electrostatic mirror then redirects the beam from the vertical direction in which it was extracted to the horizontal plane. After passing through more einzel lenses and an electrostatic quadrupole triplet, the cylindrically-symmetric beam enters the main dipole magnet. A vacuum of 10^{-7}-10^{-6} torr is maintained in the RAMA beam lines.

Mass separation is accomplished at the main dipole on the basis of magnetic rigidity. Species with the appropriate mass to charge ratio are bent through an angle of 75.5°; other species are removed by collimation. Sextupole magnets at the entrance and exit correct for edge effects of the main dipole. The magnetic field is measured continuously by observing the nuclear magnetic resonance frequency of various samples placed in the field. Mass scans have shown a full-width at one-tenth maximum mass resolution $M/\Delta M$ of 300. Tuning of the beam

through the first part of RAMA is usually performed by monitoring yields at an intermediate focal point just after the dipole, where the beam has a "pencil-like" profile 1.5 mm wide by 5.0 mm high (Ogn96).

Upon exiting the dipole, electrostatic deflection plates bend the beam an additional 10.5°. An electrostatic quadrupole triplet refocuses the beam to a cylindrically-symmetric distribution. Finally, an einzel lens focuses the beam to a spot 0.6 cm in diameter on an ~20 $\mu g/cm^2$ carbon catcher-foil, where the activity is embedded for counting. The detector station is shielded from neutrons by 0.6 m-thick walls made from containers filled with a saturated solution of borax in water.

To minimize radiation exposure to personnel during servicing of the ion source, the section of the beam line containing the He-jet target may be decoupled from the rest of the beam line and shielded. A short section of beam line upstream from the target, the target, the downstream beam line and the beam stop are all mounted on a hydraulic lift. First, the beam line section upstream of the target is valved off and let up to atmospheric pressure. Retraction of a bellows decouples the components on the lift from the remainder of the Cave 2 beam line. The lift then drops to the floor and a 10 cm-thick lead cover covers the target and beam stop assembly. The entire process is automated and may be controlled remotely; when recoupling, only the insertion of the capillary into the skimmer box must be done manually. During the entire process, vacuum is maintained in the downstream section of beam line containing the beam stop.

The RAMA beam is generally tuned first using ^{39}K from the KCl aerosols in the He-jet system; alternatively, RAMA may also be tuned using ions of Mo or W isotopes, released from the components of the ion source, or ^{23}Na, an impurity in the KCl salt. It is important to note that all of these ions are present regardless of whether the cyclotron beam is utilized or not, allowing off-line tests to be performed. Tuning to the mass of interest is then accomplished by interpolation from the parameters established from these "stable" masses. Only magnetic elements need to be readjusted, as the electric force is velocity (and thus, in this case, mass) independent.

The key consideration in choosing to use the RAMA system is the expected through-put efficiency for the species of interest. Skimming of gaseous elements from the He-jet carrier

gas is generally not effective. Additionally, RAMA works best with elements with melting points below the operating temperature of the ion source (~2300 °K). Some elements may undergo reactions to form compounds that may or may not be ionizable. For the Group I element Na, an efficiency of ~1% has been observed using arc mode; in filament mode, this is reduced by a factor of ~2 (Ogn96). Group II elements have an arc mode efficiency ~10-20 less than Group I elements; in filament mode, Group II elements are not observed.

3.2 Radiation Detection

3.2.1 Radiation Detectors

Three types of radiation detectors have been used in this work: gas-filled proportional counters, P-type ion-implanted silicon detectors and high-purity germanium detectors. The former two were combined to make particle-identification telescopes for the measurement of charged particle energies, as will be discussed in Section 3.2.2. Telescopes allow alpha and proton decays to be differentiated from the many beta-decay events also observed. High-purity germanium (HPGe) detectors were used for the measurement of gamma-ray spectra. The operating principles of these detectors will not be reviewed here; the reader is referred elsewhere (e.g., Kno79, Tso83) for more information. The different detector configurations used in each experiment will be discussed in Chapters 4-6.

3.2.2 Particle-Identification Telescopes

In this thesis, proton decay spectroscopy is used as a way of extracting information about nuclides near the proton drip line. As discussed in Chapter 1, the utility of this method comes from the fact that proton decay is not energetically viable among isotopes closer stability. However, for this approach to be successful, it is vital that proton decays can be reliably differentiated from the much more common beta- and alpha-particles that will be emitted by the other fusion-evaporation reaction products.

In order to distinguish between proton, alpha and beta decays, experiments have commonly relied on the unique variation of stopping power with respect to energy for different charged particles. The stopping power (Ber93) for ions varies as:

$$-\frac{dE}{dx} = \frac{4\pi \cdot \rho \cdot r_e^2 \cdot m_e c^2}{\beta^2} \frac{1}{u} \frac{Z}{A} z^2 L(\beta^2) \propto \frac{M z^2}{E} \qquad (3\text{-}3)$$

where -dE/dX is the stopping power; ρ is the density of the stopping material; r_e^2 and m_e are the classical electron radius and mass; β is the velocity of the incident ion relative to the speed of light; u is the atomic mass unit; Z and A are the atomic number and mass of the stopping material; z, M and E are the charge, mass and energy of the incident ion, respectively. The quantity $L(\beta^2)$ is called the stopping number; it takes into account fine details of the energy loss process and depends on specific properties of the stopping medium. Equation 3-3 does not hold for decay particles of very low energy (<~250 keV for protons, <~1 MeV for alpha particles, depending on the medium). As the particle velocity approaches the velocity of the atomic electrons, the decay particles will begin to lose their charge as they capture electrons from the stopping medium; this causes the stopping power to decrease with decreasing energy. Figure 3-6 shows stopping power curves for protons and alpha particles in silicon.

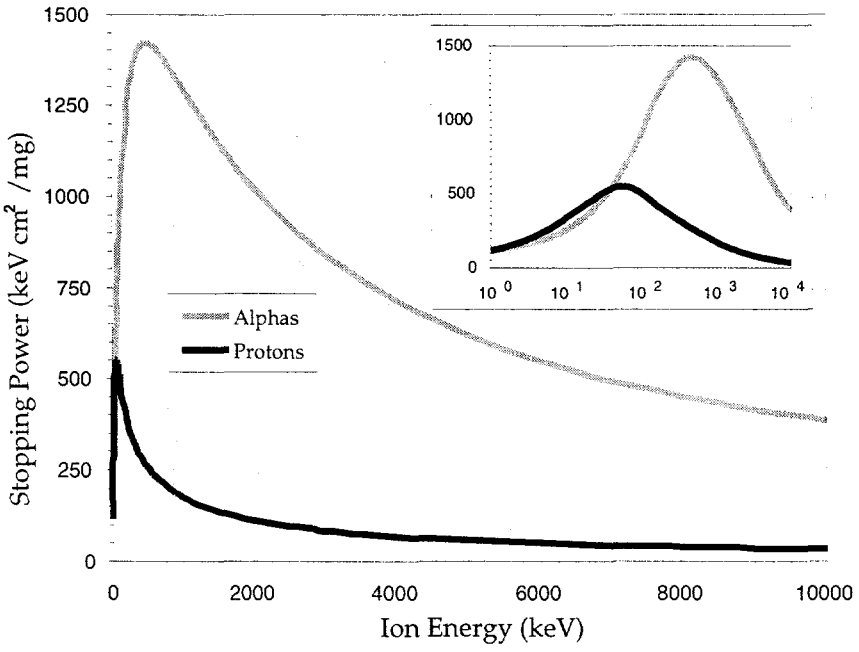

FIG. 3- 6: Stopping power curves for silicon, from the stopping power tables of the International Commission on Radiation Units and Measurements Report 49 (Ber93). The axes for the inset are the same as for the main figure.

The dependence of the stopping power on the charge and energy of the incident ion may be used to identify the ion. By taking measurements both with and without a thin degrader placed between the activity and the detectors, protons may be distinguished from other, heavier, charged particles by their characteristic differential energy loss in the degrader (e.g., in Hon79). A limitation of this method is that the decays are not identified on an event-by-event basis but rather by the energy shift of peaks. This means that better statistics are needed to identify a given decay group, making the technique far less suitable for studying nuclei very close to the drip line where millisecond half-lives and very small cross sections are the rule. Beta contamination of the spectrum at low energies is also a problem.

An alternative method that overcomes this shortcoming is the use of particle-identification (PI) telescopes (Gou75). The degrader is replaced with a very thin "ΔE" silicon detector capable of measuring the differential energy loss directly; decay particles are then stopped in the backing silicon-"E" detector, allowing measurement of the total decay energy. It has been found empirically that the ΔE and E detector signals may be combined according to the equation:

$$PI = (E + \Delta E)^{1.73} - E^{1.73} \propto Mz^2 \qquad (3\text{-}4)$$

to produce a particle identifier signal that is proportional to the mass M and the charge squared z^2 of the ion; light ions (e.g., p, α, etc.) will produce different peaks in this spectrum. By gating on these peaks, either in hardware or software, a separation of events based on the charge and mass of the species detected may be achieved.

For a particular particle-identification telescope design, this technique is limited to studying decays of sufficiently high energy that the decay particles pass through the ΔE detector and leave a signal in the E detector. The low-energy threshold with such telescopes is determined as follows: The resolution of silicon detectors is proportional to their capacitance, which is in turn inversely proportional to detector thickness. Whereas a 450 mm^2 x 300 μm detector with a capacitance of 150 pF will have a typical resolution of 25 keV for protons, the resolution of a 450 mm^2 x 10 μm detector with a capacitance of 4500 pF is on the order of 200 keV. The technological difficulties of producing very thin (<10 μm) silicon detectors combined with this loss of resolution as detectors are made thinner leads to a typical

low-energy cut off of ~700 keV for protons or ~2600 keV for alpha particles using this technique.

The ability to detect low-energy proton or alpha events is crucial to studies of proton-rich nuclides in many instances. As discussed in Section 2.2, proton-decay rates depend exponentially on the available decay energy. Because of this, direct proton emitters that emit low-energy protons are often the most easily studied since they are more likely to have half-lives long enough to permit transport away from the target for counting. When beta-delayed or direct two-proton emission is measured, the available decay energy is split between the two protons, making a low-energy threshold advantageous. Additionally, the most important resonances in stellar reactions occur at low energies, as discussed in Section 2.6. In other cases, it just happens that a state of interest is only slightly unbound to proton or alpha emission. All of these reasons have lead to considerable interest (e.g., see Vie78, Mol94, Hon96) in the development of low-energy particle-identification telescopes for decay studies.

Although several different configurations of low-energy telescopes have been used in this work, all are based on the same basic concept (Mol94, Row97). The individual telescope configurations used will be discussed in Chapters 4-6. To lower the threshold for particle identification, these telescopes use gas-filled proportional counters instead of Si detectors for the ΔE detectors. Figure 3-7 shows a schematic diagram of an idealized low-energy telescope; this design has two gas-ΔE detectors backed by the Si E detector. The gas is contained in a small chamber that is about 1 cm deep; a thin polypropylene window prevents the gas from being pumped away through the entrance of the telescope. The electric field is created co-linear with the incident radiation between a series of wire grids. The central "high-voltage" grid is biased while the outer "signal" grids float near ground; this configuration prevents sparking to the Si detector, which is only about 1 mm from the closest grid. P-type ion-implanted silicon detectors are used due to their resistance to neutron damage. During operation, the entire assembly is generally chilled to -20 °C to minimize the leakage currents of the Si detector, improving its resolution. The diameter of the openings in the telescope are chosen to maintain the same solid angle for each component detector when viewing a (hypothetical) point source of activity some distance from the entrance window.

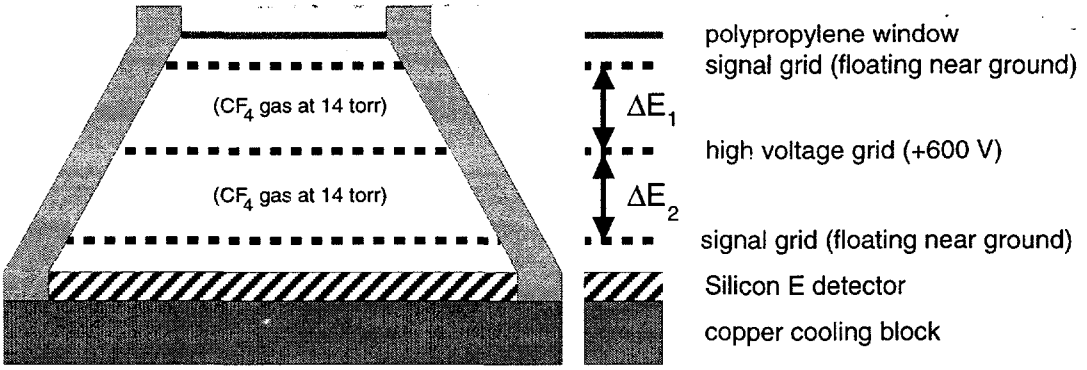

FIG. 3- 7: Cross-sectional view of a gas-ΔE/gas-ΔE/Si-E detector telescope. A description of the components is given on the right.

The original low-energy telescope design collected signals from the central high-voltage grid, creating a single gas-ΔE detector (Mol94). However, it was found that this did not provide adequate separation of protons from alpha particles and beta-decay events. The phenomenon primarily responsible for beta contamination of proton spectra taken with the single gas-ΔE telescopes, energy-loss straggling (Ber93), is a random process occurring for only a small fraction of events. This is illustrated in Fig. 3-8. On the left, ΔE signals are shown for proton events; the peak is approximately Gaussian, with a high energy tail due to straggling.

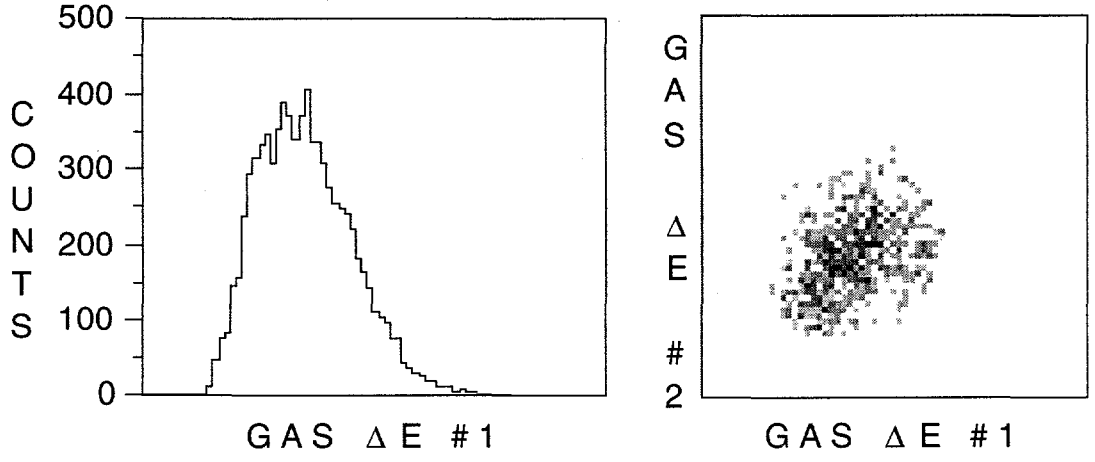

FIG. 3- 8: Gas-ΔE Signals. On the left, gas-ΔE signals are shown for the 386 keV beta-delayed proton group of ^{25}Si. On the right, a ΔE_2 vs. ΔE_1 correlation plot is shown for the same 386 keV proton events from the peak in the spectrum on the left.

On the right of Fig. 3-8, a ΔE_2 vs. ΔE_1 correlation plot is shown for a telescope with two gas-ΔE detectors; the absence of a well-defined diagonal band of events shows that the signals from the two detectors are not strongly correlated. Hence, by adding a second gas detector to the telescope and requiring that valid events have appropriate signals in both ΔE detectors and the E detector, the beta contamination of proton spectra is suppressed to less than one per 10^6 beta events (Mol94).

In the current telescope designs, the signals are collected from the outer "signal" grids using custom-designed DC-coupled preamplifiers. This configuration permits two independent signals to be measured using the single high-voltage electrode. During initial testing, the high-voltage grid was held at a negative voltage. This was thought necessary since electrons have a much higher mobility than ionized gas molecules. Presumably this would lead to more rapid charge collection and thus allow shorter shaping times to be used, which is an important consideration when operating at high count rates. However, it was found that if a positive voltage, of ~600 V, was used instead, the ionized gas molecules would pull electrons from the floating signal grids. This is called the "electron shadow" pulse; after amplification it is essentially indistinguishable from the normal electron pulse. Since

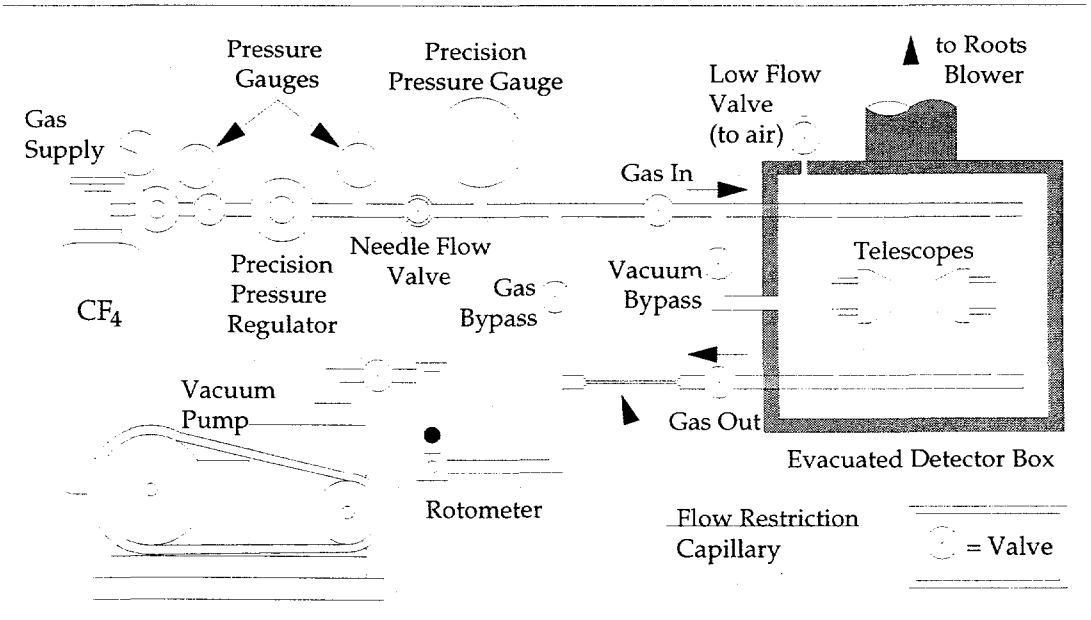

FIG. 3- 9: The gas-handling system for the low-energy particle-identification telescopes.

operation is more stable using positive voltages, this electron shadow is used as the signal for the ΔE detectors.

Tetrafluoromethane [CF_4; trade name freon-14 (DuP98)] is used for the detector gas. Several other gases, including isobutane, methane and 10% methane in argon, have been tested over a range of pressures [Mol94]; freon-14 was chosen both for its rapid charge-collection time and because it is chemically inert and has a low condensation temperature. The operating pressure of the gas is ~14 torr which corresponds to a total gas thickness of ~50 $\mu g/cm^2$. The gas is cooled prior to entering the telescopes to reduce the effects of changes in ambient room temperature on the gas density. A small capillary at the gas outlet maintains a uniform gas pressure and flow rate. The gas handling system for these telescopes is shown in Fig. 3-9.

All of the grids are made of parallel 20 μm gold-coated tungsten wires spaced 1 mm apart. The grids run in two dimensions and are supported by a ring of either brass or single-sided PC-board. By using a two-dimensional grid, field uniformity and thus signal collection is greatly improved relative to the earlier designs employing one-dimensional grids. Use of these grids yields approximately the same signal strength as Ni-foil electrodes, but the grids are less delicate. The spacing between the high-voltage grid and each of the near-ground signal grids is typically 4 mm; the spacing between the first-ΔE signal grid and the window and also between the second-ΔE signal grid and the silicon detector is ~1 mm.

In order to keep the detection threshold as low as possible, it is important to minimize the material through which the charged particles must pass prior to entering the Si E detector. Polypropylene was chosen for the entrance window material because of its high tensile strength; it may be stretched to <50 $\mu g/cm^2$ and still be strong enough to contain the detector gas. To some extent, the "thickness" of the gas may be reduced by lowering its pressure; however, this increases the amount of energy-loss straggling and may lead to degradation of the particle separation. Problems with sparking may also be encountered. Also, silicon E detectors should be chosen carefully to ensure that the dead layer on the front side is minimized.

Several considerations must be taken into account when using these gas-ΔE/Si-E telescopes to ensure that the data taken are of the highest possible quality. Because the

charge collection in gas detectors is slower than in Si detectors, the amplifiers use a 2 μs shaping time. This places a practical limit on the beta-event rate in the Si detectors of about 40 kHz. It is crucial that the detector system be allowed to fully equilibrate thermally before it is used; otherwise the calibration may change as the system cools. Depending on the particular mounting system, this cooling can take several hours.

It has also been found that pulses in the gas detectors influence the operation of the Si E detector. To observe this effect, the energies of 3183 and 5486 keV alpha particles from a $^{148}Gd/^{241}Am$ mixed source were measured while increasing the bias on the ΔE detectors; the shifts of the peaks in the E detectors were measured relative to the peaks at zero ΔE bias. Figure 3-10 shows the change in the energy (calculated from the calibration of the Si detectors with the ΔE detectors unbiased) of alpha particles detected by the Si detector as a function of ΔE-bias voltage (left) and as a function of ΔE-signal magnitude (right) in the gas detectors. It is clear from the plot on the right that the shift of the peaks in the Si detector changes linearly with the magnitude of the ΔE signal, suggesting that some of the charge produced in the gas detectors is collected by the Si detector, thus altering its signal.

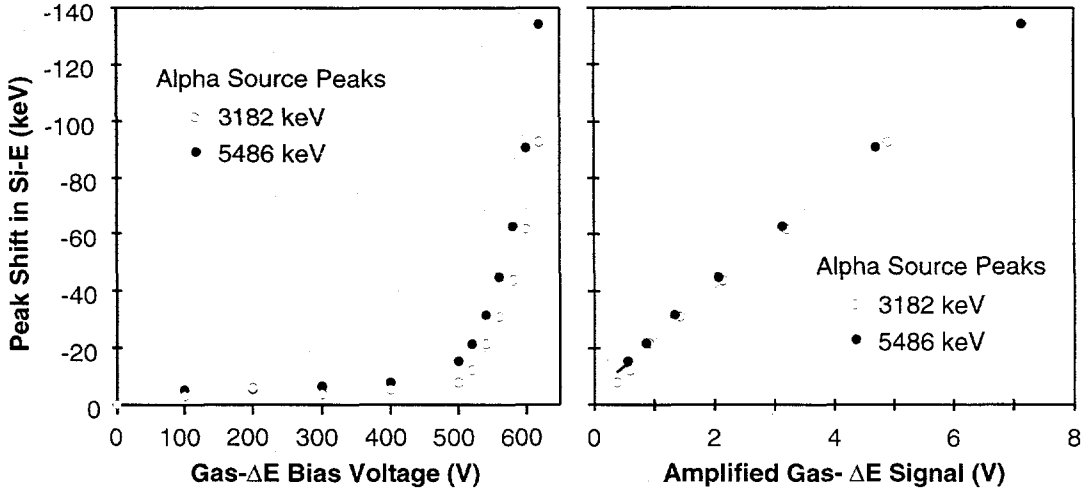

FIG. 3- 10: Influence of gas-ΔE detector bias on the Si -E detector. Change in alpha-particle signals as a function of bias voltage (left) and observed signal strength (right) in the gas-ΔE detectors, relative to data taken with the gas-ΔE detectors unbiased.

This "cross-talk" effect will add a source of non-linearity into the E detector calibration that is proportional to the energy loss of the charged particles in the gas detectors. A correction to the E signals should thus be made prior to further calibration (see Section 3.3.2). Since the magnitude of the ΔE detector pulses increases with increasing bias, it is very important that the voltage applied to the gas detectors not be changed after the calibration measurement has been performed.

3.2.3 Counting Electronics

Figure 3-11 depicts a typical electronics configuration for making measurements of the decays of proton-rich nuclei. In this arrangement there is one particle-identification telescope consisting of two gas-ΔE detectors and a silicon E detector for measuring charged particles, and a HPGe detector for gamma-rays. An event will be read whenever there is a coincidence between the "trigger" ΔE detector and the E detector, or by a gamma-ray in the Ge detector. Timing data are collected between the Si and Ge detectors. The cyclotron beam is pulsed and events are also timed relative to the start of the counting cycle. A discussion of how this is accomplished follows. This particular arrangement was chosen because it illustrates essentially all of the counting techniques used in this thesis; a similar configuration was used to study the decay of ^{77}Rb (Chapter 6).

The counting electronics may be divided into three categories by function: energy signal measurements, timing measurements between signals from different detectors and/or with respect to the beam cycle, and event discrimination. In all cases, the preamplifiers first integrate and amplify the charge collected by the detectors. The charge will be proportional to the energy lost in the active region of the detector. To reduce noise, the preamplifiers are located as close to the detectors as possible. Two signals are output by the preamplifiers. The "slow" signal goes to the shaping amplifiers used for energy measurement and event triggering; the "fast" preamplifier signal, used to measure the timing of signals in different detectors relative to each other, is passed to a fast timing amplifier.

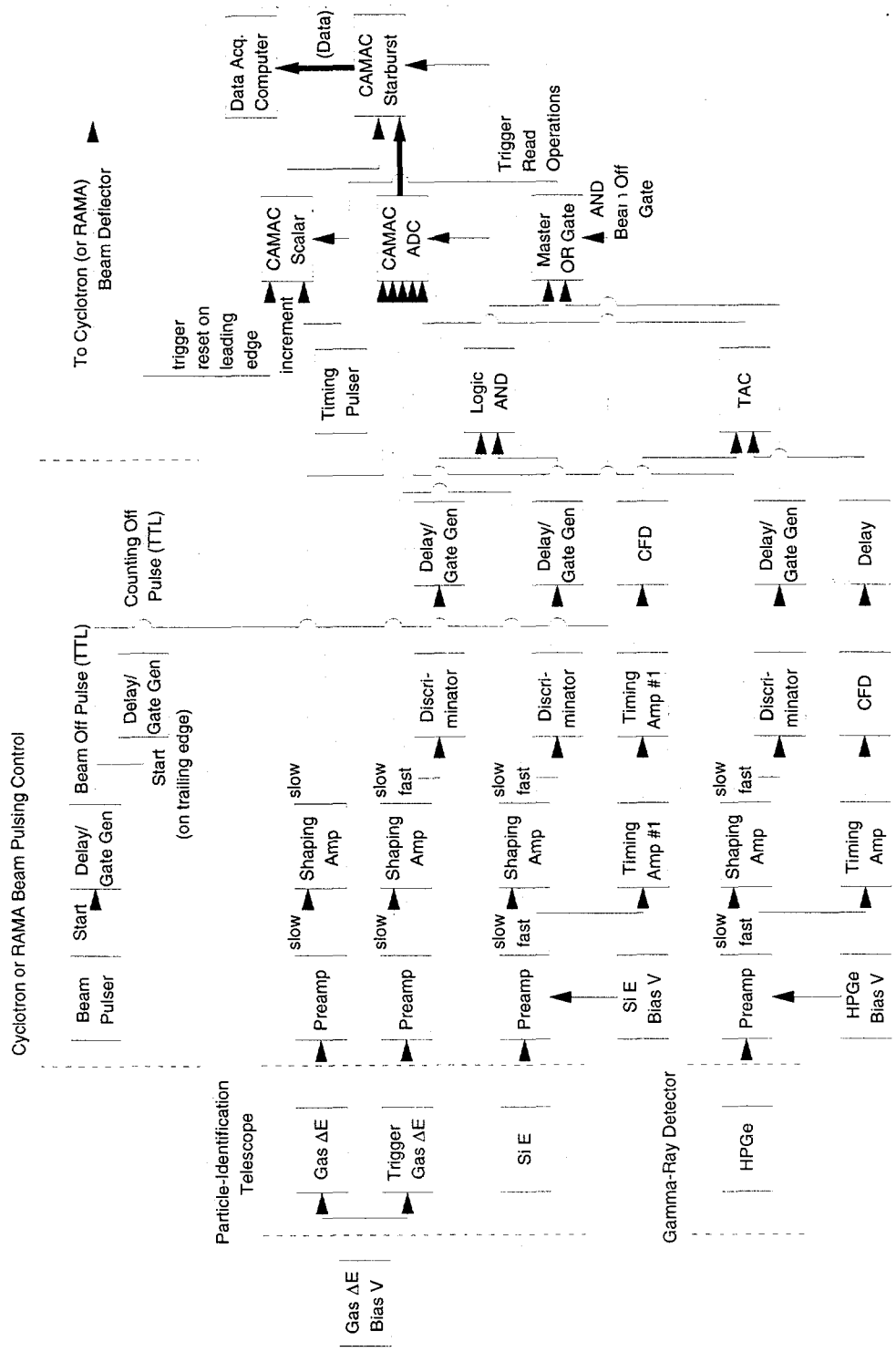

FIG. 3- 11: Generalized counting electronics. See text for an explanation of abbreviations and functions of individual modules.

The "fast" output signal from the shaping amplifiers is used for hardware-gate generation. For a gamma-ray signal to trigger an event, we simply require that its amplitude be greater than some threshold set in the discriminator; in this case the discriminator outputs a narrow NIM pulse. The delay/gate generator reads this pulse and produces a 1-μs wide NIM pulse that may be read by the logic module which generates the "master" gate; it is set to an OR configuration with the particle identification telescope so that either may trigger an event.

For an event in a telescope to be valid, we require that a coincident signal be observed in both a silicon-E detector and one of its associated gas-ΔE detectors. For each telescope, whichever ΔE detector has the best signal-to-noise ratio is chosen for this role. This varies from experiment to experiment; the gas-ΔE detector chosen is designated the "trigger" ΔE. The amplifier "fast" output of the ΔE is sent to a discriminator, and if the threshold requirement is met, pulses are sent first to the delay/gate generator, which sends a pulse to a logic module. The fast signal from the E amplifier follows a similar sequence, ending in the same logic module as the ΔE signal. This logic module is set to AND mode; it checks that the pulses are in coincidence (within ~2 μs). If so, a triggering pulse is sent to the master (OR) gate generator.

If the master gate generator detects a signal, either from the gamma-ray detector, or from the gas-ΔE and E detectors in coincidence, it triggers the analog-to-digital converter (ADC) and timing scalar CAMAC modules to read all of their inputs and will trigger the Starburst CAMAC controller (CES98) to read the ADC's and scalar. When the memory of the Starburst module is full, its contents are dumped to the data acquisition computer, where events are stored to magnetic tape and analyzed. In addition to requiring coincidences between individual telescope components, they may also be required between a telescope and a HPGe detector, or between two telescopes. The latter requirement is used in beta-delayed two-proton decay studies.

The ADC's read the slow outputs of the shaping amplifiers and the time-to-amplitude converters (TAC's, to be discussed shortly). The shaping amplifiers increase the preamplifier signals by differentiation followed by integration of the input. Gas-ΔE detectors require a 2 μs shaping time to allow for complete charge collection from the gas;

silicon and germanium detectors have more rapid charge collection and 1 μs shaping is sufficient. The ADC's are peak sensitive, producing a digitized signal proportional to the pulse amplitude. The width of the master OR gate that triggers the read operation must be matched to the longest shaping time in use to ensure that the peaks of the amplified pulses are read.

The relationship between the energy lost in the detectors and the signal measured by the ADC's may not be precisely linear. Though this minor non-linearity of the slow-signal electronics is sometimes not significant, in many cases it must be accounted for in order to obtain a reliable calibration. This is especially true when it is necessary to extrapolate to data points outside of the calibration data. The total integral non-linearity of the slow-signal electronics may be measured using a precision pulse generator. A tail pulse with a rise time of 0.5 μs and a fall time of 1 ms in conjunction with a CR-differentiator circuit simulates the silicon detector signal; the values of the capacitor and resistor should be chosen to match the range of the pulser to the range of the ADC at the chosen gain setting of the shaping amplifier. The tail pulse amplitude is then varied over the full range. The deviation from linearity of the system is measured by performing a least-squares linear fit of the pulser peak centroids to the reference voltage, then subtracting the expected centroids (as calculated from this fit) from the observed centroids. Measured in this way, the typical integral non-linearity was ~0.3% from 2% to 100% of the total spectrum (Row97). Experimental centroids are corrected for the electronics non-linearity prior to further calibration. An empirical centroid-correction function may be generated using a polynomial fit of the deviation from linearity.

For multi-particle decay studies, fast timing data are taken between all permutations of the silicon detectors; this allows true coincidences to be distinguished from uncorrelated decays that happen to fall within the same (2–μs wide) event gate. In Fig. 3-11, timing data are taken between the Si-E detector of the telescope and the HPGe detector; such an arrangement might be useful for studying particle emission to excited states in the daughter. Timing data are not generally taken with respect to the gas-ΔE detectors of telescopes because the small signals from these detectors are poorly suited for this purpose. To record timing data, the "fast" output from the preamplifiers of each detector is run through two fast-timing

amplifiers in series; to minimize noise, the first of these amplifiers is located in Cave 2 with the preamplifiers. Constant fraction discriminators (CFD) provide signal/noise discrimination while minimizing the time "walk" for different pulse amplitudes. For each pair of detectors, the CFD output of the first detector is used as the start of a time-to-amplitude converter. The CFD output of the second detector is delayed by a known amount, then used as the TAC stop signal. The TAC produces a pulse with an amplitude proportional to the time between the start and stop signals; this pulse is then read by an ADC. Typical resolving times are 15 ns FWTM.

Timing data (of lower resolution) may also be taken with respect to a pulsed beam, either the primary cyclotron beam or the mass separated beam from RAMA. Beam pulsing may be used if a half-life measurement is desired; alternatively (and more commonly in this work) the beam is pulsed primarily to reduce background radiation during counting of the activity. Pulsing the cyclotron beam causes the measured activity to drop by ~75%, since both activity production and the length of the counting cycle are halved. Control of the beam pulsing is accomplished using a pulser and delay/gate generators, as shown at the top of Fig. 3-11. The pulser is set to the total beam-cycle period, which is typically two half-lives of the activity of interest. This triggers a signal from the first gate generator that will enable the cyclotron beam; the width of this pulse determines the length of the beam-on cycle. The second gate generator is triggered by the leading edge of the complementary pulse from the first gate generator; after a delay of a few milliseconds to ensure the beam is off, a pulse is output to the master OR gate, enabling the counting electronics.

To time events relative to the start of the beam cycle, a pulser is fed into a CAMAC-based scalar module. The scalar increments every time it receives a pulse. The pulser rate is set to provide the maximum resolution possible for the given total beam-cycle length and the scalar resolution; an appropriate frequency in Hertz is given by the number of scalar channels multiplied by a safety margin (~95%), divided by the total cycle length in seconds. The scalar is reset at the start of each cycle by the same signal that enables the cyclotron beam. The scalar is read whenever there is a valid event; the time from the start of the cycle is then determined by dividing the value of the scalar by the timing pulser frequency. The half-life of the species of interest may then be determined from the decay curve that results. Activity

transport times for the He-jet may also be determined using this approach from the time between the end of the beam-on cycle and the peak of the count rate; best results will be attained when the half-life of the activity is approximately the same length as the transport time.

The count rate in each silicon detector is typically limited to 40 kHz in order to keep the number of random coincidences between the Si E and the trigger ΔE to a statistically-small level; at this count rate in the silicon detectors, the coincidence rate for each telescope is generally less than 250 Hz, indicating that relatively few beta particles lose sufficient energy in the gas to be accepted as valid events. However, using these methods alone, beta events still comprise the majority of all events taken in most experiments. In order to minimize computer processing time, as well as to simplify analysis, we often employ a software gating condition in the Starburst system which requires that the sum of the trigger-ΔE and silicon-E signals be above some threshold; conservatively set, this "triangle-gate" requirement cuts the number of beta-decay events read and stored to magnetic tape by the computer by more than 90% without sacrificing any of the proton or alpha events of interest.

3.3 Data Analysis

3.3.1 Data Reduction in Software

In addition to the hardware-gating techniques described above, software gating is used extensively to separate alpha, beta and proton events. The data acquisition and analysis code CHAOS (Rat91) allows the user to create combinations of both one-dimensional gates and/or freeform two-dimensional gates, drawn within the space defined by any pair of parameters. When particle-identification telescopes are used, one generally concentrates initially on the relationship between the energies observed in the ΔE and E detectors. The relationship between energy loss in either of the gas-ΔE detectors and the incident energy is determined by the stopping power of the gas for the particular ion being stopped (see Fig. 3-6). Later, correlations between the other detectors and the timing data are also commonly used to separate the events of interest from "background" decay events and detector noise.

When the raw data are initially displayed in either of the gas-ΔE vs. Si-E projections, there is generally not a complete separation between the regions containing beta, proton and alpha particle events. Within each of these two-dimensional density plots (2D histograms), the overlap between the different particle regions arises from both incomplete charge collection, and more importantly, energy-loss straggling in the gas-ΔE detector. It is only for a very small fraction of the events in each gas-ΔE detector that these processes cause significant overlap; in either gas-ΔE vs. Si-E spectrum, the majority of events will be cleanly separated from events of other types. For instance, tests using beta-delayed protons from ^{25}Si in the presence of electrons from a ^{207}Bi source have shown that approximately one beta event in 10^4 typically falls within the proton region of either 2D spectrum (Mol94). Furthermore, since the overlap between the different regions arises from random processes (see Fig. 3-8), it is highly unlikely that a given event will cause contamination in both gas-ΔE vs. Si-E projections.

Figure 3-12 illustrates the gating process within two-dimensional (2D-) ΔE vs. E spectra on data from a 40 MeV $^3He^{2+}$ on ^{nat}Mg calibration run; ^{25}Si (Rob93) beta-delayed protons are indicated. The beta-delayed alpha emitter ^{20}Na (Cli89, Ajz87) is also produced in this reaction, but in these spectra the alpha events are not visible due to the high gain at which the ΔE detectors were operated. To separate protons from alpha and beta particles in each telescope, rough two-dimensional gates are first drawn around the proton region in each ΔE vs. E spectrum (top row, Fig. 3-12). The subsets of the data which fall within each these gates are then "back-projected" onto the <u>other</u> ΔE vs. E spectrum for that telescope (bottom row), i.e., the subset falling within the gate defined in the ΔE_1 vs. E projection is projected onto the ΔE_2 vs. E spectrum and *vice versa*. These two subsets of the data will consist mainly of real proton events; however, some beta and alpha particles will also be included. Because it is unlikely, for any particular event, that incomplete charge collection or energy-loss straggling will occur in both gas-ΔE detectors, the protons in the back-projected ΔE vs. E spectra should be better separated from the remaining beta and alpha particles than in the original 2D spectra. Refined gates are defined within the back-projected spectra; the subsets of the data falling within these gates are then projected back to the original ΔE vs. E spectra, and the gates are again refined. By reiterating this process one can determine the optimum

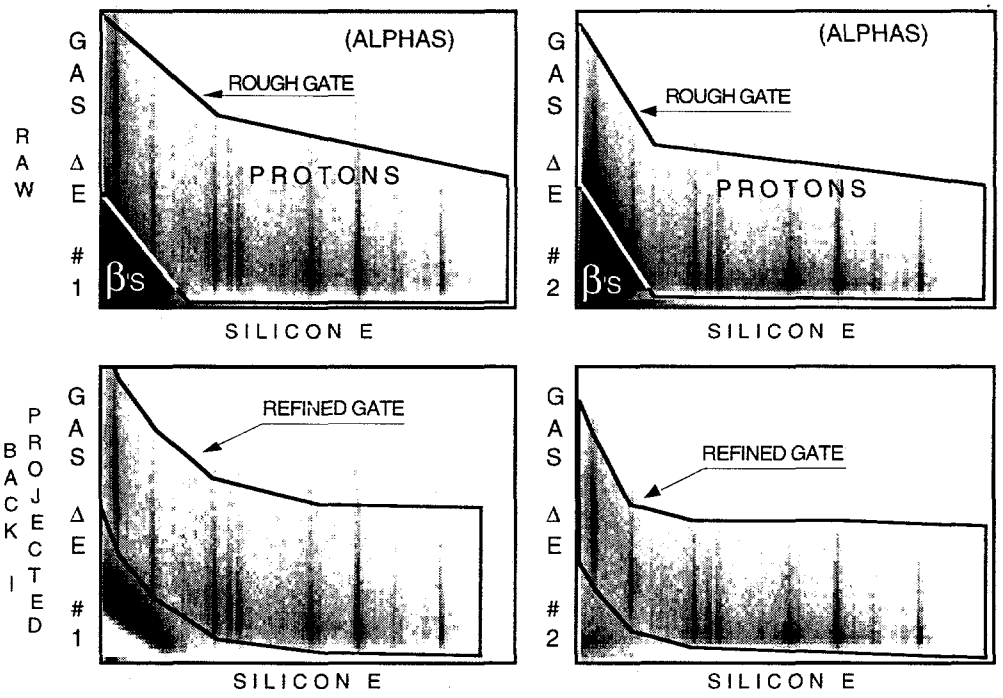

FIG. 3- 12: Standard back-projection gating. The upper two-dimensional spectra show the data prior to gating. The two lower spectra contain the subsets of the data in the upper spectra which fell within the "rough" gates defined in the upper spectra. See text.

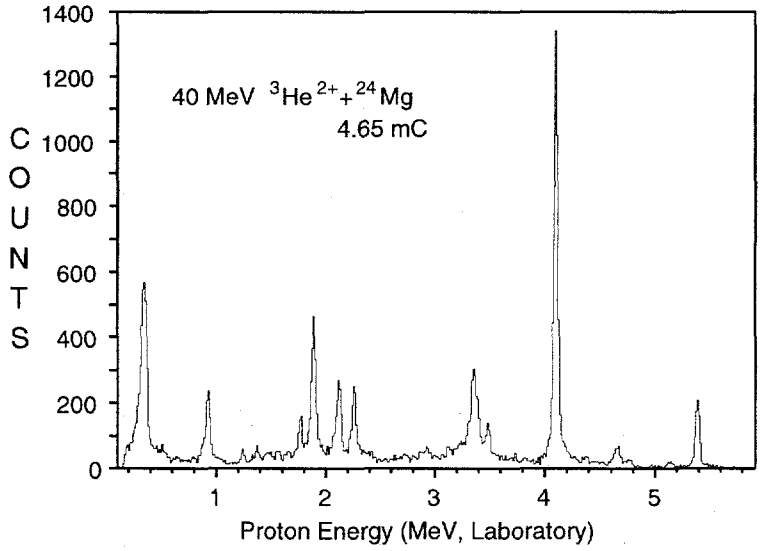

FIG. 3- 13: Silicon-25 beta-delayed proton spectrum, generated from the data shown in Fig. 3-12 using standard back-projection gating techniques.

position for the gate in each projection. The final proton spectrum is generated by requiring that events fall within both gates, with the result shown in Fig. 3-13. Again using ^{25}Si delayed-protons and ^{207}Bi electrons, tests have shown that by requiring valid events to fall within both ΔE vs. E gates, fewer than one beta event per million will contaminate the final proton spectrum. The same gates used to analyze the calibration data are then used for analysis of the main experiment. When extrapolating to energies below the lowest-energy group observed during calibration, the gates are drawn relative to the higher-energy groups using calculated energy losses in the gas.

A persistent problem with this gating technique arises from noise which has a small signal in the E detector but forms a diagonal band in the ΔE vs. ΔE plane. This noise is illustrated in Fig. 3-14, which shows a ΔE_2 vs. ΔE_1 correlation plot for events with small E signals. Although the exact cause of this noise is unknown, it seems to be correlated with high beta-decay event rates and is mainly a problem in light-ion reactions. It can also be seen in the beta region of the lower left spectrum in Fig. 3-12. Because this band appears at a constant angle in the ΔE vs. ΔE plane, gating around it is best performed by transforming this plane to a

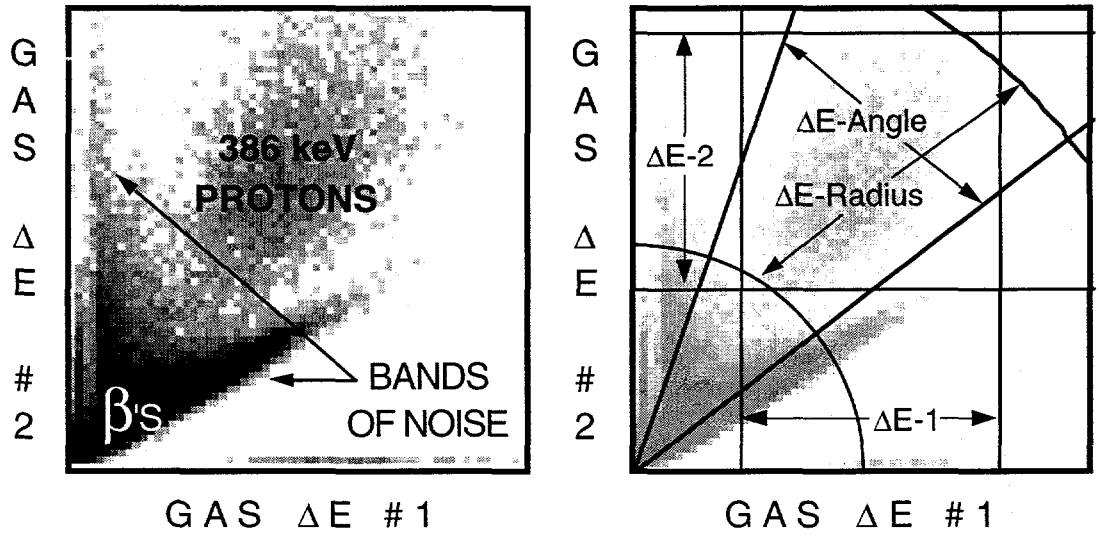

FIG. 3- 14: Band of noise, ΔE_2 vs. ΔE_1 projection. Only events with relatively small signals (< ~400 keV) in the Si-E detector are shown in these plots. On the left, events are shown corresponding to 386 keV protons, beta particles and noise. On the right, the positions of typical proton gates, defined in both Cartesian and polar ΔE vs. E projections, are indicated.

polar coordinate system, i.e., ΔE_{radius} vs. ΔE_{angle}. The signals may be transformed (as pseudo-parameters in CHAOS) using the following standard relationships:

$$\Delta E_{radius} = \sqrt{\Delta E_1^2 + \Delta E_2^2} \tag{3-5a}$$

$$\Delta E_{angle} = \arctan\left(\frac{\Delta E_2}{\Delta E_1}\right) \tag{3-5b}$$

The right half of Fig. 3-14 shows the shape of Cartesian and polar ΔE gates in the ΔE vs. ΔE plane. Figure 3-15 depicts polar ΔE back-projection spectra. The same iterative procedure followed in Cartesian ΔE coordinates is also used in polar coordinates to achieve the optimum separation of proton events. A combination of Cartesian and polar gates is often utilized.

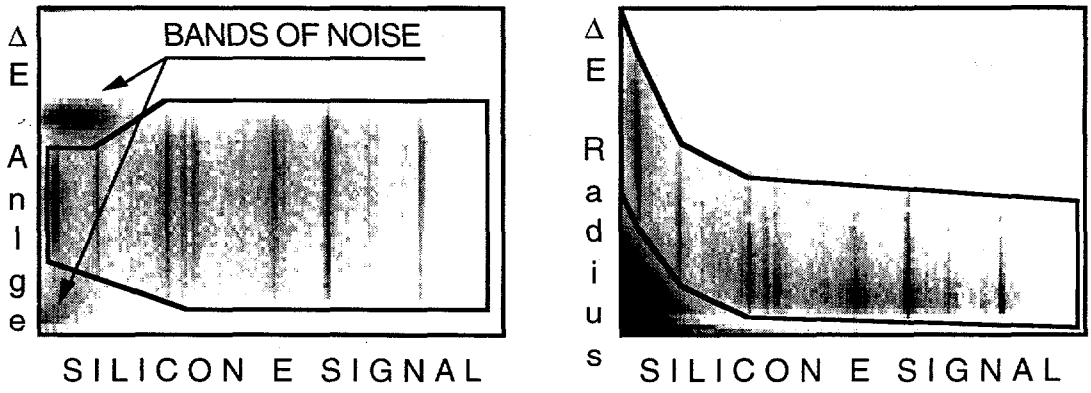

FIG. 3- 15: Polar-ΔE Back-Projection Gating. The data in these spectra are the same as shown in Figures 3-12 and 3-14.

After the initial separation of events by type (proton, alpha, beta), one may look for additional correlations with other parameters to further reduce "noise" in the data set. For instance, for beta-delayed two-proton decay studies, one usually requires that, first, protons be observed in two separate telescopes (using the proton gates described above), and second, that a "true" coincidence be observed in the appropriate TAC spectrum. Sometimes events will be recorded that are caused by the pickup of radio-frequency noise in the electronics, detectors or cabling rather than from radioactive decays. In this case, one should look for similar signals in multiple detectors, since real decay events should not be seen in more than two telescopes. If timing data have been taken relative to a pulsed-beam cycle, one may look for time correlations; for instance, if the counting cycle accidentally overlaps the beam cycle,

a large increase in events near the beginning or end of the beam-cycle timing spectrum will be observed. If two species with different half-lives have been measured simultaneously, one could look at the ratio of intensities at the beginning and end of the counting cycle to see whether a particular peak in the spectrum was due mainly to the shorter- or longer-lived activity. Gating on various other correlations may also be useful; the above list is not meant to be exhaustive.

Under highly specific circumstances, events may be observed which appear to be low-energy proton or alpha decays, but are actually not. One situation where this arises is in the beta-delayed alpha decay of ^{20}Na. The ^{16}O recoil from the 4438 keV alpha decay is sufficiently energetic to enter the E detector, and its large gas-ΔE signals make it easily distinguishable from alpha or proton decay events. *A priori*, one would not expect the 2148 keV alpha decay to present a problem either, since its ^{16}O recoil is stopped in the dead layer of the Si-E detector. However, since stopping power decreases at low energies (see Fig. 3-6), this recoil will generate signals in the gas-ΔE detectors which are of the same magnitude as expected from very low-energy alpha events. Furthermore, a percentage of recoil events commensurate with the telescope solid angle (i.e., a few percent) will be detected in coincidence with the positron from the preceding beta decay in the Si-E detector. In this case, the event will satisfy hardware gating requirements and be recorded. In the two-dimensional spectra, these ^{16}O-recoil/beta coincidence events from the 2148 keV alpha decay fall within the low-energy alpha region.

Two features allow these events to be distinguished from real low-energy proton or alpha events: First, the intensity of the low-energy peak relative to a peak corresponding to a known proton or alpha decay (i.e., the 2148 keV peak in this case) will be commensurate with the telescope solid angle as a percentage of 4π sr. Second, the peak shape and centroid in the Si-E detector would match those of the beta continuum. Such events should not be observed from the decay of higher-Z nuclides, due to the relatively low energy and short range of resulting daughter recoils. However, when low-mass beta-delayed particle emitters are present, such beta-recoil coincidences must be considered if very low-energy events are observed.

3.3.2 Calibration of Detector Systems

Calibration of gamma-ray detectors is performed in the usual manner using a range of standard gamma-ray sources that bracket the energies of interest. Calibration of charged-particle detectors for alphas may also be performed using standard alpha sources, though these tend to have relatively high alpha-decay energies. However, since proton emission only occurs from very short-lived nuclides, proton calibration is more complicated.

In most cases, calibration of particle-identification telescopes is accomplished *in situ* by measuring the decays of well-known beta-delayed proton or alpha emitters, either immediately prior to or concurrently with the main production run. For instance, ^{25}Si emits delayed protons with energies from 386 keV to more than 6.8 MeV (Rob93); the ^{20}Na beta-delayed alpha spectrum has intense peaks from 2148 to 4894 keV (Ajz87, Cli89). Within these energy ranges, a simple interpolation generally suffices to determine the energies of new groups. However, when extrapolation is necessary, it becomes crucial to account for all sources of non-linearity in the relationship between the incident energy and the detected energy. The most important deviations arise from the fact that stopping power is a non-linear function of energy (see equation 3-3 and Fig. 3-6), from the effect of the signals in the gas-ΔE detectors on the E detectors (see Fig. 3-10 and related text), and from the electronics used to amplify and measure the energy signal. As discussed in the previous section, the electronics non-linearity may be measured directly and accounted for prior to proceeding with the rest of the calibration. The energy shift in the Si E signals as a function of ΔE signal strength may be measured using an alpha source and varying the ΔE bias voltage; a correction may then be applied to the E detector signals.

The energy resolution relative to the total signal output of the gas-ΔE detectors in the low-energy telescopes is rather poor (see Fig. 3-8); thus energy measurements are often performed using the E signal exclusively. Since the energy lost in the polypropylene entrance window, Freon gas and silicon detector dead layer is not a linear function of energy, a linear fit of detected energy to incident energy will be poor, especially for low-energy events. However, given accurate knowledge of the composition and thicknesses of these entrance components, energy losses which are not measured can be calculated and used to correct for the stopping power non-linearity.

For each peak observed in the calibration spectrum, an energy loss is calculated in each entrance component using the thickness of the component and numerically integrating with respect to energy over the stopping-power curves given in the International Commission on Radiation Units Report 49 (Ber93). The total losses are then subtracted from the incident energy to find the energy which will have been detected in the active region of the silicon-E detector for each calibration peak. A least-squares linear fit of these energies to the channel numbers of the peaks observed (corrected for the measured electronics non-linearity and ΔE-signal effect) serves as a calibration of the silicon-E detector. Accurate incident energies of new peaks may then be determined by calculating the energy detected (based on the above calibration) and reversing the energy loss calculation.

The reliability of this calibration method for low-energy protons and alpha particles was tested as follows, in two separate experimental runs. Since standard radioactive sources of neither very low-energy protons nor alpha particles exist, it was decided that the best method of obtaining low-energy calibration points was to degrade protons and alpha particles of known energies using thin aluminum foils. Beta-delayed alphas from ^{20}Na and beta-delayed protons from ^{25}Si and ^{21}Mg were produced at the LBNL 88-Inch Cyclotron. During each of these measurements, the reaction products were transported via a He-jet into a shielded detector box located ~0.6 m upstream of the target. The activity was deposited onto the edge of a catcher wheel; longer-lived activities were slowly rotated away from the detector to minimize the beta-decay count rate. The beam was pulsed and data were collected only during the beam-off phase. The activity was observed by a single gas-ΔE/gas-ΔE/Si-E telescope which subtended ~4% of 4π sr. Degrader foils were placed over a series of holes along the edge a disk; by rotating this disk, foils of different thicknesses were positioned between the collection spot and the telescope, normal to the incident radiation. One hole was left blank to allow the undegraded proton and alpha spectra to be measured. For the first test, six degrader foils were used with thicknesses of 219, 320, 439, 521, 619 and 627 μg/cm^2; the second employed five foils of 290, 629, 1063, 1316 and 1621 μg/cm^2. In both cases, the typical uncertainty in the foil thicknesses was ~20 μg/cm^2. This provided a large number of degraded proton peaks with energies ranging from 180 to 5405 keV and alphas particle peaks from 290 to 4894 keV with which to calibrate.

Figure 3-16 shows proton calibration fit residuals, defined as the difference between the fit from the calibration and the known energy of the peak, for the first test. The solid line shows the errors resulting from a linear fit of incident energy (after degradation by the aluminum foils) to channel number; clearly, the fit is poor. Corrections for the integral non-linearity of the electronics and for the undetected energy losses were then applied as described above. The dashed line shows the resulting errors from a linear fit of detected energy to corrected channel. For the corrected data, the distribution of fit errors about zero with respect to incident energy is seen to be random, demonstrating the effectiveness of this calibration method. Equally satisfactory fits were observed for proton and alpha-particle

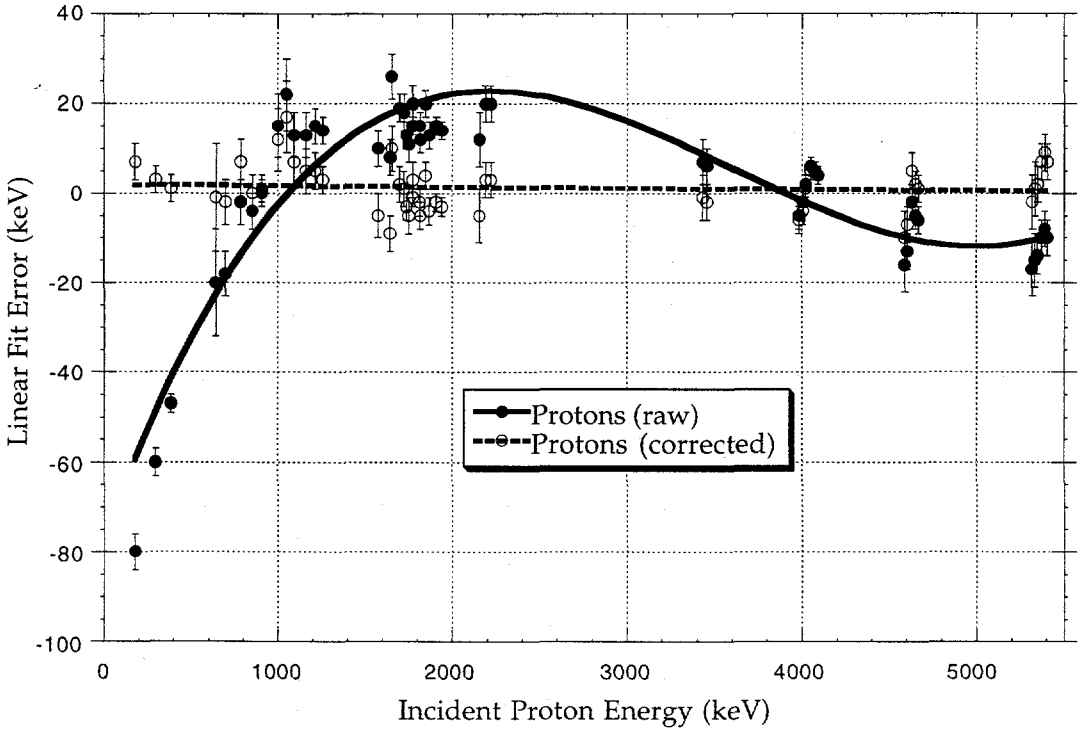

FIG. 3- 16: Proton calibration fit data. The x-axis shows the energies of the calibration points, either taken directly from the literature (undegraded proton peaks) or from the literature values minus the calculated energy losses in the Al degrader foils. The y-axis shows the deviation of the calculated energies of individual peaks (based on the calibration) from the correct values [Fit Error = E(from calibration) - E(correct)].

calibrations in both tests. Based on these calibration measurements, typical low-energy thresholds for detection of protons and alpha particles were determined to be ~180 keV and ~450 keV, respectively. This somewhat surprisingly-low alpha particle threshold is due to the reduction in average charge state, and thus stopping power, of very low-energy alpha particles as they pick up electrons from the stopping medium.

In situations where the calibration is critical, the above procedure that was used to test the energy-loss calculation method may be utilized as part of the experiment. After the initial calibration data have been taken, foils may be inserted between the detector and the activity catcher to produce degraded protons or alphas of the appropriate energy. This makes it unnecessary to rely on calculated energy losses in the detector components; the energies of new low-energy proton groups may be determined by interpolation.

C H A P T E R 4

THE BETA-DELAYED PROTON DECAY OF ^{23}AL

4.1 Introduction

4.1.1 Motivation

From a nuclear physics perspective, the beta-delayed proton decay of ^{23}Al is interesting mainly because it provides stringent tests of predictions made using the nuclear shell model. As discussed in detail in Chapter 2, the relative simplicity of nuclei in the 1s0*d*-shell has permitted an empirical two-body interaction to be deduced (Wil83). Using this interaction, the energies and wave functions of the ground and excited states of nuclides within the *sd*-shell may be calculated from a complete *sd*-shell basis. Further refinement of the calculations may be accomplished by application of the isospin non-conserving (INC) Hamiltonian of Ormand and Brown (Orm89), which will lead to mixing between states of different isospin.

One goal of this experiment is to measure the degree of isospin mixing in the ^{23}Al isobaric analog state (IAS) in ^{23}Mg (End90). It is known from reaction work (Har69, Nan81) that the IAS of ^{23}Al is unbound to proton emission by 215 ±6 keV. Because the beta decay of ^{23}Al to the IAS is superallowed, its partial half-life may be estimated with a great deal of accuracy; the branching ratio to this state may then be determined from the experimental half-life. Proton emission from the IAS will be relatively slow since the proton decay energy is small. Additionally, this decay is isospin forbidden and will thus only occur to the extent that this state contains admixtures of T = 1/2 states (Bro90b). Although proton decay

generally occurs on a much shorter time scale than gamma decay, in principle these two factors allow gamma-ray de-excitation to compete with proton decay from the IAS. The difference between the observed beta-delayed proton branching ratio through the IAS and the expected feeding of the IAS from the superallowed decay determines the proton branching ratio from the IAS. By comparing this ratio to that obtained from calculated gamma- and proton-decay rates (without taking into account isospin hindrance), the degree of isospin mixing in the IAS may be ascertained. This will then be compared with the theoretical predictions of Brown (Bro93).

A second goal of these experiments is to determine a portion of the Gamow-Teller (GT) strength function for ^{23}Mg. Because the energy available in the beta-decay of ^{23}Al is rather large (12.240 MeV, Aud93), the decay proceeds to high-lying states in ^{23}Mg that are unbound to proton emission. Gamma-ray emission will be too slow to compete with proton emission from these states (except for the IAS, as explained above); thus measurement of the intensities of the proton peaks allows the beta feeding to the states (and their energies) to be measured and the strength function to be calculated. As discussed in Section 2.5.3, a GT-decay operator may be applied to shell-model wave functions to predict the beta-decay feeding (Bro85). The simplicity of this operator makes comparison of the theoretical and experimental GT strength function an excellent test of the validity of the wave functions. Our measurements will again be compared to the predictions of Brown (Bro93).

The beta-delayed proton decay of ^{23}Al is also of interest for astrophysical reasons. Because the IAS of ^{23}Al is only slightly unbound, it may contribute an important resonance in the ^{22}Na(p,γ)^{23}Mg reaction cross section (Wie86b). The strength of this resonance will affect the reaction pathway followed in the rapid-proton (rp-) nucleosynthesis process that is thought to occur during novae in O-Mg-Ne white dwarfs (Wie86a, Wei90, Sta93), as discussed in Section 2.6. Although several reaction studies have attempted to measure the strength of this resonance (Seu90, Sch95, Ste96), thus far only rough limits have been set. The decay of ^{23}Al though the IAS provides an alternate method of estimating the proton-capture width of the IAS by determining the competition between proton and gamma-ray decay from this state, as discussed above.

The reaction pathway followed in the NeNa cycle of the rp-process will affect the abundances of ^{22}Na, and its beta-decay daughter ^{22}Ne ($t_{1/2}$ = 2.6 y). Specifically, additional resonance strength in the ^{22}Na reaction will reduce the abundances of these isotopes (Wie86a, Wie86b). It has been postulated that material ejected from novae would contain an enrichment of longer-lived rp–process nuclides relative to average galactic abundances (Seu90); this has been proposed as a possible explanation for the anomalous ^{22}Ne enrichment observed in meteoritic inclusions (Bla72, Ebe79). However, if the (p,γ) reaction occurs readily at the relevant stellar energies, it would place this interpretation of the "Ne*E*" problem in doubt. The prediction of these abundances may also have important implications for gamma-ray astronomy. Using two new Earth-orbit based gamma-ray telescopes, the Compton Gamma Ray Observatory and GRANAT (Geh98), astronomers can measure the intensity of the 1274.5 keV line from the positron decay of ^{22}Na (99.9% branch) to determine the abundance of ^{22}Na in various sites of nucleosynthesis. These observations can be compared with the predictions of nucleosynthesis network calculations (e.g., Wie86a).

4.1.2 Summary of Previous Experimental Work

Aluminum-23 was first observed in 1969 as a product of the ^{28}Si(p,^{6}He)^{23}Al reaction (Cer69); its mass excess was measured to be 6766 ±80 keV in this experiment. It is known to be the lightest member of the T_z = -3/2, A = 4n + 3 mass series that exists. Using the ^{25}Mg(p,t)^{23}Mg reaction, the T = 3/2 isobaric analog state of ^{23}Al was located at an excitation energy of 7788 ±25 keV in ^{23}Mg (Har69). The ground-state mass excess of ^{23}Al was remeasured in 1975 using the ^{28}Si(^{3}He,^{8}Li)^{23}Al reaction (Ben75); the new value of 6767 ±25 keV agrees with the earlier value. Nann, *et al.*, (Nan81) measured angular distributions of the products of the ^{25}Mg(p,t)^{23}Mg reaction at 40 MeV to determine the excitation energies, and in some cases, spins and parities, of many proton-unbound states in ^{23}Mg. They also remeasured the excitation energy of the IAS at 7795 ±6 keV.

The beta-delayed proton decay of ^{23}Al was first measured in 1972 (Gou72). Aluminum-23 was produced via the ^{24}Mg(p,2n)^{23}Al fusion-evaporation reaction at a laboratory bombardment energy of 40 MeV. Two different configurations were used for counting the activity. In the first, activity in the target was counted directly using a particle-identification telescope mounted behind the target. A slotted wheel rotating between the

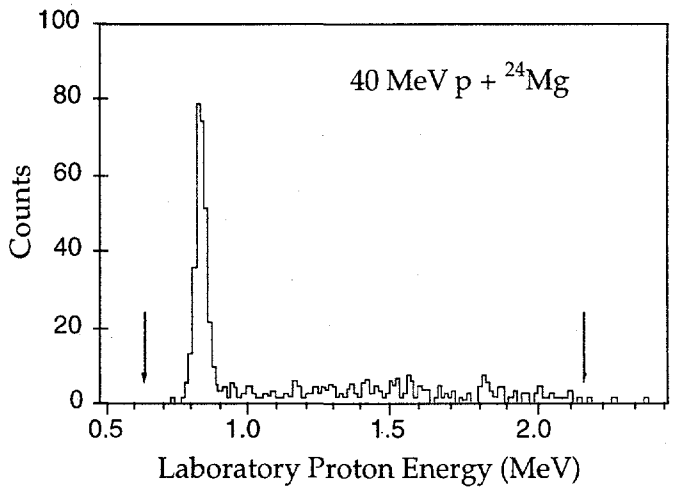

FIG. 4- 1: Beta-delayed proton spectrum of ^{23}Al (Gou72). The arrows indicate the proton-detection limits of the telescope used. Reproduced by permission of the authors.

target and telescope controlled the pulsing of the cyclotron beam. When the beam was on, the detectors were shielded by the wheel; when the beam was turned off, the slots in the wheel permitted the activity to be counted. The second configuration used a He-jet to transport the activity through an 80 cm long by 0.48 mm inner diameter (i.d.) capillary to a Ni catcher foil; a step motor moved the catcher foil from its collection position to a particle-identification telescope for counting at 1.2 s intervals. Both of these telescope configurations had a thin Si ΔE detector (8 μm and 6 μm thick for the wheel and He-jet measurements, respectively) and a 50 μm-thick Si E detector.

A single beta-delayed proton group with a half-life of 470 ±30 ms , shown in Fig. 4-1, was observed at a laboratory energy of 832 ±30 keV. Based on the center of mass energy of 870 ±30 keV, the proton is assigned to the decay of a state at 8453 ±5 keV excitation in ^{23}Mg. The cross section for production of this peak was measured to be less than ~220 nb. Measurement of its excitation function eliminated other reaction products (in particular, ^{20}Na) as the source of this activity. An unsuccessful search was also made for the beta-delayed proton decay through the IAS ($E_{p,lab}$ = 206 ±6 keV); an upper limit on the ratio of the gamma and proton decay widths of $\Gamma_\gamma / \Gamma_p \geq 50$ was set for the IAS. From these measurements and the earlier reaction work, the decay scheme shown in Fig. 4-2 was deduced.

Several reaction studies have measured or deduced resonance strengths in the ^{22}Na(p,γ)^{23}Mg reaction. The resonance for the IAS of ^{23}Al at 7795 keV excitation in ^{23}Mg occurs at a proton laboratory energy of 225 ±6 keV. Görres, *et al.*, measured resonances in ^{23}Mg at excitations above ~8 MeV using protons with energies from 400-1275 keV (Gör89); the target consisted of 60 μCi of ^{22}Na on a Ta/Ni backing. Seuthe, *et al.*, measured the same reaction at proton energies from 170-1290 keV using a target implanted with ~700 μCi of ^{22}Na (Seu90). An upper limit of $\omega\gamma < 1.3$ meV (see equation 2-76) was set on the resonance strength for the ^{23}Al IAS. Schmidt, *et al.*, used the ^{22}Na(^{3}He,d)^{23}Mg reaction to determine proton spectroscopic factors for weakly proton-unbound states of ^{23}Mg (Sch95). A 30 MeV ^{3}He beam bombarded a carbon target which had been implanted with 6 mCi of ^{22}Na; ejectiles were observed using a Q3D spectrograph (Löf73) and deuteron spectra were measured using a position-sensitive detector array. The angular distributions of the deuterons were analyzed using the distorted-wave Born approximation (DWBA). The results were used to deduce IAS-resonance strength limits of 0.05 meV < ωγ < 33 meV. The most recent measurement, by Stegmüller, *et al.*, used proton energies from 200-630 keV to study the ^{22}Na(p,γ)^{23}Mg reaction (Ste96). The target was prepared by implantation of 0.3 mCi of ^{22}Na into a Ni-Ta foil; at the time of the measurement, the activity had decreased to 0.19 mCi. Gamma rays were observed using a high-purity Ge detector. Although a new resonance was observed corresponding to the ^{23}Mg state at 7783 keV excitation, no resonance was observed through the ^{23}Al IAS. This work placed an upper limit of $\omega\gamma < 2.6$ meV for this state.

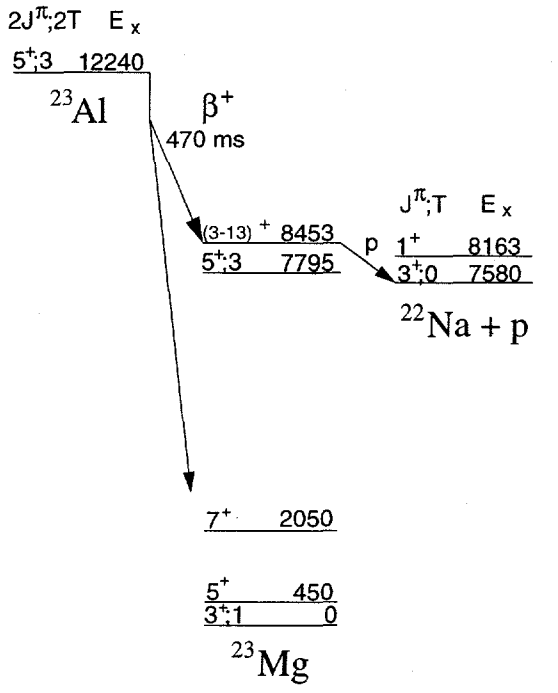

FIG. 4- 2: Decay scheme for beta-delayed proton emission from ^{23}Al.

4.2 First Low-Energy Measurements

4.2.1 Experimental

Measurement of the low-energy beta-delayed proton spectrum of ^{23}Al required the development of the gas-ΔE/gas-ΔE/Si-E telescopes described in Section 3.2.2 (Mol94). This experiment used six of these telescopes that had been incorporated into an array (Row97). Figure 4-3 shows a cross-sectional view of this low-energy particle-identification telescope array. By constructing the array from a single support structure, the mechanical overhead was minimized, thus allowing close packing of the telescopes. Detector telescopes are mounted in six of the seven faces of a Delrin (DuP98) support structure; the seventh face is left open to allow entry of a movable collection tape (for use in He-jet studies) or a collection foil (for use with mass-separated activities.) The support structure was machined from a single block of Delrin. This material was chosen because it is an electrical insulator, is easy to machine, and does not out-gas significantly in a high vacuum environment. The solid angle of each of the six detectors is ~4% of 4π sr. The angles between the faces of the support allow

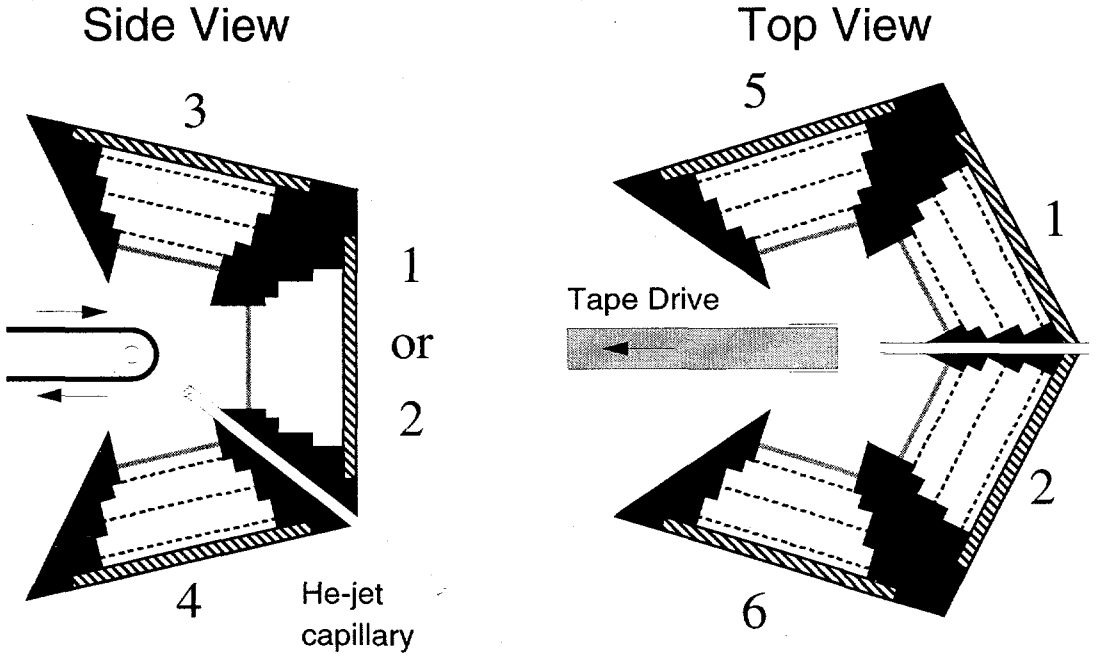

FIG. 4- 3: Low-energy particle-identification telescope array. The activity-collection tape and He-jet capillary are also indicated.

two-particle activities to be studied at various average relative-emission angles; there are four wide-angle (~141°), one narrow-angle (~54°), and ten intermediate-angle (~78°) detector combinations. Telescopes 5 and 6, shown adjacent to the collection opening in the top view shown in Fig. 4-3, are used primarily when activity is implanted in a catcher foil after mass-separation; the collection-tape support mechanism used in He-jet studies occludes these detectors by approximately 96%.

Figure 4-4 shows a cross-sectional view of one of the detector telescopes. The individual telescope components are mounted within a series of concentric bore holes in each face of the Delrin support. From the center of the ball outward, the components of each telescope are a 40-70 μg/cm^2 polypropylene window to confine the Freon-14 gas, the signal grid for the first gas-ΔE detector, the common high-voltage grid for both gas detectors, the signal grid for the second gas-ΔE detector and finally a 300 μm silicon detector. All of the components except the window are press-fit into place; Teflon (DuP98) rings placed between the components ensure a tight fit and isolate the electrically-active components. The entire assembly is held in place by a brass cooling plate through which ethanol chilled below -15°C is circulated. Calibrations using beta-delayed protons degraded by thin Al foils (see Section 3.3.2) estimated a low-energy proton threshold of ~180 keV for these telescopes.

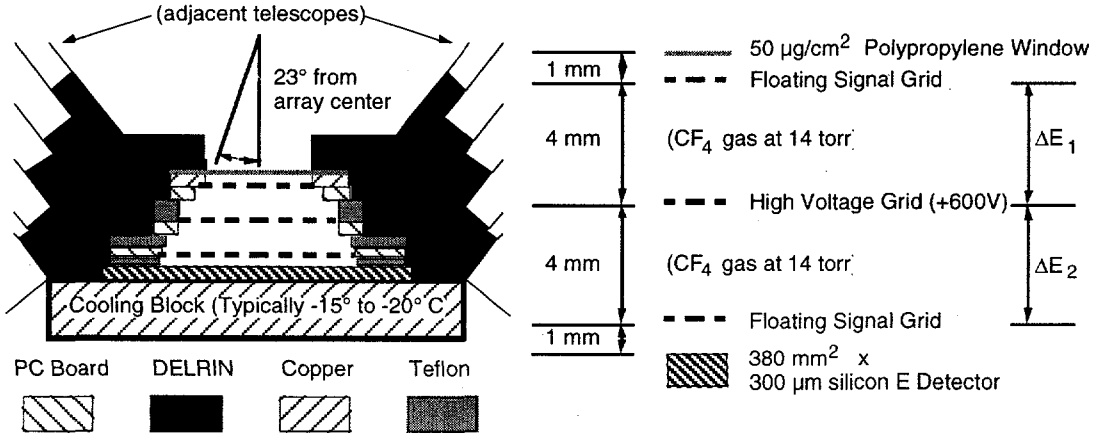

FIG. 4- 4: An individual low-energy particle-identification telescope from the detector array shown in Fig. 4-3.

The beta-delayed proton spectrum was measured in two separate bombardments; in each, 40 MeV protons produced ^{23}Al via the ^{24}Mg(p,2n)^{23}Al reaction. Beam currents of up to 2 μA were utilized; the beam was pulsed to eliminate background neutron events. The beam-on

and beam-off (counting) periods were 500 and 800 ms, respectively. The He-jet recoil transport method (see Section 3.1.3) was used in a multiple-target, multiple-capillary configuration with ten internal capillaries collecting activity from five targets, then feeding it into a single 0.9 mm i.d. × 75 cm long transport capillary. The activity exited the capillary and was deposited onto the tip of a movable tape located at the center of the array of telescopes. The detector chamber was evacuated by a high-capacity Roots blower; the vacuum in the chamber was ~20 mtorr. The target, He-jet and detector configuration is shown in Fig. 4-5.

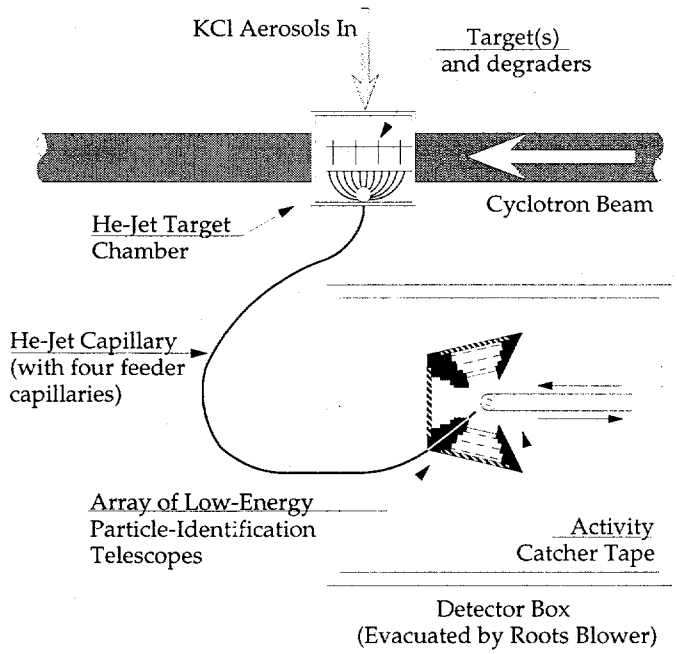

FIG. 4- 5: Experimental set-up for the first low-energy measurements. Note that the size of the detector array is somewhat exaggerated.

During the first bombardment of 17.9 mC, ~1 mg/cm^2 ^{nat}Mg targets were used. The collection tape slowly moved longer-lived activity away from the collection spot. The second bombardment of 11.6 mC used ~1 mg/cm^2 separated-isotope ^{24}Mg targets (99.9% enriched). For this measurement, the collection tape was not moved to allow the half-life of the activity to be determined more accurately. In these bombardments, the only potential beta-delayed proton emitters that could have been produced besides ^{23}Al were ^{24}Al and ^{20}Na. Thresholds for the ^{24}Mg(p,n)^{24}Al, ^{24}Mg(p,αn)^{20}Na and ^{24}Mg(p,2n)^{23}Al reactions are 15.3, 25.0 and 30.8 MeV, respectively. To check for possible contamination from these species, two other bombardments of the ^{24}Mg targets were also performed (Bat94) at proton energies of 20.0 and 28.5 MeV (13 mC

and 4.7 mC, respectively.) In both of these lower-energy bombardments, a continuum of events with signals characteristic of protons were observed at energies from ~200-1500 keV; these were assigned to the beta-delayed proton decay of ^{24}Al based on the agreement between the measured half-life of 2.5 ±1.0 s and the literature value of 2.053 s.

To calibrate the detector telescopes *in situ*, the well-known beta-delayed proton and alpha emitters ^{25}Si (Rob93) and ^{20}Na (Cli89) were produced by short bombardments of the targets by a 40 MeV $^{3}He^{2+}$ beam prior to the proton bombardments. An empirical electronics non-linearity correction (generated from later calibration work) was applied to all peak centroids. To extrapolate the calibration to energies below the lowest-energy proton group in the ^{25}Si spectrum at 386 keV, energy losses in the telescope components situated in front of the E detector (window, gas and Si dead layer) were calculated using the estimated thicknesses of these components. A least-squares fit of the ^{25}Si peaks' centroids to the remaining energy (after these losses were subtracted) was performed. The energies of the ^{23}Al proton groups were then determined by starting with the detected energies (from the ^{25}Si calibration) and then back-calculating to the incident energies using calculated energy losses. Software gating to separate protons from alpha and beta-decay events was performed using the ΔE vs. E back-projection technique described in Section 3.3.1; after suitable gates had been created using the ^{25}Si data as a guide, the same gates were applied to the ^{23}Al data. Figure 4-6 shows two-dimensional ΔE_1 vs. E spectra from the first ^{23}Al bombardment. On the left, the raw data are

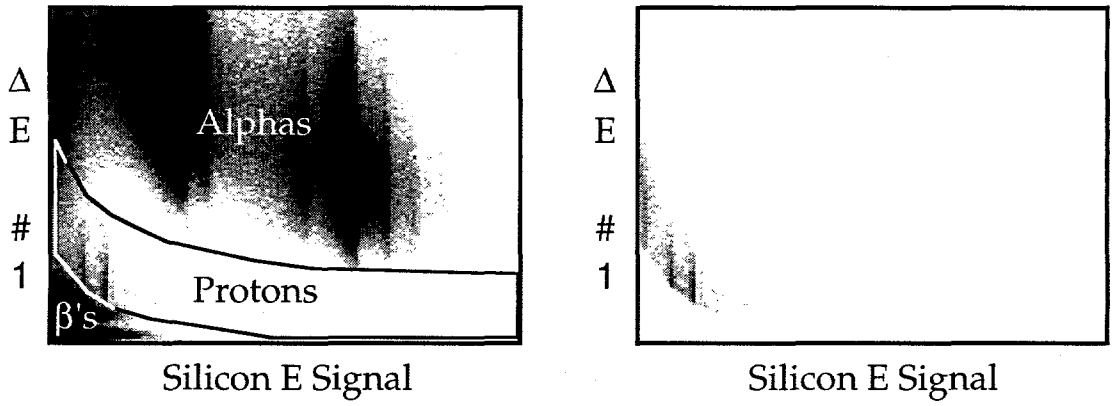

FIG. 4- 6: ΔE vs. E spectra, 40 MeV p + ^{nat}Mg bombardment. On the left, the raw data are shown prior to gating; the alpha, beta and proton regions are indicated. On the right, the proton events are shown after data reduction.

shown with a proton gate; on the right, the proton events are shown after alpha and beta decay events have been gated out.

4.2.2 Results

Figure 4-7 shows a proton spectrum collected during the ^{nat}Mg proton bombardment. In addition to the previously known beta-delayed proton group (peak 4), two new proton peaks are clearly evident (1 and 3). The lowest energy peak also appears to include a high-energy shoulder (labeled 2 in the figure). Table 4-1 lists the laboratory energies, decay assignments and relative intensities of the peaks, using data averaged from the two bombardments with the ^{24}Al proton continuum subtracted. It can be seen in each case that there is good correspondence with a known excited state of ^{23}Mg.

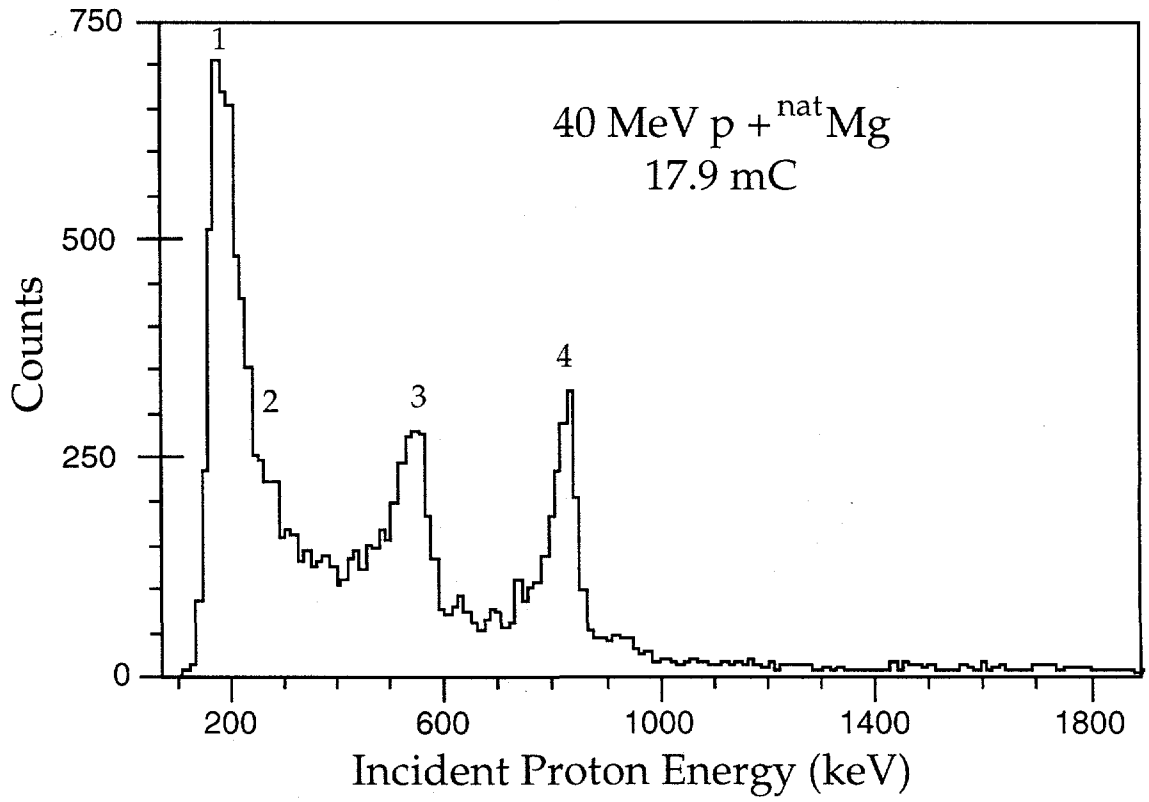

FIG. 4- 7: Beta-delayed proton spectrum from the first low-energy proton measurements.

Table 4- 1: Summary of results for proton lines observed in the first low-energy proton measurements.

Peak Number	$E_{p,lab}$ (keV)	E^* in ^{23}Mg (keV) This work	E^* in ^{23}Mg (keV) (End90)	Relative Intensity
1	223 ±20	7813 ±20	7795 ±6	2.2 ±0.5
2	285 ±20	7877 ±20	7852 ±6	0.9 ±0.3
3	560 ±5	8164 ±6	8155 ±6	0.7 ±0.1
4	839 ±5	8456 ±6	8453 ±5	1.0

4.2.3 Discussion

The results of this measurement have been reported previously (Tig95); in what follows, essentially the same arguments and conclusions will be presented as were discussed in that paper.

Given the agreement between the energy of the peak at 223 ±20 keV and the expected energy for protons emitted from the IAS of ^{23}Al (206 ±6 keV), it is reasonable to assign this peak to that decay. Based on the 220 nb cross section previously measured for production of the 839 ±5 keV proton group and the intensity of the IAS peak relative to the 839 keV peak, the cross section for production of the IAS is 480 nb. If a total ^{23}Al cross section of 100 mb as calculated by ALICE (Bla82) is assumed, this leads to a branching ratio for the decay of the IAS of 0.48%. A log*ft* of 3.28 (calculated from equations 2-47 and 2-40) for the superallowed beta decay to the IAS indicates a 13.7% branch to this state, using the experimental half-life of ^{23}Al (0.47 s). Comparing this feeding of the state to the observed intensity of the IAS peak, a 3.5% proton branch from the IAS is obtained.

To determine the isospin mixing and proton-capture strength of the IAS, it is necessary to know its gamma decay width. Although this has not been measured, the gamma width of its mirror in ^{23}Na has been measured to be 3.0 eV (End90). Shell model predictions (Wil83, Bro88b) for the width of both this state and the ^{23}Al IAS in ^{23}Mg agree with this value. Using this gamma width and the proton decay branch, the proton width for the IAS is 0.11 eV. A barrier penetration calculation for proton emission from the IAS using the code COCAGD3 (Sex73) predicts a width of 0.91 eV if a modest deformation (ε~0.15, as observed among other nuclides in this region) is assumed. Comparison of this predicted width to the measured width yields a spectroscopic factor $S_{INC,exp} = 12\ ^{+7}_{-8}\%$. This is much stronger than predicted;

using the isospin-nonconserving (INC) interaction of Ormand and Brown (Orm89), Brown predicts a spectroscopic factor $S_{INC,theo}$ of 0.24% (Tig95). From the spins of the states involved and these proton and gamma widths, the proton capture resonance strength for the IAS is estimated to be 45 ±25 meV. Again, this is significantly larger than the experimental upper limits for $\omega\gamma$ of 1.3, 33 and 2.6 meV that have been set previously in references Seu90, Sch95 and Ste96, respectively.

4.3 Second Low-Energy Measurements

4.3.1 Motivation

The measurements described in the previous section were among the first performed with this detector array; thus the behavior of the detector telescopes had not been fully characterized. After the results of that measurement were reported, it gradually became apparent that the peak assigned to the decay of the IAS might have been contaminated by activity from ^{20}Na. Combined with the disagreement between the values for the isospin mixing and resonance strength of the IAS deduced from that work versus the theoretical predictions and the other measurements, respectively, a compelling case was made that the decay should be measured again.

It was mentioned in Section 3.3.1 that the ^{16}O-recoil from the 2148 keV beta-delayed alpha decay of ^{20}Na appears to be a low energy alpha particle if it is detected in coincidence with the positron from the beta decay that feeds the alpha-unbound state in the emitter. It was during re-analysis of the ^{23}Al data from the first low-energy measurements that this was discovered. The ΔE vs. E raw-data spectrum on the left of Fig. 4-6 shows a band in the alpha-event region near the low-energy cut-off for the Si E detector. This was originally thought to be a possible new low-energy alpha decay from ^{20}Na. A measurement of the beta-delayed alpha spectrum of ^{20}Na made using the mass separator RAMA (see Section 3.1.4) confirmed that these events were associated with the decay of ^{20}Na. However, the energy of this peak seemed to change from telescope to telescope. The nature of these events was understood when this peak was compared to the peak of the beta continuum measured simultaneously; the centroids and shapes of the two peaks were nearly identical. Furthermore, the intensity of the ^{16}O-recoil/beta coincidence peak relative to the 2148 keV alpha peak was the same as

the solid angle of the telescopes (~4%); this corresponds to the percentage of beta-delayed alpha events that would normally be detected in coincidence with the preceding positron. Re-examination of the IAS proton peak showed that it too had the same centroid and shape as the beta and ^{16}O-recoil/beta peaks, suggesting that this peak was contaminated. These three peaks are shown in Fig. 4-8.

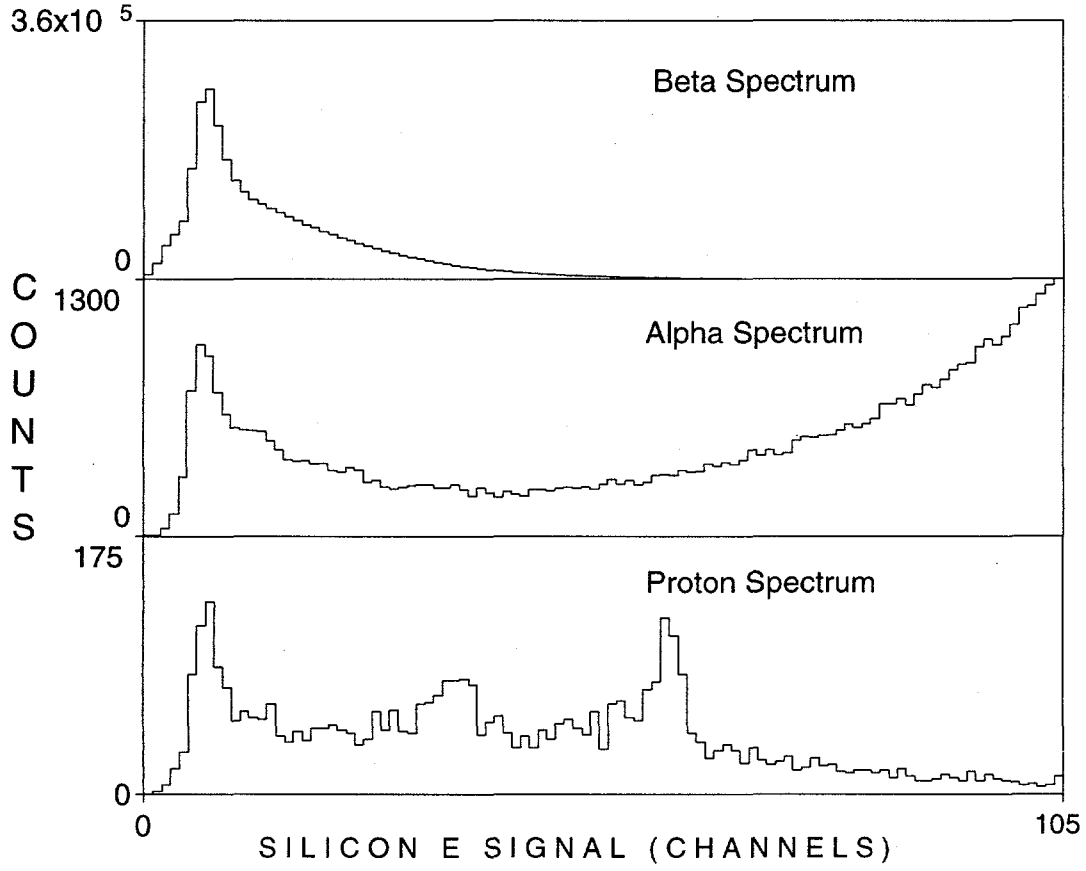

FIG. 4- 8: Beta-continuum, ^{16}O-recoil/beta and IAS proton peaks in the Si E detector, from the first series of low-energy proton measurements.

In addition to the question of contamination, it was thought that developments in calibration techniques would yield a more accurate value for the energy of the IAS peak. At the time of the first low-energy measurement, a reliable method of extrapolating below the lowest-energy proton group of ^{25}Si at 386 keV had not been developed. The technique used to calibrate the telescopes, described above, was worked out after the measurement had been

performed. Tests of this procedure demonstrated that it was valid (the data shown in Fig. 3-16 resulted from these tests); however, the thicknesses of the telescope components had to be guessed because measurements were not taken before the telescopes were disassembled. A new measurement of the decay of ^{23}Al would allow the telescopes to be calibrated *in situ* using the technique of degrading ^{25}Si protons with thin foils to extend the calibration to the low-energy cut off of the telescopes.

4.3.2 Experimental

In order to eliminate the contamination from ^{16}O-recoil/beta coincidence events from the decay of ^{20}Na, modified detector telescopes were used for these measurements. Figure 4-9 shows a schematic diagram of one of these telescopes. Each consisted of two gas proportional counters as ΔE detectors, backed by a thin (< 70 μm) Si E detector and, behind this, a 300 μm Si E_{reject} detector. Table 4-2 shows the attributes of the detector telescopes. The thicknesses of the Si E detectors were chosen to stop only low-energy protons; this was done both to minimize the number of beta-events that would be detected in the E and to reduce the energy of the peak of the beta continuum. In one telescope ("Truth"), a 28 μm E detector was used; in the other ("Beauty"), the E was 63 μm thick. The Si E_{reject} detector allowed removal of "high"-energy proton events not stopped in the E detector and beta particles. Besides gating out these single-particle events, this also allowed elimination of both ^{16}O-recoil/beta and proton/beta coincident events from the proton spectrum. Because there was insufficient space in the array

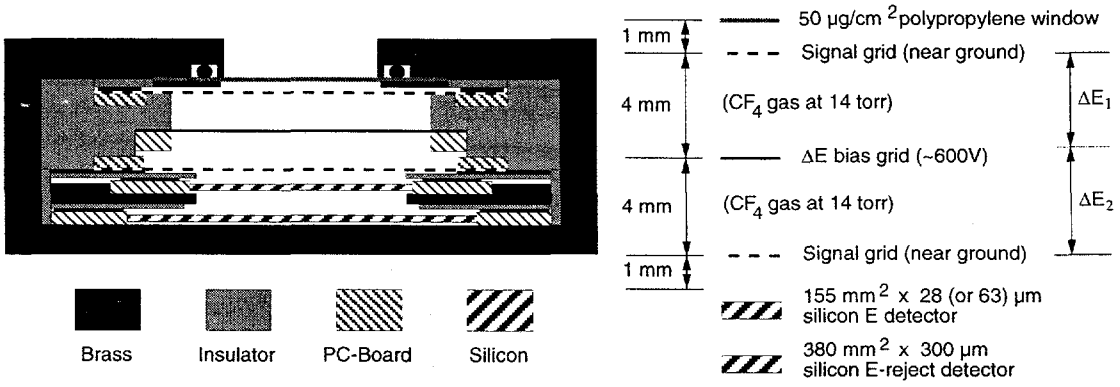

FIG. 4-9: Cross-sectional view of a modified low-energy particle-identification telescope with improved beta-particle rejection, used in the second series of measurements of the decay of ^{23}Al.

used in the earlier measurements for the additional Si detector, these measurements were made with two separate telescopes. The housing of each was made of brass; telescope components were isolated from each other and the housing by a series of plastic insulator pieces in which the grids and Si detectors were placed.

Table 4- 2: Detector telescope attributes.

	"Truth"	"Beauty"
Thickness, Window	48 ±7 μg/cm^2	51 ±3 μg/cm^2
Thickness, Gas	81 ±4 μg/cm^2	81 ±4 μg/cm^2
Thickness, E Dead Layer	139 ±7 μg/cm^2	114 ±4 μg/cm^2
Thickness, E	28 μm	63 μm
Area, E	155 mm^2	155 mm^2
Thickness, E_{reject} Dead Layer	108 ±30 μg/cm^2	120 ±11 μg/cm^2
Thickness, E_{Reject}	~300 μm	~300 μm
Area, E_{Reject}	380 mm^2	380 mm^2
Solid Angle Subtended	1.6% of 4π sr.	1.7% of 4π sr.

To calibrate the detectors *in situ*, ^{25}Si was again made with a 40 MeV $^3He^{2+}$ beam via the $^{24}Mg(^3He,2n)^{25}Si$ reaction; the ^{25}Si-degradation technique described in Section 3.3.2 was used after the undegraded proton spectrum had been measured. A plunger was added to the detector box to allow thin Al foils of known thicknesses to be positioned between the activity deposition spot on the wheel rim and the telescopes. A single set of foils was used for the first measurement; two sets were used in the second. By carefully choosing the foil thicknesses, the 386 keV protons from ^{25}Si could be degraded to energies bracketing 206 keV, eliminating the need for an extrapolation of the calibration. Table 4-3 shows the foil thicknesses used in each of the two bombardments and the energy of the ^{25}Si 386 keV peak after degradation. Aside from permitting an unambiguous extrapolation of the energy calibration down to the thresholds of the telescopes, this technique also provides an efficiency calibration in case the detection efficiency decreases near the low-energy cut-off.

Four ~1 mg/cm^2 ^{nat}Mg targets were bombarded with ~200 mC of 40 MeV protons during the first run. The He-jet system for this bombardment was the same as used for the bombardments in the previous section. Activity exiting the capillary was deposited onto the rim of an activity-catcher wheel which was rotated at 33 RPM to remove long-lived activity away from the detectors. The two telescopes viewed the activity deposition spot from above

Table 4- 3: Degradation of ^{25}Si protons for *in situ* calibration of telescopes. Thicknesses are given in μg/cm^2; energies are in keV.

telescope	"Truth" Degraders		"Beauty" Degraders	
bombardment	Run #1	Run #2	Run #1	Run #2
degrader #1 thickness	605 ±15	542 ±5	478 ±15	541 ±5
degraded 386 keV peak	188 ±6	211 ±3	234 ±5	212 ±3
degrader #2 thickness	---	564 ±5	---	563 ±5
degraded 386 keV peak	---	203 ±3	---	204 ±3

and below with solid angles of 1.6% and 1.7% of 4π sr. A single ~1.0 mg/cm^2 ^{24}Mg (99.9%) separated-isotope target was bombarded by ~100 mC of protons during the second run. A single 1.35 mm i.d. × 80 cm long capillary collected activity and transported it to the detector box, which was configured the same as in the previous run. The target, He-jet and detector arrangement for these bombardments is shown in Fig. 4-10.

A coincidence was required, either between ΔE_1 (the "trigger" ΔE) and the E detector, or between the E detector (with a large threshold in the discriminator) and the E_{reject} detector, for an event to be taken to tape. The first requirement applied primarily to low-energy proton (or alpha) events; the second ensured that "high"-energy (>1 MeV) protons that were not stopped in the E detector would also be counted. A (ΔE_1+ΔE_2) sum gate was also applied in the Starburst module to eliminate many of the remaining beta-decay events from the data set.

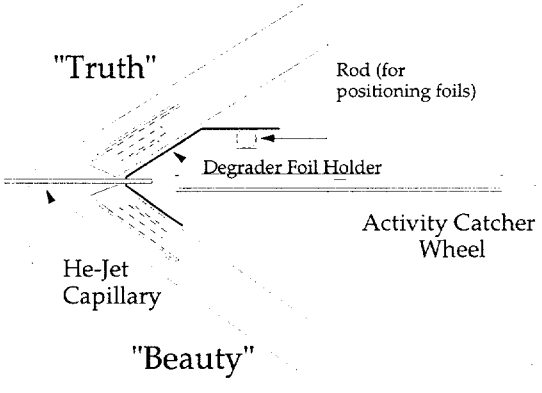

FIG. 4- 10: Detector configuration for the second low-energy measurements of the decay of ^{23}Al.

4.3.3 Results

Several difficulties were encountered during the first of the two runs. The Al degraders were each composed of several thinner foils which had been measured individually but not together. During the calibration, it was discovered that the stack of foils for the "Truth" telescope was too thick. The 386 keV protons from ^{25}Si were degraded to 188 keV, near the energy threshold of the telescope. Although a peak was observed at this energy, the efficiency for detection was only about 4%, based on the known branching ratio for the 386 keV decay. The foils for "Beauty" did not degrade the calibration protons down to the calculated energy of the IAS peak (206 ±6 keV). Thus it was unclear whether the lowest energy peak observed was being partially cut off in either telescope (though based on the subsequent measurement, the detection efficiency was actually close to 100%). However, this

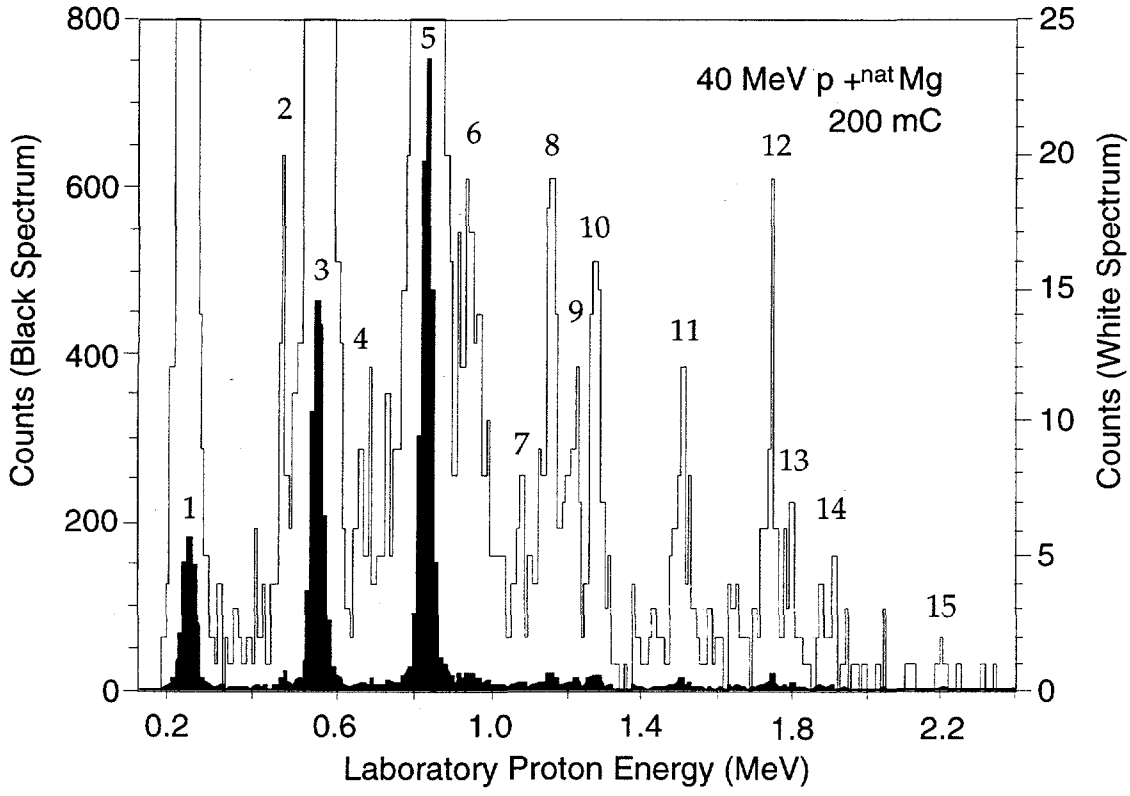

FIG. 4- 11: Proton spectrum emphasizing weak beta-delayed proton groups, from the second series of ^{23}Al measurements. The y-scale for the magnified spectrum, shown in white, is given on the right side.

first bombardment produced several weak new proton peaks that had not been observed previously. Figure 4-11 shows these new proton groups. Although fifteen peaks are labeled in the figure, some of these need additional confirmation due to poor statistics (particularly peaks 4, 14 and 15). Because the calibration for this run was unsuccessful, the second bombardment was performed.

The thicknesses of the calibration foils used for the second of these measurements were chosen more carefully; the 386 keV proton group from ^{25}Si was degraded to ~212 and ~204 keV using the first and second foil sets, respectively. Figure 4-12 shows a proton spectrum observed in this bombardment. To generate this spectrum, gating was performed in both the standard (ΔE_1 vs. E and ΔE_2 vs. E) and polar projections (ΔE_{radius} vs. E and ΔE_{angle} vs. E) projections. We gated out those events that had a signal in the E_{reject} detector; this

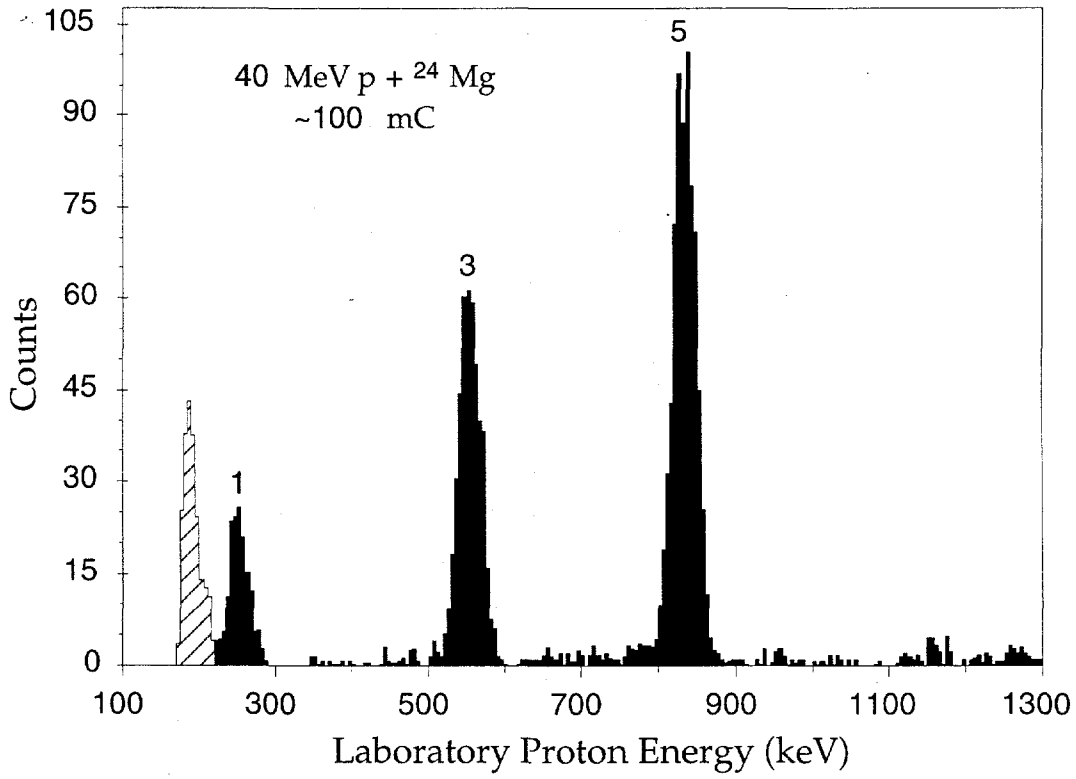

FIG. 4- 12: Proton spectrum showing "intense" beta-delayed proton groups from ^{23}Al. The cross-hatched peak near the low-energy threshold is not thought to be comprised of true proton events. Numbering of the peaks is consistent with Fig. 4-11 and Table 4-4.

significantly reduced the intensity of the lowest energy peak (#1) relative to the others. The events seen at the low-energy limit of the spectrum do not appear to be real protons. Whereas the other proton groups lie within the proton gates defined around the protons produced during the calibration runs, these events are a subset of a band of events that overlaps the proton gates but has a roughly uniform energy distribution in the ΔE detectors; it extends both above and below the expected proton region in ΔE energy. These are most likely associated with occasional discharges in these detectors, perhaps triggered by beta particles. Some of the weaker proton peaks observed in the first bombardment are also seen in this spectrum, but with lower statistics. Table 4-4 shows the energies and relative intensities of the proton groups observed in the two bombardments, as well as the corresponding excitation energy in ^{23}Mg assuming the decay goes to the ground state of ^{22}Na.

Table 4- 4: Combined results of the second series of low-energy beta-delayed proton measurements.

Peak number	Energy (lab, keV)	Energy (c.m., keV)	Relative Intensity	E^* in ^{23}Mg (keV) This work	Endt90
1	246 ±20	257 ±21	33 ±3%	7837 ±21	7795, 7852
2	468 ±10	490 ±10	2.1 ±0.3%	8070 ±10	8078
3	556 ±5	581 ±5	68 ±5%	8161 ±5	8155, 8164
4	675 ±10	706 ±10	1.9 ±0.3%	8285 ±10	8285
5	838 ±5	876 ±5	(100%)	8456 ±5	8453
6	942 ±10	985 ±10	4.4 ±0.4%	8564 ±10	8557
7	1075 ±10	1124 ±10	1.2 ±0.2%	8703 ±10	8758
8	1156 ±10	1209 ±10	3.2 ±0.4%	8788 ±10	8793
9	1215 ±10	1270 ±10	2.1 ±0.3%	8850 ±10	8870
10	1277 ±10	1335 ±10	2.5 ±0.3%	8914 ±10	8916
11	1505 ±10	1573 ±10	1.9 ±0.3%	9153 ±10	9138
12	1748 ±10	1827 ±10	2.0 ±0.3%	9407 ±10	9403
13	1797 ±10	1879 ±10	0.94 ±0.2%	9458 ±10	9465
14	1897 ±10	1983 ±10	0.6 ±0.2%	9563 ±10	9596
15	2201 ±10	2301 ±10	0.2 ±0.1%	9880 ±10	---

4.3.4 Discussion

These results differ significantly from the results of the first low-energy measurements of the beta-delayed proton decay of ^{23}Al (Tig95). Most significantly, the peak previously assigned to the decay of the IAS at 7795 keV excitation can no longer be

unambiguously assigned to that state. Furthermore, its intensity relative to the 100% transition at 838 keV has been reduced by a factor of almost seven. Several weak new delayed-proton decays have been observed, indicating beta transitions to other excited states in ^{23}Mg. Also, in the spectra shown in Figures 4-11 and 4-12, there is no obvious evidence of the beta-delayed proton continuum from the decay of ^{24}Al observed in Fig. 4-7.

4.3.4.1 Assignment of the 246 keV Proton Group (Peak #1)

Proton peak 1 (Figures 4-11 and 4-12) is observed at an energy intermediate to the low-energy peaks that were seen in the first series of low-energy measurements (peaks 1 and 2 in Fig. 4-7). Three possible assignments for this 246 ±20 keV peak immediately present themselves. The energy disagrees with the energy expected from the decay of the ^{23}Al IAS at 7795 ±6 keV by 40 ±22 keV. It seems unlikely that the calibration would be off by this much, particularly when one considers the fact that the 386.1 keV ^{25}Si protons degraded by the ~564 mg/cm^2 Al foils have an average energy of 203 keV using the same calibration as applied to the ^{23}Al data. It was calculated that they would be degraded to an energy of ~204 ±3 keV by these foils.

If, however, one assumes that this peak is from the decay of the ^{23}Al IAS, revised estimates of the resonance strength $\omega\gamma$ and the isospin mixing $S_{INC,exp}$ may be made. As a starting point, the same assumptions as used in Section 4.2.3 (from Tig95) will be used. The new relative intensity of 33 ±3% suggests a branching ratio for this beta-delayed proton branch of 0.072 ±0.038%. If 13.7 ±1.1% of ^{23}Al nuclei beta decay to this state, as estimated from the energy and log*ft*, then the proton branching ratio for the IAS is 0.53 ±0.28%. Combined with the estimated gamma-decay width Γ_γ of 3.0 ±0.2 eV from the measured width of its ^{23}Na mirror, this branching ratio corresponds to a proton-decay width Γ_p for the IAS of 16 ±8 meV. Comparison with the predicted width of 0.91 ±0.34 eV produces a spectroscopic factor $S_{INC,exp}$ of 1.7 ±1.1%, in much better agreement with Brown's prediction of 0.24% than the earlier value of 12 ±7%. The recalculated ^{22}Na(p,γ)^{23}Mg resonance strength $\omega\gamma$ is 6.7 ±3.8 meV, also much closer to the measured limits, e.g., $\omega\gamma \leq 2.6$ meV, set by Stegmüller, *et al.* (Ste96).

Unfortunately, these results are rather sensitive to the assumptions made. For instance, the barrier penetration approach to calculating proton decay widths as outlined by

Hofmann (Hof89, Hof93) has been shown to give more accurate predictions than COCAGD3 for the measured direct-proton emitters. The width Γ_p using this type of calculation (see Appendix A) is 20.5 eV, considerably larger than the COCAGD3 value 0.91 eV used above. Similarly, the statistical fusion-evaporation code PACE2 predicts a larger value for the total ^{23}Al production cross section of 165 μb than the ALICE value of 100 μb. Using these revised values, $S_{INC,exp}$ is calculated to be 0.05 ±0.03%, which is smaller than predicted by Brown (Tig95). The revised value for $\omega\gamma$ is 4.1 ±1.8 meV; this agrees (within the error bars) with the limit set by Stegmüller, *et al.* (Ste96). Thus, it is unlikely that the IAS contains a significantly-larger admixture of T=1/2 states than was predicted using Ormand and Brown's INC Hamiltonian, and it is also doubtful that the ^{22}Na(p,γ)^{23}Mg resonance corresponding to the IAS is stronger than the reaction studies have measured. This is especially true since the assignment of the 246 keV peak to the IAS decay is probably incorrect.

One may start with the Stegmüller, *et al.*, and Brown values and work backwards to determine the number of proton events that should have been observed from the IAS decay. If one does this using the assumptions from Section 4.2.3 (Tig95), it is expected that 61 (Brown) or 28 (Stegmüller) counts would be observed at the appropriate energy in the two telescopes (combined) during the final run. It is trivial to determine where this energy range is, since the 386 keV ^{25}Si protons were degraded to the expected energy of the IAS; this energy is at the minimum between peak 1 and the cross-hatched peak in Fig. 4-12. The number of counts observed in both telescopes in this region is in agreement with these expectations. However, the cross-hatched peak is not believed to consist of real proton events; the events in the minimum between the two peaks are also suspect and may not all be from protons.

A second possibility, not indicated in Table 4-4, is that the peak at 246 keV originates with the decay of the state at 8420 keV excitation in ^{23}Mg to the $J^\pi=1^+$ first-excited state of ^{22}Na, at 583 keV. This would produce a proton with an energy of 246 ±6 keV in the laboratory frame, in excellent agreement with the observed energy. However, energetics favor the emission of an 804 ±6 keV proton from the intermediate state to the 3^+ ground state of ^{22}Na over decay to the 1^+ first-excited state. This is true even if the centrifugal barrier for the decay to the ground state is larger. The spin and parity of the 8420 keV state are unknown, but it is reasonable to assume it is fed by either an allowed or first-forbidden beta decay from the

^{23}Al $J^{\pi}=\frac{5}{2}^{+}$ ground state, which will limit the possible J^{π} values. The greatest differences in the centrifugal barrier between the decays to the ground and first-excited states occur if J^{π} were $\frac{3}{2}^{+}$ (allowed) or $\frac{1}{2}^{-}$ (first-forbidden). Even for these cases, barrier penetration calculations suggest that the decay to the ground state should be favored by a factor of at least 20. No peak at 804 keV has been seen, though it is possible that the peak observed at 838 keV contains a small contribution from this decay since these peaks are not fully resolved. While this makes this explanation of the 246 keV state unlikely, it can not be ruled out; it is possible that nuclear structure features ignored in the barrier penetration calculation hinder the decay to the ground state.

The third possibility is probably the most plausible. In this scenario, the 246 keV proton originates in the decay of the state at 7852 keV excitation (the next state known above the IAS) to the ground state of ^{22}Na. The proton emitted would have an energy of 261 keV ±6 keV in the laboratory frame; this energy agrees (within the error bars) with the measured energy. This would simply indicate that the beta decay to this state is allowed, with a log*ft* value of ~5.8.

4.3.4.2 Gamow-Teller Strength

The ^{23}Al beta-decay strength to unbound states in ^{23}Mg may be estimated from the observed proton intensities. The Fermi (phase-space) factor is calculated using the same method outlined by Brown and Wildenthal (Bro85). The partial half-life for the decay of the state at 8453 keV may be calculated from the measured cross section for the 838 keV proton peak from this state (220 nb, Gou72) and the total production cross section of 165 μb, predicted using PACE2. This results in a log*ft* of 4.94, in good agreement with the value estimated by Gough, *et al.*, of 5.0 for this decay. The values for the beta-decay branching ratio, production cross section σ and log*ft* for the other decay groups are determined from their intensities relative to the 838 keV peak. The results are shown in Table 4-5.

Table 4- 5: The beta decay of ^{23}Al to highly excited states of ^{23}Mg. The first two states listed (†) correspond to two possible assignments of the 246 keV proton peak (see the previous subsection).

E* in ^{23}Mg (keV)	σ (nb)	beta decay branch × 10^5	log(f_At)	GT strength $<\sigma\tau>^2 \times 10^4$
7837†	72 ±6	44 ±4	5.82 ±0.04	59 ±5
8420†	72 ±6	44 ±4	5.45 ±0.04	138 ±12
8070	4.6 ±0.7	2.8 ±0.4	6.87 ±0.07	5 ±1
8161	150 ±11	91 ±7	5.31 ±0.03	192 ±14
8285	4.2 ±0.6	2.5 ±0.4	6.78 ±0.07	6 ±1
8456	220	133	4.94	445
8564	9.7 ±0.9	5.9 ±0.5	6.22 ±0.04	23 ±2
8703	2.6 ±0.4	1.6 ±0.3	6.68 ±0.08	8 ±1
8788	7.0 ±0.9	4.3 ±0.5	6.19 ±0.06	25 ±3
8850	4.6 ±0.7	2.8 ±0.4	6.32 ±0.07	18 ±3
8914	5.5 ±0.7	3.3 ±0.4	6.20 ±0.06	25 ±3
9153	4.2 ±0.7	2.5 ±0.4	6.11 ±0.07	30 ±5
9407	4.4 ±0.7	2.7 ±0.4	5.84 ±0.07	56 ±8
9458	2.0 ±0.4	1.2 ±0.3	6.13 ±0.11	29 ±6
9563	1.3 ±0.4	0.8 ±0.3	6.19 ±0.18	25 ±8
9880	0.4 ±0.2	0.3 ±0.1	6.28 ±0.30	21 ±10

Figure 4-13 shows a portion of the Gamow-Teller strength function for ^{23}Mg covering excitation energies accessible in this measurement [as defined by the proton separation energy ($-S_p$ = 7580 keV) and the Q-value for positron emission from ^{23}Al ($Q_{\beta+}$ = 11.218 MeV)]. The top half of the figure shows the strength $<\sigma\tau>^2$ estimated from this work. The lower half shows the strength predicted by Brown (Bro93) using a full-basis *sd*-shell model calculation (see Sections 2.5.2 and 2.5.3); the strength for each state has been convoluted with a Gaussian distribution with a full width at half maximum (FWHM) equal to the experimental value of ~35 keV. It should be noted that the y-axis scale is different for each plot. The position of the ^{23}Al IAS is indicated in each plot, based on the measured (upper plot; Nan81) and predicted (lower plot; Bro93) energies. The dotted curve shown on each graph indicates the strength corresponding to a single count observed at each energy; it is meant to show the

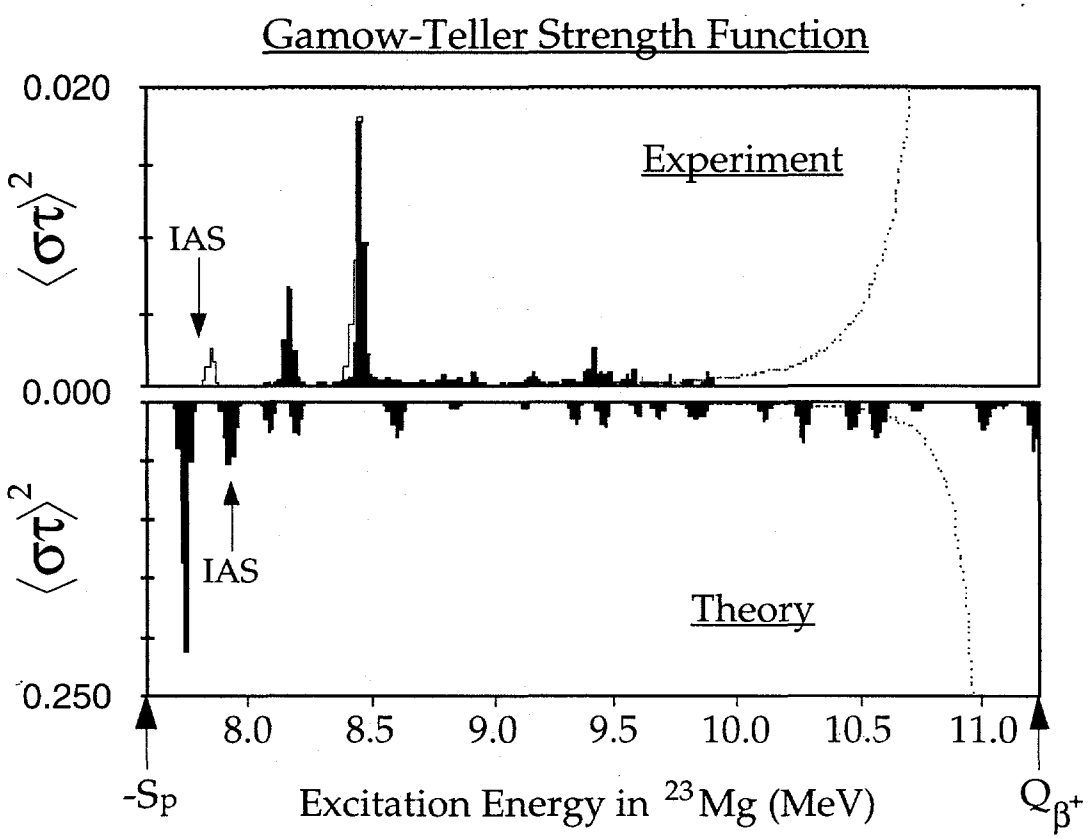

FIG. 4- 13: Gamow-Teller strength function of ^{23}Al. Top, as deduced from experimental proton intensities. Bottom, as calculated by Brown (Bro93) for discrete states, distributed as Gaussian peaks with the experimental resolution (~35 keV FWHM). Note that the strength shown for each peak in Table 4-5 is the *total*, integrated strength for that peak; it has been distributed over several bins in this strength function.

decreasing sensitivity of the experiment to GT strength at high excitation energies[†]. Since the strength corresponding to the 246 keV proton peak may be from either a state near 7840 keV to the ground state of ^{22}Na, or from the ^{23}Mg state at 8420 keV to the first excited state of ^{22}Na at 583 keV, it is indicated at each excitation by the white peaks.

[†] As $Q_{\beta+}$ decreases for increasing excitation, the branching ratios decrease as well due to the influence of the Fermi factor. The predicted strength which lies below the dotted line could not have been observed, since the predicted branching ratio would result in less than one count.

It is clear from this figure that there is much less GT strength in this excitation region than was predicted; the summed GT strength observed is ~1.07, approximately an order of magnitude less than the shell model estimates. No GT quenching factor has been included in either the experimental or theoretical predictions. This result would seem to suggest a serious deficiency in the method of calculating the strength, caused by either the wave functions or the GT operator itself. However, because the GT strength has been calculated relative to the yield of the 835 keV proton peak, and the strength for that peak deduced from an upper limit set on its cross section (Gou72) and the calculated total-production cross section, these results are very sensitive to errors in those numbers. If the branching ratio for this peak were four times larger than estimated, its log*ft* value would be ~4.1, which is reasonable for an allowed decay. The integrated GT strength recalculated using this branching ratio would then be ~60%; this is in line with quenching previously observed in the *sd*-shell (e.g., see Wil73, Bro83, Bor87). Clearly what is needed to resolve the ambiguity is a measurement of the branching ratio of this decay. Such a measurement would be difficult using a He-jet system due to uncertainties in the He-jet transport efficiency.

4.3.4.3 The Absence of the Low-Energy Proton Continuum

As noted previously, in the second low-energy measurements there is no evidence of the proton continuum that was observed in the earlier measurements and was ascribed to the beta-delayed proton decay of ^{24}Al on the basis of the results of lower-energy bombardments and half-life. It is likely that the continuum was actually beta events tailing into the proton gates. Reanalysis of the old data supports this interpretation. If narrow gates are placed on the E spectrum within the continuum and the ΔE spectra of the events within these gates are then examined, it is seen that most of these events have very small signals in the ΔE detectors and are clearly beta particles. The number of events falls off from the low-energy limit smoothly with an exponential function. There is no kink or minimum to indicate the onset of the proton region at higher ΔE signal. The proton gates used to generate the continuum included part of the high-energy tail from the beta region.

During the first ^{23}Al runs and the subsequent low-energy bombardments, large amounts of beta activity were produced. Even if only a very small fraction of all beta particles lose sufficient energy in the gas-ΔE detectors to contaminate the proton gates, this contamination

will be significant if enough activity is produced. The improved beta-event rejection of the telescopes used in the second series of measurements virtually eliminated this problem. The low-energy proton bombardments should be repeated using the new telescope design to confirm this hypothesis.

4.4 Conclusion

We have measured the beta-delayed proton decay of ^{23}Al, in two series of experiments. The first measurements (Tig95) used a new array of low-energy particle-identification telescopes. Four proton peaks were observed, including one assigned to the decay from the IAS of ^{23}Al at 7795 ±6 keV in ^{23}Mg. The intensity of this peak suggested unusually strong isospin mixing, based on a comparison of the deduced spectroscopic factor with the value predicted by Brown using an INC Hamiltonian (Orm88). The experimental intensity also indicated a much larger ^{22}Na(p,γ)^{23}Mg resonance strength ωγ than the limits set by various reaction studies.

Reanalysis of the data taken in the first measurements suggested a possible contamination of the proton spectra by events associated with the beta-delayed alpha decay of ^{20}Na. In particular, ^{16}O-recoils detected in coincidence with the positron feeding the alpha-decaying state at 7421.9 keV (2148 keV α) were found to mimic very low-energy proton events. This prompted the second series of measurements.

The second series of measurements utilized a modified particle-identification telescope design intended to overcome these contamination problems. A proton peak was observed at an energy of 246 ±20 keV with an intensity ~6.8 times less than the 223 ±15 keV peak observed previously. This is the lowest-energy proton decay ever observed. The energy of the 246 keV peak places its assignment as the decay of the IAS in doubt; it is more likely that this peak is from another excited state fed by allowed beta decay. If, however, this peak were from the IAS, the intensity observed is in much better agreement with the predictions of Brown (Bro93). This makes it unlikely that the IAS contains an unusually large component of T=1/2 states due to isospin mixing. The observed intensity is also in approximate accord with the limits set by various measurements of the ^{22}Na(p,γ)^{23}Mg resonance strength; this would indicate that this resonance is not of primary importance in determining the rp-

process pathway. If the 246 keV peak is not from the decay of the IAS, no conclusions can be drawn from this work regarding resonances in this astrophysically-interesting reaction.

In the second series of measurements, several new proton-decay groups from other excited states of ^{23}Mg were also observed for the first time. The energies and beta-feeding to these states have been compared to the predictions of Brown. The portion of the Gamow-

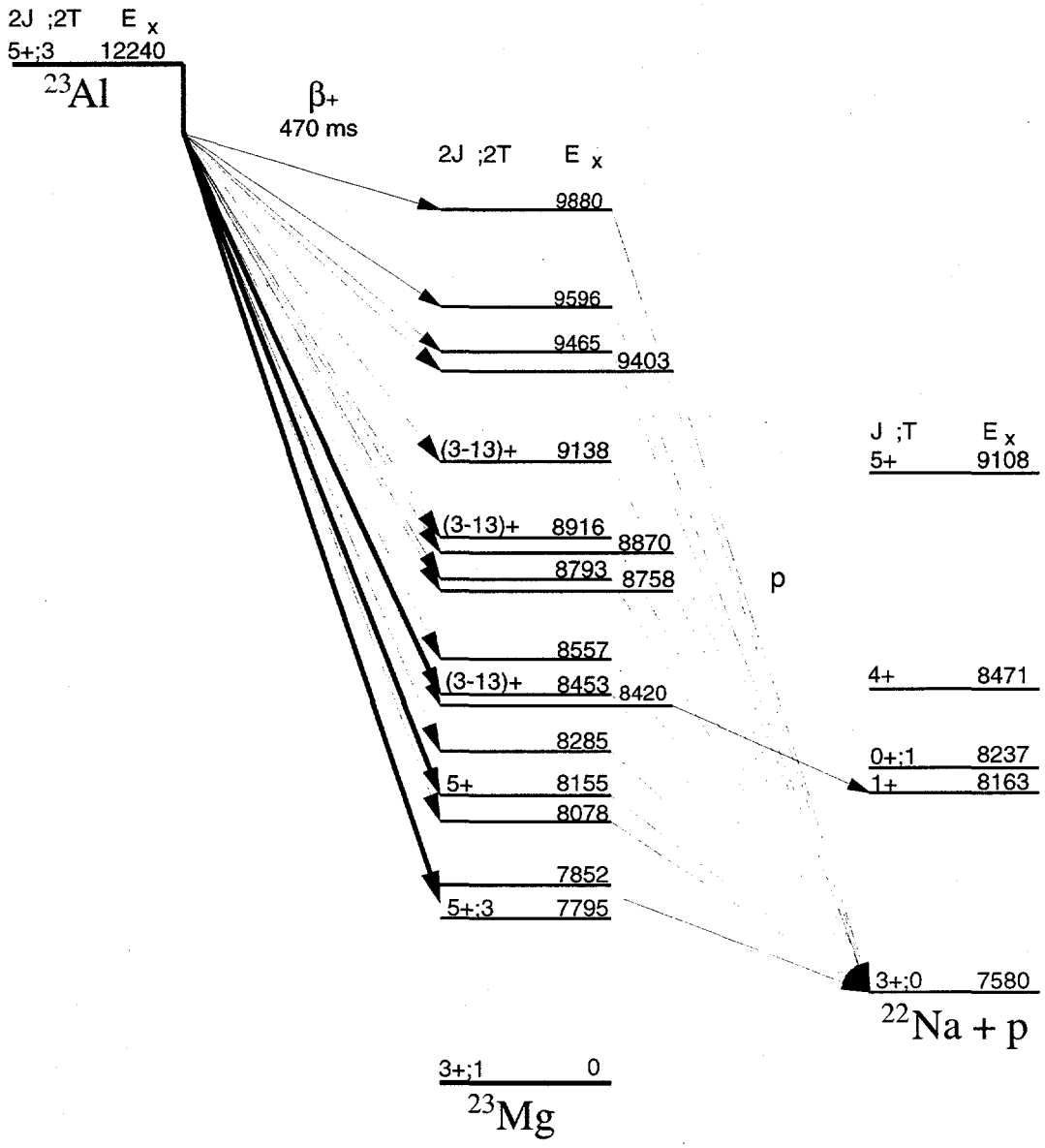

FIG. 4- 14: Revised decay scheme for the beta-delayed proton decay of ^{23}Al. Note that the energy scale has been exagerated in the region of interest for the sake of legibility.

Teller strength function of ^{23}Mg deduced from the measured proton intensities is approximately ten times less than predicted using a full-basis shell model calculation. However, this result is strongly influenced by the magnitude of the beta-decay branch that is assumed for the 835 keV proton peak, since the strength of the other groups was determined relative to this peak. In this region, GT quenching of ~50-80% has generally been observed in previous measurements. A continuum of low-energy events, previously assigned to the beta-delayed proton decay of ^{24}Al (Bat94), was not observed in the later measurements. A revised decay scheme, based on the results of the present work, is shown in Fig. 4-14.

Although the second series of measurements yielded much useful information about the beta-delayed proton decay of ^{23}Al, additional information is needed in order to make conclusive statements regarding the isospin mixing and proton-capture strength of the IAS or the Gamow-Teller strength function. In particular, measurements of the branching ratio for the 835 keV state and the gamma-decay width of the IAS would allow conclusions to be drawn from this work with much greater certainty.

C H A P T E R 5

THE BETA-DELAYED PROTON DECAYS OF ^{23}SI AND ^{22}AL

5.1 Introduction

5.1.1 Motivation

The lightest aluminum isotope, ^{22}Al, has been studied extensively (and nearly exclusively) using beta-delayed proton techniques. These measurements serve as an excellent example of the use of proton-decay spectroscopy to obtain information about very proton-rich nuclides. First discovered in 1982 via its beta-delayed proton-decay branch (Cab82), ^{22}Al was the first odd-odd T_z = -2 nuclide observed. In that experiment the energy of its isobaric analog state (IAS) in ^{22}Mg was determined, which permitted comparison with the value predicted from the Coulomb displacement energy (CDE). Knowledge of the mass of the IAS, along with other known members of the mass 22, T=2 isobaric quintet ^{22}F and ^{22}Ne*, allowed the coefficients of the quadratic form of the isobaric multiplet mass equation (IMME; equation 2-51) to be determined; these were used to estimate the mass of the ground state of ^{22}Al. A rough half-life of 70^{+50}_{-35} ms was also measured.

In later work (Cab83a, Cab84, Jah85), ^{22}Al was shown to also decay by beta-delayed two-proton emission; this was the first example of this decay mode, which had been previously predicted by Gol'danskiĭ (Gol80). Much effort has gone into understanding the mechanism for this decay (see Section 2.4.3). It has been shown (Cab84, Jah85) that the protons are primarily emitted sequentially from ^{22}Al; to date, simultaneous (^{2}He) emission has not been observed from any β-2p emitter. The ^{22}Al decay proceeds to both the ground state

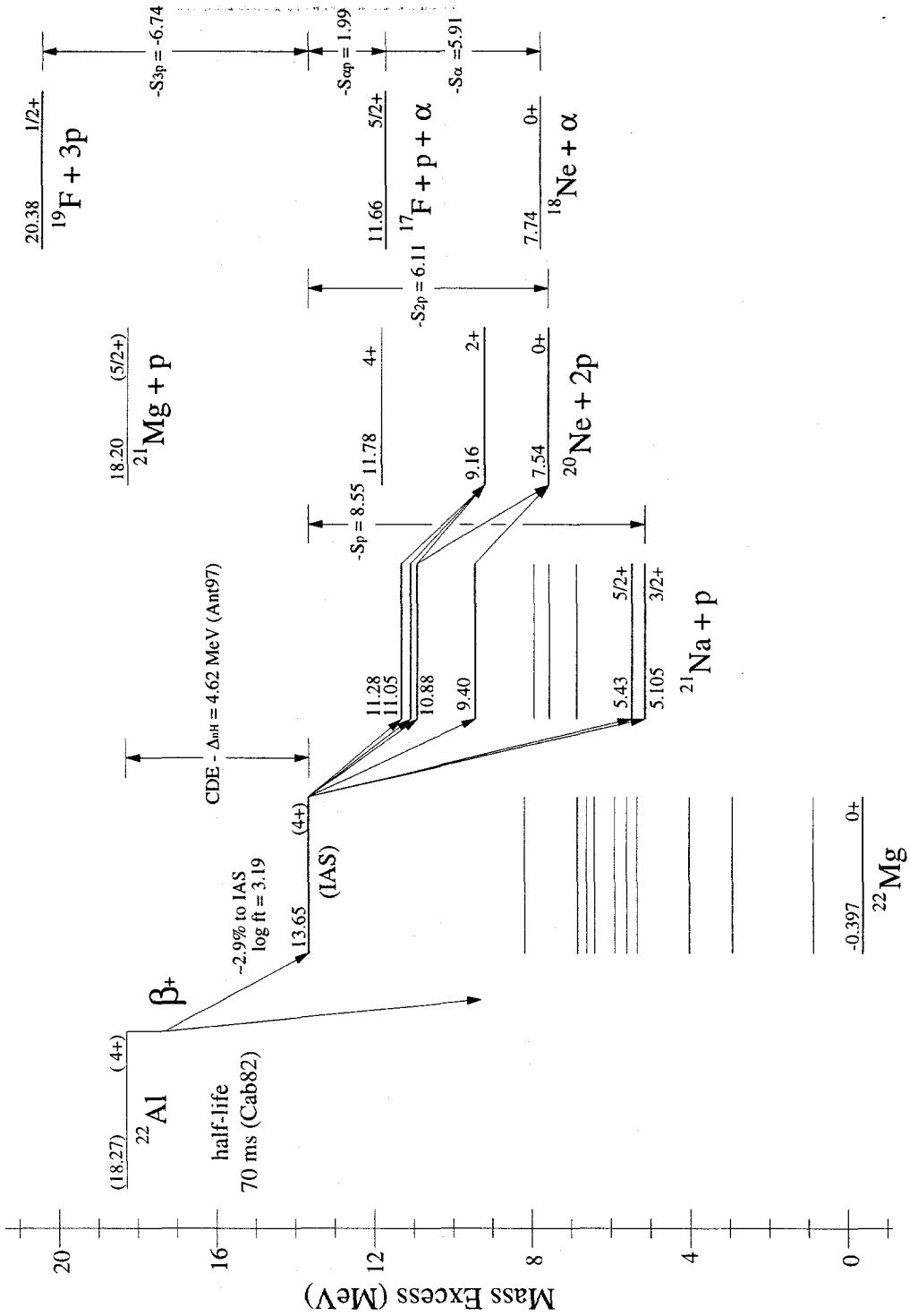

FIG. 5- 1: Decay scheme for ^{22}Al. Based on the measurements in Cab82, Cab83a and Cab84.

and the first-excited state of the second proton daughter, ^{20}Ne, via at least four excited states of the first proton daughter, ^{21}Na. The earlier beta-delayed proton work was important in understanding the beta-delayed two-proton decay, since it allowed the two-proton separation energy to be precisely calculated based on the energy of the IAS. The decay scheme for ^{22}Al is shown in Fig. 5-1.

One would like to extend this approach to the even more neutron-deficient nuclide ^{23}Si. Silicon-23 was observed by Langevin, *et al.*, in 1986 using mass separation of Ni(^{40}Ca,X) projectile fragmentation reactions (Lan86); it is predicted to be the lightest T_Z = -5/2 nuclide to exist (Aud93). No information was obtained pertaining to the mass or decay of ^{23}Si in this measurement.

As discussed in Section 2.5.1, mass is one of the most important nuclear properties, both because it guides the experimentalist and because it serves as a test of nuclear models. As attempts are made to predict the masses of nuclides ever further from stability, mass predictions tend to diverge. Table 5-1 shows predictions of the mass of ^{23}Si generated by a wide range of mass models; the predictions vary over ~2 MeV. A predicted decay scheme for ^{23}Si (using the mass predicted by Wapstra and Audi, Aud95) is shown in Fig. 5-2.

TABLE 5- 1: Mass predictions for ^{23}Si.

Mass Model	Mass Excess (MeV)
Isobaric Multiplet Mass Equation (Pap88)	23.44
Unified Macroscopic-Microscopic Model (Möl88a)	23.86
Finite-Range Droplet Macroscopic Model and Folded Yukawa Single-Particle Potential (Möl88b)	24.39
Modified Ensemble Averaging (Com88)	23.51
Infinite Nuclear Matter Model (Sat88)	25.37
Empirical Model with Proton-Neutron Interaction (Tac88)	23.84
Garvey-Kelson Mass Relations (Jan88)	23.43
Inhomogeneous Partial Difference Equation with Higher-Order Isospin Contributions (Mas88)	23.94
Finite-Range Droplet Macroscopic Model with Folded Yukawa Single-Particle Microscopic Model (Möl95)	23.60
1995 Mass Evaluation Estimate (Aud95)	23.77

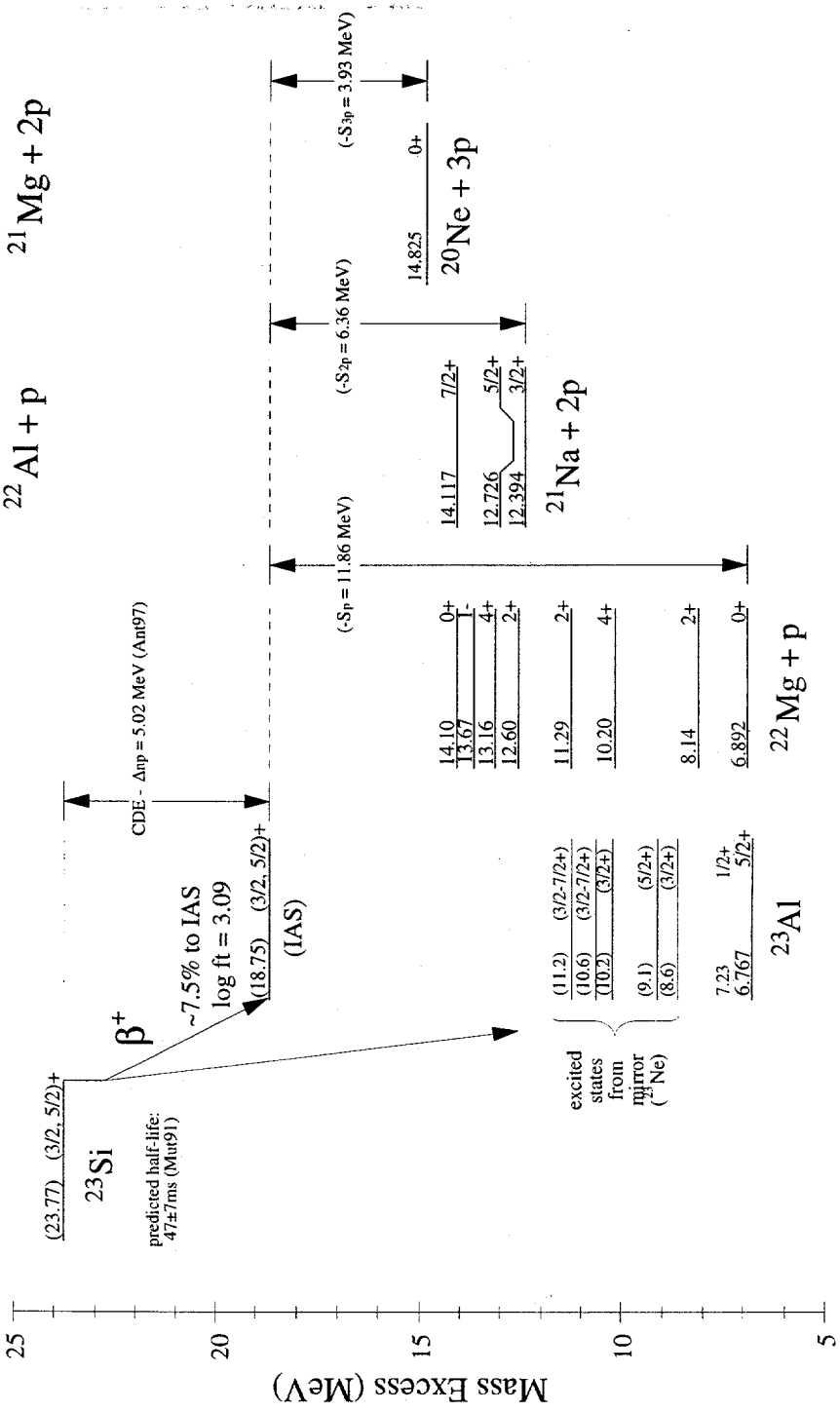

FIG. 5- 2: Predicted decay scheme for ^{23}Si. The mass excess of ^{23}Si is taken from Aud95; the energy of its isobaric analog state is derived from a Coulomb displacement energy calculation.

As discussed in Section 2.4.2, by measuring beta-delayed proton emission through the IAS and calculating the CDE, the mass of ^{23}Si may be accurately estimated. This was the primary goal of this experiment. Because the beta-delayed two-proton emitter ^{22}Al is produced simultaneously with ^{23}Si, its decay was also studied. Brown has predicted that ~14% of the beta-delayed proton decay of ^{22}Al feeds a $9/2^+$ state at 2779 keV excitation in ^{21}Na (Bro90); this presumably corresponds to a 9/2 state that has been measured at an excitation of 2829.4 keV (End90). This state is unbound to proton emission by 398.4 keV. We have also sought to observe this beta-delayed two-proton decay channel where the energy is split very unevenly (~14:1, c.m.) between the two protons.

5.1.2 Experimental considerations

The fusion-evaporation code ALICE (Bla82; also see Section 3.1.2) predicts a maximum ^{23}Si yield of ~450 nb is achieved using the ^{24}Mg(^{3}He,4n)^{23}Si reaction at a laboratory bombardment energy of 105 MeV. Both ^{23}Si and ^{22}Al are produced in this bombardment; the ^{24}Mg(^{3}He,p3n)^{22}Al reaction at 110 MeV has been used previously to produce ^{22}Al (Cab82, Cab83a, Jah85). The reaction thresholds for these reactions, 61.9 and 54.8 MeV, respectively, preclude the possibility of eliminating ^{22}Al by reducing the beam energy below its threshold. The ^{22}Al yield is estimated to be about 15 times greater than the ^{23}Si yield; its presence complicates identification of ^{23}Si decay events.

As shown in Fig. 5-2, the IAS of ^{23}Si is predicted to be unbound to one-, two- and three proton emission. Beta-delayed two-proton decay searches are generally very sensitive, because a proton-proton coincidence requirement will eliminate virtually all background from other species produced simultaneously. However, the two-proton sum energies from the ^{22}Al and ^{23}Si isobaric analog states are 6.11 MeV (calculated from Cab82 results) and ~6.36 MeV (predicted), respectively; the similarity between the beta-delayed two-proton decay energetics will probably not allow a ^{23}Si decay event to be identified on the basis of energy. Unlike ^{22}Al, ^{23}Si can also undergo beta-delayed three-proton emission, making this a possible signature of ^{23}Si decay. Unfortunately, the coincidence requirement using ~4% of 4π sr. detectors (as in the array shown in Fig. 4-3) for the three proton branch decreases the detection efficiency too much to make such a search practical given the low yield of ^{23}Si and low 3p-branching ratio expected.

However, the large center-of-mass proton energy of ~11.7 MeV available for the beta-delayed proton branch from the ^{23}Si IAS prevents interference from ^{22}Al, since delayed protons from the ^{22}Al IAS have a maximum center-of-mass energy of 8.55 MeV. Proton decays from states near or above the ^{22}Al IAS energy are unlikely to be observed given the much-smaller beta-decay branch expected to any such states. Other proton emitters such as ^{25}Si (Rob93) and ^{21}Mg (Sex73a) produced simultaneously (see below) also have less energy available for beta-delayed proton emission.

Aside from the smaller production cross section for ^{23}Si, Muto *et al.* (Mut91) predict a ^{23}Si half-life of only 47±7 ms, which is a bit shorter than the measured ^{22}Al half-life of 70^{+50}_{-35} ms (Cab82). However, the smaller yield due to these factors is somewhat offset by two other factors which may be expected to increase the branching ratio for single proton decay through the ^{23}Si IAS. Based on the decay energy from the calculated CDE and an assumed log*ft* of 3.09 for this superallowed decay, ~7.5% of the decay of ^{23}Si is expected to proceed through its IAS, compared to only ~2.9% for the ^{22}Al superallowed decay. Furthermore, Détraz (Dét91) calculates a (ß-2p)/(ß-p) ratio for the decay of ^{22}Al of 5; this falls within the range of 1.9 to 5.5 observed experimentally (Cab84). For the decay of ^{23}Si, Détraz calculates this ratio to be 1. Combined, these factors suggest that ^{23}Si beta-delayed protons should be observed at roughly 70% of the level that ^{22}Al beta-delayed protons have been seen in the past. Based on this estimate, ^{23}Si beta-delayed protons would likely have been detected during the 110 MeV ^{3}He^{2+} on ^{24}Mg bombardment in which ^{22}Al beta-delayed proton emission was first observed (Cab82). These numbers must thus be overly optimistic to some degree. However, the chances for successful observation of ^{23}Si decay may be increased (relative to the Cab82 measurement) by reducing the number of "background" events, minimizing the transport time, and collecting more statistics than in the earlier work (Cab82).

Calibration of the detector telescopes is complicated by the paucity of known beta-delayed proton emitters which emit high-energy protons. The beta-delayed proton emitters ^{21}Mg (Sex73a, Zho85) and ^{25}Si (Rob93, Zho85) are produced concurrently with ^{23}Si; these provide calibration peaks at 6.227 (^{21}Mg), 6.520 (^{25}Si+^{21}Mg), 6.720 (^{25}Si) and 6.855 MeV (^{25}Si), as well as many other peaks below 6 MeV. The two known beta-delayed proton groups of ^{22}Al provide points at 7.839 and 8.149 MeV (Cab82). Although ^{17}Ne has a 9.957 MeV beta-delayed

proton group (Bor88), He-jet systems employing aerosols do not transport gaseous elements effectively. While ^{25}Si and ^{21}Mg decays permit continuous, *in situ* calibration of the detector telescopes, these decays also interfere with the observation of low-energy beta-delayed proton emission from either ^{22}Al or ^{23}Si.

5.2 Experiment

5.2.1 Production

Silicon-23 was produced via a 110 MeV $^{3}He^{2+}$ bombardment of a single 1.34 mg/cm^2 ^{24}Mg separated-isotope target. The beam was pulsed to eliminate possible neutron-induced events in the detector telescopes; a 60 ms beam-on cycle was followed by a 55 ms beam-off cycle during which activity was counted. The on-target beam current was ~4.9 eμA (~2.6 eμA time-averaged). Reaction products were thermalized in ~1.3 atm He and transported via He-jet from the target to a detector box, where they were deposited onto the rim of a slowly-rotating activity-catcher wheel. Because it was crucial that the transport time be minimized, the single-capillary configuration of the He-jet system was used (see Section 3.1.3) with a 1.35 mm i.d. × 75 cm long capillary. The measured transport time for this configuration was ~ 20 ms.

5.2.2 Detection

Charged particle spectra were taken using particle-identification telescopes capable of measuring protons with energies from ~0.35 to ~14 MeV. This wide range was necessary in order to observe both beta-delayed protons from the IAS of ^{23}Si (predicted laboratory energy ~11.3 MeV) and to search for a beta-delayed two-proton decay branch of ^{22}Al in which one of the protons was emitted with an energy of 380 keV. The particle-identification telescopes used in this measurement were very similar to those shown in Fig. 4-9. To reduce the chance of events due to protons "knocked out" of the entrance window by alpha particles or neutrons, the standard polypropylene [$(CH_2)_n$] window was replaced with a 469 μg/cm^2 Al foil. The two ΔE-signal grids were wired together to create a single gas proportional counter in order to increase sensitivity to high-energy proton events. Each telescope had two 450 mm circular Si detectors. A 300 μm detector was used as an E detector for alpha and low-energy (< 6 MeV) proton events and also served as a second ΔE detector for high-energy proton events; this was

located where the Si E detector is in Fig. 4-9. Behind this, the second, ~1000 μm, Si detector allowed proton decays of up to 14 MeV to be measured. Two of these telescopes were placed above and below the collection point on the activity-catcher wheel in a configuration similar to that shown in Fig. 4-10. The solid angle subtended by each telescope was ~5% of 4π sr.; the average relative-emission angle for events observed in coincidence between the two telescopes was 117°.

5.2.3 Counting Electronics

To take full advantage of this telescope configuration, events were recorded if they met either of two coincidence criteria. As usual, low energy events were recorded if they had coincident signals in the gas-ΔE detector and the 300 μm Si detector of one of the telescopes. Alternatively, a coincident signal in both Si detectors of a single telescope would also trigger an event to be read; this prevented a loss of efficiency for high-energy proton events, that produce very weak signals in the gas-ΔE detectors. To prevent an unnecessarily large number of beta-decay events from being recorded, the discriminator threshold of the 300 μm Si detectors was set above 1 MeV for this second coincidence criterion. Unfortunately, this threshold was set too high for one of the telescopes; thus only one of the telescopes was sensitive to proton events above 8 MeV.

In order to allow random coincidences between Si detectors to be separated from true coincidences, fast timing data were taken between the two Si detectors in each telescope (for high-energy single-proton events) and between the 300 μm Si detectors of the two telescopes (for two-proton or proton-alpha events). Timing data were also collected relative to the start of the beam-off cycle to permit measurement of half-lives.

Occasional bursts of bipolar noise, presumably due to radio-frequency pickup in the cabling or the gas-detector grids, were observed in amplifier signals, generally from several detectors simultaneously. Since real particles produce a unipolar signal from these amplifiers, a bipolar noise "marker" was set up in hardware to label any events that were in coincidence with a negative signal in any of the detectors. Gating on this marker signal permitted any events detected in coincidence with this noise to be removed from the data set in software.

5.3 Results

5.3.1 Beta-Delayed Proton Emission

Figure 5-3 shows a proton spectrum for events with less than ~6 MeV that were detected in the gas-ΔE and 300 μm Si E detector of either telescope. The peaks in the spectrum can be attributed to the decays of ^{25}Si or ^{21}Mg. Based on the calibrations established from these peaks, the low-energy threshold of each of the telescopes was ~350 keV. The calibration procedure incorporated energy losses in inactive detector components as described in Section 3.3.2; the rms error in the fit of the calibration peaks was ~5 keV for each telescope.

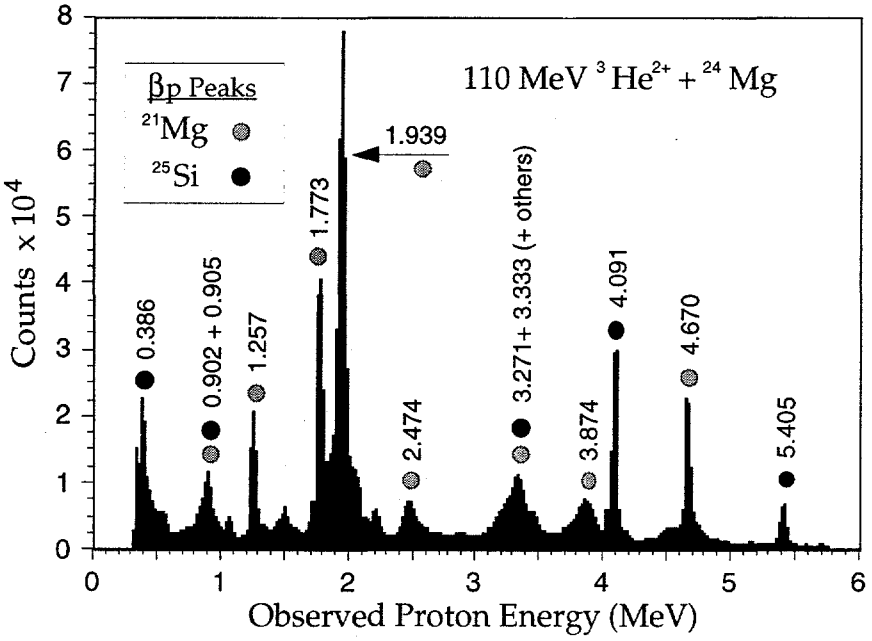

FIG. 5- 3: Beta-delayed proton spectrum, E < ~6 MeV. These protons were stopped in the first Si detector. Peaks from ^{25}Si and ^{21}Mg beta-delayed proton decays, used for calibration, are indicated.

Figure 5-4 shows a spectrum from one telescope of protons with energies from 6-8 MeV; these are events that were not stopped in the 300 μm Si detector. (As stated previously, the other telescope was insensitive to high-energy proton events.) To produce this spectrum, events were required to have a valid TAC signal between the 300 and 1000 μm Si detectors and a valid particle-identification signal (see equation 3-4) after calibration. Furthermore, it was required that their gas-ΔE signal be small (i.e., not as large as an alpha-particle ΔE signal) and that they were not detected in coincidence with the bipolar noise. Two prominent

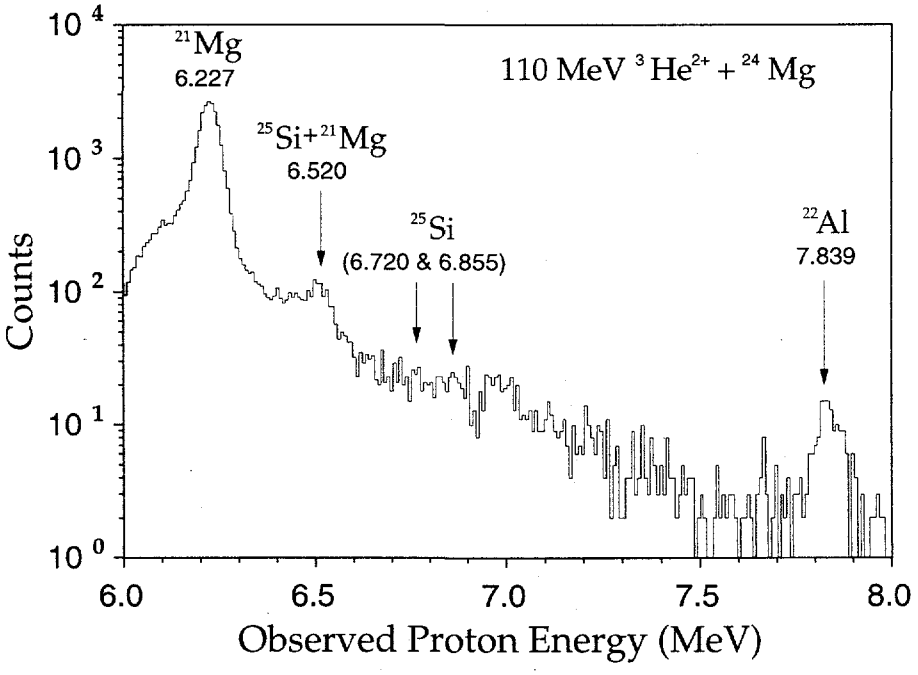

FIG. 5- 4: Proton spectrum, 6 MeV < E < 8 MeV. The peaks at 6.227 and 7.839 MeV were used for calibration. The expected energies of other weak proton groups are also indicated.

peaks are observed in this spectrum at 6.227 and 7.839 MeV due to the decays of ^{21}Mg and ^{22}Al, respectively. A two-point calibration was performed using these peaks; calculated energy losses in the window, gas and dead layers of the Si detectors were accounted for. Of the other high-energy ^{25}Si and ^{21}Mg peaks cited in Section 5.1.2, only the proton group at 6.520 MeV is evident. Underlying the low-energy part of this spectrum is a continuum of events. The detector telescope configuration used makes it very difficult to eliminate contamination of the proton spectrum at these energies by positrons detected in coincidence with medium-energy

beta-delayed protons (~3-6 MeV) from the same decay. Fortunately, this contamination extends to only about 7.5 MeV.

Figure 5-5 shows proton events from the same telescope with energies from 7.5-12.0 MeV; this spectrum was generated using the same criteria as the previous spectrum (Fig. 5-4). The gray line is the result of applying a Gaussian smoothing procedure to the data; each count is distributed as a Gaussian with the experimental resolution (70 keV FWHM) of the telescope. A scattering of events is seen in this spectrum above the two known groups from the beta-delayed proton decay of ^{22}Al at 7839 and 8130 ±37 keV. Several other possible peaks are labeled with their energies (in the laboratory frame). The peak at 7673 ±33 keV is also seen in Fig. 5-4 just below the ^{22}Al 7839 ±15 keV group.

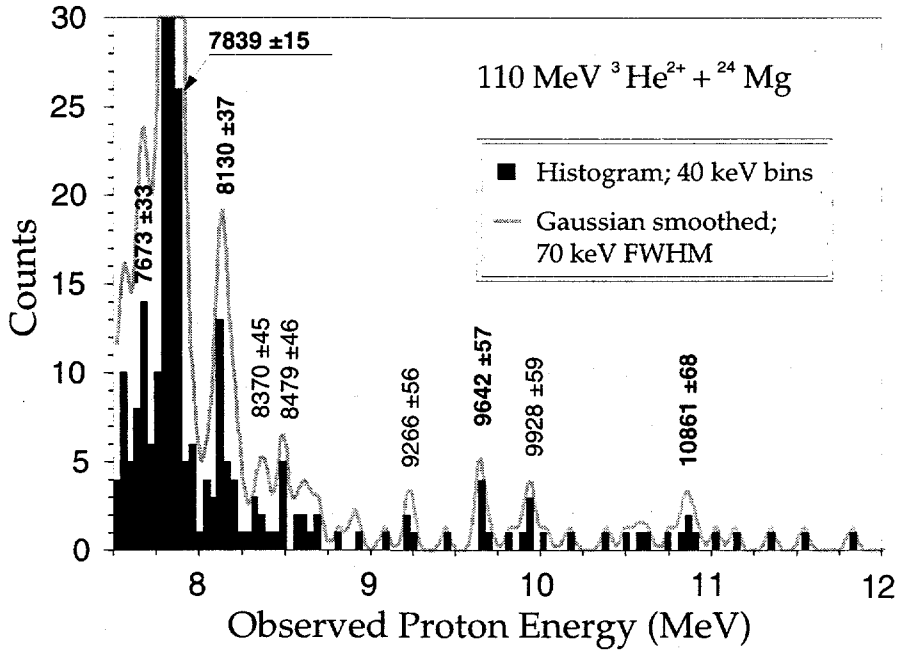

FIG. 5- 5: Proton spectrum, 7.5 MeV < E < 12.0 MeV. The gray line indicates the results of a Gaussian smoothing operation applied to the data. The known beta-delayed proton peaks of ^{22}Al are indicated, as well as other potential new peaks.

5.3.2 Beta-Delayed Two-Proton Emission

Figure 5-6 shows the spectrum of two-proton events observed in this bombardment, where the observed energies of the individual protons have been converted to the center-of-

mass frame (using equation 2-54) and summed. The energy of each proton was calculated from the calibration of each telescope separately prior to summing. The black line shows the results of applying a Gaussian smoothing procedure to the data with the combined resolution of the two detector telescopes (120 keV FWHM). To produce this spectrum, both protons were required to meet the criteria used to generate the single-proton spectrum shown in Fig. 5-3; additionally, a valid TAC signal was required between the 300 μm Si detectors of the two telescopes. The two most prominent peaks in the spectrum have energies of 4490 ±15 and 6113 ±15 keV. These agree with the two-proton decay energies from the ^{22}Al IAS to the first-excited and ground state of ^{20}Ne of 4478 ±15 and 6111 ±15 keV, respectively, based on previous measurements of the excitation of the IAS (Cab82, Cab84). The decays of ^{22}Al to the second- and third-excited states of ^{20}Ne, with expected energies of 1686 ±15 and 1145 ±15 keV, respectively, are not observed. Many other counts, in some cases grouped in such a way as to suggest peaks, are observed at 2p-sum energies from ~0.9 to ~7.3 MeV.

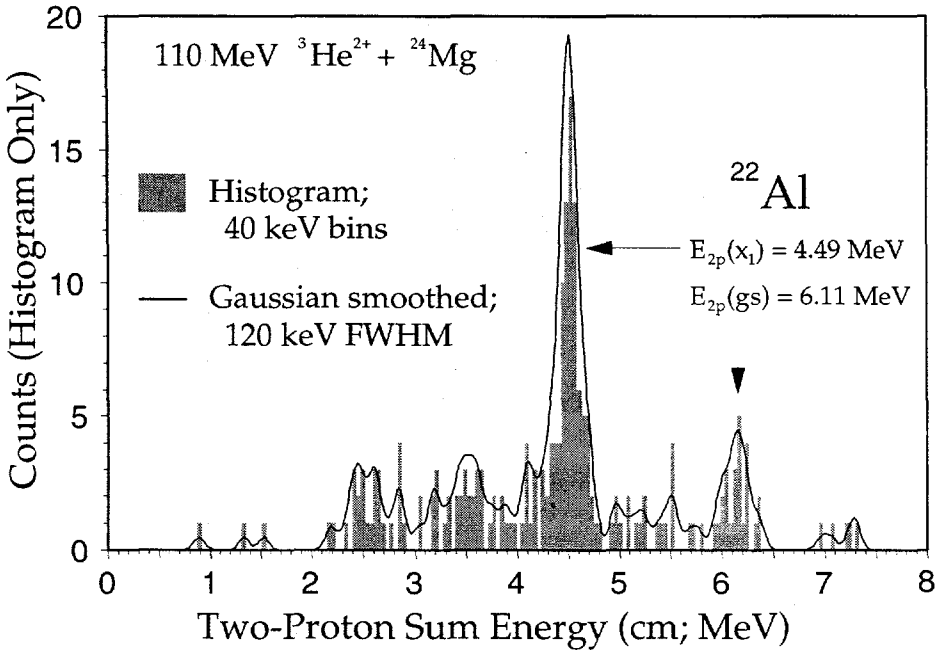

FIG. 5- 6: Two-proton sum spectrum. Energies are given in the center of mass frame. See text. The known groups of the beta-delayed two-proton emitter ^{22}Al are indicated.

The spectra of individual proton energies, in the laboratory frame, for the beta-delayed two-proton decays of ^{22}Al to the ground and first-excited states of ^{20}Ne are shown in Figures 5-7 and 5-8, respectively. Note that for each two-proton decay event, two counts are shown in the appropriate spectrum. In each case, the results of a Gaussian smoothing operation, indicated by the heavy black line, have again been applied to the data. Both spectra are very similar to the spectra of these decays presented by Cable, *et al.*, (Cab84) at "wide" relative-emission angles (=120°, vs. 117° for the present work). This is particularly true of the spectrum shown in Fig. 5-8. The differences observed between Cable's spectra and these are probably due to statistics. In Fig. 5-7, the most asymmetric split in the 2p-decay energy observed is < 5:1; the very asymmetric two-proton decay predicted by Brown (Bro90) is not observed.

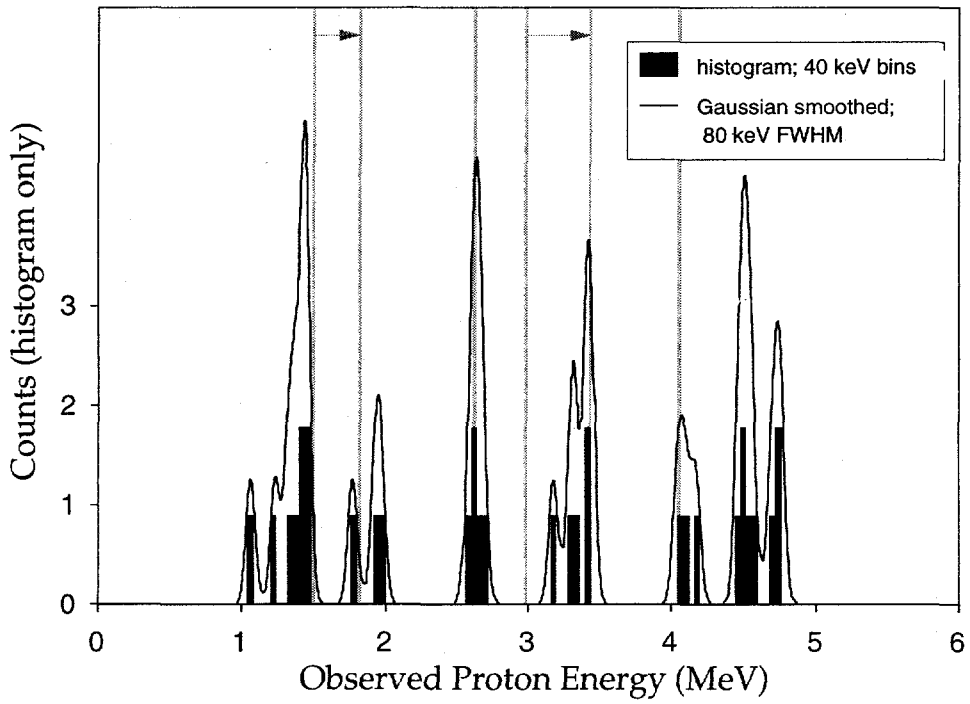

FIG. 5- 7: Spectrum of individual protons for the 6.11 MeV two-proton sum peak shown in Fig. 5-6. The heavy black line indicates the results of Gaussian smoothing of the data. The vertical lines indicate the energies of peaks observed in previous measurements. The arrows indicate the shift in the energy of the second proton emitted in each decay when the protons are observed at 120° instead of 45° relative emission angle. See text.

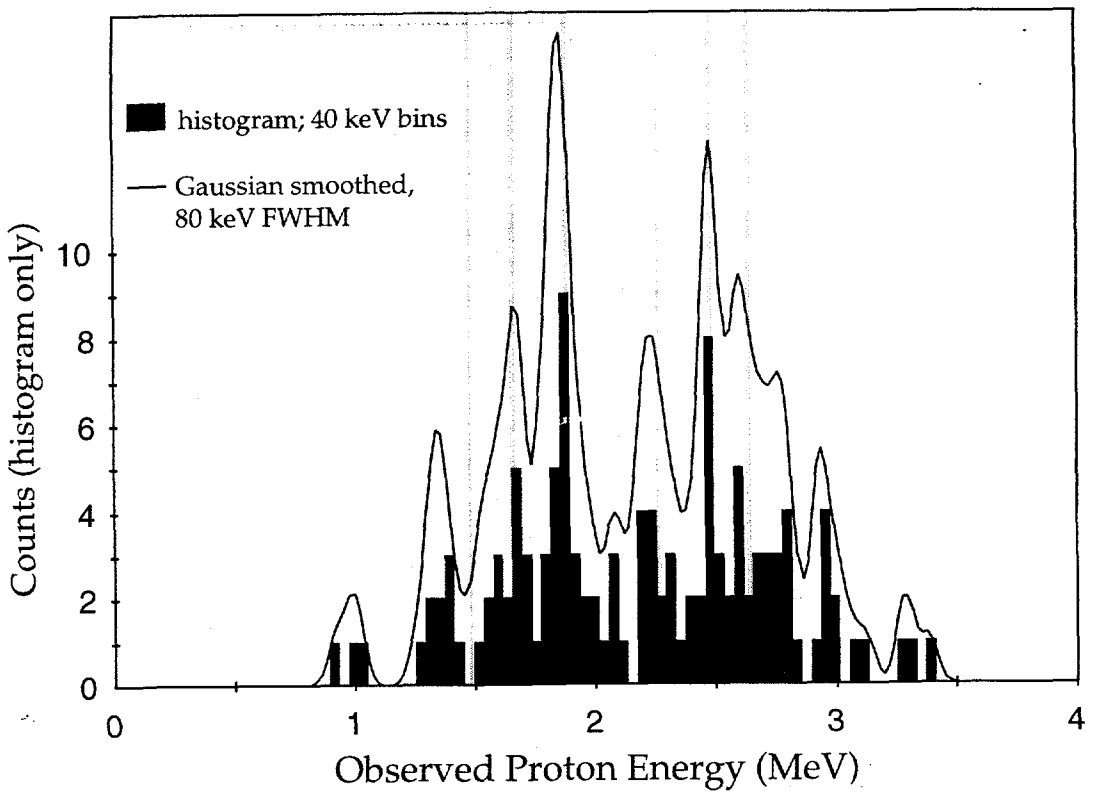

FIG. 5- 8: Spectrum of individual protons for the 4.48 MeV two-proton sum peak shown in Fig. 5-6. The heavy black line indicates the results of Gaussian smoothing of the data. The vertical lines indicate the energies of peaks observed in previous measurements at narrow angles. See text.

5.4 Discussion

5.4.1 The Decay of ^{22}Al

As noted above, the results of our measurements of the decay of ^{22}Al are in good agreement with previous measurements. The beta-delayed proton decays to the ground and first-excited states of ^{21}Na have been observed; the energy of the former agrees within error bars with the original measurement (Cab82). The energy of the latter decay was used as a calibration point and thus can not be compared. Similar agreement with earlier measurements has been obtained for the decay energies of the beta-delayed two-proton branches (Cab82, Cab83a, Cab84).

A goal of this experiment was to observe the beta-delayed two-proton decay branches with better resolution than had been observed in the past at wide (~120°) angles (Cab84). At narrow angles (45°), Cable, *et al.*, observed a number of well-resolved peaks in the single-proton spectra for the two-proton decays to the ground and first-excited state of ^{20}Ne. Assuming that the two protons are emitted sequentially through a discrete intermediate state (see Fig. 2-7, Section 2.4.3), kinematics calculations predict that the energy of the peak from the first proton emitted would not change with relative-emission angle, whereas the peak from the second proton would shift to higher energies in the laboratory frame for wider angles. Although this behavior was observed by Cable, *et al.*, for the decay branch to the ^{20}Ne ground state (Cab84), they were unable to resolve the individual proton peaks of the decay to the first-excited state at wide angles.

In Figures 5-7 and 5-8, the gray, vertical lines indicate the energies of peaks measured in the work of Cable, *et al.* In Fig. 5-7, the positions of the peaks are indicated for both the narrow- and wide-angle data; the arrows denote the shift in the energy of the peak assigned to emission of the second proton (from each of the two different intermediate states) as the relative emission angle was increased from 45° to 120°. There is a peak in the current data for each of the peaks observed at wide angles previously. There also appears to be a peak due to a transition through a third intermediate state which was not observed previously; because the energy difference between the protons for this third transition is greater, it was probably not observed due to the relatively high energy thresholds of the telescopes used in those measurements.

In Fig. 5-8, the vertical lines indicate the positions of the peaks for a 45° relative-emission angle. There is a peak in the new, wide-angle spectrum associated with each of these lines except for the lowest at 1.48 MeV; this would seem to indicate that the complimentary peak at ~2.64 MeV is from the first proton emitted for that decay branch, since its energy did not shift. The peak formerly at 1.48 MeV is calculated to shift to 1.72 MeV for 120° relative emission. Further deconvolution of this spectrum is made difficult by the apparent presence of additional transitions not measured in the earlier work at narrow angles.

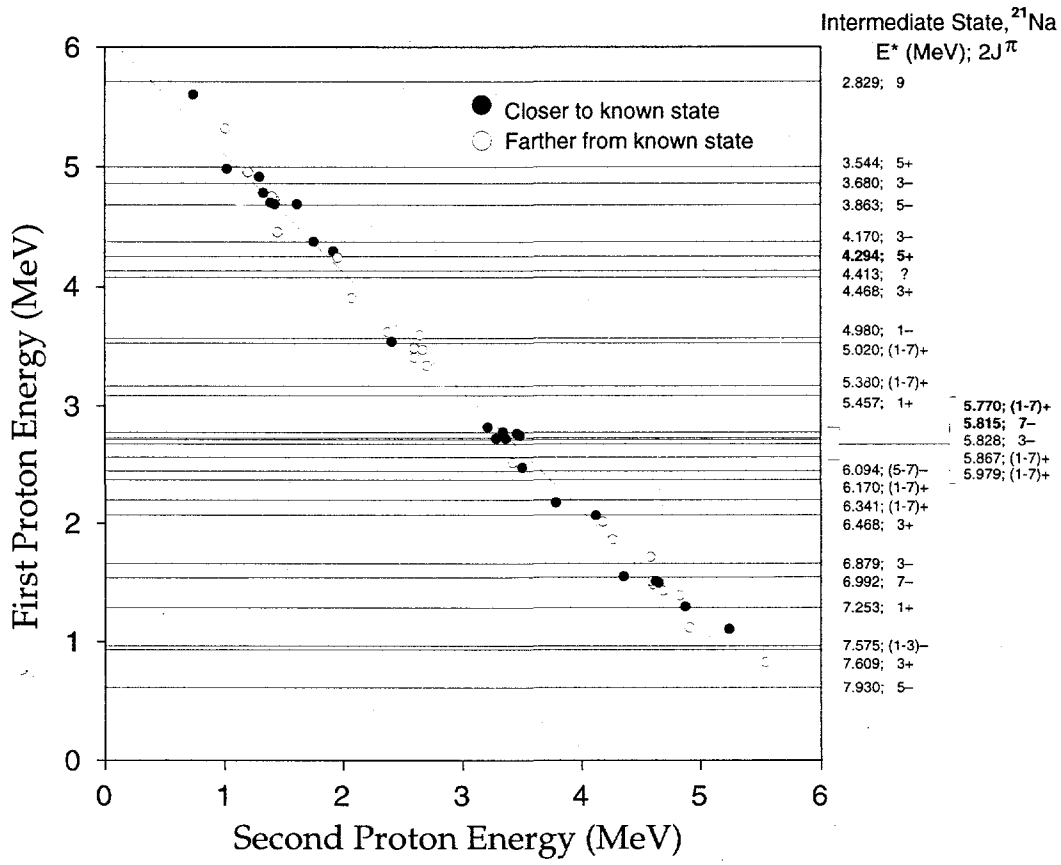

FIG. 5- 9: Proton-proton correlation plot for the 6.11 MeV two-proton sum peak shown in Fig. 5-6. For each event, two points are plotted since it is not known whether the high or low energy proton was emitted first. The horizontal lines indicate possible intermediate states in the one-proton daughter. See text.

Figures 5-9 and 5-10 are proton-proton correlation plots for the beta-delayed proton transitions to the ground and first-excited states of ^{20}Ne, respectively. Since it was not known which of the two protons in each event was emitted first, the proton energies were converted to the center-of-mass frame for each possibility; thus the points plotted in the upper left of each plot were calculated assuming that the higher-energy proton was emitted first, whereas the opposite was assumed for those points plotted in the lower right half of the charts. Since the two-proton decay energy for each of these final states is known, it is possible to calculate energies expected for emission of the first proton for a transition to a given intermediate state. This has been done for possible intermediate states in ^{21}Na that are known (End90). The

corresponding energies are indicated by the horizontal lines; to the right of each figure the excitation energies, spins and parities (where known) of these states are listed. The states denoted in bold type are states to which transitions were assigned previously (Cab84). Whichever of the two calculated points for each event gave better agreement with a known intermediate state is plotted as a black dot; the complimentary points are white. In Fig. 5-9, the diameter of the points has been chosen to match the experimental resolution; in Fig. 5-10, the resolution is indicated by an error bar. The diagonal line corresponds to the average two-proton sum energy of the points, 4.48 and 6.11 MeV, in Figs. 5-9 and 5-10, respectively.

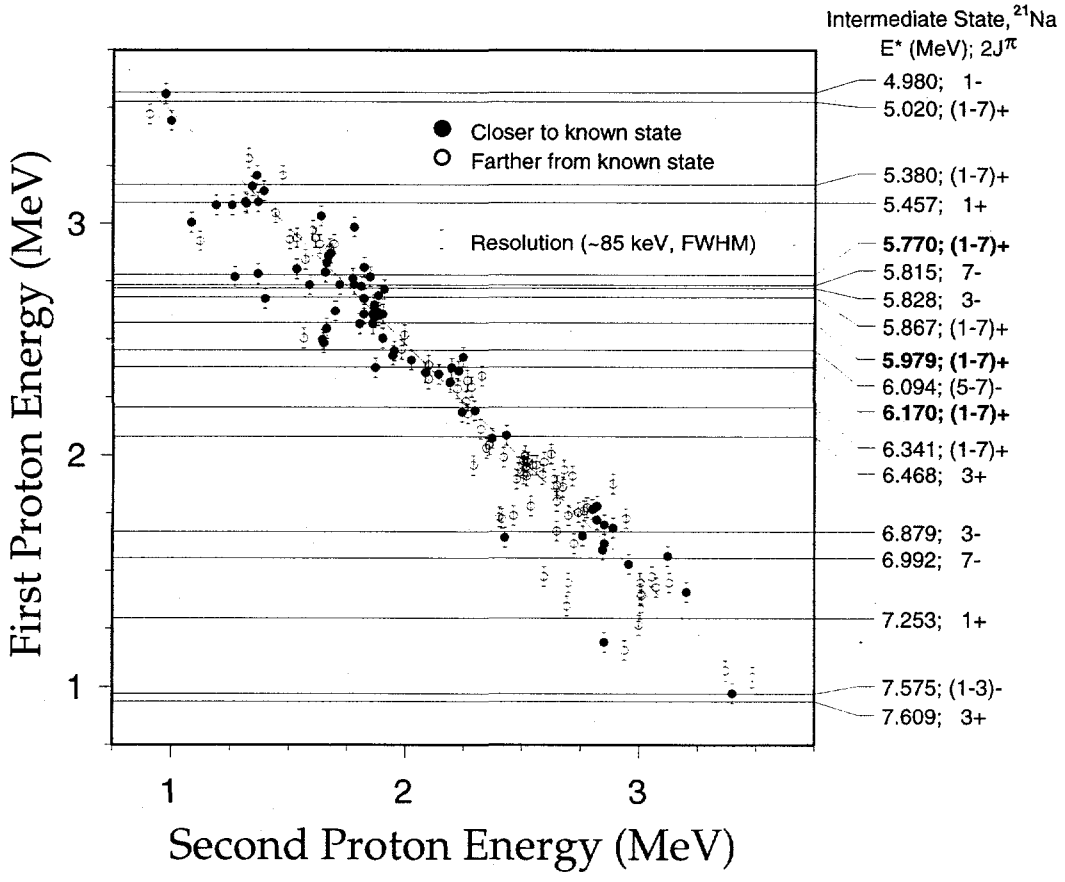

FIG. 5- 10: Proton-proton correlation plot for the 4.48 MeV two-proton sum peak shown in Fig. 5-6. For each event, two points are plotted since it is not known whether the high or low energy proton was emitted first. The horizontal lines indicate possible intermediate states in the one-proton daughter. See text.

All the black points in these plots should agree with some state. In many cases, especially in Fig. 5-10, the agreement is rather poor. This is unexpected given the accuracy of the calibration as demonstrated by the relatively small errors in the fits to the calibration points. It is possible that other unknown states exist in this energy range. In some regions, the density of states is such that a given data point is in agreement with two or more states. It is not clear from these plots that the observed decays can be assigned to specific intermediate states. This may indicate that another decay mechanism besides sequential emission is occurring at least some of the time. Pre-equilibrium emission is the most likely candidate (see Section 2.4.3), since diproton decay with this Q_{2p} value will emit the protons only at smaller relative-emission angles (see equation 2-57) than were measured in this experiment. Alternatively, the ^{22}Al two-proton sum peaks may contain some ^{23}Si beta-delayed two-proton events. This is particularly likely in the case of the 6.11 MeV sum peak, since this energy is close to the predicted β-2p energy for ^{23}Si.

As stated above, the 6.11 MeV beta-delayed two-proton decay though the ^{21}Na intermediate state at 2.829 MeV, predicted to have a large branching ratio by Brown, was not observed. The measured proton thresholds of the telescopes of ~350 keV should have been sufficiently low to permit detection. However, the second, low-energy proton would produce a very small signal in the 300 μm Si detector after passing through the window, gas and Si dead layer; such low-energy protons might not produce a valid TAC signal and thus be gated out of the data set. Alternatively, either the decay strength to the state may be significantly less than predicted, or it may decay primarily by gamma de-excitation.

The results of the present study may be compared to those of a recent measurement by Blank, *et al.*, (Bla97) at the LISE3 facility of GANIL (Mue91). Reaction products were embedded into Si detectors where their decays could be observed either in these detectors or in a micro-strip anode gas counter (Bla93). In this experiment, a beta-delayed alpha decay branch was measured for the first time. The LISE3 spectrometer allows the identification of nuclides to be made on an event by event basis; this allowed the beta-delayed proton spectrum of ^{22}Al to be measured down to much lower energies than had been done previously. An improved half-life of 59 ±3 ms was also determined. The 4.48 MeV beta-delayed two-proton decay branch was measured in this experiment, but the spectra obtained are not discussed in

any detail. A branching ratio of 0.9 ±0.5% for two-proton emission from the IAS to the first-excited state of ^{20}Ne is also calculated. The authors present arguments that the ground state of ^{22}Al might have a spin and parity of 3^+ rather than 4^+ as previously assumed. If the spin and parity of the IAS were also 3^+, than diproton emission would be forbidden to the three-lowest states of ^{20}Ne ($J^\pi = 0^+$, 2^+ and 4^+, respectively) due to conservation of angular momentum and parity ($J^\pi = 0^+$ for ^{2}He).

5.4.2 The Decay of ^{23}Si

Three of the high energy "peaks" shown in Fig. 5-5 have energies of 7673 ±33, 9642 ±57 and 10861 ±68 keV; these would correspond to center-of-mass decay energies of 8022 ±35, 10080 ±60 and 11355 ±71 keV if attributed to the decay of ^{23}Si. The 11355 keV decay is in reasonable agreement with expectations for beta-delayed proton emission from the ^{23}Si IAS to the ground state of ^{22}Mg based on the predictions listed in Table 5-1. Furthermore, the energy spacings between this peak and the other two peaks (1275 ±93 and 3333 ±79 keV in the center of mass, respectively) agree with the excitation energies of the first two excited states of ^{22}Mg (1246.3 and 3308.2 keV, respectively). These peaks are tentatively assigned to the beta-delayed proton decay of ^{23}Si based on this agreement, though it is clear that this result must be confirmed due to the poor statistics (and significant "background") observed at these energies.

The average Q-value for beta-delayed proton emission from the IAS of ^{23}Si is 11.34 ±0.03 MeV based on the energies (and uncertainties) of these three peaks. This would place the IAS at an excitation of 11.47 ±0.03 MeV in ^{23}Al, corresponding to a mass excess of 18.23 ±0.04 MeV. From this result, the expected Q-value for beta-delayed two-proton decay of the ^{23}Si IAS to the ground state of ^{21}Na is 5.84 ±0.03 MeV. Using a calculated Coulomb displacement energy (CDE) of 5.797 MeV (from the global fit shown in Fig. 1 of Ant97) and the neutron-proton mass difference, the estimated mass excess of ^{23}Si is 23.25 ±0.05 MeV.

In another recent measurement, Blank, *et al.*, (Bla97) have measured the decay of ^{23}Si, again using the LISE3 spectrometer and the same detection system as in the ^{22}Al measurement. In this experiment, beta-delayed proton decays were observed with (c.m.) energies from 0.60 ±0.06 to 11.62± 0.10 MeV; the latter peak was attributed to the decay of the IAS. The statistics for the high-energy peaks are very low (i.e., comparable to those observed in the

present study). However, two peaks at 6.18 ±0.10 and 5.86 ±0.10 MeV are also observed which are attributed to the decay of the IAS by beta-delayed two-proton emission, detected in a single detector. The energy difference between these peaks is in very good agreement with the excitation of the first-excited state of ^{21}Na at 0.3319 MeV and the former energy is consistent with both the energy of the IAS from their beta-delayed proton measurement and with expectations based on the predictions listed in Table 5-1. From the excitation of the IAS, the CDE and the neutron-proton mass difference, a mass excess of 23.42 ±0.10 MeV is estimated for the ground state of ^{23}Si.

In addition to these results, the half-life of ^{23}Si was measured to be 42.3 ±0.4 ms. This is very similar to the measured ^{22}Al half-life of 59 ±3 ms, making it virtually impossible to differentiate the decays of these nuclides on the basis of half-life, as had hoped might be done in future He-jet measurements. Relatively low-resolution beta-delayed two-proton spectra are presented for the decays to the ground and first-excited states of ^{21}Na, though no details are presented regarding intermediate states in these decays.

In Fig. 5-6, many beta-delayed two-proton events are observed which can not be attributed to the decay of the IAS of ^{22}Al. It is interesting to compare the other "peaks" in this spectrum with the energy predictions (and measurements) for decay from the ^{23}Si IAS. Figure 5-11 shows this spectrum again, with a grid overlaid that allows this comparison to be made visually. On the left side of the grid are labels for various mass predictions (taken from Table 5-1), and the results of Blank, *et al.* (Bla97), and the present study. On the right of the grid the Q(2p) values are shown, calculated from either the measured value of the IAS, or estimated by subtracting the CDE and proton-neutron mass difference from the ^{23}Si mass excess predictions. The diagonal line next to the Q(2p) values corresponds to these energies for the decay to the ground state. Each of the other diagonal lines corresponds to a measured excited state of ^{21}Na, labeled at the top of the grid. For a particular prediction or measurement, the corresponding 2p-decay energy from the IAS to a particular final excited state may be found by following the horizontal line from the prediction to where it crosses the line for the final state. To allow easy comparison, vertical lines are drawn from the peaks in the spectrum to the grid. Agreement between a prediction for a specific final state and an observed peak is

indicated by a circle, the width of which is equal to the experimental resolution (120 keV FWHM).

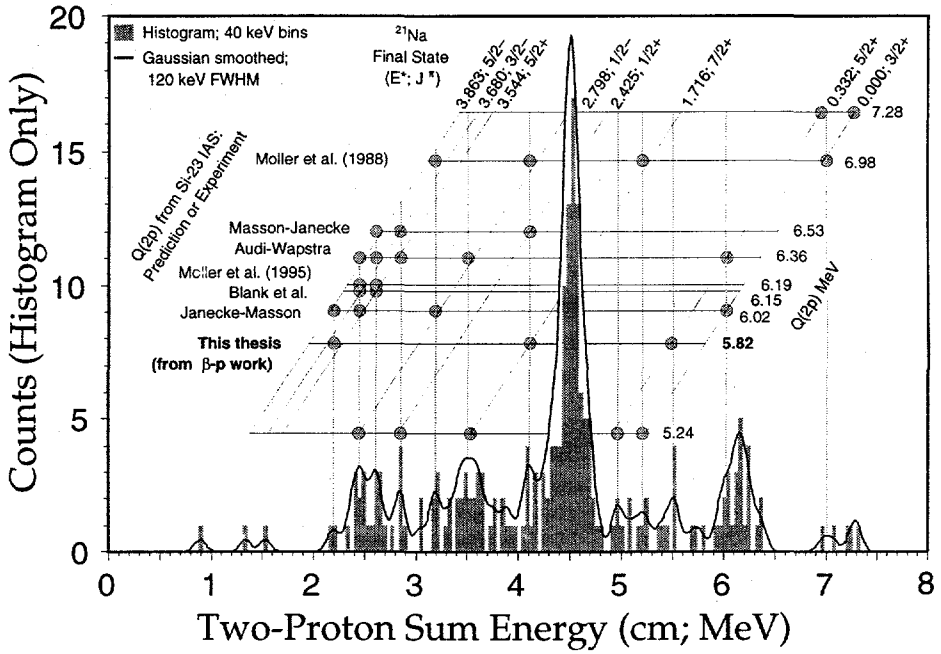

FIG. 5- 11: Possible ^{23}Si beta-delayed two-proton peaks. The grid allows comparison between the energies of unassigned peaks in the spectrum and the two-proton decay energies for various final states based on the predictions and measurements listed on the left of the grid. See text.

It is seen in this figure that none of the predictions or measurements would predict the energies of more than a few of these peaks. The energy for the decay to the ^{21}Na ground state derived from the work of Blank, *et al.*, (Bla97) lies at approximately the same energy as the ^{22}Al β-2p decay at 6.11 MeV. If one were to assume the Q_{2p} value derived from the beta-delayed proton measurement in this thesis were correct, peaks are observed at approximately the expected energies for two-proton emission to the first- and second-excited states of ^{21}Na.

A proton-proton correlation plot of the unassigned peaks below ~4 MeV in Fig. 5-6 is depicted in Fig. 5-12. The plot is similar to those shown in Figs. 5-9 and 5-10, but proton energies are given in the lab frame rather than the center of mass. The diagonal lines correspond to the two-proton sum energies of the peaks in Fig. 5-11; these would presumably correspond to transitions to different final states in the two-proton daughter. The spectrum

shown to the right of the figure shows the distribution of first proton energies; the y-axis for this plot is the same as for the correlation plot. Peaks in this spectrum would presumably correspond to different intermediate states in the one-proton daughter. Although many "peaks" are seen in this spectrum, it is not possible to assign them to specific excited states without accurately knowing the Q(2p) value for the decay.

Table 5-2 compares the results of the present work and that of Blank, *et al.*, (Bla97) with the theoretical values for the mass excess of ^{23}Si given earlier in Table 5-1. Generally the Garvey-Kelson mass relations and the IMME give the most accurate predictions for light

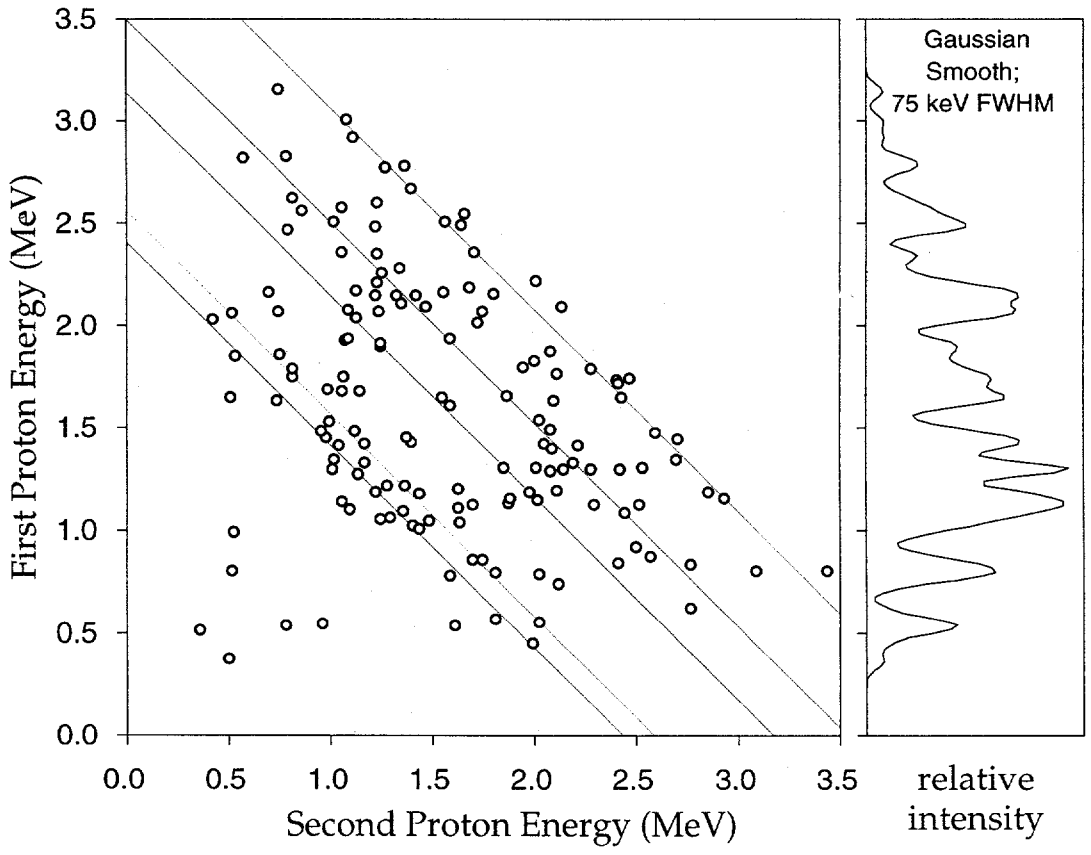

FIG. 5- 12: Proton-proton correlation plot for unassigned two-proton sum peak shown in Fig. 5-6. Energies are in the lab frame. For each event, two points are plotted since it is not known whether the high or low energy proton was emitted first. The diagonal lines indicate the "peaks" in Fig. 5-6. The spectrum on the right shows peaks in the first proton spectrum. See text.

proton-rich nuclides. It is seen that the result of the present work is lower than any of the other values; it is about 180 keV less than given by the predictions just mentioned. The Blank result is in good agreement with these values, and is more believable as it is based on both β–p and β–2p measurements. However, the two experimental mass estimates agree within 2σ error bars. A lower than predicted mass could occur due to a Thomas-Ehrman shift near the drip line.

TABLE 5- 2: Comparison of mass results to predictions for ^{23}Si.

Mass Model	Mass Excess (MeV)
Isobaric Mass Equation (Pap88)	23.44
Unified Macroscopic-Microscopic Model (Möl88a)	23.86
Finite-Range Droplet Macroscopic Model and Folded Yukawa Single-Particle Potential (Möl88b)	24.39
Modified Ensemble Averaging (Com88)	23.51
Infinite Nuclear Matter Model (Sat88)	25.37
Empirical Model with Proton-Neutron Interaction (Tac88)	23.84
Garvey-Kelson Mass Relations (Jan88)	23.43
Inhomogeneous Partial Difference Equation with Higher-Order Isospin Contributions (Mas88)	23.94
Finite-Range Droplet Macroscopic Model with Folded Yukawa Single-Particle Microscopic Model (Möl95)	23.60
1995 Mass Evaluation Estimate (Aud95)	23.77
This work, beta-delayed proton measurement	**23.25 ±0.05**
Blank, *et al.* measurement (Bla97)	23.42 ±0.10

5.5 Conclusion

A 110 MeV $^{3}He^{2+}$ bombardment of a ^{24}Mg target produced the exotic nuclides ^{22}Al and ^{23}Si. Particle-identification telescopes, sensitive to proton decays over a wide range of energies, were used to measure beta-delayed one- and two-proton decays. These telescopes were used to search for high-energy beta-delayed proton decays of ^{23}Si through its IAS in order to obtain information regarding its mass. Three peaks observed at laboratory energies of 7673 ±33, 9642 ±57 and 10861 ±68 keV have been tentatively assigned to this decay on the basis of their approximate agreement with predictions of the mass excess of the IAS and the known level energies of the first three states of ^{21}Na. This assignment indicates a mass excess of 18.23 ±0.04 MeV for the ^{23}Si IAS in ^{23}Al. Using a calculated Coulomb displacement energy

and the neutron-proton mass difference, the estimated mass excess of ^{23}Si is 23.25 ±0.05 MeV. Though this result is ~180 keV lower than any mass predictions for ^{23}Si, it does agree (within 2σ error bars) with the experimental result of Blank, *et al.*, (Bla97) of 23.42 ±0.10 MeV, derived from their beta-delayed one- and two-proton decay measurements.

The beta-delayed two-proton decay of ^{22}Al was measured again. Although general agreement was observed between the results of this measurement and earlier work (Cab84), assignments to specific intermediate states could not be made for many of the peaks in the individual proton spectra. This may indicate that another decay mechanism besides sequential emission is occurring at least some of the time, or that some of the two-proton events originate with the decay of ^{23}Si. A very energy-asymmetric beta-delayed two-proton decay branch that had been predicted to have significant strength by Brown (Bro90) was not observed.

Besides the known groups of ^{22}Al in the beta-delayed two-proton sum spectrum, several unassigned "peaks" were also observed. These were compared to estimates of two-proton decay energies from the ^{23}Si IAS to various excited states in its two-proton daughter. Some agreement was observed between the measured peak energies and the Q_{2p} values derived from various mass predictions, as well as the measurement by Blank, *et al.* (Bla97). However this may be attributable to random agreement between the large numbers of "peaks" and possible excited states, as well as poor statistics.

C H A P T E R 6

SEARCH FOR PROTON EMISSION FROM A PREDICTED ISOMER OF ^{77}Rb

6.1 Introduction

Direct proton emission was first observed from an isomeric state of ^{53}Co (Jac70, Cer70, Cer72). The isomer decays primarily by positron emission to a 2.5 min, $J^{\pi} = \frac{19}{2}^-$, isomer of ^{53}Fe with a half-life of 247 ms. However, 1.5% of the decays proceed to the ^{52}Fe ground state by emission of a 1.59 MeV (c.m.) proton. Decay energetics, the observed half-life, and shell-model calculations strongly suggest that the ^{53}Co isomer is the isobaric analog of the ^{53}Fe isomer and thus has a spin and parity of $\frac{19}{2}^-$. The observed proton branching ratio from ^{53m}Co leads to an estimated proton-decay partial half-life of ~17 s. This is far longer than is typical in proton decay, in part because of the large centrifugal barrier between the initial and final states. In addition, major differences between the initial- and final-state wave functions further retard proton emission. Shell model calculations suggest that the emitting state is formed by a high-spin coupling between an $f_{7/2}$ proton hole and a pair of $f_{7/2}$ neutron holes. ^{53}Co remains the only nuclide observed to date that is bound to proton emission from its ground state but emits protons from an isomeric state. [Although proton emission has been observed (Dav96, Dav97) from isomers of ^{165}Ir and ^{185}Bi exclusively, both of these nuclides are also predicted to be unbound to proton emission from their ground states.]

Shortly after the discovery of ^{53m}Co, Peker, *et al.*, (Pek71) published a paper in which they used the shell model to predict the existence of several three- and four-particle high-

spin ($J \geq \frac{17}{2}$) isomers of medium-mass nuclides that would be unbound to proton emission, including the ^{53}Co isomer. Among the predictions is a $\frac{19}{2}^-$ isomer of ^{77}Rb, formed by the coupling of an $f_{5/2}$ hole state with a pair of $g_{9/2}$ neutrons. The predicted excitation of this isomer is ~6.07 MeV, which leaves it unbound to proton emission in the center of mass by 2.93 MeV. Bugrov, *et al.*, (Bug85b) have predicted partial half lives for proton decay from many of these isomers, using an integral formula developed in analogy with work on alpha decay rates (see equation 2-27, Section 2.2.2). For this $l = 9$ proton decay, they predict a partial half-life of 240 ms, significantly longer than is typical for proton decays of this energy. Relative to the ground-state proton emitters that have been observed (see Table 2-1), ^{77}Rb may be produced in high yield via the ^{40}Ca(^{40}Ca, 3p) reaction. Thus it could represent a more experimentally-accessible example of direct-proton emission.

The region of the chart of the nuclides surrounding ^{77}Rb has generated much interest because collectivity in this region has been shown to change very rapidly with changes in microscopic structure. Among the light Kr, Rb, Sr and Y isotopes, various nuclides have been shown to be prolate, oblate and triaxial (Lis81, Lis82, Pan81, Pan82). Shape coexistence has also been observed in this region (Pie81). Prediction of the isomer's existence is based on the assumption of a spherical collective shape with high spin due to the coupling of a few valence nucleons residing in high-spin orbitals. However, the ground state of ^{77}Rb is known to be highly prolate from measurements of its spin and magnetic moment (Eks78, Thi81). This does not *a priori* preclude the possibility that spherical excited configurations could exist, stabilized by the minimization of the surface energy.

In order for proton decay from an isomer to be observed, gamma decay must be strongly hindered. There are many states known in ^{77}Rb at lower excitations than the predicted isomeric state. A few excited states of ^{77}Rb were observed at low excitation energies in the beta-delayed gamma decay of ^{77}Sr (Lis83). Additionally, in-beam gamma-decay studies of ^{77}Rb (Lis83, Har96) have reported three rotational bands. These bands include high-spin members to which the predicted isomer could potentially decay via E1 transitions of ~3 MeV. However, differences between the wave functions of these collective-mode states and the many-particle isomeric state may lead to significant gamma-decay suppression. By contrast, the structure of the ^{53}Co-mirror nucleus ^{53}Fe suggests that there are only a few states between

the $\frac{7}{2}^-$ ground state and the isomeric state in ^{53}Co (Fir96). Assuming that these mirror states are present in ^{53}Co, any gamma-ray emission from the isomer must be hexadecapole (l=4) or higher order. This is a significant difference between the cases of ^{77m}Rb and ^{53m}Co.

Two interrelated questions are to be addressed by this work. The first is whether the isomeric state, if it exists, will be populated by the decay of the ^{80}Zr compound nucleus. If so, the second question is whether its wave function is sufficiently dissimilar from lower-lying collectively-deformed states to allow proton decay to compete with gamma emission. Aside from testing the predictions of the proton-decay rate from this many-particle state, this experiment examines the relationship between high-spin states formed from the coupling of individual nucleons and those created from rotational excitation of a collectively-deformed nucleus.

6.2 Experiments

The ^{40}Ca(^{40}Ca,3p) reaction was used to produce ^{77}Rb during three separate bombardments. During each measurement, a helium-jet system was used to transport the activity away from the target area; see Section 3.1.3. In the first two measurements, the activity was transported to a detector box approximately 75 cm from the target. For the third measurement, the activity was transported approximately 30 cm to the ion source of the Recoil Atom Mass Analyzer (RAMA) for mass separation prior to counting. RAMA is discussed in Section 3.1.4; a schematic diagram of RAMA is shown in Fig. 3-4.

6.2.1 Measurements Without Mass Separation

The measurements without mass separation use He-jet transport and detector systems similar to those used in the first low-energy measurement of the beta-delayed proton decay of ^{23}Al, depicted in Fig. 4-5. For the first measurement a 245 MeV ^{40}Ca beam was degraded by the HAVAR entrance windows to a mid-target energy of ~160 MeV. A 1.9 mg/cm^2 ^{40}Ca separated-isotope target was used. Reaction products were degraded by a 1.7 mg/cm^2 Al foil to increase collection efficiency in the helium gas. The target and degrader were placed in the first and second slots in the He-jet chamber, respectively. After thermalization in the gas,

reaction products were swept from the target chamber by a single 1.07 mm inner diameter capillary and transported to a neutron-shielded detector box.

The activity was deposited onto the tip of a moving tape located at the center of an array of six particle identification telescopes (Row97), each consisting of two gas-ΔE detectors backed by a 300 μm Si E detector. The array and its individual telescopes are shown in Figures 4-3 and 4-4, respectively. The catcher tape was slowly moved to prevent the build-up of long-lived activity. Because the tape drive occludes two of the six telescopes, they were not used; a third telescope became inoperative during the experiment. Each telescope subtended a solid angle of ~4% of 4π sr and was capable of observing protons with energies from 200 to 6000 keV. To calibrate the detectors *in situ*, a separate 40 MeV ^{3}He bombardment on ^{nat}Mg was performed to produced the beta-delayed proton emitter ^{25}Si (Rob93).

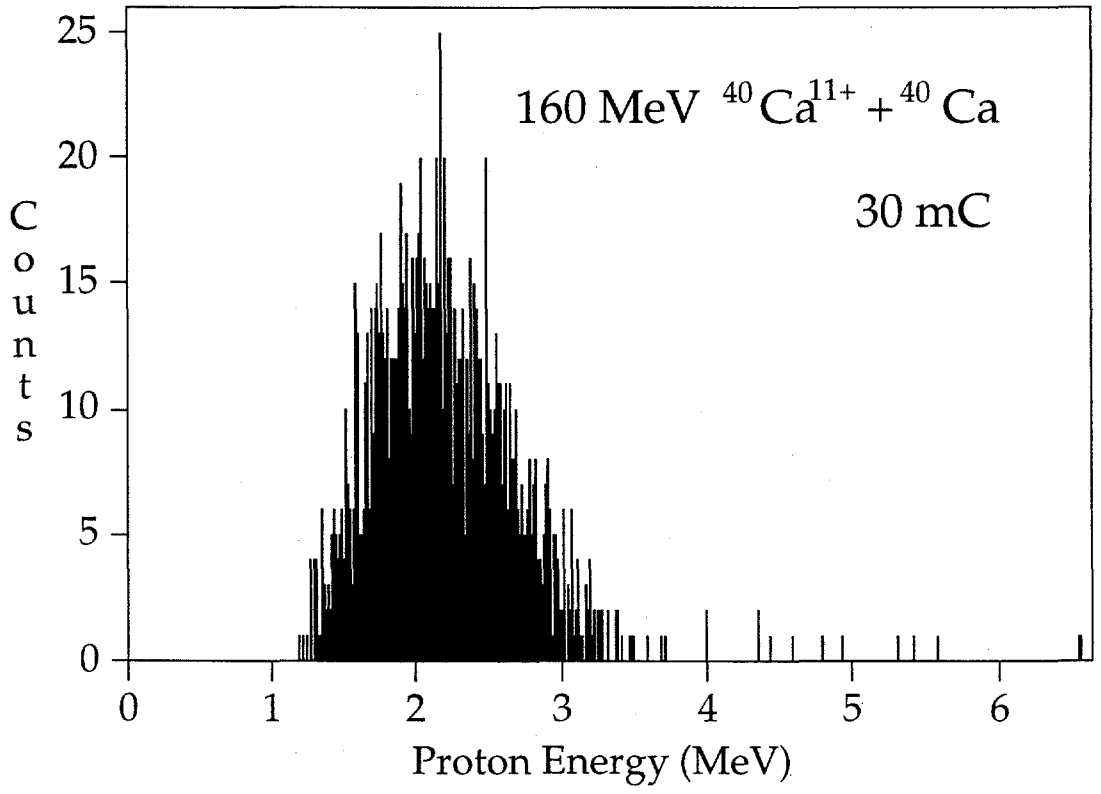

FIG. 6- 1: Proton spectrum resulting from a 160 MeV ^{40}Ca bombardment of ^{40}Ca targets (no mass separation).

Figure 6-1 shows the results of this 30 mC $^{40}Ca^{11+}$ bombardment, during which the average beam current was 30 enA. The spectrum is dominated by a broad continuum due to the beta- and EC-delayed proton decays of ^{77}Sr and ^{69}Se (Har76). A scattering of proton events up to ~5 MeV was also observed, probably due to the decays of one or more weak proton emitters produced in this reaction whose decays have yet to be studied. It is known from other work that products made in the entrance windows of the helium-jet chamber are stopped in the target and do not introduce significant contamination. There is no compelling evidence for the ^{77m}Rb decay group near the predicted proton energy of 2.93 MeV.

A second bombardment of 70 mC was performed using a 260 MeV $^{40}Ca^{11+}$ beam; the helium-jet windows, a 2.4 mg/cm^2 Al degrader and two ^{40}Ca targets of 1.9 and 1.2 mg/cm^2 degraded the beam to 145 MeV in the part of the (first) target sampled. Few reaction products made in the second target were stopped in the helium gas; this target acted primarily as a degrader for products made in the first target. The helium-jet transport and the detection system were identical to those used in the previous measurement. Although there were fewer high-energy events, there was again no evidence of a peak due to the decay of the predicted isomer that could be clearly identified in the presence of the other reaction products.

6.2.2 Measurement Utilizing RAMA

The measurements without mass separation, discussed in the previous section, precluded the possibility of a large branching ratio for the isomeric state. Simultaneous production of beta- and EC-delayed protons prevented observation of a weak branch. Mass separation was employed for the third measurement in an attempt to improve the sensitivity by eliminating all or most of the proton background shown in Fig. 6-1. Two target configurations were utilized. During the first 24 hours of the experiment, the 250 MeV $^{40}Ca^{11+}$ beam was first degraded by a 0.9 mg/cm^2 ^{nat}Ni foil before impinging on a 4.4 mg/cm^2 ^{nat}Ca target. With this configuration, approximately 40% of the target thickness was sampled; the on-target beam energy over this thickness ranged from 110 to 140 MeV. On-target beam currents of 35 to 90 enA were employed. In the second configuration, the degrader and thick Ca target were replaced by two 2.8 mg/cm^2 ^{nat}Ca targets. The first of these targets acted primarily as a degrader. Approximately 60% of the second target was sampled; over this thickness the beam energy ranged from 125 to 145 MeV. The four-capillary helium-jet system

was used to transport the activity to RAMA. This helium-jet arrangement has a transport time of ~50 ms, which is a factor of ~4 longer than the single-capillary configuration. It was reasoned that the improved collection efficiency using this arrangement would more than compensate for half-life losses.

The presence of the beta-delayed proton continuum from ^{77}Sr limited the sensitivity of the earlier measurements. RAMA cannot separate ^{77}Sr from ^{77}Rb by mass, but the different chemical properties of the two isotopes affect their ionization efficiencies. Rb and Sr belong to Groups I and II of the periodic table, respectively. Tests have shown (Ogn96) that running the ion source in the arc mode ionizes both Group I and Group II elements, but the efficiency for ionizing Group II elements is a factor of 20 less. Alternatively, when run in surface-ionization mode Group II elements are not ionized. However, the yield of Group I elements is also reduced relative to the arc mode by a factor of two. Arc mode was chosen for this experiment since the absolute ^{77}Rb yield would be better; although not eliminated, the level of contamination from ^{77}Sr would be about twenty times less than in the earlier helium-jet measurements.

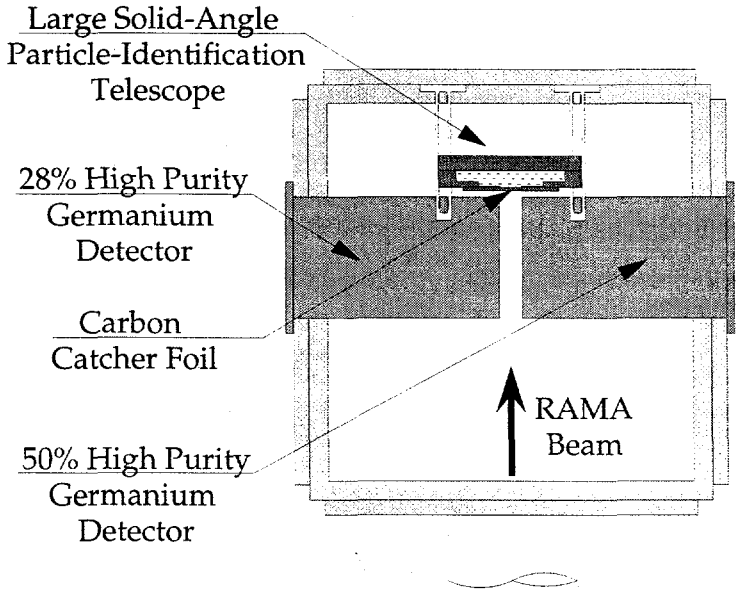

FIG. 6- 2: Detector configuration used with RAMA, top view. This detector chamber is located inside the shielded detector station shown at the upper left of Fig. 3-4.

The detector configuration for this experiment is shown in Fig. 6-2. After separation, the mass 77 beam was deposited onto a ~20 μg/cm^2 carbon foil placed directly in front of a gas-ΔE/gas-ΔE/Si-E particle-identification telescope. The square Si E detector was 50 mm on a side by 300 μm thick; it was placed at a distance of 17 mm from the catcher foil. Using a Monte Carlo simulation of the distributed source, the solid angle for the telescope was calculated to be 23.0 ±0.5% of 4π sr. Two high purity germanium (HPGe) γ-ray detectors, with relative efficiencies of 28% and 50%, were placed upstream and to either side of the catcher foil; a gap of 2 cm between the gamma detectors permitted the RAMA beam to pass through.

The RAMA beam-transport optics were tuned on the stable isotopes ^{39}K and ^{85}Rb, which were introduced into the helium-jet as chloride salts. Fine tuning was accomplished by monitoring the rate of 66.5 keV beta-delayed gamma rays from the 3.70 min decay of the ^{77}Rb

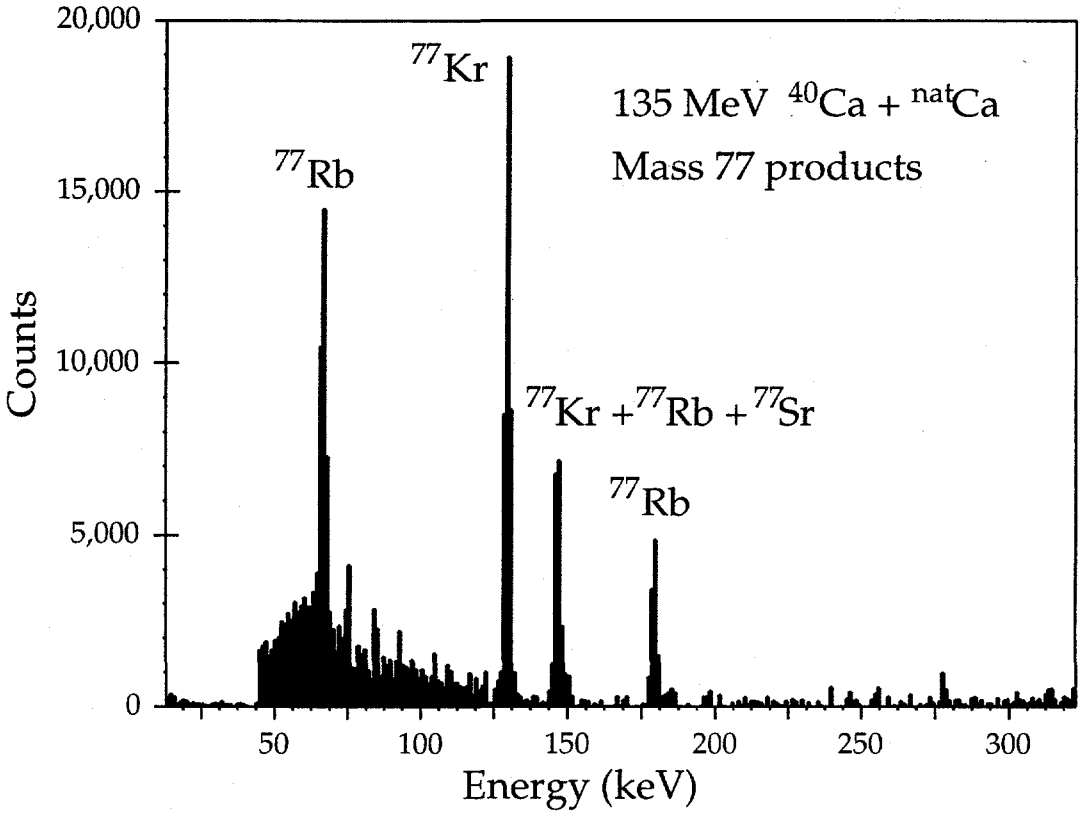

FIG. 6- 3: Gamma-ray spectrum of mass-77 reaction products. The spectrum of long-lived species, taken during the 24 hour period after the main experiment was completed, has been subtracted.

ground state. Based on the intensities of the ^{77}Rb 66.5 and 178.8 keV gamma-ray peaks observed in the two HPGe detectors, 1.58 ±0.08 x 10^6 atoms of ^{77}Rb were transported to the detector station during the bombardment. Figure 6-3 shows the gamma-ray spectrum collected with the 28% efficiency detector after subtraction of long-lived background events. This yield is at least 10 times less than had been expected based on the previously observed efficiency for ^{20}Na, though it is difficult to estimate the absolute efficiency due to uncertainties in the production cross section and the helium-jet transport efficiency for this symmetric heavy-ion production reaction. After completion of the main experiment, background data were collected for an additional 24 hours (with RAMA running, but without beam on target).

Three proton events were observed during this measurement, with energies of 1674, 2725 and 4420 keV. Calibration was performed with a ^{148}Gd/^{241}Am alpha source; corrections were made for energy losses (see Section 3.3.2) in the carbon catcher foil and the inactive entrance components (window, gas and silicon dead layer) of the detector telescopes. The 2725 keV event could be from the decay of the predicted ^{77}Rb isomer but the observation of only a single event prevents a positive assignment. More importantly, both this event and the 1674 keV event could be beta-delayed protons from ^{77}Sr, since protons with energies from ~1 - 3.5 MeV are observed in this decay. It should be noted that the scarcity of proton events from ^{77}Sr is consistent with the number of ^{77}Sr gamma decays detected, based on the known beta-delayed proton branching ratio. Thus suppression of Sr relative to Rb by selective ionization was successful. The origin of the event at 4420 keV is unknown.

6.3 Results

In order to choose an appropriate beam energy and to interpret the results of the measurements, it has been important to estimate the production cross sections for the ^{40}Ca + ^{40}Ca compound-nuclear reaction. Two different statistical codes were used for this purpose: ALICE (Bla82) and PACE2 (Gav80). Whereas ALICE calculates the evaporation probabilities analytically, PACE2 uses a Monte Carlo approach to assess the likelihood of producing the various reaction residues (see Section 3.1.2). ALICE predicts a maximum cross section for production of ^{77}Rb of ~240 mb at a laboratory beam energy of ~140 MeV; the excitation function is predicted to be rather flat from ~120 to ~200 MeV. PACE2 predicts that

the peak cross section is ~130 mb at 125 MeV and that the excitation function is more sharply peaked, falling off rapidly above ~140 MeV. An experiment using the velocity filter SHIP (Mün79) measured a cross section of 29.0 mb at a bombardment energy of 145 MeV (Hof86). This agrees closely with the prediction of PACE2 of ~32 mb at this energy, suggesting that this is the more accurate of the two codes. ALICE and PACE2 predict ^{77}Rb/^{77}Sr relative yields of ~20 and ~15, respectively.

Prediction of the yield of the ^{77}Rb isomer relative to its ground state is more difficult. To estimate this ratio for the case of ^{53}Co, Kochan, *et al..*, (Koc73) assumed that all high-spin ($J \geq \frac{17}{2}$) excited states above the isomer would eventually decay into the isomer. We do not believe this approach is valid for the present calculation. In ^{77}Rb, excited states which are populated after the evaporation of three protons from the ^{80}Zr compound nucleus will tend to decay into the yrast band if they have high spin but relatively low excitation. PACE2 allows the decay sequences leading to a specific residue to be examined in detail. To estimate the population of the isomer relative to the ground state, we first determined the percentage of all decays that proceed through $J^{\pi} = \frac{19}{2}^{-}$ excited states at excitations within 2 MeV of the predicted isomer. This feeding was divided by the number of $\frac{19}{2}^{-}$ states in this energy range as estimated by treating the system as a Fermi gas with equidistant level spacings and subtracting the (measured) energy of the $\frac{19}{2}^{-}$ yrast level from the excitation energy. Using this method, the expected population of the isomer relative to the ground state is ~1/1500. This estimate should be taken as an upper limit only since microscopic properties of the intermediate states feeding the isomer have been ignored.

During the measurements without mass separation, no evidence of the decay of a high-spin proton-emitting isomer of ^{77}Rb was observed. Because the radiation flux during the measurement was very high, no gamma decay data were taken which would have indicated the amount of ^{77}Rb produced. However, approximately 1300 proton events were observed, the majority of which may be attributed to the beta-delayed proton decay of ^{77}Sr (Har76). The measured branching-ratio limit for this decay mode is <0.25%. If we take the relative yield predicted by ALICE (~20:1) for production of ^{77}Rb relative to ^{77}Sr as an upper limit, then the number of ^{77}Rb atoms whose proton decays could have potentially been measured is approximately 1.0×10^{7}. The presence of the ^{77}Sr protons in the spectrum in the energy range

predicted for the isomeric decay protons reduces the sensitivity by a factor of ~50. This implies a sensitivity to proton emission of $1:2x10^5$ relative to the yield of the ^{77}Rb ground-state atoms. The transport time for these measurements was ~15 ms.

More precise limits may be set from the mass-separated data. Based on the number of ground-state beta-delayed gamma-ray decays observed and the measured gamma-detector efficiencies, $1.6x10^6$ atoms of ^{77}Rb were transported to the shielded detector station. The solid angle of the particle-identification telescope was 23.0 ±0.5% of 4π sr. If, somewhat arbitrarily, it is assumed that four proton events of the same energy would have been sufficient to conclude that the decay had been observed (given the extremely low background), one can estimate that this measurement had a sensitivity to proton emission of $1:1x10^5$, again relative to the ground state yield. The transport time for this measurement was ~50 ms.

6.4 Discussion

6.4.1 Limits Set by the Present Study

The fact that no evidence for proton emission from the predicted isomer of ^{77}Rb has been observed may indicate that the state does not exist. Alternatively, it may be attributed to a lack of feeding to the isomeric state from the compound nucleus, preferential gamma-ray de-excitation of the state or to a combination of these causes. Figure 6-4 shows a graphical representation of the limits set by the measurements with and without mass separation. The total half-life plotted along the x-axis assumes that the proton partial half-life is 240 ms, as predicted by Bugrov, *et al.* (Bug85b). The region above and to the right of the curves is experimentally accessible; that is, the isomer would have been observed had its half-life and feeding been within this region. The sharp decline in sensitivity for isomer half-lives less than ~25 ms is due to half-life losses during transit. Note that if the half-life of the isomer were longer than predicted, the limits would be the same as shown for the predicted half-life.

Although the sensitivity is better for the helium-jet only measurements, the limit set with mass separation is more stringent, since the former limit relies on a ^{77}Rb yield estimated from the approximate ^{77}Sr yield. Also, the RAMA measurements were made at somewhat

lower bombardment energies. The PACE2 predictions suggest that the measurements without mass separation may not have sampled the peak of the excitation function as effectively. However, the use of thick targets in all instances caused a range of beam energies to be sampled.

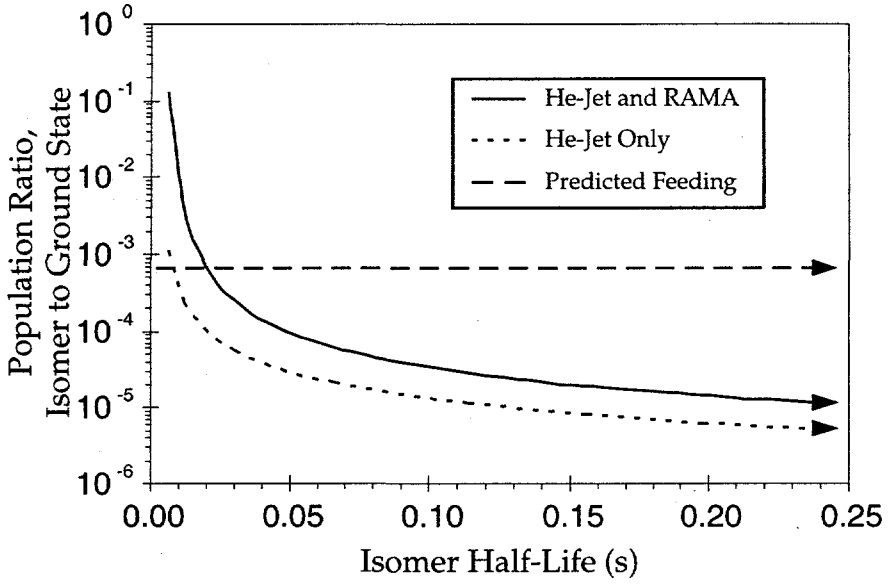

FIG. 6- 4: Experimental limits on the population of the isomer relative to the ground state of ^{77}Rb. A proton-decay partial half-life of 246 ms (Bug85b) has been assumed.

6.4.2 Other Relevant Work

The structure of ^{77}Rb has been studied extensively through atomic beam, beta-delayed gamma-ray and in-beam gamma-ray measurements. Atomic beam experiments (Eks78, Thi81) deduced a ^{77}Rb ground-state spin of $\frac{3}{2}$ and a magnetic moment of 0.652 n.m. from magnetic resonance measurements. Based on this information, the valence proton of the ground state was assigned to the [312 $\frac{3}{2}$] Nilsson level corresponding to a deformation of $\varepsilon_2 \cong 0.38$. A beta-delayed gamma-ray measurement (Lis83) deduced the existence of a few excited states. All of these states are well below the excitation of the predicted isomer. Beta decay from the $\frac{5}{2}^+$ ground state of ^{77}Rb to the $\frac{19}{2}^-$ predicted isomer is highly forbidden and was not observed. Subsequent in-beam gamma-decay studies (Lis83, Har96) of ^{77}Rb have revealed the presence of three rotational bands, built on the $\frac{3}{2}^-$ ground state, the $\frac{5}{2}^+$ second-excited state at 147 keV,

and upon a $\frac{9}{2}^+$ excited state at 1153 keV; the highest members of these bands measured are at excitations of 1715, 12265 and 18376 keV and have spins of $\frac{15}{2}^-$, $\frac{45}{2}^+$, and $\frac{57}{2}^+$, respectively. The bands based on the 147 keV and 1153 keV states correspond to different deformations, with ε_2 values of ~0.38 and ~0.29, respectively. The highest-energy neutron pair of the former band is thought to occupy the $[422\frac{5}{2}]$ Nilsson level; in the latter band, this pair occupies the $[301\frac{3}{2}]$ level. In both cases, the valence proton is thought to occupy the $[431\frac{3}{2}]$ level. The rotational bands of ^{77}Rb are plotted in Fig. 6-5, along with the predicted isomer.

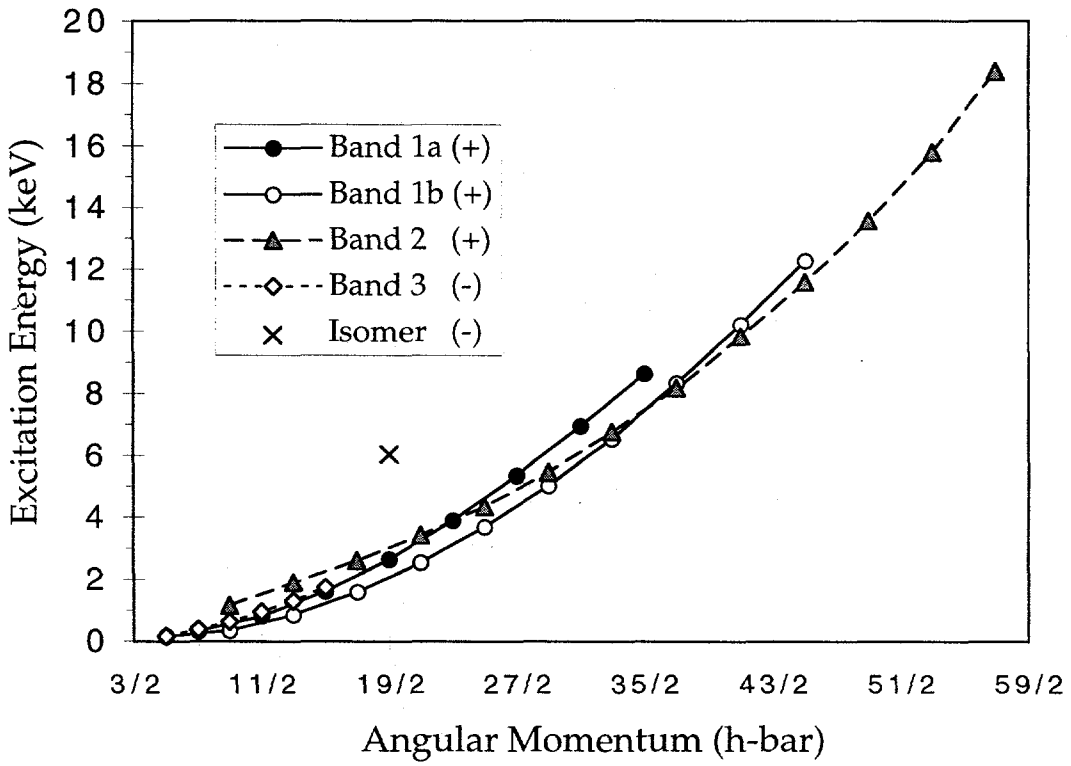

FIG. 6- 5: Yrast plot of the known levels of ^{77}Rb, and the predicted isomer. The band labeled "1b" is the unfavored signature partner of band 1a (Har96).

The presence of many high-spin excited states below the predicted isomer in excitation energy presents several possible pathways for the isomer to de-excite to the ground state. In particular, E1 decays to the $\frac{17}{2}^+$ excited states at 1576 or 2596 keV might be expected. If proton emission is to be a viable decay mode, these gamma transitions would have to be severely hindered due to differences between the wave functions and/or collective shapes of the initial and final states. If the gamma-ray decay is not hindered, it could in principle

have been observed in the in-beam gamma studies discussed above. No evidence for the predicted isomer was noted in these measurements. Since the energy of the decay would likely be ~3 MeV, the efficiency for detection would be poor.

Although the experiment by Hardy, *et al.*, (Har76) which first measured the decay of ^{77}Sr could potentially have measured protons from an isomer of ^{77}Rb, such an observation was highly unlikely given the limits set in this paper. First, the transport time for the activity was given as ~2 s, so if the prediction by Bugrov, *et al.*, (Bug85b) is taken as an upper limit, the activity would have decayed prior to counting. Second, in that experiment only p-γ, p-X, p-e^+ and X-γ coincidences were recorded; coincident X-rays from EC decay were used to identify what element had decayed. Since the isomeric state would be produced directly (rather than being fed by highly-forbidden beta decay), proton emission would not occur in coincidence with X- or γ-ray emission unless it populated an excited state of ^{76}Kr rather than the ground state.

A search (Hof86) for proton-unstable isomers in this region that discovered a 3.2 μs isomer of ^{76}Rb also looked at the decay of ^{77}Rb using both gamma and proton detectors. This measurement utilized the velocity filter SHIP (Mün79) and was sensitive to isomers with half-lives of 1 μs to 1 ms. ^{77}Rb was produced via the ^{40}Ca(^{40}Ca, 3p) reaction at an energy of 142 MeV; ~14000 counts were observed in the 66.5 and 178.8 keV gamma peaks. No evidence of the predicted isomer is given. Assuming that the Bugrov estimate for the proton-decay partial half-life is reasonable, the proton branching ratio would have to have been very small (<0.5%) if the isomer half-life were within the range of sensitivity. Because of this, the cross section for the isomeric state would have had to have been comparable to that of the ground state for the proton decay branch to have been observed. In principle, gamma de-excitation of the isomer could have been measured. The relative efficiency quoted for the germanium detector (12%) suggests that the sensitivity to gamma-rays from the isomer would be rather low. It is interesting to note that the ^{76}Rb isomer observed at SHIP had a large hindrance factor of 3×10^6 for E1 gamma-ray emission, which the authors attribute to a possible change in the core-particle structure between the initial and final states.

6.5 Conclusion

A search has been made for a predicted many-particle $\frac{19}{2}^-$ isomer of ^{77}Rb. The ^{40}Ca(^{40}Ca,3p)^{77}Rb reaction was utilized at energies from 110 to 160 MeV on target. Two measurements using a helium-jet to transport the activity to an array of particle-identification telescopes set an upper limit for the production cross section of ~5 x 10^{-6} for the isomeric state relative to the ground state. The same reaction was used in a third bombardment at lower energies in which reaction products were mass separated using the on-line mass separator RAMA. Gamma-ray and charged-particle decays were measured and used to monitor the yield of ^{77}Rb. This measurement set a more precise upper limit of 1 x 10^{-5} for production of the isomeric state relative to the ground state. Both of the above limits assume a half-life for the isomer that is longer than the helium-jet transport times of ~15 ms and ~50 ms for the direct and mass-separated measurements, respectively. Because no evidence of the decay was observed, it is not possible to say whether the isomer is populated by the reaction used (or if it exists at all). If the isomer is produced by the ^{40}Ca(^{40}Ca,3p)^{77m}Rb reaction, it probably decays primarily by gamma-ray emission; however, no estimate of the proton partial half-life (or the proton or gamma branching ratios) can be made from the available data.

C H A P T E R 7

CONCLUSION

Proton-decay spectroscopy has been shown to be a useful tool for studying nuclides at or near the proton drip line. A discussion of proton-, beta- and beta-delayed decay modes has shown how proton spectroscopy can extract information in this region, where more traditional decay studies are hindered by "background" radiation and where diminishing cross sections often make direct-reaction studies impractical. As part of this discussion, the concepts of isospin and strength functions were introduced, and possible mechanisms for two-proton emission were presented.

The information gained from proton-decay spectroscopy may be used to test the predictions of various nuclear models. The nuclear properties predicted include ground-state masses and the energies, spins, parities and wave functions of excited states. A brief overview of mass models has been presented. A discussion of "realistic" shell models described empirical methods for determining two-body interactions in various mass regions. The wave functions generated from such shell models may be used to predict decay rates; a method for determining Gamow-Teller beta-decay rates has been presented. Prediction of isospin-mixing amplitudes has also been discussed. Proton decay spectroscopy can be useful in elucidating nucleosynthesis processes. An overview of nucleosynthesis near the proton drip line was followed by a discussion of the calculation of reaction rates in stars.

Experimental techniques used in proton decay measurements have been discussed, including methods of production, transport, mass separation and detection of proton-rich nuclei. Particular attention was paid to the use of low-energy particle-identification

telescopes, which allow proton decays to be identified unambiguously in a high-radiation background. Methods of data reduction and detector calibration have also been presented.

A series of 40 MeV proton bombardments of Mg targets measured the beta-delayed proton decay of ^{23}Al. New, relatively intense, proton peaks were observed at energies of 246 ±20 keV and 556 ±5 keV, with intensities of 33 ±3% and 68 ±5% relative to the previously observed (Gou72) group at 838 ±5 keV. The peak at 246 keV is from the lowest-energy proton decay ever observed. Two likely assignments of this decay to intermediate states in ^{23}Mg have been discussed; in each case, the deduced log*f* values for these assignments suggest that these states are fed by allowed beta decay. If, however, this peak were from the (superallowed) decay of the ^{23}Al IAS, the intensity observed is in reasonable agreement with the predictions of Brown (Tig95) based on isospin-mixing amplitudes (Orm89) for the IAS. The observed intensity is also in approximate accord with the limits set by various measurements (e.g., Ste96) of the ^{22}Na(p,γ)^{23}Mg resonance strength of the IAS; this would indicate that this resonance is not of primary importance in determining the rp-process pathway of explosive hydrogen burning in novae (Wal81, Wie86a). Several new, weak proton-decay groups from other excited states of ^{23}Mg were also observed for the first time. The energies and beta-feeding to these states have been compared to the full-basis shell-model predictions of Brown (Bro90, Tig95); the total Gamow-Teller strength at the appropriate excitation energies in ^{23}Mg is approximately an order of magnitude less than predicted. However, this result is strongly influenced by the magnitude of the beta decay branch that is assumed for the 835 keV proton peak. A continuum of low-energy events, previously assigned to the beta-delayed proton decay of ^{24}Al (Bat94), was not observed in the second series of ^{23}Al measurements.

During a 110 MeV ^{3}He bombardment of ^{24}Mg targets, particle-identification telescopes were used to search for high-energy beta-delayed proton decays of ^{23}Si through its IAS in order to obtain information regarding its mass. Three peaks observed at laboratory energies of 7673 ±33, 9642 ±57 and 10861 ±68 keV have been tentatively assigned to this decay on the basis of their approximate agreement with predictions of the mass excess of the IAS and the known level energies of the first three states of ^{21}Na. This assignment indicates a mass excess of 18.23 ±0.04 MeV for the ^{23}Si IAS in ^{23}Al. Using a calculated Coulomb displacement energy (Ant97) and the neutron-proton mass difference, the estimated mass excess of ^{23}Si is 23.25 ±0.05

MeV. This result agrees (within 3σ error bars) with the experimental result of Blank, *et al.*, (Bla97) of 23.42 ±0.10 MeV, derived from their beta-delayed one- and two-proton decay measurements.

The beta-delayed two-proton decay of ^{22}Al was measured in parallel with the ^{23}Si search. General agreement was observed between the results of this measurement and earlier work (Cab84). A very energy-asymmetric beta-delayed two-proton decay branch that had been predicted to have significant strength by Brown (Bro90) was not observed. Besides the known groups of ^{22}Al in the beta-delayed two-proton sum spectrum, several unassigned "peaks" were also observed. No decay assignments were made for these two-proton decays.

A search has been made for a predicted (Pek71) many-particle $\frac{19}{2}^-$ isomer of ^{77}Rb. The ^{40}Ca(^{40}Ca,3p)^{77}Rb reaction was utilized at energies from 110 to 160 MeV on target. Two measurements used a helium-jet to transport the activity to an array of particle-identification telescopes; in a third bombardment, reaction products were separated using the on-line mass separator RAMA and observed with gamma ray detectors and a single particle-identification telescope. The He-jet (only) and mass-separated measurements set upper limits of ~5 x 10^{-6} and 1 x 10^{-5}, respectively, for the production cross section of the isomeric state relative to the ground state. The latter limit is more precise; both limits assume a (total) half-life for the isomer that is longer than the helium-jet transport times of ~15 ms and ~50 ms for the direct and mass-separated measurements, respectively.

It is clear from these measurements of ^{23}Al, ^{23}Si, ^{22}Al and ^{77m}Rb decays that the techniques of proton decay spectroscopy can contribute useful information about the properties of very proton-rich nuclides. However, it is also clear from this work that the He-jet transport technique is reaching the limits of applicability. This is primarily due to the very short half-lives and low production cross sections for nuclides farther from stability; the latter problem is exacerbated by the low selectivity, and thus high background, from the production reactions.

It is expected that future work on proton-rich nuclides will rely heavily on mass separators and/or radioactive ion beams. Although use of mass separators, analyzers or velocity filters may lead to significant loss of yield, the benefits of direct identification of reaction products and reduction in background often more than compensate. Additionally,

nuclides with half-lives of only a few microseconds may be studied with these systems. At the current time, radioactive beam intensities are insufficient for significant production of very neutron-deficient isotopes. However, due to current world-wide interest in the development of these beams, it is expected that microampere or higher intensities will be achieved within a few years, at least for some beams. Although new experimental techniques are likely to increasingly dominate research on exotic nuclides, more traditional methods will remain complimentary in the forseeable future. By providing stringent tests of nuclear models that have been deduced primarily from trends among nuclei closer to stability, proton-decay studies of exotic nuclides will continue to improve the overall understanding of the nucleus.

L I S T O F
REFERENCES

Abbreviations

Ann. Phys.	Annals of Physics
Ann. Rev. Nucl. Part. Sci.	Annual Review of Nuclear and Particle Science
Ann. Rev. Nucl. Sci.	Annual Review of Nuclear Science
Astron. Astrophys.	Astronomy and Astrophysics
Astrophys. J.	Astrophysical Journal
Astrophys. J. Suppl.	Astrophysical Journal Supplement Series
At. Dat. Nucl. Dat. Tables	Atomic and Nuclear Data Tables
Geoch. Cosmoch. Acta	Geochimica and Cosmochimica Acta
JETP Lett.	Journal of Experimental and Theoretical Physics Letters (*Pis'ma Zh. Eksp. Teor. Fiz.*)
Nucl. Instrum. Methods Phys. Res.	Nuclear Instruments and Methods in Physics Research
Nucl. Phys.	Nuclear Physics
Nuovo Cim. Suppl.	Nuovo Cimento Supplemento
Phil. Mag.	The Philosphical Magazine
Phys. At. Nucl.	Physics of Atomic Nuclei (was *Sov. J. Nucl. Phys.*)
Phys. Lett.	Physics Letters
Phys. Rep.	Physics Reports
Phys. Rev.	Physical Review
Phys. Rev. Lett.	Physical Review Letters

Rep. Prog. Phys.	Reports of Progress in Physics
Rev. Mod. Phys.	Reviews of Modern Physics
Rev. Sci. Instrum.	Review of Scientific Instruments
Sov. J. Nucl. Phys.	Soviet Journal of Nuclear Physics
Sov. J. Part. Nucl.	Soviet Journal of Particles and Nuclei
Sov. Phys. JETP	Soviet Physics– Journal of Experimental and Theoretical Physics
Sov. Phys. Usp.	Soviet Physics Uspekhi
Z. Phys.	Zeitschrift für Physik

Citations

(Åbe97) S. Åberg, P. B. Semmes and W. Nazarewicz, Phys. Rev. C **56**, 1762 (1997).

(Ajz87) F. Ajzenberg-Selove, Nucl. Phys. A **475**, 1 (1987).

(Aki95) Akimuni, I. Daito, Y. Fujita, M. Fujiwara, M. B. Greenfield, M. N. Harakeh, T. Inomata, J. Jänecke, K. Katori, S. Nakayama, H. Sakai, Y. Sakemi, M. Tanaka and M. Yosoi, Phys. Rev. C **52**, 604 (1985).

(And61) J. D. Anderson and C. Wong, Phys. Rev. Lett. **7**, 250 (1961).

(And62) J. D. Anderson, C. Wong and J. W. McClure, Phys. Rev. **126**, 2170 (1962).

(Ant85) M. S. Antony, J. Britz, J. R. Bueb and A. Pape, At. Dat. Nucl. Dat. Tables **33**, 447 (1985).

(Ant97) M. S. Antony, A. Pape and J. Britz, At. Dat. Nucl. Dat. Tables **66**, 1 (1997).

(Aud93) G. Audi and A. H. Wapstra, Nucl. Phys. A **565**, 1 (1993).

(Aud95) G. Audi and A. H. Wapstra, Nucl. Phys. A **595**, 409 (1995).

(Äys89) J. Äystö and J. Cerny, in *Treatise on Heavy Ion Science*, Vol. 8, D. A. Bromley, ed. (Plenum Publishing Co.,New York, 1989), p. 207.

(Bat93) J. C. Batchelder, D. M. Moltz, T. J. Ognibene, M. W. Rowe and J. Cerny, Phys. Rev. C**47**, 2038 (1993).

(Bat94) J. C. Batchelder, R. J. Tighe, D. M. Moltz, T. J. Ognibene, M. W. Rowe and Joseph Cerny, Phys. Rev. C **50,** 1807 (1994).

(Bat98) J. C. Batchelder, C. R. Bingham, K. Rykaczewski, K. S. Toth, T. Davinson, J. A. McKenzie, P. J. Woods, T. N. Gintner, C. J. Gross, J. W. McConnell, E. F. Zganjar, J. H. Hamilton, W. B. Walters, C. Baktash, J. Greene, J. F. Mas, W. T. Milner, S. D. Paul, D. Shapira, X. J. Xu and C. Y. Yu, Phys. Rev. C **57**, R1042 (1998).

(Bec69) F. D. Becchetti, Jr. and G. W. Greenlees, Phys. Rev. **182**, 1190 (1969).

(Ben75) W. Benenson, A. Guichard, E. Kashy, D. Mueller, H. Nann and L. W. Robinson, Phys. Lett. **58B**, 46 (1975).

(Ber81) G. Bertsch, D. Cha and H. Toki, Phys. Rev. C **24**, 533 (1981).

(Ber90) S. O. Berezinskii, G. V. Matveev and S. G. Yavshits, Sov. J. Nucl. Phys. **51**, 424 (1990).

(Ber93) M. S. Berger, ed., *Stopping Powers and Ranges for Protons and Alpha Particles,* (ICRU Report 49, International Commission on Radiation Units and Measurements, 1993).

(Bie60) L. C. Biedenharn, in *Nuclear Spectroscopy*, F. Ajzenberg-Selove, ed. (Academic Press, New York, 1960), Part B, p. 732.

(Bla52) J. M. Blatt and V. F. Weisskopf, *Theoretical Nuclear Physics* (John Wiley and Sons, New York, 1952).

(Bla72) D. C. Black, Geoch. Cosmoch. Acta **36**, 347 (1972).

(Bla82) M. Blann and J. Birplinghoff, Lawrence Livermore National Laboratory Report No. UCID-19614, 1982 (unpublished).

(Bla93) B. Blank, C. Marchand, R. Del Moral, J. P. Dufour, L. Faux, A. Fleury, and M. S. Pravikoff, Nucl. Instrum. Methods Phys. Res. A **330**, 83 (1993).

(Bla97) B. Blank, F. Boué, S. Andriamonje, S. Czajkowski, R. Del Moral, J. P. Dufour, A. Fleury, F. Pourre, M. S. Pravikoff, E. Hanelt, N. A. Orr and K.-H. Schmidt, Z. Phys. A **357**, 247 (1997).

(Bla97a) B. Blank, F. Boué, S. Andriamonje, S. Czajkowski, R. Del Moral, J. P. Dufour, A. Fleury, F. Pourre, M. S. Pravikoff, N. A. Orr, K.-H. Schmidt and E. Hanelt, Nucl. Phys. A **615**, 52 (1997).

(Bli69) R. J. Blin-Stoyle, in *Isospin in Nuclear Physics*, D. H. Wilkinson, ed. (North Holland Publishing Co., Amsterdam, 1969), p. 115.

(Bog58) N.N. Bogolyubov, V. V. Tolmachov, Fortschritte der Physik **6**, 605 (1958).

(Boh69) A. Bohr and B. R. Mottelson, *Nuclear Structure*, vol. II (W. A. Benjamin, Inc., New York, 1969).

(Bor87) M. J. G. Borge, P. Dassagne, G. T. Ewan, P. G. Hansen, A. Huck, B. Jonson, G. Klotz, A. Knipper, S. Mattsson, G. Nyman, C. Richard-Serre, K. Riisager, G. Walter and the ISOLDE Collaboration, Physica Scripta **36**, 218 (1987).

(Bor88) M. J. G. Borge, H. Cronberg, M. Cronqvist, H. Gabelmann, P. G. Hansen, L. Johannsen, B. Jonson, S. Mattsson, G. Nyman, A. Richter, K. Riisager, O. Tengblad and M. Tomaselli, Nucl. Phys. A **490**, 287 (1988).

(Bra89) B. H. Bransden and C. J. Joachain, *Introduction to Quantum Mechanics* (Longman Scientific and Technical/John Wiley and Sons, New York, 1989).

(Bro78) B. A. Brown, W. Chung and B. H. Wildenthal, Phys. Rev. Lett. **40**, 1631 (1978).

(Bro83) B. A. Brown and B. H. Wildenthal, Phys. Rev. C **28**, 2397 (1983).

(Bro85) B. A. Brown and B. H. Wildenthal, At. Dat. Nucl. Dat. Tables **33**, 348 (1985).

(Bro88a) B. A. Brown, W. A. Richter, R. E. Julies and B. H. Wildenthal, Ann. Phys. **182**, 191 (1988).

(Bro88b) B. A. Brown and B. H. Wildenthal, Ann. Rev. Nucl. Part. Sci. **38**, 29 (1988).

(Bro90a) B. A. Brown, Nucl. Phys. A **507**, 25c (1990).

(Bro90b) B. A. Brown, Phys. Rev. Lett. **65**, 2753 (1990).

(Bro93) B. A. Brown, personal communication (1993).

(Bru77) P. J. Brussaard and P. W. M. Glaudemans, *Shell-Model Applications in Nuclear Spectroscopy* (North Holland Publishing Co., Amsterdam, 1977).

(Bug85a) V. P. Bugrov, S. G. Kadmenskii, V. I. Furman and V. G. Khlebostroev, Sov. J. Nucl. Phys. **41**, 717 (1985).

(Bug85b) V. P. Bugrov, V. E. Bunakov, S. G. Kadmenskii and V. I. Furman, Sov. J. Nucl. Phys. **42**, 34 (1985).

(Bug89) V. P. Bugrov and S. G. Kadmenskii, Sov. J. Nucl. Phys. **49**, 967 (1989).

(Bur57) E. M. Burbridge, G. R. Burbridge, W. A. Fowler and F. Hoyle, Rev. Mod. Phys. **29**, 547 (1957).

(Cab82) M. D. Cable, J. Honkanen, R. F. Parry, H. M. Thierens, J. M. Wouters, Z. Y. Zhou and J. Cerny, Phys. Rev. C **26**, 1778 (1982).

(Cab83a) M. D. Cable, J. Honkanen, R. F. Parry, S. H. Zhou, Z. Y. Zhou and J. Cerny, Phys. Rev. Lett. **50**, 404 (1983).

(Cab83b) M. D. Cable, Ph.D. Thesis, University of California, Berkeley, 1983 (Lawrence Berkeley Laboratory Report No. LBL-15742, unpublished).

(Cab83c) M. D. Cable, J. Honkanen, R. F. Parry, S. H. Zhou, Z. Y. Zhou and J. Cerny, Phys. Lett. **123B**, 25 (1983).

(Cab83d) J. Honkanen, M. D. Cable, R. F. Parry, S. H. Zhou, Z. Y. Zhou and J. Cerny, Phys. Lett. **133B**, 146 (1983).

(Cab84) M. D. Cable, J. Honkanen, E. C. Schloemer, M. Ahmed, J. E. Reiff, Z. Y. Zhou and J. Cerny, Phys. Rev. C **30**, 1276 (1984).

(Cam57) A. G. W. Cameron, Atomic Energy of Canada, Ltd., CRL-41.

(Cas90) Richard F. Casten, *Nuclear Structure from a Simple Perspective* (Oxford University Press, New York, 1990).

(Cer69) J. Cerny, R. A. Mendelson, Jr., G. J. Wozniak, J. E. Esterl and J. C. Hardy, Phys. Rev. Lett. **22**, 612 (1969).

(Cer70) J. Cerny, J. E. Esterl, R. A. Gough and R. G. Sextro, Phys. Lett. **33B**, 284 (1970).

(Cer72) Joseph Cerny, R. A. Gough, R. G. Sextro and John E. Esterl, Nucl. Phys. A **188**, 666 (1972).

(CES98) Creative Electronics Systems, *STARBURST Fast Processors*, Document ACC 2180 family.ma Rev. No. 2.01., CES, Route du Pont Butin 70, Petite Lancy CH1213, Geneva, Switzerland.

(Cha92) A. E. Champagne and M. Wiescher, Ann. Rev. Nucl. Part. Sci. **42**, 39 (1992).

(Cla83) D. J. Clark, J. G. Kalnius and C. M. Lyneis, Procedings of the Particle Accelerator Conference on Accelerator Engineering and Technology, Santa Fe, NM, March 21-23, 1983.

(Cli89) E. T. H. Clifford, E. Hagberg, J. C. Hardy, H. Schmeing, R. E. Azuma, H. C. Evans, V. T. Koslowsky, U. J. Schrewe, K. S. Sharma and I. S. Towner, Nucl. Phys. A **493**, 293 (1989).

(Coc95) A. Coc, R. Mochkovitch, Y. Oberto, J.-P. Thibaud and E. Vangioni-Flam, Astron. Astrophys. **299**, 479 (1995).

(Coh65) S. Cohen and D. Kurath, Nucl. Phys. A **73**, 1 (1965).

(Col96) B. J. Cole, Phys. Rev. C , 1240 (1996).

(Com88) E. Comay, I. Kelson and A. Zidon, At. Dat. Nucl. Dat. Tables, **39**, 236 (1988).

(Con80) T. V. Congedo, I. S. Lee-Fan and B. L. Cohen, Phys. Rev. C **22**, 985 (1980).

(Dan97) N. D. Dang, A. Arima, T. Suzuki and S. Yamaji, Phys. Rev. Lett. **79**, 1638 (1997).

(Dav96) C. N. Davids, P. J. Woods, H. T. Penttilä, J. C. Batchelder, C. R. Bingham, D. J. Blumenthal, L. T. Brown, B. C. Busse, L. F. Conticchio, T. Davinson, D. J. Henderson, R. J. Irvine, D. Seweryniak, K. S. Toth, W. B. Walters and B. E. Zimmerman, Phys. Rev. Lett. **76**, 592 (1996).

(Dav97) C. N. Davids, P. J. Woods, J. C. Batchelder, C. R. Bingham, D. J. Blumenthal, L. T. Brown, B. C. Busse, L. F. Conticchio, T. Davinson, S. J. Freeman, D. J. Henderson, R. J. Irvine, R. D. Page, H. T. Pentillä, D. Seweryniak, K. S. Toth, W. B. Walters and B. E. Zimmerman, Phys. Rev. C **55**, 2255 (1997).

(Dav98) C. N. Davids, P. J. Woods, D. Seweryniak, A. A. Sonzogni, J. C. Batchelder, C. R. Bingham, T. Davinson, D. J. Henderson, R. J. Irvine, G. L. Poli, J. Uusitalo and W. B. Walters, Phys. Rev. Lett. **80**, 1849 (1998).

(Dét91) C. Détraz, Z. Phys. A **340**, 227 (1991).

(Doe75) R. R. Doering, A. Galonsky, D. M. Patterson and G. F. Bertsch, Phys. Rev. Lett. **35**, 1691 (1975).

(Dud81) J. Dudek, Z. Szymanski and T. Werner, Phys. Rev. C **23**, 920 (1981).

(DuP98) Teflon, Freon and Delrin are trademarks of E. I. DuPont de Nemours and Co., 1007 Market St., Wilmington, DE 19880-0010.

(Dus88) G. Dussel, E. Caurier and A. P. Zuker, At. Dat. Nucl. Dat. Tables, **39**, 205 (1988).

(Ebe79) P. Eberhardt, M. H. A. Jungck, I. O. Meier and F. Niederer, Astrophys. J. Lett. **234**, L169 (1979).

(Eks78) C. Ekström, S. Ingelman, G. Wannberg and M. Skarestad, Nucl. Phys. A **311**, 269 (1978).

(End90) P. M. Endt, Nucl. Phys. A **521**, 1 (1990).

(Fae84) T. Faestermann, A. Gillitzer, K. Hartel, P. Kienle and E. Notle, Phys. Lett. **137B**, 23 (1984).

(Fer50) E. Fermi, *Nuclear Physics: Notes*, compiled by J. Orear, A. H. Rosenfeld and R. A. Schluter (U. of Chicago Press, Chicago, 1950).

(Fes92) H. Feshbach, *Theoretical Nuclear Physics: Nuclear Reactions* (John Wiley and Sons, New York, 1992).

(Fir96) Richard B. Firestone, *Table of the Isotopes*, 8th ed. (John Wiley and Sons, New York, 1996).

(Gaa80) C. Gaarde, J. S. Larson, M. N. Harakeh, S. Y. van der Werf, M. Igarashi and A. Muller-Arnke, Nucl. Phys. A **334**, 248 (1980).

(Gav76) A. Gavron, Phys. Rev. C **13**, 98 (1976).

(Gav80) A. Gavron, Phys. Rev. C **21**, 230 (1980).

(Geh98) N. Gehrels and J. Paul, Physics Today **51**, 26 (1998).

(Gol60) V. I. Goldansky, Nucl. Phys. **19**, 482 (1960).

(Gol61a) V. I. Goldansky, Nucl. Phys. **27**, 648 (1961).

(Gol61b) V. I. Gol'danskii (*sic*), Sov. Phys. JETP **12**, 348 (1961).

(Gol62) V. I. Gol'danskij (*sic*), Nuovo Cim. Suppl. **25**, 123 (1962).

(Gol66) V. I. Gol'danskii (*sic*), Sov. Phys. Usp. **8**, 770 (1966).

(Gol66a) V. I. Goldanskii (*sic*), Ann. Rev. Nucl. Sci. **16**, 1 (1966).

(Gol80) V. I. Gol'danskiî (*sic*), JETP Lett. **32**, 554 (1980).

(Goo82) C. Goodman, Nucl. Phys. A **374**, 241c (1982).

(Gör89) J. Görres, M. Wiescher, S. Graff, V. B. Vogelaar, B. W. Filippone, C. A. Barnes, S. E. Kellogg, T. R. Wang and B. A. Brown, Phys. Rev. C **39**, 8 (1989).

(Gou72) R. A. Gough, R. G. Sextro and J. Cerny, Phys. Rev. Lett. **28**, 510 (1972).

(Gou75) F. S. Goulding and B. G. Harvey, Ann. Rev. Nucl. Sci. **25**, 167 (1975).

(Ham98) HAVAR is a trade name for an alloy consisting of Co (42.0%), Cr (20.0%), Fe (19.9%), Ni (12.5%), Mn (1.6%), Mo (2.2%), W (2.7%) and trace amounts of C, Si, P and S (<0.2%). It has a density of 8.3 g/cm^3. It is manufactured by Hamilton Precision Metals, a division of HMW Industries Inc., Lancaster, PA 17604.

(Han92) X. L. Han, C. L. Wu, D. H. Feng and M. W. Guidry, Phys. Rev. C **45**, 1127 (1992).

(Har69) J. C. Hardy, H. Brunnader, J. Cerny and J. Jänecke, Phys. Rev. **183**, 854 (1969).

(Har71) J. C. Hardy, J. E. Esterl, R. G. Sextro and J. Cerny, Phys. Rev. C **3**, 700 (1971).

(Har76) J. C. Hardy, J. A. MacDonald, H. Schmeing, T. Faestermann, H. R. Andrews, J. S. Geiger, R. L. Graham and K. P. Jackson, Phys. Lett. **63B**, 27 (1976).

(Har89) J. C. Hardy and E. Hagberg, in *Particle Emission from Nuclei*, D. N. Poenaru and M. S. Ivascu, eds. (CRC Press, Boca Raton, Florida, 1989), Vol III, p. 99.

(Har96) A. Harder, F. Dönau, K. P. Lieb, R. A. Cunningham, W. Gelletly, C. J. Gross, F. Hannachi, M. K. Kabadiyski, H. A. Roth, D. Rudolph, J. Simpson, Ö. Skeppstedt, B. J. Varley and D. D. Warner, Phys. Lett. **374B**, 277 (1996).

(Hau88) P. E. Haustein, At. Dat. Nucl. Dat. Tables, **39**, 186 (1988).

(Hei32) W. Heisenberg, Z. Phys. **77**, 1 (1932).

(Hen69) E. M. Henley, in *Isospin in Nuclear Physics*, D. H. Wilkinson, ed. (North Holland Publishing Co., Amsterdam, 1969), p. 15.

(Hey94) K.L.G. Heyde, *The Nuclear Shell Model*, 2nd ed. (Springer-Verlag, Berlin, 1994).

(Hof82) S. Hofmann, W. Reisdorf, G. Münzenberg, F. P. Heßberger, J. R. H. Schneider and P. Armbruster, Z. Phys. A **305**, 111 (1982).

(Hof86) S. Hofmann, I. Zychor, F. P. Hessberger and G. Münzenberg, Z. Phys. A **325**, 37 (1986).

(Hof89) S. Hofmann, in *Particle Emission from Nuclei*, D. N. Poenaru and M. S. Ivascu, eds. (CRC Press, Boca Raton, Florida, 1989), Vol II, p. 25.

(Hof93) S. Hofmann, Gesellschaft für Schwerionenforschung mbH Preprint No. GSI-93-04, 1993 (unpublished).

(Hon79) J. Honkanen, M. Kortelahti, K. Valli, K. Eskola, A Hautojärvi and K. Vierinen, Nucl. Phys. A **330**, 429 (1979).

(Hon97) A. Honkanen, M. Oinonen, K. Eskola, A. Jokinen and J. Äystö, Nucl. Instrum. Methods Phys. Res. A **395**, 217 (1997).

(Hot87) M. A. C. Hotchkis, J. E. Reiff, D. J. Vieira, F. Blönnigen, T. F. Lang, D. M. Moltz, X. Xu and J. Cerny, Phys. Rev. C **35**, 315 (1987).

(Hse86) S. T. Hseih, X. Ji, R. B. M. Mooy and B. H. Wildenthal, Proc. AIP Conf. on nuclear structure at high spin, excitation and momentum transfer, H. Nann, ed. (Am. Inst. of Phys., New York, 1986).

(Hua76) K. Huang, M. Aoyagi, M. H. Chen, B. Crasemann and H. Mark, At. Data Nucl. Data Tables **18**, 243 (1976).

(Ike63) K. Ikeda, S. Fujii and J. I. Fujita, Phys. Rev. Lett. **3**, 271 (1963).

(Irv97) R. J. Irvine, C. N. Davids, P. J. Woods, D. J. Blumenthal, L. T. Brown, L. F. Conticchio, T. Davinson, D. J. Henderson, J. A. Mackenzie, H. T. Pentillä, D. Seweryniak and W. B. Walters, Phys. Rev. C **55**, R1621 (1997).

(Jac70) K. P. Jackson, C. U. Cardinal, H. C. Evans, N. A. Jelley and Joseph Cerny, Phys. Lett. **33B**, 281 (1970).

(Jah78) R. Jahn, D. P. Stahel, G. J. Wozniak, R. J. Meijer and J. Cerny, Phys. Rev. C **18**, 9 (1978).

(Jah85) R. Jahn, R. L. McGrath, D. M. Moltz, J. E. Reiff, X. J. Xu, J. Äysto and J. Cerny, Phys. Rev. C **31**, 1576 (1985).

(Jän88) J. Jänecke and P. J. Masson, At. Dat. Nucl. Dat. Tables, **39**, 265 (1988).

(Jun71) H. Junglas, R. D. MacFarlane and Y. Fares, Phys. Rev. Lett. **27**, 556 (1971).

(Kad71) S. G. Kadmenskii, and V. E. Kalechtis, Sov. J. Nucl. Phys. **12**, 37 (1971).

(Kad75) S. G. Kadmenskii and V. I. Furman, Sov. J. Part. Nucl. **6**, 189 (1975).

(Kad96) S. G. Kadmensky (*sic*), and V. P. Bugrov, Phys. At. Nucl. **59**, 399 (1996).

(KeK78) G. J. KeKelis, M. S. Zisman, D. K. Scott, R. Jahn, D. J. Vieira, J. Cerny and F. Ajzenberg-Selove, Phys. Rev. C **17**, 1929 (1978).

(Kel62) E. L. Kelley, in *Sector Focused Cyclotrons*, K. Siegbahn and F. T. Howard, eds. (North Holland Publishing Co., Amsterdam, 1962) p. 63.

(Kle82) O. Klepper, T. Batsch, S. Hofmann, R. Kirchner, W. Kurcewicz, W. Reisdorf, E. Roeckl, D. Schardt and G. Nyman, Z. Phys. A **305**, 125 (1982).

(Kno89) G. F. Knoll, *Radiation Detection and Measurement*, 2nd ed., (John Wiley and Sons, New York, 1989).

(Koc73) S. Kochan, B. Rosner, I. Tserruya and R. Kalish, Nucl. Phys. A **204**, 185 (1973).

(Lan86) M. Langevin, A. C. Mueller, D. Guillemaud-Mueller, M. G. Saint-Laurent, R. Anne, M. Bernas, J. Galin, D. Guerreau, J. C. Jacmart, S. D. Hoath, F. Naulin, F. Pougheon, E. Quiniou and C. Détraz, Nucl. Phys. A **455**, 149 (1986).

(Lis81) C. J. Lister, P. E. Haustein, D. E. Alburger and J. W. Olness, Phys. Rev. C **24**, 260 (1981).

(Lis82) C. J. Lister, B. J. Varley, H. G. Price and J. W. Olness, Phys. Rev. Lett. **49**, 308 (1982).

(Lis83) C. J. Lister, B. J. Varley, D. E. Alburger, P. E. Haustein, S. K. Saha, J. W. Olness, H. G. Price and A. D. Irving, Phys. Rev. C **28**, 2127 (1983).

(Liv93) K. Livingston, P. J. Woods, T. Davinson, N. J. Davis, S. Hofmann, A. N. James, R. D. Page, P. J. Sellin and A. C. Shotter, Phys. Rev. C **48**, R2151 (1993).

(Liv93a) K. Livingston, P. J. Woods, T. Davinson, N. J. Davis, S. Hofmann, A. N. James, R. D. Page, P. J. Sellin and A. C. Shotter, Phys. Lett. **312B**, 46 (1993).

(Liv94) M. Livio and J. W. Truran, Astrophys. J. **425**, 797 (1994).

(Löf73) M. Löffler, H. J. Scheerer and H. Vonach, Nucl. Instrum. Methods Phys. Res. **111**, 1 (1973).

(Lyn98) C. M. Lyneis, in *Nuclear Science Division 1997 Annual Report*, R. B. Firestone, ed. (Lawrence Berkeley National Laboratory Report LBNL-39764/UC-413, Berkeley, CA, 1998) p. 43.

(Mac69) R. D. MacFarlane, R. A. Gough, N. S. Oakey and D. F. Torgerson, Nucl. Instrum. Methods Phys. Res. **73**, 285 (1969).

(Mac74) R. D. MacFarlane and W. C. McHarris, in *Nuclear Spectroscopy and Reactions, Part A*, J. Cerny, ed. (Academic Press, New York, 1974), p. 249.

(Mar15) E. Marsden, Phil. Mag. **30**, 240 (1915).

(Mar69) P. Marmier and E. Sheldon, *Physics of Nuclei and Particles* (Academic Press, New York, 1969).

(Mas88) P. J. Masson and J. Jänecke, At. Dat. Nucl. Dat. Tables, **39**, 273 (1988).

(May55) M. G. Mayer and J. H. D. Jensen, *Elementary Theory of Nuclear Shell Structure* (John Wiley and Sons, New York, 1955).

(Mic67) A. Michalowicz, *Kinematics of Nuclear Reactions*, R. A. Giles, ed. (Iliffe Books, London, 1967).

(Mil90) G. A. Miller, B. M. K. Nefkens and I. Slaus, Phys. Rep. **194**, 1 (1990).

(Möl88a) P. Möller and J. R. Nix, At. Dat. Nucl. Dat. Tables, **39**, 213 (1988).

(Möl88b) P. Möller, W. D. Myers, W. J. Swiatecki and J. Treiner, At. Dat. Nucl. Dat. Tables, **39**, 225 (1988).

(Möl95) P. Möller, J. R. Nix, W. D. Myers and W. J. Swiatecki, At. Dat. Nucl. Dat. Tables, **59**, 185 (1995).

(Mol80a) D. M. Moltz, R. A. Gough, M. S. Zisman, D. J. Vieira, H. C. Evans and Joseph Cerny, Nucl. Instrum. Methods Phys. Res. **172**, 507 (1980).

(Mol80b) D. M. Moltz, J. M. Wouters, J. Äystö, M. D. Cable, R. F. Parry, R. D. vonDincklage and J. Cerny, Nucl. Instrum. Methods Phys. Res. **172**, 519 (1980).

(Mol89) D. M. Moltz and J. Cerny, in *Particle Emission from Nuclei*, D. N. Poenaru and M. S. Ivascu, eds. (CRC Press, Boca Raton, Florida, 1989), Vol III, p. 133.

(Mol94) D. M. Moltz, J. D. Robertson, J. C. Batchelder and J. Cerny, Nucl. Instrum. Methods Phys. Res. A **349**, 210 (1994).

(Mue91) A. C. Mueller and R. Anne, Nucl. Instrum. Methods Phys. Res. B **56**, 559 (1991).

(Mün79) G. Münzenberg, W. Faust, S. Hofmann, P. Armbruster, K. Güttner and H. Ewald, Nucl. Instrum. Methods Phys. Res. **161**, 65 (1979).

(Mut91) K. Muto, E. Bender and T. Oda, Phys. Rev. C **43**, 1487 (1991).

(Mye66) W. D. Myers and W. J. Swiatecki, Nucl. Phys. **81**, 1 (1966).

(Nan81) H. Nann, A. Saha and B. H. Wildenthal, Phys. Rev. C **23**, 606 (1981).

(Nay95) R. Nayak, V. S. U. Maheswari and L. Satpathy, Phys. Rev. C **52**, 711 (1995).

(Nil55) S. G. Nilsson, Kgl. Danske Videnskab. Selskab., Mat.-Fys. Medd. **29**, no. 16 (1955).

(Nit70) J. M. Nitschke, in Proceedings of the International Conference on the Properties of Nuclei Far From Satbility, Leysin, 1970 (CERN report 70-30, 1970) p. 153.

(Nor70) L. C. Northcliffe and R. F. Schilling, Nucl. Data Tables A **7**, 233 (1970).

(Ogn96) T. J. Ognibene, Ph.D. Thesis, University of California, Berkeley, 1996 (Report No. UC-413/LBNL-38848, unpublished).

(Orm86) W. E. Ormand and B. A. Brown, Phys. Lett. **174B**, 128 (1986).

(Orm89) W. E. Ormand and B. A. Brown, Nucl. Phys. A **491**, 1 (1989).

(Orm95) W. E. Ormand and B. A. Brown, Phys. Rev. C **52**, 2455 (1995).

(Pag92) R. D. Page, P. J. Woods, R. A. Cunningham, T. Davinson, N. J. Davis, S. Hofmann, A. N. James, K. Livingston, P. J. Sellin and A. C. Shotter, Phys. Rev. Lett. **68**, 1287 (1992).

(Pag94) R. D. Page, P. J. Woods, R. A. Cunningham, T. Davinson, N. J. Davis, A. N. James, K. Livingston, P. J. Sellin and A. C. Shotter, Phys. Rev. Lett. **72**, 1798 (1994).

(Pan81) J. Panqueva, H. P. Hellmeister, F. J. Bergmeister and K. P. Lieb, Phys. Lett. **98B**, 248 (1981).

(Pan82) J. Panqueva, H. P. Hellmeister, L. Lühmann, F. J. Bergmeister, K. P. Lieb and T. Otsuka, Nucl. Phys. A **389**, 424 (1982).

(Pap88) A. Pape and M. S. Antony, At. Dat. Nucl. Dat. Tables, **39**, 201 (1988).

(Pie81) R. B. Piercey, J. H. Hamilton, R. Soundranayagam, A. V. Ramayya, C. F. Maguire, X. -J. Sun, Z. Z. Zhoa, R. L. Robinson, H. J. Kim, S. Frauendorf, J. Döring, L. Funke, G. Winter, J. Roth, L. Cleemann, J. Eberth, W. Neumann, J. C. Wells, J. Lin, A. C. Rester and H. K. Carter, Phys. rev. Lett. **47**, 1514 (1981).

(Pek71) L. K. Peker, E. I. Volmyansky, V. E. Bunakov and S. G. Ogloblin, Phys. Lett. **36B**, 547 (1971).

(Pre92) W. H. Press, S. A. Teukolsky, W. T. Vetterling and B. P. Flannery, *Numerical Recipes in C: The Art of Scientific Computing*, 2nd ed. (Cambridge University Press, Cambrdige, 1992).

(Rat91) W. Rathbun, Lawrence Berkeley National Laboratory Report No. LBL-29734/UC-405, 1991 (unpublished).

(Ree73) B. Reehal, and B. H. Wildenthal, Particles and Nuclei, **6**, 974 (1973).

(Rob93) J. D. Robertson, D. M. Moltz, T. F. Lang, J. E. Reiff, Joseph Cerny and B. H. Wildenthal, Phys. Rev. C **47**, 1455 (1993).

(Roe92) E. Roeckl, Rep. Prog. Phys. **55**, 1661 (1992).

(Rol88) C. E. Rolfs and W. S. Rodney, *Cauldrons in the Cosmos* (University of Chicago Press, Chicago, 1988).

(Row97) M. W. Rowe, D. M. Moltz, J. C. Batchelder, T. J. Ognibene, R. J. Tighe and Joseph Cerny, Nucl. Instrum. Methods Phys. Res. A **397**, 292 (1997).

(Row98) M. W. Rowe, D. M. Moltz, T. J. Ognibene, J. Powell and Joseph Cerny, Phys. Rev. C **57**, 2222 (1998).

(Row98a) M. W. Rowe, Ph.D. Thesis, University of California, Berkeley, 1998 (unpublished), Appendix A.

(Sai87) M. G. Saint-Laurent, J. P. Dufour, R. Anne, D. Bazin, V. Borrel, H. Delagrange, C. Détraz, D. Guillemaud-Mueller, F. Hubert, J. C. Jacmart, A. C. Mueller, F. Pougheon, M. S. Pravikoff and E. Roekl, Phys. Rev. Lett. **59**, 33 (1987).

(Sat83) G. R. Satchler, *Direct Nuclear Reactions* (Oxford University Press, New York, 1983).

(Sat88) L. Satpathy and R. C. Nayak, At. Dat. Nucl. Dat. Tables, **39**, 242 (1988).

(Sch95) S. Schmidt, C. Rolfs, W. H. Schulte, H. P. Trautvetter, R. W. Kavanaugh, C. Hategan, S. Faber, B. D. Valnion and G. Graw, Nucl. Phys. A **591**, 227 (1995).

(Sel93) P. J. Sellin, P. J. Woods, T. Davinson, N. J. Davis, K. Livingston, R. D. Page, A. C. Shotter, S. Hofmann and A. N. James, Phys. Rev. C **47**, 1933 (1993).

(Seu90) S. Seuthe, C. Rolfs, U. Schröder, W. H. Schulte, E. Somorjai, H. P. Trautvetter, F. B. Waanders, R. W. Kavanagh, H. Ravn, M. Arnould and G. Paulus, Nucl. Phys. A **514**, 471 (1990).

(Sex73) R. G. Sextro, Ph.D. Thesis, University of California, Berkeley, 1973 (Report No. LBL-2360, unpublished).

(Sex73a) R. G. Sextro, R. A. Gough and J. Cerny, Phys. Rev. C **8**, 258 (1973).

(Sim67) W. D. Simpson, W. R. Jackson and G. C. Phillips, Nucl. Phys. A **163**, 97 (1967).

(Spa88) L. Spanier and S. A. E. Johansson, At. Dat. Nucl. Dat. Tables, **39**, 259 (1988).

(Sta79a) D. P. Stahel, R. Jahn, G. J. Wozniak and J. Cerny, Phys. Rev. C **20**, 1680 (1979).

(Sta79b) D. P. Stahel, Ph.D. Thesis, University of California, Berkeley, 1979 (Lawrence Berkeley Laboratory Report No. LBL-9706, unpublished).

(Sta93) S. Starrfield, J. W. Truran, M. Politano, W. M. Sparks, I. Nofar and G. Shaviv, Phys. Rep. **227**, 223 (1993).

(Ste96) F. Stegmüller, C. Rolfs, S. Schmidt, W. H. Schulte, H. P. Trautvetter and R. W. Kavanagh, Nucl. Phys. A **601**, 168 (1996).

(Str67) V. M. Strutinsky, Nucl. Phys. A **95**, 420 (1967).

(Tac88) T. Tachibana, M. Uno, M. Yamada and S. Yamada, At. Dat. Nucl. Dat. Tables, **39**, 251 (1988).

(Thi81) C. Thibault, F. Touchard, S. Büttgenbach, R. Klapisch, M. deSaintSimon, H. T. Duong, P. Jacquinot, P. Juncar, S. Lieberman, P. Pillet, J. Pinard, J. L. Vialle, A. Pesnell and G. Huber, Phys. Rev. C **23**, 2720 (1981).

(Tig94) R. J. Tighe, D. M. Moltz, J. C. Batchelder, T. J. Ognibene, M. W. Rowe and Joseph Cerny, Phys. Rev. C **49**, R2871 (1994).

(Tig95) R. J. Tighe, J. C. Batchelder, D. M. Moltz, T. J. Ognibene, M. W. Rowe, J. Cerny and B. A. Brown, Phys. Rev. C **52**, R2298 (1995).

(Tru85) J. W. Truran, in *Nucleosynthesis: Challenges and New Developments*, W. D. Arnett and J. W. Truran, eds. (University of Chicago Press, Chicago, 1985), p. 292.

(Tso95) N. Tsoulfanidis, *Measurement and Detection of Radiation*, 2nd ed., (Taylor and Francis Publishing, Washington, D. C., 1995).

(van81) A. G. M. van Hees and P. W. M. Glaudemans, Z. Phys. A **303**, 267 (1981).

(Vie78) D. J. Vieira, Ph.D. Thesis, University of California, Berkeley, 1978 (Report No. LBL-7161, unpublished).

(Wak97) T. Wakasa, H. Sakai, H. Okamura, H. Otsu, S. Fujita, S. Ishida, N. Sakamoto, T. Uesaka, Y. Satou, M. B. Greenfield and K. Hatanaka, Phys. Rev. C **55**, 2909 (1997).

(Wal81) R. K. Wallace and S. E. Woosley, Astrophys. J. Suppl. **45**, 389 (1981).

(Wei35) C. F. von Weizsäcker, Z. Phys. **96**, 431 (1935).

(Wei90) A. Weiss and J. W. Truran, Astron. Astrophys. **238**, 178 (1990).

(Wie86a) M. Wiescher, J. Görres, F.-K. Thielemann and H. Ritter, Astron. Astrophys. **160**, 56 (1986).

(Wie86b) M. Wiescher and K. Langanke, Z. Phys. A **325**, 309 (1986).

(Wig57) E. P. Wigner, Proc. of the Robert A. Welsch Conference on Chemical Research (R. A. Welsch Foundation, Houston Texas, 1957), vol. 1, p. 67.

(Wil69) D. H. Wilkinson, in *Isospin in Nuclear Physics*, D. H. Wilkinson, ed. (North Holland Publishing Co., Amsterdam, 1969), p. 1.

(Wil73) D. H. Wilkinson, Nucl. Phys. A **209**, 470 (1973).

(Wil74) D. H. Wilkinson and B. E. F. Macefield, Nucl. Phys. A **232**, 58 (1974).

(Wil77) B. H. Wildenthal, in *Elementary Modes of Excitation in Nuclei*, A. Bohr and R. A. Broglia, eds. (North Holland Publishing Co., Amsterdam, 1977), p. 383.

(Wil83) B. H. Wildenthal, in *Progress in Particle and Nuclear Physics*, vol. **11**, D. Wilkinson, ed., (Pergammon Press, Oxford, 1983), p. 5.

(Wol76) H. Wollnik, Nucl. Instrum. Methods Phys. Res. **139**, 311 (1976).

(Woo93) P. J. Woods, T Davinson, N. J. Davis, A. N. James, K. Livingston, R. D. Page, P. J. Sellin and A. C. Shotter, Nucl. Phys. A **553**, 485 (1993).

(Woo97) P. J. Woods and C. N. Davis, Ann. Rev. Nucl. Part. Sci. **47**, 541 (1997).

(Xie91) Z. Xie, C. M. Lyneis, R. S. Lam and S. A. Lundgren, Rev. Sci. Instrum. **62**, 775 (1991).

(Zho85) Z. Y. Zhou, E. C. Schloemer, M. D. Cable, M. Ahmed, J. E. Reiff and J. Cerny, Phys. Rev. C **31**, 1941 (1985).

A P P E N D I X A

PROTON DECAY CODE

Description

This Appendix contains the C++ source code for the barrier-penetration program "thruBarrier 2.1", which has been used to calculate proton-decay rates several times in this thesis. It is based on the WKB approximation approach described in Section 2.2.2.1 (see also Hof89, Hof93). As a default, it uses the optical-model parameters of Becchetti and Greenlees (Bec69) to calculate the barrier for proton decay. These parameters were extracted from a fit of experimental (E < 50 MeV) proton-scattering data on A > 40 targets. Although Becchetti and Greenlees report that this parameterization does not fit the data for lower mass targets well, they ascribe this to deficiencies in the imaginary part of the potential, which is not used in these calculations. Thus it is uncertain whether these parameters should be used for low-mass (beta-delayed?) proton emitters.

This code is able to reproduce (within ~1%) the (WKB-) calculated proton-decay half-lives given in references Irv97, Dav97, Woo97 and Bat98. It gives reasonable agreement (within ~10%) with the calculated half-lives in Hof89. Among the light (A < 60) nuclei, it sometimes fails due to one of two problems. For decays with relatively-large Q-values and small angular momenta, the proton energy is often "above" the barrier; the partial half-life is then determined solely by the frequency factor. In other cases, the proton energy is such that it lies below the minimum of the potential inside the well; this causes the calculation to abort. In either case, the user is notified of the problem. I hope to address the latter problem in the near future.

If you find this code to be useful, I would be interested in any feedback you could give me. If you use it in the preparation of a published work, please cite this dissertation as a reference.

Source Code in C++

```
/* thruBarrier:  Barrier penetration code to calculate proton-decay
transition probabilities using the WKB approximation, following the
discussion of S. Hofmann in Particle Emission from Nuclei, D. N.
Poenaru and M. S. Ivascu, eds. (CRC Press, Boca Raton, FL 1983) vol.
II, pp. 27-31.  Uses numerical integration to determine the Gamow
factor as a function of the potential.

Version 2.1:  Allows calculations for multiple cases, by looping.
After initial calculation, permits user to change the optical model
parameters.  Fixed problem with calculation of angular momentum from
selection rules.

Sorry for the ugly code.  It works pretty well though.

Copyright M.W.Rowe, Lawrence Berekeley National Laboratory, 1998  */

#include <math.h>
#include <iostream.h>
#include <iomanip.h>
#include <stdlib.h>
int main () {
  const double e_sqrd = 1.439976;     //  MeV*fm (unit charge squared)
  const double h_bar = 6.58217e-22;   //  MeV*s (h/2π)
  const double lambda_pi_sqrd = 1.9980;
                                // fm*fm (pion Compton wavelength sqr'd)
  const double h_bar_c = 197.329;     //  MeV*fm
  const double pi = 3.14159265359;
  const double lightSpeed = 2.99792458e8; // m/s
  const double amu = 931.49386;           // atomic mass unit, MeV
  //  Get decay parameters for specific decay from user.
  cout << "-----------------------------------------------------""";
  cout << "------------------------" << endl << endl;
  cout << "Program ThruBarrier 2.1" << endl << endl << endl;
  cout << "This code calculates proton decay partial half-lives, ";
```

```
cout << "using the semi-classical" << endl << endl;
cout << "(WKB) approximation.  The decay barrier is a sum of ";
cout << "nuclear, spin-orbit, Coulomb" << endl << endl;
cout << "and centrifugal components which are calculated using the ";
cout << "Becchetti and " << endl << endl;
cout << "Greenlees optical model parameters [A>40, E<50 MeV; ";
cout << "Phys. Rev. 182, 1190 (1969)]." << endl << endl;
cout << "The proton energy is corrected for electron screening ";
cout << "based on the tables of " << endl << endl;
cout << "Huang et al. [At. Data Nucl. Data Tables 18, 243 ";
cout << "(1976)]. The integration is " << endl << endl;
cout << "carried out numerically.  See S. Hofmann, in ";
cout << "*Particle Emission From Nuclei*," << endl << endl;
cout << "vol. II, D. N. Poenaru and M. S. Ivascu, eds., ";
cout << "(CRC Press, Boca Raton, 1989)"<< endl << endl;
cout << "pp. 29-31." << endl << endl << endl;
cout << "Copyright 1998, M. W. Rowe and Lawrence Berkeley National ";
cout << "Laboratory" << endl << endl;
cout << "-------------------------------------------------";
cout << "------------------------------" << endl << endl;
double particle_A = 1.0072764666;        // (nuclear) mass of proton
int particle_Z = 1;
cout << endl << "Enter the atomic number (Z) of the proton emitter:"
  << endl;
int parent_Z, daughter_Z;
cin >> parent_Z;
daughter_Z = parent_Z - 1;
cout << endl << "Enter the mass (A) of the proton emitter:" << endl;
float parent_A, daughter_A;
cin >> parent_A;
daughter_A = parent_A - 1;
cout << endl << "Enter the laboratory proton energy in keV:" << endl;
double E_lab;
cin >> E_lab;
E_lab /= 1000;
double Q_value = E_lab * (daughter_A + 1.0) / daughter_A;
// get  J,    of transition; determine angular momentum of the proton
cout << endl << "Enter  J between the inital and final state as a"
  << " decimal:" << endl;
double delta_J;
cin >> delta_J;
```

```
cout << endl << "Is there a parity change between the states? (Y/N)"
  << endl;
char parity_change = '-';
while (!(((parity_change == 'y') || (parity_change == 'Y')) ||
  ((parity_change == 'n') || (parity_change == 'N'))))
  cin >> parity_change;
int l_value = ((parity_change=='n') || (parity_change=='N')) ? 0: 1;
while (abs(2*delta_J - 2*l_value) != 1) l_value = l_value + 2;
//  optical model parameters from Becchetti and Greenlees.
bool becchetti_Greenlees_depth = true;
double r_nought_const =     1.17; //fm  (nuclear radius)
double r_spinOrbit_const =  1.01; //fm  (spinOrbit radius)
double r_Coulomb_const =    1.21; //fm  (Coulomb radius)
double diffuse =            0.75; //fm  (nuclear diffuseness)
double diffuse_spinOrbit =  0.75; //fm  (spin-orbit diffuseness)
double V_depth_spinOrbit =  6.2;  //MeV (depth of spinOrbit potential)
double V_depth;                   //  MeV (nuclear well depth)
bool warningFlag;
do {
  warningFlag = false;
  cout << endl << "-----------------------------------------";
  cout << "-----------------------------------" << endl << endl;
  double E_screening = -0.022518 + 0.036558*(daughter_Z+1.0)
    + 0.0052761*pow((daughter_Z+1.0),2)
    - 0.00011501*pow((daughter_Z+1.0),3)
    + 1.7462E-6*pow((daughter_Z+1.0),4)
    - 1.3334E-8*pow((daughter_Z+1.0),5)
    + 4.2095E-11*pow((daughter_Z+1.0),6);
  double Q_p_nucl = Q_value + E_screening/1000;
  cout << "parent (Z,A): " << parent_Z << ", " << parent_A << endl;
  cout << "E(p,lab) = " << E_lab*1000 << " keV" << endl;
  cout << "E(p,cm) = " << Q_value*1000 << " keV" << endl;
  cout << "screening = " << E_screening << " keV" << endl;
  cout << "Q(p,nuclear) = " << Q_p_nucl*1000 << " keV" << endl;
  cout << "l = " << l_value << ",  J = " << round(delta_J*2)
    << "/2" << endl << endl;
  //  Calculate derived parameters and constants.
  if (becchetti_Greenlees_depth) {
    V_depth = 54.0 - 0.32*E_lab
      + 0.4*daughter_Z/pow(daughter_A,1.0/3.0)
      + 24.0*(daughter_A - 2.0*daughter_Z)/daughter_A;
```

```
}
double reduced_mass =
  amu*particle_A*daughter_A/(particle_A+daughter_A);
double r_nought = r_nought_const*pow(daughter_A,1.0/3.0);
double r_Coulomb = r_Coulomb_const*pow(daughter_A,1.0/3.0);
double r_spinOrbit = r_spinOrbit_const*pow(daughter_A,1.0/3.0);
double sigma_dot_l;
if (delta_J > l_value) sigma_dot_l = l_value;
else sigma_dot_l = -(l_value + 1);
cout << "Nuclear well depth: " << V_depth << " MeV" << endl;
cout << "Nuclear radius (r_o = " << r_nought_const << "): " <<
  r_nought << " fm" << endl;
cout << "Nuclear skin thickness: a = " << diffuse << " fm" << endl;
cout << "Spin-orbit well depth: " << V_depth_spinOrbit << " MeV"
  << endl;
cout << "Spin-orbit radius (r_so = " << r_spinOrbit_const << "): "
  << r_spinOrbit << " fm" << endl;
cout << "Spin-orbit skin thickness: a = " << diffuse_spinOrbit
  << " fm" << endl;
cout << "Coulomb radius (r_c = " << r_Coulomb_const << "): "
  << r_Coulomb << " fm" << endl << endl;
//  Calculate the frequency factor.
double frequency =
  sqrt(2.0)*pi*pi*h_bar*h_bar*lightSpeed*lightSpeed*lightSpeed
  /(r_Coulomb*r_Coulomb*r_Coulomb*pow(reduced_mass,1.5)*1e-45*
  sqrt(daughter_Z*particle_Z*e_sqrd/r_Coulomb - Q_p_nucl));
cout << "frequency factor = " << frequency << " Hz" << endl;
cout << "minimum half-life = " << log(2.0)/frequency << " s"
  << endl;
//  Calculate the Gamow factor by numerical integration;
double dRadius = 0.001;                    //  radius step
double radius = dRadius/2.0;
double prev_V_total = 0.0;
double V_nuclear, V_Coulomb, V_spinOrbit, V_centrifugal, V_total;
double GamowIntegral = 0.0;
bool enteredWell = false;
  // for small r, Q < barrier; true if Q > barrier
bool isIn = false;     // has the proton entered the outer barrier?
bool isOut = false;    // has the proton passed out of the barrier?
double barrier_height = 0.0;  // maximum height of barrier
while (!isOut) {
```

```
V_nuclear = -V_depth/(1.0 + exp((radius - r_nought)/diffuse));
if (radius < r_Coulomb) {
  V_Coulomb = (daughter_Z*particle_Z*e_sqrd/(2.0*r_Coulomb))
    * (3.0 - (radius*radius)/(r_Coulomb*r_Coulomb));
}
else V_Coulomb = daughter_Z*particle_Z*e_sqrd/radius;
V_spinOrbit =
  V_depth_spinOrbit*sigma_dot_l*lambda_pi_sqrd/radius;
double deriv_V_spinOrbit = ((1.0/(1.0+exp((radius+dRadius*0.5
  -r_spinOrbit)/diffuse_spinOrbit)))-(1.0/(1.0+exp((radius-
  dRadius*0.5-r_spinOrbit)/diffuse_spinOrbit))))/dRadius;
V_spinOrbit *= deriv_V_spinOrbit;
V_centrifugal = l_value*(l_value+1.0)*h_bar_c*h_bar_c
  /(2.0*reduced_mass*radius*radius);
V_total = V_nuclear + V_Coulomb + V_spinOrbit + V_centrifugal;
// OUTPUT POTENTIALS as function of radius; UNCOMMENT TO ACTIVATE
// cout << endl << radius << "   " << V_nuclear << "   "
// << V_Coulomb << "   " << V_spinOrbit << "   " << V_centrifugal
// << "   " << V_total;
if (((prev_V_total+V_total)/2.0 > Q_p_nucl) && enteredWell) {
  if (!isIn) {
    isIn = true;
    cout << endl << "Entered barrier at " << radius << " fm.";
  }
  GamowIntegral += sqrt((prev_V_total+V_total)/2.0 - Q_p_nucl) *
    dRadius;
}
else {
  if ((prev_V_total+V_total)/2.0 < Q_p_nucl) enteredWell = true;
  if (isIn) {
    isOut = true;
    cout << endl << "Exited barrier at " << radius << " fm."
      << endl;
  }
}
if (enteredWell && (barrier_height < V_total))
  barrier_height=V_total;
if ((radius > 10.0 * r_nought) && (barrier_height < Q_p_nucl)) {
  cout << endl << endl;
  warningFlag = true;
  if (barrier_height > 0) {
```

```
        cout << "WARNING: Proton energy is greater than the barrier "
          << "height (";
        cout << barrier_height*1000.0 << " keV)." << endl << endl;
      }
      else {
        cout << "Potential-energy minimum is greater than the proton"
          << " energy." << endl << endl;
      }
      cout << "UNABLE TO CALCULATE PROTON DECAY HALF-LIFE FOR THESE"
        << " CONDITIONS";
      cout << endl << endl;
      break;              // ABORT THIS HALF-LIFE CALCULATION
    }
    radius += dRadius;
    prev_V_total = V_total;
  }
  if (!warningFlag) {
    GamowIntegral *= -2.0*sqrt(2.0*reduced_mass/(h_bar_c*h_bar_c));
    double half_life = log(2.0)/(frequency * exp(GamowIntegral));
    cout << "Maximum barrier height = " << barrier_height*1000.0
      << " keV." << endl << endl
      << "The calculated half-life for this decay is:"
      << endl << endl << half_life << " s.   (width = "
      << log(2.0)*h_bar/half_life << " MeV)" << endl << endl;
  }
  int choice;
  cout << "-----------------------------------------------------";
  cout << "--------------------------";
  do {
    cout << endl << "Enter one of the following: " << endl;
    cout << "(0)  Quit" << endl;
    cout << "(1)  Change nucleus" << endl;
    cout << "(2)  Change decay energy" << endl;
    cout << "(3)  Change angular momentum" << endl;
    cout << "(4)  Change optical model parameters" << endl;
    cout << "(5)  Recalculate half-life" << endl;
    cin >> choice;
    cout << endl;
    if (choice == 0) {
      cout << endl << "Program execution terminated (choose Quit"
        << " from the File menu.)";
```

```
    exit(1);
  }
  else if (choice == 1) {
    cout << "Current proton emitter (Z,A): " << parent_Z << ", "
      << parent_A << endl << endl;
    cout << "Enter new atomic number (Z) of the proton emitter:"
      << endl;
    cin >> parent_Z;
    daughter_Z = parent_Z - 1;
    cout << endl << "Enter new mass (A) of the proton emitter:"
      << endl;
    cin >> parent_A;
    daughter_A = parent_A - 1;
  }
  else if (choice == 2) {
    cout << "Current proton energy: " << E_lab*1000.0 << " keV"
      << endl;
    cout << endl << "Enter new laboratory proton energy:" << endl;
    cin >> E_lab;
    E_lab /= 1000;
    Q_value = E_lab * (daughter_A + 1.0) / daughter_A;
  }
  else if (choice == 3) {
    cout << "For current transition,  J = " << trunc(2*delta_J) <<
      "/2,    = ";
    if ((parity_change == 'n') || (parity_change == 'N'))
      cout << "NO";
    else cout << "YES";
    cout << ", l = " << l_value << endl;
    cout << endl << "Enter  J between the inital and final state "
      << "as a decimal:" << endl;
    cin >> delta_J;
    cout << endl << "Is there a parity change between the states?"
      << " (Y/N)" << endl;
    parity_change = '';
    while (!(((parity_change=='y') || (parity_change=='Y')) ||
      ((parity_change=='n') || (parity_change=='N'))))
        cin >> parity_change;
    l_value = ((parity_change=='n')||(parity_change=='N')) ? 0: 1;
    while (abs(2*delta_J - 2*l_value) != 1) l_value = l_value + 2;
  }
```

```
    else if (choice ==4) {
      cout << "You will be asked for new values for each constant. "
        << " The values shown in parenthesis" << endl;
      cout << "are the Becchetti and Greenlees values.  The current "
        << " values are also shown." << endl << endl;
      cout << "nuclear well depth (V = " <<
        54.0 - 0.32*E_lab + 0.4*daughter_Z/pow(daughter_A,1.0/3.0)
        + 24.0*(daughter_A - 2.0*daughter_Z)/daughter_A << " MeV): "
        << V_depth << " MeV" << endl;
      cout << "[enter 0 for Becchetti and Greenlees value (A, Z "
        << "dependent)]" << endl;
      cin >> V_depth;
      becchetti_Greenlees_depth = !round(V_depth);
      cout << "nuclear radius constant (R_o = 1.17): "
        << r_nought_const << " fm" << endl;
      cin >> r_nought_const;
      cout << "nuclear skin thickness (a = 0.75): " << diffuse
        << " fm" << endl;
      cin >> diffuse;
      cout << "spin-orbit well depth (V_so = 6.2 MeV): "
        << V_depth_spinOrbit << " MeV" << endl;
      cin >> V_depth_spinOrbit;
      cout << "spin-orbit radius constant (R_so = 1.01): "
        << r_spinOrbit_const << " fm" << endl;
      cin >> r_spinOrbit_const;
      cout << "spin-orbit skin thickness (a_so = 0.75): "
        << diffuse_spinOrbit << " fm" << endl;
      cin >> diffuse_spinOrbit;
      cout << "Coulomb radius constant (R_c = 1.21): "
        << r_Coulomb_const << " fm" << endl;
      cin >> r_Coulomb_const;
    }
    cout << endl;
  } while (choice != 5);
} while (true);
return 0;
}
```